Unravelling the Kinematic Evolution of Segmented Rift Systems

Alodie Bubeck

School of Earth and Ocean Sciences
Cardiff University

Submitted in partial fulfilment of the requirements for the degree of
Doctor of Philosophy.

May 2016

Summary

Normal fault systems within incipient rifts comprise an array of small-scale structures, including networks of fractures and small displacement faults (<15 m) that represent the incremental strains that develop during rift propagation. To constrain the evolution of volcanic rift systems, I investigate rift-fault propagation and localisation at a range of scales using laboratory-based mechanical characterisation of host rocks, and high-resolution structural mapping of faults, and fault-related deformation in an incipient (Koa'e fault system, Hawai'i), and evolved (Krafla fissure swarm, Iceland) rift system.

Experimental analysis of pahoehoe lava from Kilauea's south flank, Hawai'i, highlight a distinctive physical and mechanical stratigraphy related to the volume, and geometry, of voids within the lava. The resulting variability in intact strength produces the effect of a multi-layered sequence within a single lava, and will exert significant control on the segmentation and linkage of initial cracks (mm-scale or less) that develop. High-resolution mapping of the distribution, geometry, and kinematics of cm- to km-scale extensional strains in the Koa'e fault system (Hawai'i) and the Krafla fissure swarm (Iceland) also reveals evidence for segmented fault propagation, linkage and non-coaxial strain. This segmentation is a function of the varying natural mechanical anisotropy of the deforming sequence and non-uniform strain rates.

Results from the Koa'e and Krafla rifts are compared with break-up related deformation from the NE Atlantic margins to model the evolution of non-coaxial fault sets at the margin scale. Fault and intrusion data from the Faroe Islands and East Greenland highlights geometrically and kinematically comparable structural sets, implying an analogous kinematic evolution of inter-rift strains. I infer that stress transfer during NE Atlantic opening took place by sub-basin scale ancillary faults and dikes, associated with two overlapping, active rift systems in the Paleogene – a NE-propagating Reykjanes ridge, and a SW-propagating Aegir ridge – rather than via *transfer fault segmentation*.

Acknowledgements

Well then, here I am. Writing my acknowledgements. This is not something I ever envisaged doing during the last 3.5 years and it is surprisingly difficult to know where to start. This thesis has been influenced and supported by many.

My thanks are first extended to my supervisor in Cardiff, Chris MacLeod for helping me navigate the early stages of my project and always providing me with advice and encouragement. I would also like to acknowledge the wonderful Jonny Imber from Durham University who gave up many hours of his time to discuss fault growth and read the fault-data chapters in this thesis.

Special thanks must go to the staff and postgraduate community in the Geology Department at the University of Leicester who made me feel instantly welcomed and included when I moved from Cardiff. Particular thanks goes to the postgraduates in Leicester and Cardiff who cheered me through this journey and lifted me during the darker periods: Phil Smith, Thomas Clements, Tara Stephens, Angie Castagna, Takkie Kawanzaruwa, Matt Loocke (Cardiff) and Dan Morgan (also Cardiff). My work, and my understanding of research has also benefitted from lengthy discussions with Richard England and Dave Holwell.

The list of thanks to those who led me here and those who provided technical help, discussion and support is throughout is extensive, and without it none of this work would have been possible. Massive thanks goes to Bones, Bob, Ken and Mark Pearce from Durham University who took me on as a recent undergraduate to GRL, turned me into a geologist and encouraged me to research and apply for PhDs. Thank you to Åke Fagereng and Tom Blenkinsop in Cardiff for extensive discussion, encouragement and advice. Also at Cardiff: Tony Oldroyd, Andrew Wiltshire and Gwen Pettigrew for IT support. At the BGS, I would like to extend my thanks to Marcus Dobbs, Audrey Ougier-Simonin and Matt Kirkham. At the University of Leicester my thanks are extended to Colin Cunningham (for help with XRF tests and for allowing me do the hot and dangerous bit), Andrew Myers for many, many hours of IT support and Cheryl Haidon for the seemingly endless hours on the CT scanner. This work has also benefitted from many lengthy discussions and with staff at HVO, Hawaii, in particular Don Swanson who gave an unforgettable tour of the Koa'e fault system and went out of his way to gather and digitise notebook data from 1965 for me, and always made time to send long and considered responses to my emails. My thanks also to Mike Poland who also provided me with a dGPS during my first field season, taught me to operate it and helped process my data.

Perhaps the easiest person to thank (though certainly not to his face) is Richard Walker. Rich has been an endlessly supportive and encouraging supervisor throughout my PhD, and while this support always manifested itself in different forms, their true meaning and purpose has always been clear: to make me a better, more confident researcher. He is also happy to share food, beer and an umbrella-shelter when it starts to snow on a cliffside in the Faroe Islands, even after you have spent several minutes mocking him for carrying one in the first place. This I am also rather grateful for…

And finally, without the support of my family and my friends, none of this would have been possible: Mum, Kit, Grandad, Lizzy, Christie, Max, Geoff and Therese. You all gave me the confidence to take the leap and have cheered me on the whole way.

Table of Contents

Summary i

Acknowledgements ii

Table of Contents iii

List of Figures ix

Chapter 1.

Introduction

1.1 Introduction *1*

1.2 Thesis Structure *3*

1.3 Terminology *6*

Chapter 2.

Scientific Background

2.1 **Growth of Normal Faults** *9*

2.1.1 Observations from Field-Based Studies of Segmented Faults *16*

2.1.1.1 Soft Linked Relay Zones *17*

2.1.1.2 Transfer Zones *19*

2.1.2 Rock Fracture *22*

2.1.2.1 Modes of Fracturing *22*

2.1.2.2. Theoretical Fracture Development in Intact Materials *28*

2.1.3 Scaling of Fault Populations *35*

2.1.4. 2D Analytical Modelling *38*

Chapter 3.

Physical and Mechanical Properties of Basaltic Lavas: Kilauea Pahoehoe

3.1 **Introduction** *43*

3.2 **Background** *46*

3.2.1. Rock Strength *46*

3.2.2. Stress Concentrations *50*

3.2.3. Compound Lava Unit Characterisation *53*

3.3 **Datasets** *57*

3.3.1. Sample Collection: The Kulanaokuaiki Fault Trace *57*

3.3.2. Sample Preparation *64*

3.3.3. Measuring Porosity and Density *66*

3.3.4. Unconfined Compressive Strength *67*

3.4 **Results** *71*

3.4.1. Porosity and Density *71*

3.4.2. Unconfined Rock Strength *73*

3.4.3. Young's Modulus *81*

3.5 **Discussion** *83*

3.5.1. Mechanical Properties of Porous Solids *85*

3.5.5.1. Mechanical Properties of Basalt *87*

3.5.2. Effect of Porosity on Fracture Growth *90*

3.5.3. Effect of Pore Geometry *93*

3.5.4. Fault Propagation in Basaltic Sequences *97*

3.6 **Summary** *100*

Chapter 4.

Rift-fault Segmentation: the Koa'e Fault System, Hawai'i

4.1 **Introduction** *103*

4.2 **Background** *106*

4.2.1. Geological Setting *106*

4.2.2. The Hilina Fault System *111*

4.2.3. The Koa'e Fault System *111*

4.3 **Datasets** *114*

4.3.1. Data Analysis *114*

4.3.2. Field Mapping *119*

4.4 **Results** *121*

4.4.1. Fracture Geometry and Distribution *121*

4.4.4.1. Fracture Distribution and Scaling *121*

4.4.4.2. Fracture Kinematics and Segmentation *125*

4.4.4.3. Fracture Interaction *134*

4.4.2. Surface Flexure *137*

4.4.3. Fault Geometry and Distribution *143*

4.5 **Discussion** *150*

4.5.1. Segmentation and Interaction in the Koa'e Fault System *152*

4.5.1.1. Evidence for Segmentation and Interaction: Path Geometry *153*

4.5.1.2. Evidence for Segmentation and Interaction: D-L Profiles *156*

4.5.2. Mechanical Layering *158*

4.5.2.1. Pre-Existing Cooling Joints *159*

4.5.2.2. Magmatic Influence 164

4.5.3. Lateral Fault Propagation 166

4.6 **Summary** 171

Chapter 5.

Rift-Fault Segmentation: the Krafla Fissure Swarm, NE Iceland

5.1 **Introduction** 173

5.2 **Geological Setting** 175

5.2.1. The Krafla Fissure Swarm 179

5.3 **Datasets** 180

5.3.1 Field Mapping 182

5.4 **Results** 184

5.4.1. Fracture Distribution and Scaling 184

5.4.1.1. Fracture Kinematics and Segmentation 187

5.4.2. Fault Geometry and Distribution 193

5.4.2.1. Fault Kinematics and Segmentation 202

5.4.3. Surface Flexure 206

5.5 **Discussion** 208

5.5.1. Segmentation and Interaction in the Krafla Fissure Swarm 209

5.5.1.1. Evidence for Segmentation and Interaction: Path Geometry 209

5.5.1.2. Evidence for Segmentation and Interaction: D-L Profiles 212

5.5.2. Lateral Fault Propagation 213

5.5.3. Implications for Rift Zone Kinematics 217

5.6 **Summary** *224*

Chapter 6.

Discussion

6.1 **Comparison of the Koa'e Fault System and Krafla Fissure Swarm** *226*

6.1.1 Structural Style *226*

6.1.2. Magmatic Effects *229*

6.1.3. Mechanical Stratigraphy *234*

6.2 **Rift Fault Development in Layered Basaltic Sequences** *238*

6.3 **Implications for Porosity Maintenance** *243*

6.4 **Evolution of Inter-Rift Zones: the NE Atlantic** *247*

6.4.1 European Margins (Faroe Islands) *249*

6.4.2 North American Margin (Kangerlussuaq, E Greenland) *251*

6.4.3. Comparison with the Krafla Analogue *253*

6.4.4. Scaling of Interpretations *259*

6.4.5. A Dual-Rift Model *261*

Chapter 7.

Conclusions and Further Research

7.1 **Conclusions** *266*

7.2 **Further Research** *269*

7.2.1 Rock Strength Anisotropy *269*

7.2.2. Crack Propagation in Porous Solids *272*

7.2.3. Numerical and Analogue Modelling *274*

7.2.4. The role of Cooling Joints in Normal Fault Growth *276*

Appendices

Appendix I *278*

References

References *294*

List of Figures

Chapter 2.

Scientific Background

2.1	Schematic illustration of the isolated and coherent fault model	*11*
2.2	Evolution of an isolated normal fault array	*14*
2.3	Strain transfer in an accommodation zone	*17*
2.4	Types of antithetic accommodation zone	*18*
2.5	Types of synthetic accommodation zone	*19*
2.6	Types of transfer zone	*20*
2.7	Fracture modes	*23*
2.8	Mohr-Coulomb failure in a compressional setting	*25*
2.9	Failure envelope for intact rock and the re-shear condition	*27*
2.10	Example of a crack in a linear elastic solid	*29*
2.11	Stress conditions surrounding the tip of a crack	*34*
2.12	Plot of maximum displacement against length from a range of fault studies	*36*
2.13	State of stress surrounding two en echelon spreading ridge segments	*39*
2.14	State of stress surrounding two en echelon normal fault segments	*41*

Chapter 3.

Physical and Mechanical Properties of Basaltic Lavas: Kilauea Pahoehoe

3.1	Examples of refracted fault geometries and cutting of pre-existing cooling joints by fault sets	*44*
3.2	A typical stress-axial strain curve	*47*
3.3	Stress-strain curve showing axial, lateral and volumetric strain	*49*
3.4	Pore-emanating crack model	*52*
3.5	Examples of basaltic lavas	*54*
3.6	Lava stratigraphy	*55*
3.7	Location of the Kulanaokuaiki Fault in the Koa'e Fault System, Hawai'i	*58*
3.8	Schematic stratigraphic logs through 3 separate lava units	*61*
3.9	Stratigraphy through a 3.00 x 0.58 m lava lobe	*62*
3.10	Example of lava unit	*63*
3.11	Images of sample collection and core orientations	*65*
3.12	Sample preparation	*66*
3.13	Images of sample cores	*68*
3.14	UCS test sample setup	*69*
3.15	Stress-strain curves depicting class I and class II behaviour	*70*
3.16	Variation of effective porosity with dry density for each orientation	*72*
3.17	Variation of effective porosity with dry density for all samples	*73*
3.18	Images of a selection of tested samples	*74*
3.19	Variation in unconfined compressive strength (density/porosity)	*75*

3.20	Example of axial stress Vs strain curves for (upper) top lava samples	*77*
3.21	Example of axial stress Vs strain curves for (lower) top lava samples	*78*
3.22	Example of axial stress Vs strain curves for lava core samples	*79*
3.23	Example of axial stress Vs strain curves for lava base samples	*80*
3.24	A comparison of full stress-strain curves for all samples	*81*
3.25	Comparison of Young's modulus and UC strength	*82*
3.26	Summary of the vertical mechanical stratigraphy through a lava	*83*
3.27	Comparison of Young's modulus with varying porosity	*84*
3.28	Comparison of Young's modulus results for porous ceramics	*86*
3.29	Engineering classification of vesicular basalts and result errors	*88*
3.30	Crack propagation pathways in tested samples	*91*
3.31	Summary of tested samples from the lava base	*94*
3.32	Model of vertical segmentation of fractures in multilayer sequences	*98*
3.33	Fault propagation through basaltic sequence	*99*

Chapter 4.

Rift-fault Segmentation: the Koa'e Fault System, Hawai'i

4.1	Map of the Hawaiian-Emperor Chain	*107*
4.2	Topographic and bathymetric image of Hawai'i and the study area	*108*
4.3	A cross-section through Kilauea Volcano	*109*
4.4	Model of fault development	*113*
4.5	Use of satellite and aerial LiDAR-derived hillshade images	*116*
4.6	Use of satellite and aerial LiDAR-derived hillshade images	*117*

4.7	Map of fault and fracture map of the Koa'e fault system	*118*
4.8	Method of data collection	*120*
4.9	Extension fractures in the Koa'e fault system	*122*
4.10	Distribution of fracture lengths and apertures	*123*
4.11	Population distribution plots	*124*
4.12	Aerial LiDAR-derived DEM for the mapped area	*126*
4.13	Total displacement profiles for fractures in the AOI	*127*
4.14	Flexure height/aperture - length profile for fracture set A	*128*
4.15	D-L profiles for fracture set B	*130*
4.16	Throw-aperture-length profile for fractures set C	*131*
4.17	D-L profiles for fracture set D	*132*
4.18	D-L profiles for fracture set E	*133*
4.19	Calculating D-L profile asymmetry	*135*
4.20	Example of profile asymmetry	*136*
4.21	Example of profile asymmetry	*136*
4.22	Aerial and cross-sectional view of a surface flexure	*138*
4.23	Examples of laterally continuous surface flexures	*139*
4.24	Examples of laterally discontinuous surface flexures	*140*
4.25	Map view of discontinuous surface flexures	*142*
4.26	Examples of surface-breaching fault segments	*144*
4.27	Satellite image of the full extent of Fault A	*145*
4.28	Deformation associated with set A	*146*
4.29	Deformation associated with set C	*148*
4.30	Characteristic views of the relay bounding faults in the AOI	*149*
4.31	Theoretical fracture propagation pathways	*154*

4.32	Example of fracture pathways from the Koa'e	*154*
4.33	Fracture segment linkage	*156*
4.34	Displacement asymmetry	*157*
4.35	Theoretical reactivation of joints	*160*
4.36	Joint strength influence on fault growth	*162*
4.37	Distribution of seismicity and fault deformation	*165*
4.38	Model of lateral fault growth in the Koa'e fault system	*168*
4.39	Location of new fractures related to the 1965 cracking event	*170*

Chapter 5.

Rift-Fault Segmentation: the Krafla Fissure Swarm, NE Iceland

5.1	Map of Iceland	*176*
5.2	Seismicity map of Iceland and tectonic features of the TFZ	*178*
5.3	Map of the Krafla and Theistareykir fissure swarms	*181*
5.4	Method of measuring fracture geometry and kinematics	*182*
5.5	Mapped structures in the Gjastykki Valley	*185*
5.6	Distribution of fracture lengths	*186*
5.7	Frequency of fracture orientations	*187*
5.8	Mapped structures in the AOI	*188*
5.9	Examples of linkage shown in displacement profiles	*189*
5.10	D-L Profiles for rift-parallel fracture sets	*190*
5.11	D-L Profiles for rift-normal fracture sets	*191*
5.12	D-L Profiles for oblique fracture sets	*192*

5.13	Examples of surface-breaking faults in the AOI	*194*
5.14	Mapped structural sets and relay zone geometry	*195*
5.15	Views of faults in AOI	*197*
5.16	Segmentation at the lateral terminations of faults in the AOI	*199*
5.17	Location of minor graben in the Gjastykki valley	*200*
5.18	Images of minor graben-bounding faults	*201*
5.19	Mapped fracture orientations and extension direction for each set	*203*
5.20	Summary of kinematics and throw profiles in the AOI	*204*
5.21	Examples of surface flexure in the Krafla fissure swarm	*207*
5.22	Aerial image of the AOI	*210*
5.23	Analytical solution for shear stress surrounding en echelon faults	*211*
5.24	Inferred progressive stress rotation model evolution of the AOI	*215*
5.25	Comparison fault-scale with en echelon rift segment-scale	*218*

Chapter 6.

Discussion

6.1	Comparison of structural styles	*227*
6.2	Seismicity maps for the Koa'e and Krafla fault systems	*232*
6.3	Comparison of borehole data	*235*
6.4	Effect of pore fluid increase on rock failure	*237*
6.5	Dike propagation and fault development	*240*
6.6	Types of porosity in lavas	*244*
6.7	Porosity and bulk moduli data for the Berea sandstone	*246*

6.8	Tectonic element map for the NE Atlantic	*248*
6.9	Tectonic evolution of onshore deformation in the Faroe Islands	*250*
6.10	Structural sets identified in the Kangerlussuaq region of E Greenland	*252*
6.11	Summary of structural sets in the Krafla AOI	*254*
6.12	Reflection of structural sets from Krafla into the NE Atlantic trend	*255*
6.13	Rotation of structural sets from Krafla into the NE Atlantic trend	*257*
6.14	Comparison of rotated data and data from the NE Atlantic margins	*258*
6.15	Map of the Hold With Hope relay zone in NE Greenland	*260*
6.16	A dual rift model for the NE Atlantic	*263*

Chapter 1

Introduction

1.1 Introduction

The growth of normal faults in basaltic sequences has important application in continental and oceanic extensional systems, on Earth as well as other planets. The growth, or termination of normal fault systems has implications for models of extension, hydrocarbon exploration, seismic hazard assessment, and mineral resources (e.g. Gibbs, 1984; Morley et al., 1990; Gawthorpe and Hurst, 1993; Faulds and Varga, 1998). Much of our current understanding of the growth of normal fault populations comes from studies of faults in sedimentary sequences using combinations of: (1) fault analysis and scaling relationships based on field and seismic data-derived measurements of displacement and length/width (e.g. Peacock and Sanderson, 1991; Childs et al., 1995; Ferrill and Morris, 2001; Meyer et al., 2002; Peacock, 2002; Walsh et al., 2003; Nicol et al., 2010; Nixon et al., 2014); (2) scaled-analogue modelling (e.g. McClay and White, 1995; Acocella et al., 1999; Clifton et al., 2000; Holland et al., 2006; Tentler and Acocella, 2010; Van Gent et al., 2010); and (3) numerical modelling (e.g. Willemse et al., 1996; Crider and Pollard, 1998; Maerten et al., 2002; Imber et al., 2004). Rift zone extension is not accommodated by cumulative slip on a single, discrete fault surface throughout its evolution, but rather it is partitioned across a segmented array of individual faults, dikes and extensional fractures that interact and link with increasing strain (e.g. Forslund and Gudmundsson, 1991; Ebinger and Casey, 2001; Meyer et al., 2002; Walsh et al., 2003; Imber et al., 2004; Gudmundsson and Loeveit, 2005; Wright et al., 2006). Normal fault segmentation can occur as a function of the heterogeneous mechanical properties of the deforming sequence (e.g. Ferrill

and Morris, 2003; Ferrill and Morris, 2008; Crider and Peacock, 2004; Schöpfer et al., 2006; Schöpfer et al., 2007). The linkage of segmented normal faults by either the formation of a discrete secondary structure, or the continuation of one or multiple fault tips, is implied to be an instantaneous process using a set of static stages where linkage follows immediately after a single overlapping configuration (e.g. Peacock and Sanderson, 1994; Childs et al., 1995). It has been shown numerically, however, that superposition of stresses surrounding the tip zones of en echelon faults will generate complex triaxial stress perturbations and progressive deformation that is characterised by bedding rotations and multiple sets of ancillary faults, which develop at high angles to the main bounding faults and transfer strain between the bounding structures (Segall and Pollard, 1980; Pollard and Aydin, 1984; Crider and Pollard, 1998; Imber et al., 2004). A progressive geometric and kinematic evolution of strain should be expected within an overlap zone, or *relay zone,* where continued tip propagation and fault slip takes place prior to linkage.

Recent interest in normal faulting has focussed on their development in layered crystalline-volcaniclastic sequences, driven by the growing significance of volcanic passive margin hydrocarbon plays (e.g. Walker et al., 2012, 2013; Crider, 2015). Volcanic passive margins (VPMs), inherited from volcanic rifts, are characterised by substantial and transient volcanism, related to elevated mantle temperatures that results in thermal thinning of the base of the lithosphere (e.g. Karson and Brooks, 1999; Planke et al., 2000; Geoffroy, 2005). More than 50% of rifted passive margins are thought to fall into this category, including the NE Atlantic margins (Self et al., 2015). Drilling of the NE Atlantic margins has revealed that up to 70% of the region is dominated by basaltic material (Planke et al., 1999; Self et al., 2015) including intrusive and extrusive basaltic volcanism during Paleogene continental break up, driven by the impingement of the Icelandic plume beneath the rifting Pangaean continent (Planke and Eldholm, 1994; Ritchie et al., 2003; Planke et al., 2000; Smallwood and White, 2002; Gernigon et al., 2012). The result was the emplacement of ~1.8 x 106 km^3 of basalt

between the Greenland and NE European margins, covering pre-magmatic basin sediments (e.g. Eldholm and Grue, 1994; Geoffroy, 2005). The NE-SW trend of Cretaceous-Cenozoic rift basins along the European margin is widely inferred to be segmented by a series of NW-SE lineaments, identified from regional magnetic and gravity datasets (Rumph et al., 1993), which are thought to represent pre-existing Caledonian structures that were reactivated as large-scale strike slip faults during NE Atlantic opening (e.g Doré et al., 1997; Ellis et al., 2009). The presence of these margin-normal strike-slip faults is believed to have resulted in the segmentation of previously continuous basins along the NE Atlantic margins (e.g. Doré et al., 2008). Recent analyses of transfer zone fault structures both onshore in the Faroe Islands and offshore in the Faroe-Shetland Basin, however, have questioned their origins and extent, as well as their kinematics and tectono-stratigraphic significance (Moy and Imber, 2009; Walker, 2010; Walker et al., 2011).

To date, although the regional-scale segmentation of faults in extensional systems is well studied, the growth of normal faults in layered basaltic sequences, as well as the distribution and kinematics of the incremental strains surrounding the tips of en echelon faults is less well constrained and the contribution of these structures to the overall evolution of the rift remains poorly understood. The purpose of this body of research is to: (1) constrain the evolution of propagation and segmentation of normal faults in layered basaltic sequences across a range of scales; and (2) investigate the progressive deformation that takes place during the inelastic break-down of inter-fault relay zones by studying the distribution and kinematics of ancillary strains surrounding fault terminations.

1.2 Thesis Structure

A summary of Chapters 2-6 are summarised below. The first data chapter (Chapter 3) introduces the smallest scale of observation and analysis in this thesis: initial crack nucleation

and intact lava strength. Data chapters 4 and 5 follow a progressive up-scaling of observations, from segmentation and fault growth at the cm-hundreds of metre-scale (Chapter 4), up to the tens of metre to 1 km-scale (Chapter 5). Background sections in Chapters 4 and 5 provide the geological and geodynamic context for the Hawaiian and Icelandic study areas, respectively. The first half of Chapter 6 forms a combined analysis of observations from the Hawaiian and Icelandic study areas and discussion of the different controls on fault growth in volcanic rift zones. The second half discusses existing models of NE Atlantic opening in the context of findings from this thesis and in light of recent onshore data collected from the European (Faroe Islands) and N American (E Greenland) margins.

Chapter 2 summarises the current body of literature concerning normal fault growth in sedimentary sequences that is based on field-based studies and analytical solutions, the physical characteristics of lavas, and the principles of intact rock strength and linear elastic fracture mechanics.

Chapter 3 involves the physical and mechanical characterisation of lava samples from Kilauea's south flank, Hawai'i. The chapter attempts to identify a physical and mechanical stratigraphy to answer the following thesis question:

1. *Do faults initially develop as segmented structures in a single lava? If so, what are the potential causes of this segmentation?*

Chapter 4 is a structural study of the distribution, geometry, and kinematics of extensional strains in the Koa'e fault system, Hawai'i, a zone of normal faulting that links two low-strain, evolving rift zones on the south flank of Kilauea. Using detailed remote-sensed mapping, field-measurements, and structural analyses the following thesis questions are considered:

1. *What scales of segmentation are observed in the early stages of rift development?*
2. *What are the possible influences on segmentation at these scales and how important is the intact strength of lavas in fault growth?*
3. *Is there evidence for progressive deformation and stress rotation, prior to linkage of fault segments, or is the process instantaneous with strain transferred on a single, structure in a coherent, and plane-strain array? Do all faults follow a linear progression?*

Chapter 5 is a structural study of the distribution, geometry, and kinematics of extensional strains in the Krafla fissure swarm, NE Iceland, one of five systems of normal faulting within the Neo-Volcanic Zone of Iceland that accommodates the separation of the North American and Eurasian tectonic plates. Detailed field mapping and structural analysis of ancillary strains surrounding the terminations of en echelon rift faults are used to discuss the following thesis questions:

1. *What scales of segmentation are observed in an evolved rift zone?*
2. *What are the possible influences on segmentation at these scales?*
3. *Is there evidence for a progressive kinematic development of ancillary deformation surrounding en echelon faults?*

Chapter 6 expands on, and combines, discussion sections in the preceding data chapters to produce a model of normal fault growth in basaltic sequences that is focussed on the following questions:

1. *How do normal fault populations grow in near-surface, basaltic sequences?*
2. *What factors influence the style and distribution of faults in layered basaltic sequences?*

This consolidated discussion and fault model is then used to reassess segmentation models and the tectonic and kinematic nature of margin-oblique lineaments that are interpreted to segment depocentres along the NE Atlantic margins. Comparison of field data and field-derived models are compared to published and unpublished structural data from the Faroe Islands and Kangerlussuaq, E Greenland, to discuss the following thesis questions:

1. *Are patterns of segmentation and linkage of faults in layered basaltic sequences consistent with margin-scale models of segmentation along the NE Atlantic margins?*
2. *What are the possible tectonic origins and kinematics of transfer zone structures in the NE Atlantic?*

Chapter 7 Concludes the major findings of this body of research, and highlights areas of interest for further research that have been raised by findings in this thesis, but were beyond the scope of this work to answer.

1.3 Terminology

Extension fracture is used in this thesis to describe brittle structures formed in mode I (extension-mode) failure, that show opening normal to the fracture walls, with no lateral or vertical offsets at the centimetre-metre scale. Extension fractures that demonstrate an opening component in addition to a shear offset of the fracture walls are referred to as *extensional-shear fractures or strike-slip/oblique-slip faults*. Open extension fractures that demonstrate vertical displacement (throw) in addition to significant horizontal opening are identified as *normal faults*. To separate scales in this thesis, extension fractures that represent the smallest increments of strain considered (micron to millimetre length scale) are referred to as *cracks;* the linkage of cracks lead to through-going cm-scale extension fractures.

I refer to *composite fractures* as extension fractures that are composed of multiple segments that behave as a coherent single structure (see also Walsh and Watterson, 1991, Childs et al., 1995; Hus et al., 2006; Nicol et al., 2006). Extension fracture or fault *length* is defined as the visible trace length in map view, and *aperture* refers to the opening component of an extension fracture, measured perpendicular to its walls. Normal faults at the free surface have dips that are sub-vertical so heave is considered negligible and is therefore not considered here.

Monoclinal-folds and rotations of the hanging wall are common structural features above upward propagating normal faults. They are classically referred to as *monoclines* (e.g. Grant and Kattenhorn, 2004; Martel and Langley, 2006) or *fault-propagation folds* (e.g. White and Crider, 2006; Ferrill et al., 2012). In this thesis, the term *surface flexure* is used to describe laterally continuously or discontinuously folded, or rotated hanging wall blocks, where a single genetic- and systematic-cause cannot be accurately determined.

The zone surrounding the terminations of en echelon fault or extension fracture segments has a plethora of names with the style of strain transfer being the defining characteristic. Confusingly, the same name is used to describe different styles. Two major styles exist:

(1) Soft-linked, actively interacting zones where strain transfer is accommodated in ductile rotations and/or minor ancillary (but not connecting) fault or extension fracture growth. Such zones have been termed overlap zones, relay zones (e.g. Peacock and Sanderson, 1991; Gawthorpe and Hurst, 1993; Childs et al., 1995; Huggins et al., 1995), transfer zones (Morley et al., 1990) or accommodation zones (Faulds and Varga, 1998).

(2) Hard-linked zones, which describe relay zones where a connecting fault has developed between en echelon fault segments. The connecting fault can develop as a single discrete fault, or represent the continued growth of one, or both fault tip(s). These zones are also

sometimes referred to as transfer zones (Gawthorpe and Hurst, 1993; Faulds and Varga, 1998; Ferrill and Morris, 2001; Ellis et al., 2009).

It is not the purpose of this thesis to redefine this terminology, hence the following terms are adopted to remain consistent with existing literature of segmentation in the NE Atlantic region: (1) *soft-linked relay zone* where evidence of strain transfer is inferred from multiple sets of ancillary, obliquely oriented fracture and/or fault sets, but a single discrete structure is absent; and (2) *transfer zone*, where the transfer of strain occurs across a single, discrete fault structure (*transfer zone fault*) that shows strike-slip-to-oblique-slip kinematics.

Chapter 2

Scientific Background

When a rock demonstrates a decreasing load bearing capacity under an increasing applied stress, and responds by fracture formation, the material is said to behave in a brittle manner (e.g. Jaeger et al., 2007, Gudmundsson, 2011). Section 2.1 of this background chapter summarises our current understanding of normal fault growth in sedimentary sequences. Section 2.2 discusses the principles of rock fracture, beginning with the theoretical, and experimental understanding of stress distributions and magnitude in fracture nucleation and growth, and how these scale with fracture size. The section also covers our understanding of fault and relay zone scaling. Both of these sections will inform data chapters on the formation of extension fractures in subaerially emplaced basaltic lavas and the initial growth and interaction of normal faults in layered basaltic sequences at depths less than 4 km. Observations made will extend our understanding of these subjects, beyond the summaries here.

2.1. Growth of Normal Faults

The primary, regional scale segmentation of extending terranes is controlled by the development of networks of normal fault systems and the partitioning of extension across them. It is well known that normal faults comprise multiple discontinuous, non-collinear segments, with overlaps and segment linkage forming characteristic en echelon geometries at a range of scales (e.g. Segall and Pollard, 1980; Aydin and Schultz, 1990; Peacock, 2002). At their lateral terminations we find structural domains, characterised by zones of folding and

cross-faults, which conserve regional extension (e.g. Gibbs, 1984; Rosendahl, 1987; Morley et al., 1990). Such structural elements have a profound influence on the evolving tectono-stratigraphy of rift basins (e.g. Lambiase and Bosworth, 1995; Sharp et al., 2000; Hus et al., 2006) as well as the sealing potential or fluid flow properties of fault zones (e.g. Morley et al., 1990; Caine et al., 1996; Faulkner et al., 2010; Manzocchi et al., 2010; Seebeck et al., 2014).

Two origins for segmented faults are proposed: an *isolated fault model* where segments grow in isolation (Figure 2.1a*i-iii*), and a *coherent fault model* (Figure 2.1b*i-iii*) where faults nucleate and propagate as kinematically related components of an array. In the isolated model, faults are viewed as single continuous discontinuities where growth is fundamentally controlled by a scaling relationship between length and displacement, producing longer faults that exhibit greater displacements than shorter faults (e.g. Walsh and Watterson, 1987; Cowie and Scholz, 1992; Gillespie et al., 2001; Dawers and Anders, 1995; Cartwright et al., 1996; Kim and Sanderson, 2005). Profiles of length and displacement for an isolated fault segment reflect cumulative slip events and show symmetric geometries with centrally located maxima that taper to zero at the fault tips (e.g. Peacock and Sanderson, 1991; Gupta and Scholz, 2000; Soliva and Benedicto, 2004).

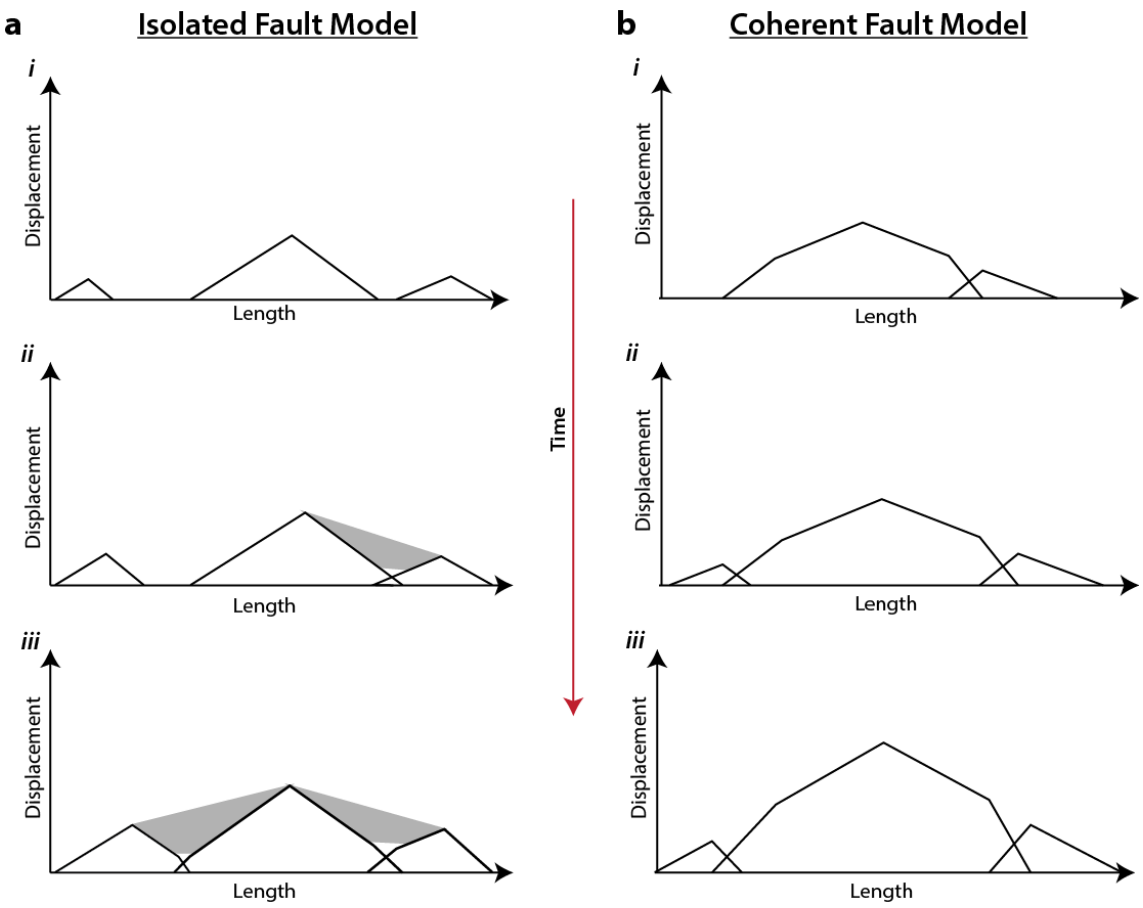

Figure 2.1. Schematic illustration of displacement-length profiles for faults in a) an isolated fault model, and b) a coherent fault model. In the isolated model, faults initiate as kinematically independent structures (a*i*) and profiles demonstrate multiple displacement maxima (a*ii*) until a fully linked structure develops (a*iii*). Grey shading indicates areas of displacement deficit. In the coherent example, profiles demonstrate a centrally located displacement maxima, with no deficits, throughout their evolution (b*i-iii*). (Modified from Walsh et al., 2003).

Field data of fault displacement patterns, however, have highlighted distinctive variations in slip to length ratios related to interaction and linkage of en echelon fault segments. Two-dimensional analyses of the stresses surrounding en echelon faults and dikes support this observation and have demonstrated that mechanical interaction of opposing elastic stress fields produce areas of highly perturbed stress, which exert a significant control on the growth, slip distribution, and geometry of faults (e.g. Segall and Pollard, 1980; Delaney and Pollard,

1981; Bürgmann and Pollard, 1994; Nicol, 1996; Crider and Pollard, 1998). For displacement-length scaling relationships to be satisfied, significant strain must therefore be accommodated in the inter-fault region of perturbed stress through components of continuous (i.e. elastic) and discontinuous (i.e. brittle) deformation (e.g. Dawers and Anders, 1995; Childs et al., 1995; Huggins et al., 1995; Ferrill and Morris, 2001; Walsh et al., 2003; Long and Imber, 2010).

As an alternative to the isolated model (Figure 2.1b, *i-iii*), the coherent fault model was proposed where fault segments represent co-evolving, or geometrically coherent, components of an array that are offset by soft-, or hard-linked domain boundaries and demonstrate systematic geometries throughout their evolution and across a range of scales (e.g. Childs et al., 1995; Walsh et al., 2003; Long, 2011). Faults that initiate as a coherent array will share a finite displacement distribution, i.e. the aggregate sum of displacement is systematic and resembles that of an isolated structure throughout their evolution, rather than exhibiting multiple displacement minima (e.g. Childs et al., 1995; Walsh et al., 2003). This is referred to as kinematic coherence. The fundamental difference between the two models is the kinematic independence of isolated faults, but in essence, both models may be applicable under differing circumstances (Walsh et al., 2003).

In both models, the presence of crustal heterogeneities are a critical component in fault evolution, with nucleation taking place along pre-existing discontinuities such as joints, or reactivation of pre-existing faults, both of which represent areas of low strength compared to intact rock. Fault evolution is summarised as a staged evolution:

Stage I:

Faults initiate as offset and spatially (and/or kinematically) isolated segments and propagate radially with slip decreasing to zero at the fault tips, producing symmetrical displacement profiles (Ferrill et al., 1999; Gupta and Scholz, 2000; Figure 2.2a). Scaling relationships are thought to be exponential during this stage with extensional strain taken up by a growing

population of smaller displacement faults that are isolated (Ackermann et al., 2001). It has also been proposed that fault lengths may be established instantaneously by the reactivation of pre-existing structures where subsequent interaction restricts further lateral propagation (Walsh et al., 2002). It is unclear, however, how the model applies to non-reactivated faults and such systems may instead follow the isolated or coherent model (Walsh et al., 2002, 2003).

Stage II:

As faults grow in length and displacement accumulates, fault segments begin to overlap and relay zones begin to form with the mechanical interaction and modification of opposing elastic stress fields (Figure 2.2b). Depending on the degree of overlap, lateral propagation can be inhibited when faults propagate into the stress drop region surrounding neighbouring faults, leading to displacement anomalies and asymmetrical displacement profiles (e.g. Segall and Pollard, 1980; Peacock and Sanderson, 1991; Mansfield and Cartwright, 1996; Nicol et al., 1996; Gupta and Scholz, 2000; Soliva and Benedicto, 2004).

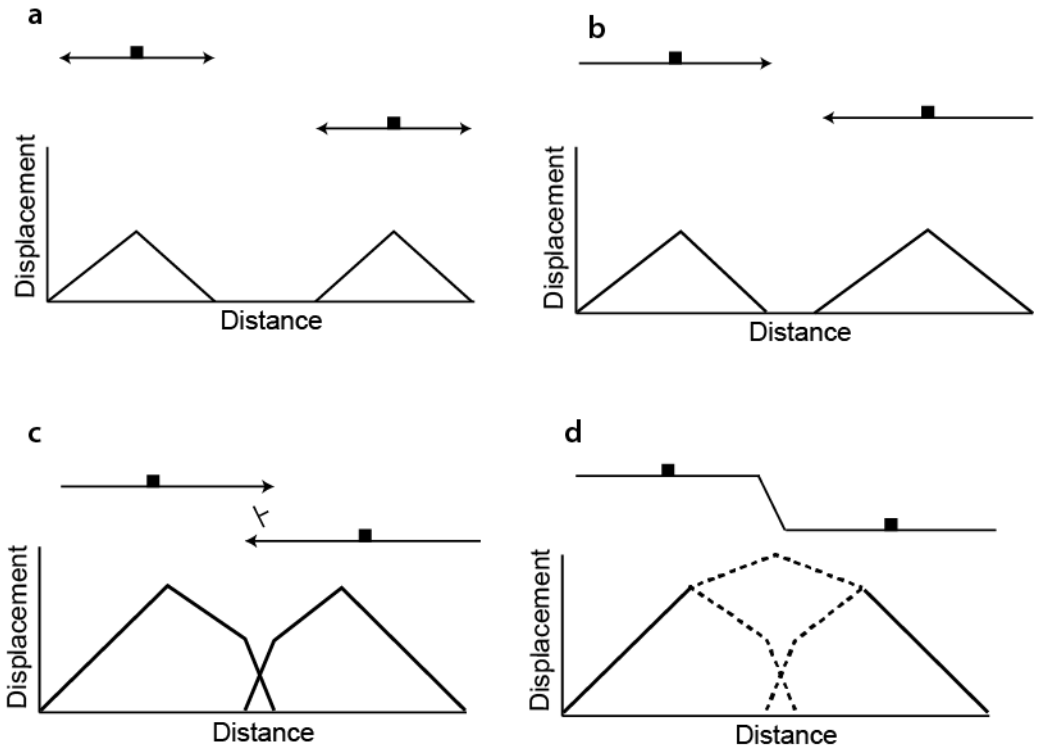

Figure 2.2. Evolution of an isolated normal fault array. (a) Nucleation of fault segments. (b) Displacement and length of segments increases. (c) Segment tips approach one another and interference of their opposing stress fields begins to inhibit further lengthening. (d) A linking structure connects the fault segments and produces a fault step, with a new centrally located displacement maxima (modified from Peacock and Sanderson, 1991 and Gupta and Scholz, 2000).

At this stage, interacting tips are effectively locked and displacement accumulates without radial propagation, and maxima are no longer centrally located, but migrate towards the restricted tip and relay zone. Such anomalous slip gradients are therefore interpreted as a strong indication of fault interaction. For a coherent fault array, individual profiles of length and displacement may be asymmetrical but aggregate profiles resemble that of an isolated structure (e.g. Peacock and Sanderson, 1991; Bürgmann and Pollard, 1994; Walsh et al., 2003).

Stage III:

With persistent tip inhibition but continued displacement on the bounding faults (Figure 2.2c), accommodation of the differential strains is initially accommodated in progressive continuous rotations and secondary inelastic deformation in the deforming relay zone between bounding segments (e.g. Peacock and Sanderson, 1994; Childs et al., 1995; Cartwright et al., 1996; Ferrill et al., 1999; Imber et al., 2004; Long and Imber, 2010). The development of such zones obey power-law scaling and have been observed across 8 orders of magnitude, implying that they are a scale invariant product that forms during the growth of segmented brittle structures (Peacock, 2003; Long and Imber, 2011).

Stage IV:

Eventually, hard linkage and coalescence of the two fault segments takes place with the formation of either an oblique transfer fault in the relay zone, or continued propagation of one or both bounding faults, along modified trajectories, forming tip-to-plane linkage(s) (e.g. Childs et al., 1995; Ferrill et al., 1999; Peacock, 2002; Hus et al., 2006; Figure 2.2d). Scaling relationships are thought to become exponential during this stage, as mechanical interaction and coalescence of existing faults is favoured over the formation of new faults and strain is eventually localised and released by repeated slip on a small number of major structures in the fault system (Ackerman et al., 1997, 2001; Cowie, 1998). Linkage with connecting faults preserves the abandoned fault tip and relay zone in the footwall (or hanging wall) of the fully linked, composite fault (Ferrill et al., 1999; Imber et al., 2004).

In models for normal fault system evolution, segmentation is a characteristic feature at a variety of scales, and this is widely documented from studies in a variety of settings and host rock lithologies from the m-scale (e.g. Peacock and Sanderson, 1991; Acocella et al., 2000; Grant and Kattenhorn, 2004; Tentler, 2005; Martel and Langley, 2006) to the km-scale (e.g. Nelson et al., 1992; Gawthorpe and Hurst, 1993; Trudgill and Cartwright, 1994; Morewood and

Roberts, 2000; Manighetti et al., 2004), and up to crustal scales (e.g. Pollard and Aydin, 1984; Macdonald et al., 1987; Morley et al., 1990; Hayward and Ebinger, 1996; Ferrill et al., 1999; Peacock et al., 2000). The scale invariant presence of relay zones suggests they are important and fundamental products of fault population development across all scales and provide evidence for a process of segment linkage, rather than radial (lateral and vertical) propagation.

2.1.1. Observations From Field-Based Studies of Segmented Faults

Discontinuous normal faults commonly terminate in relay zones, which are responsible for facilitating the lateral termination of normal fault systems and conserving regional extensional strain (Morley et al., 1990; Faulds and Varga, 1998). Relay zones are known by various names including, accommodation zones, transfer zones, interference zones, overlap zones, step-over zones, and segment boundaries (Stewart and Hancock, 1991; Gawthorpe and Hurst, 1993; Childs et al., 2005; Faulds and Varga, 1998; Morewood and Roberts 2000 and Peacock, 2002). The range of terminology is confusing but definitions are broadly similar, with the mode of strain transfer representing the fundamental difference between them. This strain transfer can take place in one of two ways (e.g. Childs et al., 1995; Acocella et al., 2005):

1) Hard linkage (Figure 2.3a): transfer along subvertical, strike-slip or oblique-slip *transfer* faults that link the adjacent bounding faults.
2) Soft linkage (Figure 2.3b): transfer across broad areas of ductile strain between two normal faults, with no connection in 2D. Most commonly referred to as an accommodation zone.

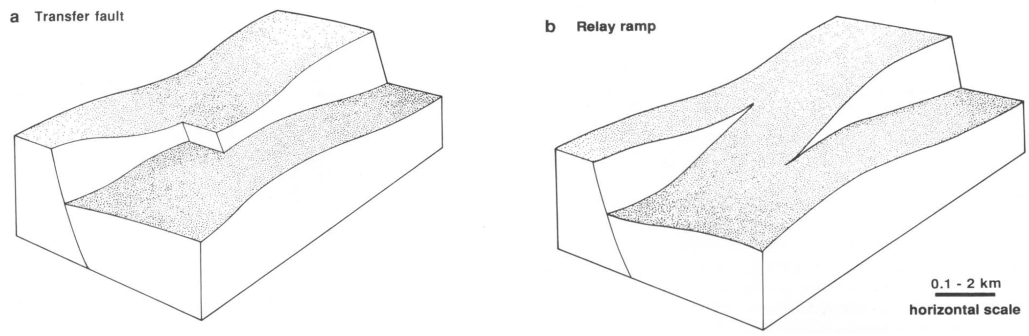

Figure 2.3. Two forms of strain transfer between en echelon fault segments in extensional settings: (a) a hard linked relay zone with strain transferred across a discrete *transfer* fault and (b) soft linkage and rotation across a relay ramp (from Gawthorpe and Hurst, 1993).

2.1.1.1. Soft-Linked Relay Zones

Soft-linked relay zones are typically described using the dip directions of adjacent faults on either side of the domain and the degree of overstep (separation normal to the fault strike), and overlap (separation parallel to the strike of fault segments) between them. The zones may trend parallel, oblique or normal to the regionally applied extension direction and result in complex bed reorientations and ancillary brittle deformation. Based on these characteristics, the following types of soft-linked relay zones are identified (e.g. Morley et al., 1990; Gawthorpe and Hurst, 1993; Childs et al., 1995; Faulds and Varga, 1998; Peacock, 2002):

1) *Antithetic (divergent) soft-linked (accommodation) zones*, where linkage occurs on overlapping normal faults that dip in opposite directions. This configuration is dominant in developing rifts, such as the East African Rift, but less prevalent in regions of distributed continental extension (e.g., the highly extended Basin and Range Province, North America). Common features include inter-basin ridges or footwall highs where fault dip polarity changes. Their geometry is strongly influenced by the degree of overlap and overstep affecting the faults, with inter-fault highs developing where the along-strike overlap is

relatively large and the overstep is small, compared to their length. Further subdivision can also be made based on the degree of overlap between adjacent faults and the overall orientation of the zone with respect to the regional extension vector (Figure 2.4: transverse, oblique and strike-parallel).

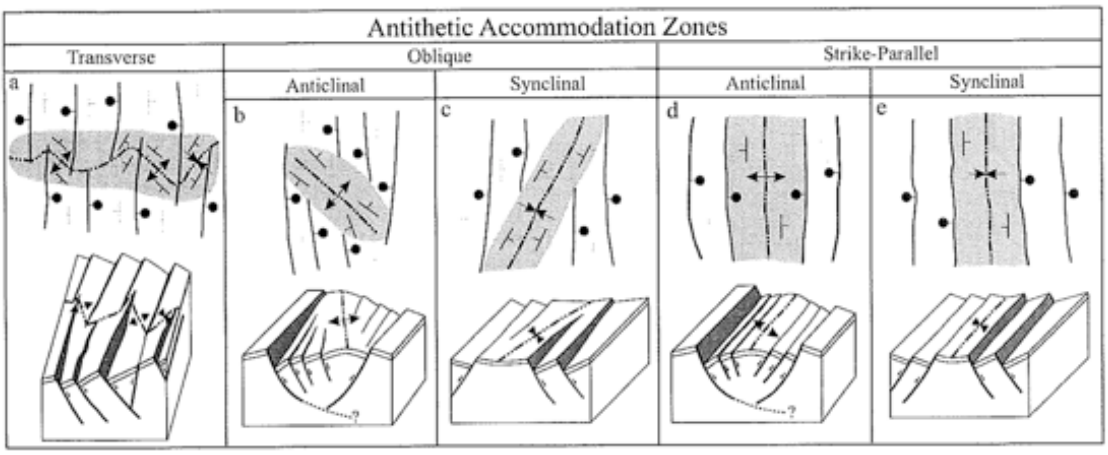

Figure 2.4. Division of antithetic soft-linked relay (accommodation) zones based on fault dip polarity and degree of overlap between interfering segments (from Faulds and Varga, 1998).

2) *Synthetic (convergent) soft-linked (accommodation) zones*, where linkage takes place on overlapping, normal fault segments that dip in the same direction. Synthetic accommodation zones tend to be dominant in regions of distributed continental extension (Faulds and Varga, 1998). Subdivisions based on the degree of overlap and the overall orientation of the zone with respect to the regional extension vector applied to antithetic zones, may also be applied to synthetic zones (Figure 2.5):

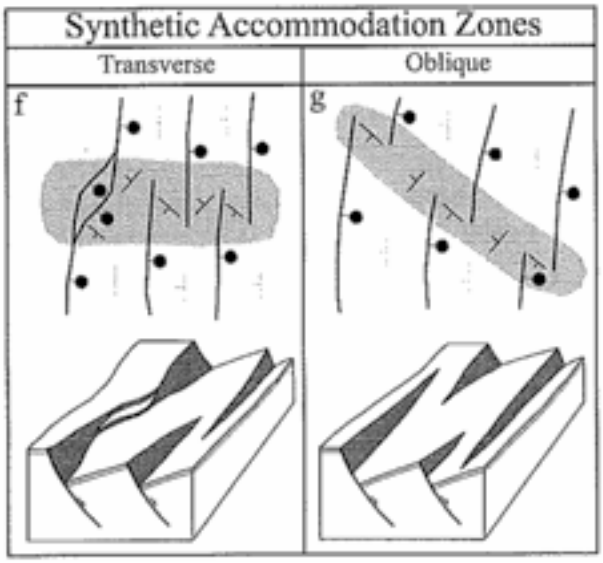

Figure 2.5 Division of synthetic accommodation zones based on fault dip polarity and degree of overlap between faults (from Faulds and Varga, 1998).

Strike-slip faulting in soft-linked relay zones is uncommon, with strain transfer more commonly accommodated by folding and ancillary fault development rather than across an intervening discrete fault.

2.1.1.2. Transfer Zones

An alternative method for the preservation of extensional strain across adjacent faults, or basins, is the development of discrete *transfer faults* that strike at high angles to the bounding structures and show strike-slip or oblique-slip components of displacement that are approximately parallel to the extension direction (e.g. Gibbs, 1984; Gawthorpe and Hurst, 1993; Child et al., 1995; Faulds and Varga, 1998; Hus et al., 2006).

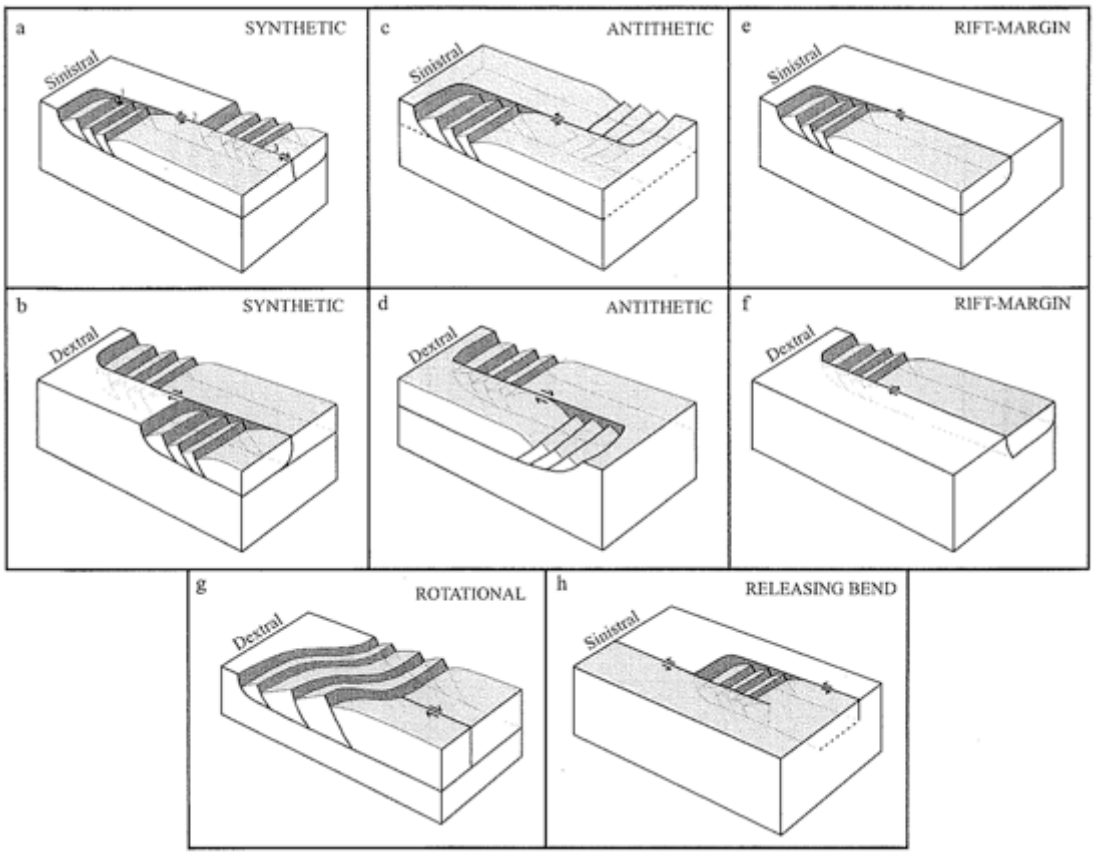

Figure 2.6. Schematic representations of hard-linked relay zones and subdivisions thereof (from Faulds and Varga, 1998).

Two types of hard-linked zone are typically recognised, based on the dip polarity of the fault systems they connect (Faulds and Varga, 1998):

1) Antithetic transfer zones, where bounding faults dip in opposite directions.
2) Synthetic transfer zones, involving uniformly dipping bounding faults; these are observed more commonly than antithetic examples.

Each of these may be further subdivided based on the relative motion between fault domains on either side of the transfer zone (dextral or sinistral: Figure 2.6) and the orientation of the transfer zone, which may induce releasing (localised extension) or restraining (localised contraction or transpression) bends.

Soft-linked relay zones are widely documented in many extensional settings, including the East Africa Rift (EAR) and Iceland, (e.g. Nelson et al., 1992; Acocella et al., 2000; Grant and Kattenhorn, 2004) whereas hard-linked relay zones and transfer faults are more commonly identified in wider rift zones (e.g. the North Sea, Basin and Range province) and passive margin settings (Acocella et al., 2005). The transition from soft to hard linkage has been proposed to be a function of the total extension across the system; at values <21% soft-linked relay zones are believed to dominate and >21% hard-linkage along high-angle strike- to oblique-slip faults will take over (Trudgill and Cartwright, 1994; Acocella et al., 2005). Alternatively, the mode of strain transfer may be related to brittle-ductile coupling of the upper and lower crust; for low viscosities in the lower crust, strain has been shown to localise quickly on transfer structures and for higher viscosities deformation becomes more distributed and soft-linked relays dominate (Allken et al., 2012). Notably, analogue models of transfer zone evolution suggest that they do not always reactivate pre-existing structures nor represent the final stage of accommodation zone evolution; localised transfer faults can develop near-instantaneously (Gerya, 2012).

In nature, examples of relay zones (soft- and hard-linked) can be complex combinations of the examples above. Studies in the East African Rift have revealed that minor faulting in soft-linked relay zones result in triaxial strains and play an important role in the regional conservation of strain (Griffiths, 1980; Morley, 1990; Nelson et al., 1992). Groupings of short, usually curved faults that intersect the major faults at oblique angles have previously been termed “box faults” (Griffiths, 1980). Similar triaxial strains have also been observed in other extending regions including: Canyonlands, Utah (Trudgill and Cartwright, 1994), in the Gulf of Corinth (Stewart and Hancock, 1991), in the Hold With Hope region of NE Greenland (Peacock et al., 2000) and the central Apennines (Morewood and Roberts, 2000).

2.1.2. Rock Fracture

A discussion of scaling of faults in this section will begin with a summary of the different fracture modes (which are ubiquitous in developing rift zones, across all scales), the fundamental principles behind their growth and the scaling of stress and resultant strains.

2.1.2.1. Modes of fracturing

A fracture may be classified by one of three modes, depending on the relative displacement of the fracture walls (e.g. Atkinson, 1987; Engelder, 1993; Figure 2.7):

1) Mode I: extension or opening mode, where fracture walls are separated without shear (e.g. extension veins).
2) Mode II: sliding mode (in-plane shear), where fracture walls are separated by mutual shearing of the fracture walls and the shear couple is oriented normal to the fracture front.
3) Mode III: tearing mode (anti-plane shear), where fracture walls are subject to a shear couple oriented parallel to the fracture front. Mode II/III displacements should operate in unison at different positions along the same tip line (Figure 2.7).

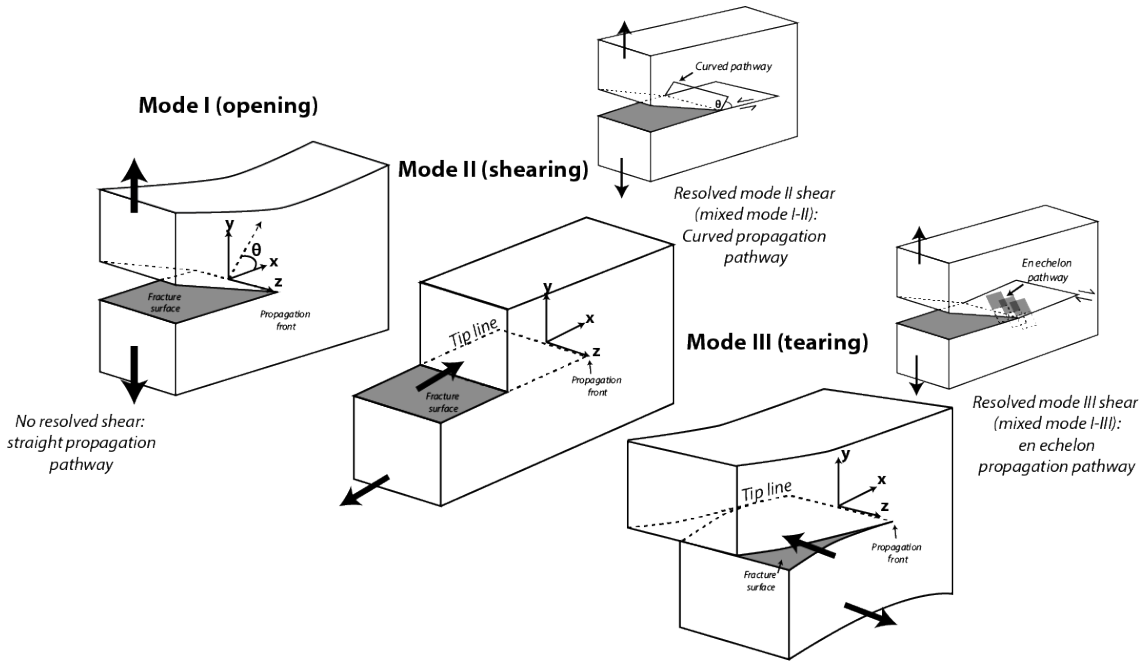

Figure 2.7. Schematic modes of fracture and propagation pathway, classified by the relative displacement of fracture walls (after Pollard and Fletcher, 2005).

The maximum load a rock will accommodate before failure depends on the strength of the rock, defined in terms of the stress state the rock experiences is known as the brittle strength. This can be defined in two ways:

1) **Tensile strength** (T): the tensile stress in a rock where a fracture nucleates. T represents the critical tensile stress required to form a mode I crack, where the shear stress is zero.
2) **Shear strength** or **Cohesion** (C): the shear stress in a rock where a shear fracture, or fault, develops. *C* represents the critical shear stress across a surface where the normal stress is zero (see Figure 2.8). Mohr-Coulomb Criterion states that *C* is typically twice the tensile strength (C = 2T).

The stress conditions for a rock at failure can be calculated using the Coulomb failure criterion:

Equation 2.1:

$$\tau = \sigma_N \tan\phi$$

Where:

τ is the critical shear stress at failure, σ_N is the normal stress, ϕ is angle of internal friction ($\tan\phi = \mu$ which is the coefficient of internal friction). For most solid rocks, μ is a simplified to a constant that varies from 0.6-0.85, but more typically is 0.75 (e.g. Sibson, 1994). For in intact rock, a fracture will only develop when the internal, cohesive strength of the material is overcome. Brittle failure may therefore be described by a modified Coulomb criterion: the Mohr-Coulomb fracture criterion (Figure 2.8a and b).

Equation 2.2:

$$\tau = C + \sigma_N \tan\phi = C + \sigma_N \mu$$

The response of a rock to an applied stress also depends on the differential stress, or maximum stress difference a rock can accommodate before failure occurs, and the mean stress (Figure 2.8a). A rock experiencing a large differential stress will be unable to accommodate such a stress and will respond by deforming in either a brittle or ductile manner (e.g. Engelder, 1993). The strength of the material is therefore largely responsible for dictating how great a differential stress the rock will accommodate before failure; this is in turn controlled by the strain rate, confining pressure and/or pore fluid pressure. At low strain rates, ductile deformation is dominant; higher strain rates will typically result in brittle failure. With increasing confining pressures, rock strength will increase due to the difficulty in opening fractures at depth – the surrounding material effectively confines the rock (e.g. Fossen, 2010). At greater depths, therefore, larger differential stresses are required to cause failure.

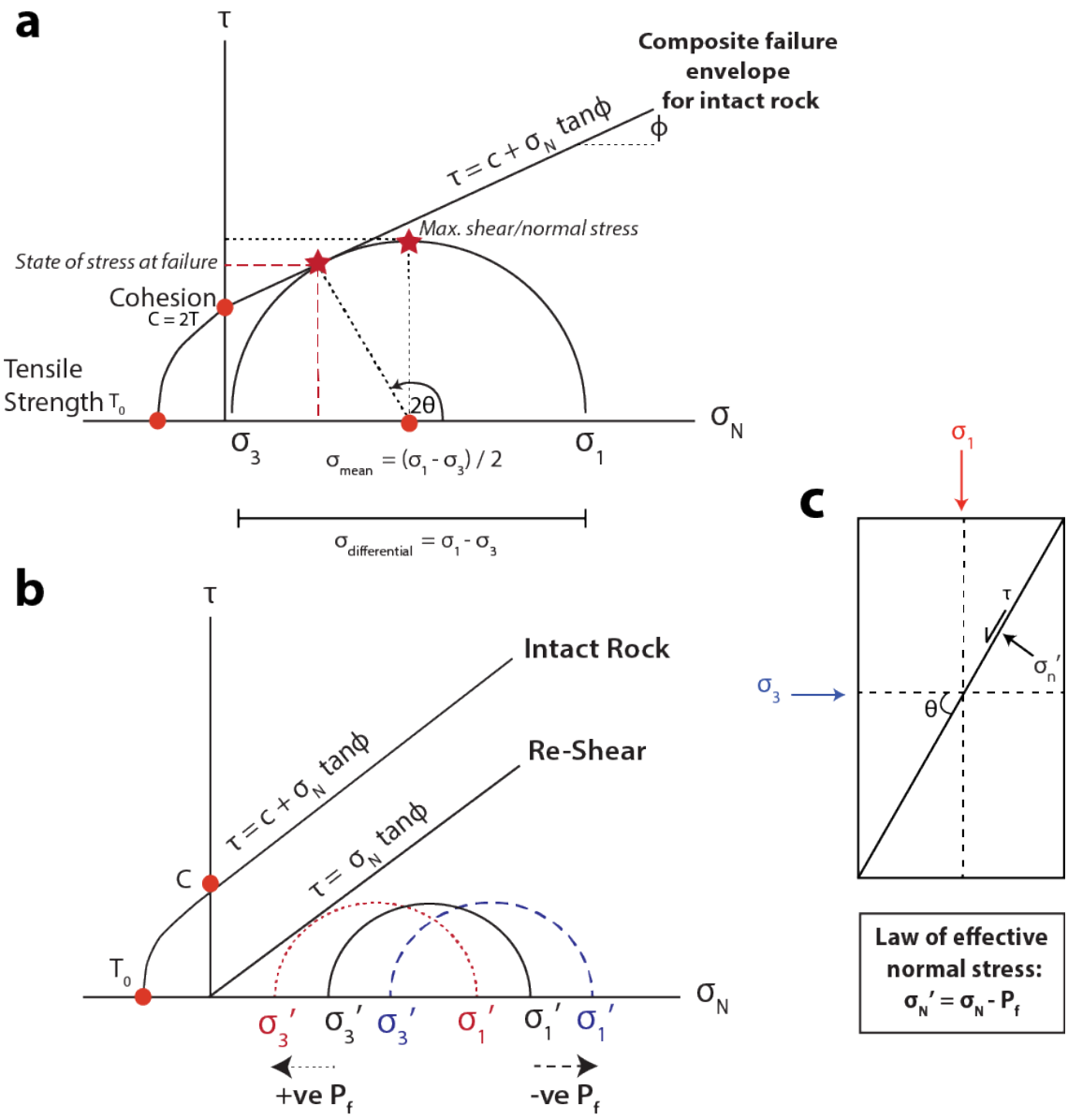

Figure 2.8. a) Mohr-Coulomb failure in a compressional setting (after Fossen, 2010). A Mohr circle is drawn through the maximum (σ_1) and minimum (σ_3) compressive stresses, the diameter of which is equal to the differential stress. With Initiation of a shear fracture oriented at ~60° from σ_1 we can find the shear stress and normal stress acting on that plane at failure (red star). b) Mohr diagram illustrating the effects of increasing or decreasing fluid pressure on the fracture stability of rocks (after Healy, 2009). c) Resolved components of effective and normal shear stress acting on a fracture (after Sibson, 1994).

The effect of increasing the confining pressure can be counteracted by the pressure exerted by pore fluids present in the rock mass (Figure 2.8b), which have the effect of lowering the normal stress by an amount that is equal to the fluid pressure (e.g. Hubbert and Rubey, 1959; Sibson, 1990; Sibson, 1994). This is know as the effective normal stress (σ_N'):

Equation 2.3:

$$\boldsymbol{\sigma_N{}' = \sigma_N - P_f}$$

Where σ_N is the normal stress and P_f is the pore fluid pressure (Figure 2.8c). The fracture criterion (Equation 2.2) describes the critical stress condition at which failure occurs; this may be visualised and interpreted using a Mohr diagram, which is used to plot the field of possible shear stress for a given differential stress, with respect to the failure criterion. The point at which a *Mohr circle* touches the failure envelope, represents the orientation at which a fracture will form, and the value of shear stress and normal stress acting on the plane at failure (Figure 2.8 and 2.9). A Mohr circle that does not touch the failure envelope for homogenous intact rock is considered to be in a stable stress state. The orientation of the fracture from σ_1 can be described using the angle of internal friction (ϕ) (e.g. Fossen, 2010):

Equation 2.4:

$$\theta = 90° + \phi$$

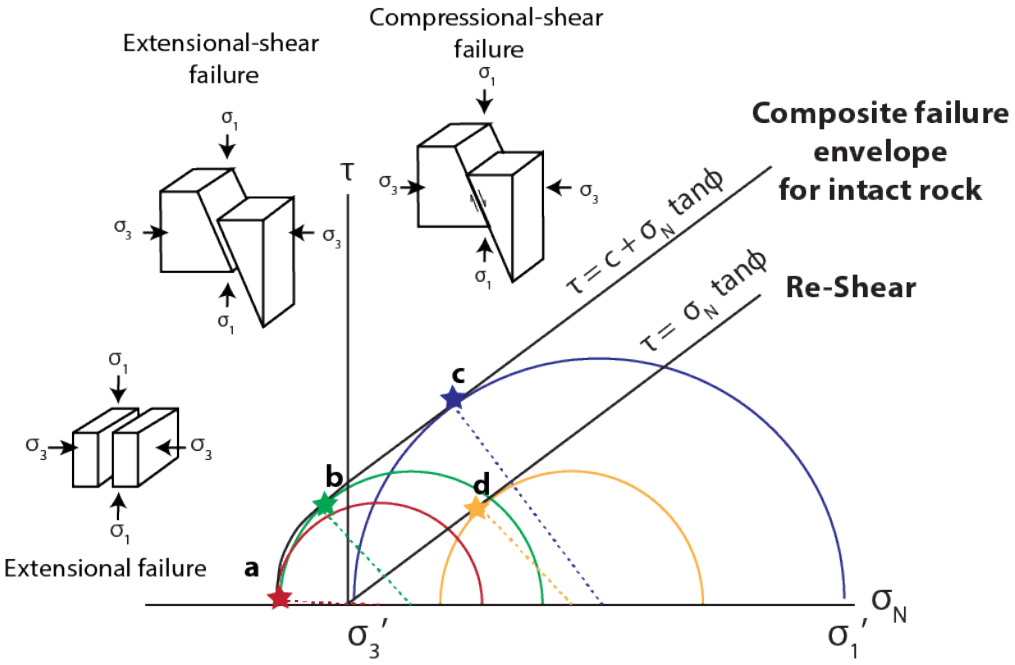

Figure 2.9. A Mohr diagram of shear stress (τ) against effective normal stress (σ_N) showing the composite failure envelope for intact rock and the re-shear condition for reactivation of a cohesionless fracture (after Ferrill and Morris, 2003). a) The critical stress circle for extensional failure (mode I); b) critical stress circle for extensional-shear failure (mode II/III); c) critical stress circle for shear failure (mode II/III); and d) critical stress circle for reactivation of a favourably oriented pre-existing fracture (mode II/III).

To characterise the range of stress states we find in the crust, the three different fracture modes and re-shear of a pre-existing fracture (Figure 2.9) are considered (e.g. Jaeger and Cook, 1979; Sibson, 1985; Ferrill and Morris, 2003; Sibson, 2004):

a) **Extensional failure** (Figure 2.9a): Displacement occurs across planes that lie normal to the minimum compressive stress (σ_3) where the effective normal stress is <0 (i.e. tensile) at failure. Opening occurs at low differential stresses (less than four times the tensile strength: $\sigma_1 - \sigma_3 = <4T$), and fractures will develop when σ_3' equals the tensile strength.

b) **Extensional-shear failure** (Figure 2.9b): Displacement involves opening oblique to the fracture plane, where the effective normal stress is <0. Failure angles will lie between 0

and the angle predicted by Equation 2.4 with faults forming an acute angle about the maximum principal stress axis (σ_1).

c) **Compressional-shear failure** (Figure 2.9c): Displacement occurs parallel to the fracture walls where the effective normal stress is >0. The failure angle is predicted by Equation 2.4; typically, normal faults dip about 60° from horizontal; ~30° for thrust faults.

d) **Shear reactivation** (Figure 2.9d): Frictional reactivation of optimally oriented existing (cohesionless) fractures requires much lower differential stresses. Sibson (1985) shows that the optimal orientation for frictional reactivation is ~30° for frictional coefficients of 0.75. For reactivation of steeper fractures, effective normal stresses must still be greater than zero and differential stresses must decrease progressively with increasing steepness.

2.1.2.2. Theoretical Fracture Development in Intact Materials

Laboratory testing of the tensile and shear strength of solid materials have shown that the measured strength of rocks is consistently lower (<1%) than the theoretical strengths, which are typically in the range 1-10 GPa, or ~10% of the Young's modulus (Gudmundsson, 2011). The differences between observed and theoretical strengths of rocks are considered to represent the presence of microcracks, or Griffith flaw, which are elliptical flaws or fine cracks, that may result in local tensile stress concentrations that reduce the required driving stress for failure (Blenkinsop, 2000; Gudmundsson, 2011). A rock-crack system includes the following internal components: a crack, with length 2c, and the intact solid host rock, characterised by its elastic properties (Young's Modulus and Poisson's Ratio). Applying a stress to this system involves the conversion of an external force into potential strain energy. If the stress is removed, potential energy is released and results in the formation of new surfaces (Figure 2.10) that have a higher energy state than the surrounding intact material (e.g. Fischer-Cripps, 2007). The energy release associated with the work done in removing tractions provides the surface energy

required for incremental propagation; a crack will not grow until the energy released equals the surface energy requirement, and the amount of energy released is a linear function of the crack length (e.g. Engelder, 1993; Blenkinsop, 2000; Gueguen et al., 2004).

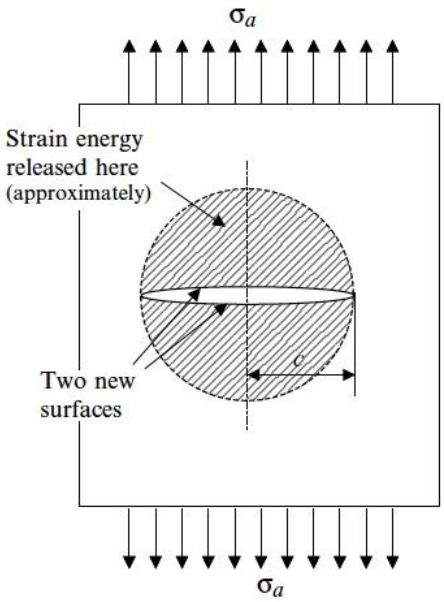

Figure 2.10. Example of a crack in a linear elastic solid, under a uniformly applied tensile stress. The crack has a unit width and a unit length (2c) with mechanical energy released across an area of approximately c. The amount of energy released is a linear function of the crack length (image from Fischer-Cripps, 2007).

At a critical length, more mechanical energy is released than is needed for the new surfaces and crack growth accelerates, becoming unstable and ultimately resulting in failure (e.g. Lawn, 1993; Fischer-Cripps, 2007). The critical stress at which unstable crack growth occurs (e.g. Engelder, 1993; Blenkinsop, 2000; Dresen and Gueguen, 2004) becomes:

Equation 2.5:

$$\sigma_c = \sqrt{\frac{2\,\gamma\,E}{\pi\,c\,(1-\upsilon^2)}}$$

Where:

E is the Young's Modulus

a is the half crack length

ν is the Poisson's ratio

γ is the surface energy per unit area.

Critical stress is therefore a function of the length of the crack, the Poisson's ratio, and Young's Modulus, or elastic modulus. Poisson's ratio is defined as the dimensionless negative ratio of transverse strain to axial strain, with values typically in the range of 0-0.5 (e.g. Jaeger and Cook, 2007). Young's modulus defines the ratio of applied stress (force per unit area) to strain (e.g. Jaeger and Cook, 2007). To characterise the stability of a crack, in terms of energy, solutions based on *linear elastic fracture mechanics* (LEFM) are used. The basic elements of these solutions are as follows (e.g. Krantz, 1979; Pollard et al., 1982; Ingraffea, 1989; Thomas and Pollard, 1993):

1) A **stress intensity factor** (K), which provides an estimate of the magnitude of stresses acting on a crack tip, and determines whether these stresses will result in crack growth. Based on linear elastic assumptions, the analysis is valid while any zone of non-linear strain is small relative to crack geometry (e.g. Atkinson, 1987; Blenkinsop, 2000). Stress intensity factors for each of the three modes of fracture (i.e mode I/II/III) becomes (e.g. Gudmundsson, 2011):

   Equation 2.6:

$$K_I = \sigma_{yy} \sqrt{\pi c}$$

$$K_{II} = \sigma_{xy} L \sqrt{\pi c}$$

$$K_{III} = \sigma_{yz} L \sqrt{\pi c}$$

Where σ_{yy} is the applied tensile stress, σ_{xy}/ σ_{yz} is the applied shear stress, and *c* is the crack half-length. For a linear elastic material undergoing plane strain (no shape change in the y-axis), stress intensity factors are controlled by the applied stress and the crack geometry only. According to LEFM, when K exceeds a critical value (K_C), a crack will propagate.

2) In addition to a material strength and stress intensity factor, a material is also characterised by an intrinsic property known as **fracture toughness** (K_{ic}: equivalent to critical stress intensity, K_C, and theoretically proportional to fracture energy, G), which represents the characteristics of the host and defines the largest flaw that will be accommodated before failure. Fracture toughness provides an estimate of the resistance a material demonstrates to the breaking of atomic bonds during crack growth (Sih, 1976). A crack will propagate in a plane normal to the minimum compressive stress when the stress intensity factor exceeds the fracture toughness of the intact rock ($K_{I/II/III} > K_{ic}$).

3) Cracks will propagate in a direction that maximises the **energy release rate**. LEFM models assume elastic behaviour so additional energy is necessary to propagate a crack tip and cause breakdown of the atomic bonds at the tip in a local zone of non-linear, inelastic deformation (e.g. Blenkinsop, 2000). The additional energy is referred to as the crack extension force (G), or strain energy release rate (rate with respect to length), and is uniquely determined by the instantaneous elastic stress field surrounding the tip. The fracture energy, G, provides an estimate of the energy available for an increment of crack growth and is proportional to $(K_C)^2$ (e.g. Atkinson, 1987; Cowie and Scholz, 1992; Rubin, 1995). For each fracture mode, and assuming linear elasticity and plane strain conditions, G becomes (Atkinson, 1987):

Equation 2.7.

$$G_I = K_I^2 (1 - P^2)/E$$

$$G_{II} = K_{II}^2 (1 - P^2)/E$$

$$G_{III} = K_{III}^2 (1 - P^2)/E$$

Where (1 - P^2) is the plane stress factor. Experimental studies have shown that *G* is only constant when the applied stress and length of the fracture are constant; in nature *G* varies with the frictional resistance of natural surfaces and increases with fault length and displacement (Cowie and Scholz, 1992). Crack propagation is predicted when G exceeds a critical value (G_c), related to the surface energy in the rock (e.g. Krantz, 1979; Engelder, 1993; Rubin, 1993). Crack initiation and propagation is therefore predicted when the following criteria are met (e.g. Wang and Shrive, 1999):

1) The local tensile stresses exceed the fracture toughness/tensile strength of the surrounding intact material.
2) The energy released during each increment of growth is at least as much required for that increment.

LEFM models are typically applied to brittle failure under uniaxial tension with assumptions based on plane stress conditions in linear elastic host materials where the zone of inelastic deformation is small compared to the crack length. Brittle failure of rock under compression however is significantly more complex than failure in tension. At increasing confining pressures, extension mode (I) fracturing is increasingly suppressed in favour of extensional or compressional shear fracturing (mode II/III), which are in turn controlled by the coefficient of friction across those fracture surfaces. Consequently, rocks are significantly stronger in compression (by a factor of ~10) than in tension (e.g. Gueguen et al., 2004). For anisotropic materials, crack or pore geometry exerts a strong control on the distribution of stresses and therefore, on the mechanical response of the host rock to an applied stress, even at low total porosities (e.g. Jaeger et al., 2007). Failure in these rocks occurs through the

nucleation and linkage of cracks that are initially localised by the presence of pre-existing "Griffith" flaws, acting as stress concentrators, which lowers the applied stresses required to induce failure. Purely elastic models are unable to predict crack initiation, with models assuming cracks are single, sharp structures where stresses at the tip are infinite and strengths are near zero. In reality, the response of a material to the stresses in this tip region is more complex as a result of the (non-zero) mechanical properties of the host material (e.g. the tensile strength). This produces a complex "process" zone where stresses become non-linear and the breakdown of bonds results in the formation of microcracks (e.g. Atkinson, 1987; Ingraffea, 1989; White and Crider, 2006). The size of the process zone (r_y) is given by (Gueguen et al., 2004):

Equation 2.8:

$$r_y = \frac{K^2}{2\,\pi\,\sigma y^2}$$

Where *σy* is the plastic yield stress across the zone (assumed to be equal to the applied stress).

Figure 2.11 (a*i* and a*ii*) shows the stress components at the tip of a crack for a linear elastic medium. Stresses are proportional to $r^{-1/2}$, where r is the distance, in polar coordinates, measured from the crack:

Equation 2.9:

$$r = \sqrt{(x^2 + y^2)}$$

Remote stresses are locally amplified at pores or cracks, with amplification decreasing with distance (d) from the edge, or tip (Figure 2.11b). The size and geometry of the process zone is a function of the stress intensity factor at the tip (Figure 2.11c*i-iii*), and therefore the size of the crack, and the applied stress (Cowie and Scholz, 1992). Numerical studies of earthquake ruptures have demonstrated that the distance at which tip stresses decay to approximately

10% of the regionally applied stress is ~10-15% of the total fault length (Cowie and Shipton, 1998).

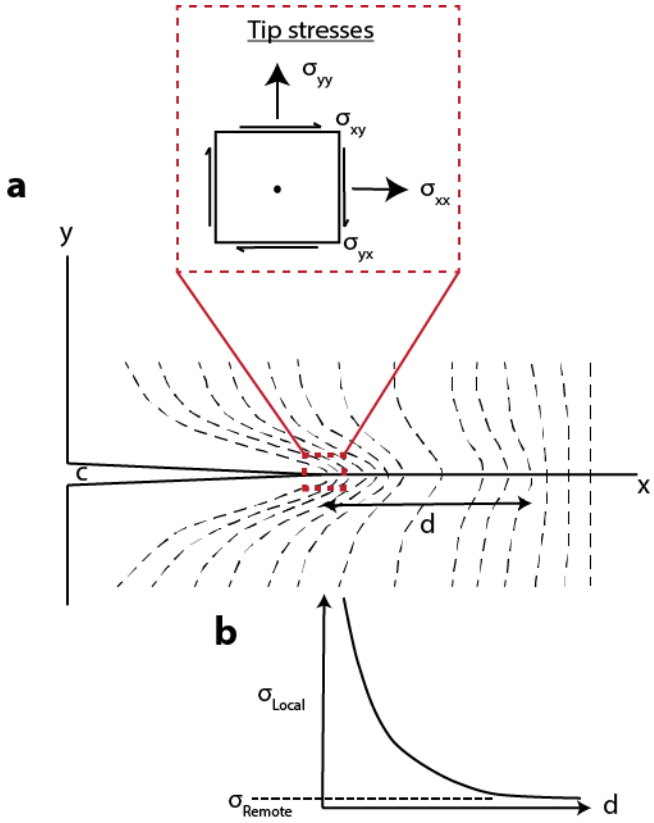

Figure 2.11. Stress conditions surrounding the tip of a crack: a) Stress contours highlight the distance (d) over which local stress perturbations result in incremental extension; and b) amplified stresses decrease from a maximum value at the crack tip with distance (*d).* In a perfectly elastic host, tip stresses are infinite. In nature they are finite, and do not exceed the fracture toughness of the host.

The propagation of a macroscopic fracture will occur through the linkage of smaller scale, ancillary cracks that develop in this inelastic process zone as the rock is subject to increasing load, rather than the simple in-plane propagation of a single surface (e.g. Reches and Lockner, 1994; Vermilye and Scholz, 1998; Healy et al., 2006; Blenkinsop, 2008).

2.1.3. Scaling of Fault Populations

Models based on linear elastic fracture mechanics (LEFM) assume that the deforming volume is perfectly elastic and hence, predict that fault displacement will be greatest at the fault tip where stresses are predicted to be infinite (e.g Cowie and Scholz, 1992). In nature, the strength of the host material, which is finite, prevents this and a process zone (Figure 2.11) develops at the tip where peak stress is equal to the shear strength of the host material (e.g. Cowie and Scholz, 1992; Cowie and Shipton, 1998; Gupta and Scholz, 2000). This correlation is used to investigate the relationship between fault trace length and maximum displacement, which is used as a description of the size and frequency relationships for fault populations (e.g. Cowie, 1998; Walsh et al., 2002; McCaffrey et al., 2003; Kim and Sanderson, 2005). This scaling relationship is thought to follow:

$$D = c\,L^n$$

Where c is a constant

And n is between 1-2.0

Regardless of the value of n, it is expected that it reflects a growth process where faults increase in size as a result of progressive and systematic increases in maximum displacement and length (e.g. Walsh and Watterson, 1987; Walsh et al., 2002). For isolated faults, displacement is predicted to vary from a maximum in the centre of the fault, to zero at the lateral tipline loop; within this loop, displacement contours plot as concentric ellipses around a maximum displacement point, resulting in a linear profile (e.g. Muraoka and Kamata, 1983; Walsh and Watterson, 1987; Cowie and Scholz, 1992).

For many fault populations, there is significant scatter in plots of maximum displacement to length (Figure 2.12) and displacement-length plots for en echelon faults show lower ratios and non-linear profiles where faults show high displacement gradients at their tips (e.g. Peacock and Sanderson, 1991; Willemse et al., 1997).

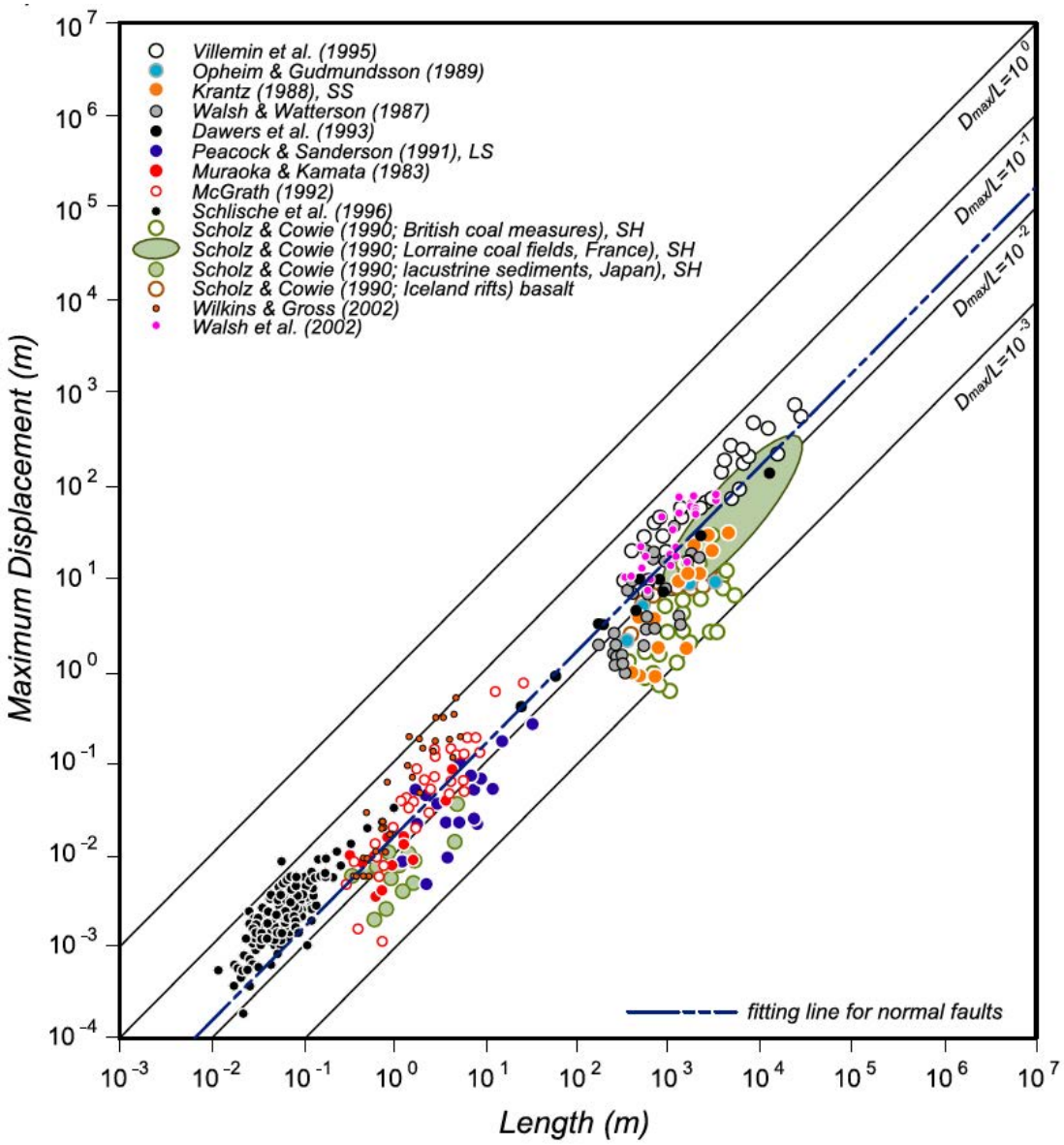

Figure 2.12. Plot of maximum displacement and fault trace length for a selection of normal faults, thrust faults and strike-slip faults in sandstone (SS), limestone (LS) and shale (SH). For a given length scale, maximum displacement values can vary by 2-3 orders of magnitude. From Kim and Sanderson, 2005.

Ratios of displacement-length, and displacement-length profiles are strongly affected by the (1) sampling techniques; (2) reactivation of pre-existing structures; (3) local stress distributions associated with fault interaction; (4) inelastic deformation, variations in frictional strength; and (5) material properties of the host material (e.g. Peacock and Sanderson, 1991; Burgmann et al., 1994; Willemse et al., 1996; Gupta and Scholz, 2000; Peacock, 2002; Kim and Sanderson,

2005; Nicol et al., 2010). The use of isolated fault populations can greatly improve how robust these datasets are (e.g. Schultz et al., 2013).

Size populations of faults are most commonly described using power-law distributions where faults show self-similar, or fractal, size scaling (e.g. Gillespie et al., 1993; Nicol et al., 1996). On a log-log graph, power-law distributions will plot as straight lines when:

$$N \propto S^{-D}$$

Where

N is the number of faults with sizes greater than, or equal to, S

D is the power-law exponent, which can vary from 0.4-1.0 (Nicol et al., 1996).

For fault populations that fit a power-law distribution, the initial stages of growth are characterised by strain accumulation on an increasing number of small faults (e.g. Cowie, 1998). Growth and coalescence of existing faults progressively dominates the formation of new faults until strain is accommodated by repeated slip on a smaller number of faults or fault zones (e.g. Cowie, 1998).

Characterisation of fault systems has also highlight non-fractal, exponential and dynamic displacement-length scaling patterns in both oceanic (e.g. Cowie, 1998) and continental rift zones (e.g. Gupta and Scholz, 2000b; Soliva and Benedicto, 2005). Such scaling distributions have been linked to vertical restriction (e.g. Soliva and Benedico, 2005), scale-dependent processes or controls (e.g. Nicol et al., 1996). It has also been proposed that such scaling can reflect a temporary departure from linear scaling due to segment interaction and linkage (Cartwright et al., 1995). Alternatively, it has been suggested that fault populations may be power-law, but with a wider range of temporally variable C values and spatial densities at different scales (Nicol et al., 1996).

2.1.4. 2D Analytical Modelling

Analogue modelling provides a good estimation of overlapping fault geometries but generally depict soft-linkage or the instantaneous development of a hard linkage. In nature it has been noted that relay zone breaching is not an instantaneous process (Imber et al., 2004) and the differential strain between overlapping fault segments is not necessarily accommodated on a single structural set but rather through a combination of brittle fracturing and ductile rotations (Imber et al., 2004; Long et al., 2011). We should therefore expect the relay zone to undergo a temporal development and observe incremental strains as fault tip lines propagate progressively closer together (e.g. Pollard and Aydin, 1984; Crider and Pollard, 1998).

Analytical solutions for isolated cracks under a uniform applied stress produce resolvable sets of internal stresses. Once additional cracks are introduced, the effect is more complicated. Superposition of the opposing three-dimensional elastic fields surrounding en echelon cracks results in their modification (e.g. Segall and Pollard, 1980; Delaney and Pollard, 1981; Pollard and Aydin, 1984; Crider and Pollard, 1998; Maerten et al., 2002). The resolved stress affecting the cracks becomes:

Equation 2.10.

$$\sigma_{total} = \sigma_{ij}{}^{a} + \tilde{\sigma}_{ij}$$

Where $\sigma_{ij}{}^{a}$ is the applied stress, and $\tilde{\sigma}_{ij}$ is the non-uniform (perturbed) stress component introduced by the interaction of neighbouring stress fields. The radius of the area over which these locally perturbed stresses act is a function of the proportion of the perturbed stress in the total applied stress, and the three-dimensional geometry of the bounding structures. Longer fractures will produce stress fields that can interact over greater distances, whereas shorter structures show little interaction as stress decays significantly with distance from the tip line (e.g. Segall and Pollard, 1980; Willemse et al., 1996; Crider and Pollard, 1998). This

prediction is based on *St. Vernants Principle* in that stress perturbations are local effects and at distances that are great relative to the size of the discontinuities the stress field is unaffected (Gudmundsson, 2011). The magnitude of the resulting stress field is approximated by the stress intensity factor (K), a function of the applied stress, geometry (length, depth) and position of a crack (e.g. Sih, 1976; Segall and Pollard, 1980; Engelder et al., 1993; Crider and Pollard, 1998). Thus, for a given overlap and separation, stresses can become sufficiently high to overcome the fracture toughness of the deforming material, resulting in inelastic breakdown in the relay zone and the formation of obliquely oriented ancillary fractures (Figure 2.13). The structural sets that develop are analogous to fractures that form a hard linkage between the en echelon master faults to accommodate the increased strains in the region (e.g. Childs et al., 1995; Ferrill et al., 1999; Walsh et al., 2003).

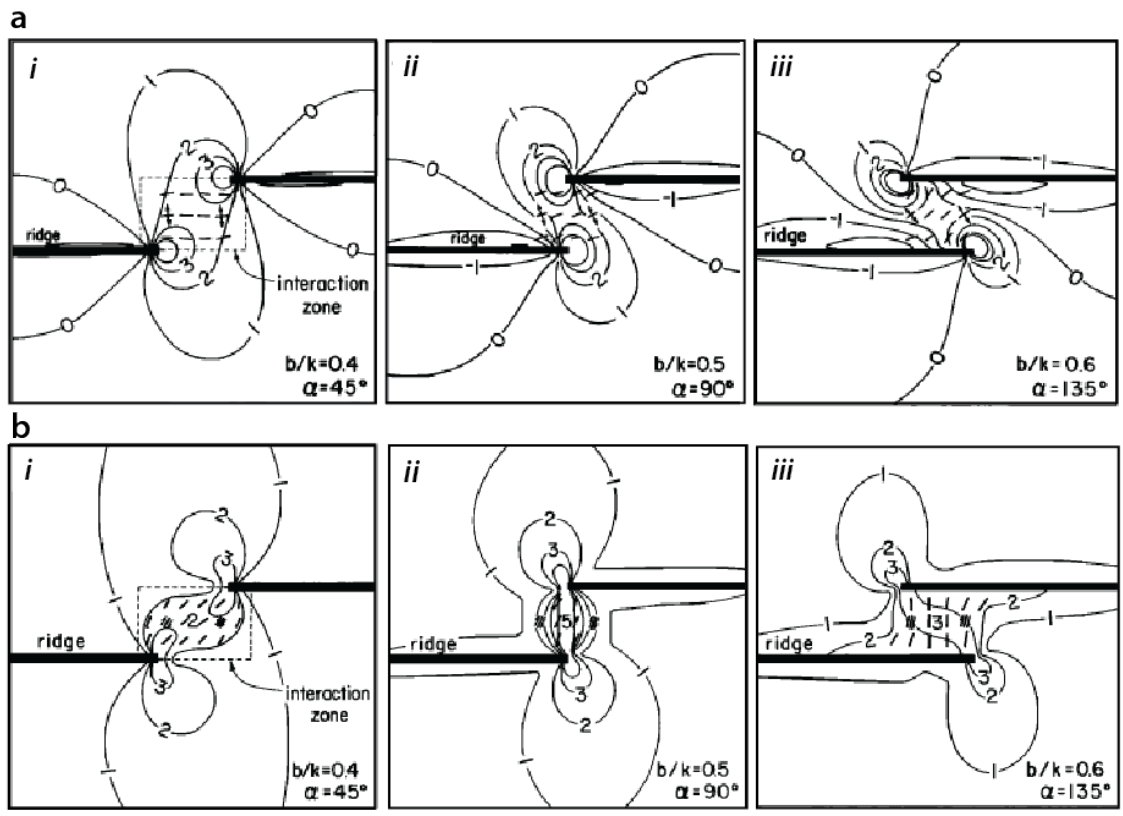

Figure 2.13. State of stress surrounding two en echelon spreading ridge segments: a) Contours highlight the distribution of mean normal stress for (i) underlapping, (ii) approaching and (iii) overlapping configurations; and (b) contours highlight the distribution of maximum shear stresses for (i)

underlapping, (ii) approaching and (iii) overlapping configurations. Sets of extensional and shear fractures are predicted to develop in the anticipated relay zone between the adjacent segments with progressive propagation and vertical axis rotation of the stress contours (from Pollard and Aydin, 1984).

The geometry and occurrence of the anticipated relay zone is therefore governed by the size (length, depth) of the faults, their separation, and their relative displacements (e.g. Willemse et al., 1996; Crider and Pollard, 1998; Figure 2.14). An increase in fault depth (and therefore, length) will produce greater overall stress change magnitudes, and increase the potential for secondary fault development. The geometry of stress change contours varies with overlap distance (Figure 2.14): small overlaps produce more widely-spaced contours, with a smaller overall stress increase. An intermediate overlap, where opposing tip lines are closest, results in contours of greater stress increase that trend at a high angle to the bounding faults (e.g. Gudmundsson et al., 1993; Gudmundsson, 2007; Willemse et al., 1996).

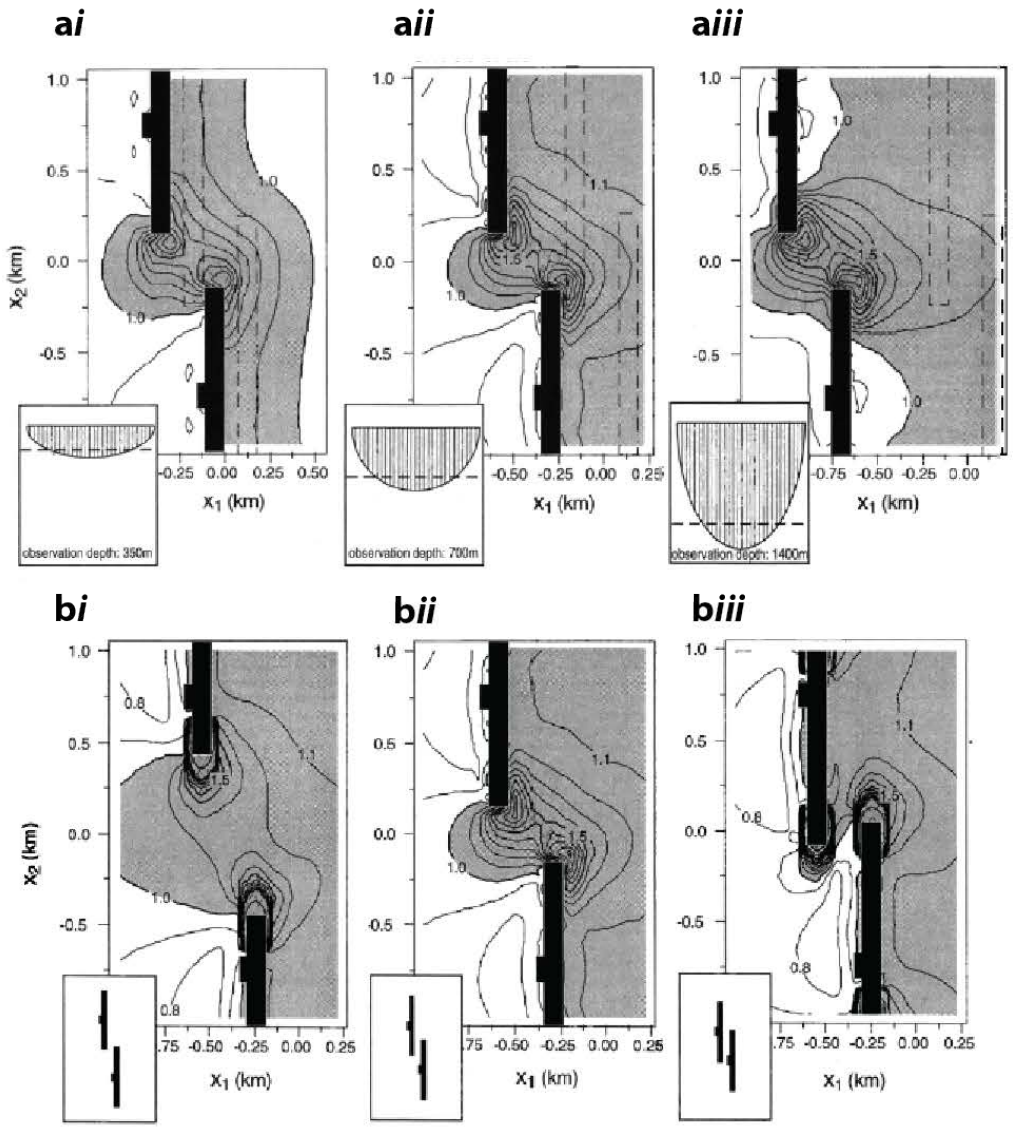

Figure 2.14. Static models of the state of stress surrounding two en echelon normal fault segments: a) Maximum shear stress contours for faults with a depth of (i) 300 m, (ii) 750 m and (iii) 1400 m; (b) Maximum shear stress contours for faults showing (i) underlapping, (ii) approaching and (iii) overlapping configurations (from Crider and Pollard, 1998).

Within the relay zone, shear stresses can be 40-50% higher than the applied stress (Crider and Pollard, 1998) but the effect is not constant through time; displacement on one of the master faults will alter the stress intensity factor at its tip and therefore the distribution of shear stress in the relay, resulting in the lateral inhibition of the opposing structure and non-linear displacement-length ratios (e.g. Huggins et al., 1995; Gupta and Scholz, 2000; Peacock, 2002).

Notably, models such as those in Figure 2.14 are static representations of a dynamic process. Natural relay zones may feature deformation consistent with a progressive changes in normal and shear stresses, as well as their trajectories prior to breaching taking place.

At distances that are more than twice the depth of faulting, elastic interaction is less significant and the contribution of the perturbed stress to the total stress is considered to be minimal. At this stage they are believed to be isolated structures (e.g. Segall and Pollard, 1980). The components of the modified stress field are additive (e.g. Lawn, 1993) and the configuration is asymmetrical with normal and shear stresses enhanced in some areas, and reduced in others. This pattern is governed by the geometric configuration of the bounding structures and the effect of the resulting interference patterns of the stress field components and resulting crack propagation force. This can be summarized to three configurations: (1) interaction of two tensile stress field components, results in increased tensile mean stress and promotes dilation; (2) interaction of a tensile and compressive component produces a reduced tensile mean stress; or (3) interaction of two compressive components produces a greater compressive mean stress, opposing dilation (e.g. Pollard and Aydin, 1984; Reches and Lockner, 1994**;** Crider and Pollard, 1998; Healy et al., 2006).

The process of fault interaction and linkage is likely to be further complicated in areas where syn-tectonic volume change results in heterogeneous and anisotropic driving stresses and it has important implications for (1) the temporal development and distribution of depocentres in developing rift systems; (2) the temporal variability of sediment distribution; and (3) the potential for both increased fluid flow and structural complexity and closure. This knowledge is especially relevant in volcanic passive margin sequences, where detailed analysis and exploration is impeded by poor resolution seismic reflection datasets.

Chapter 3

Physical and Mechanical Properties of Basaltic Lavas: Kilauea Pahoehoe

3.1. Introduction

The storage and transmission of fluid- and gas-related resources and wastes, such as hydrocarbons, water or carbon dioxide, and natural gas within crystalline rocks that are overlain by sedimentary sequences can represent economically significant exploitation opportunities if the basement rock is heavily fractured and/or faulted (Petford and McCaffrey, 2003; Schutter, 2003). Discoveries within crystalline basement rocks overlain by a sedimentary cover are expected to obey the same principles of sourcing, migration, and trapping that apply to fields in siliclastic sequences (Petford, 2003; Petford and McCaffrey, 2003). The geometry, distribution, and segmentation of fracture systems within crystalline sequences has a direct impact on fluid flow and sealing potential, and therefore the development and exploitation of fluid-related resources (McCaffrey, 2003; Walker et al., 2013). With the increasing economic viability of intra- and sub-volcanic hydrocarbon plays (e.g., the NE Atlantic basins: Davison et al., 2004), as well as water aquifer resources that rely on basaltic stratigraphy (e.g. Anderson and Bowers, 1995; Saar and Manga, 1999; Helm-Clark et al., 2004), understanding controls on the geometry and architecture of faults that develop within crystalline sequences is becoming increasingly important. Furthermore, fault segmentation has significant implications for the distribution of surface sedimentation (e.g. Morley et al., 1990; Gawthorpe and Hurst, 1993) and the emplacement and eruption of volcanic material (e.g. Walter and Amelung, 2006), hence understanding primary

controls on segment formation is critical to the study of these systems. Fault architecture and fault permeability structure models are based largely on siliclastic or carbonate systems. Studies of extensional fault geometry in layered clastic sequences have shown that changes in fault dip reflect variations in the mechanical strength of the layered host rocks (e.g. Peacock and Sanderson, 1991; Ferrill and Morris, 2003; Crider and Peacock, 2004; Figure 3.1a).

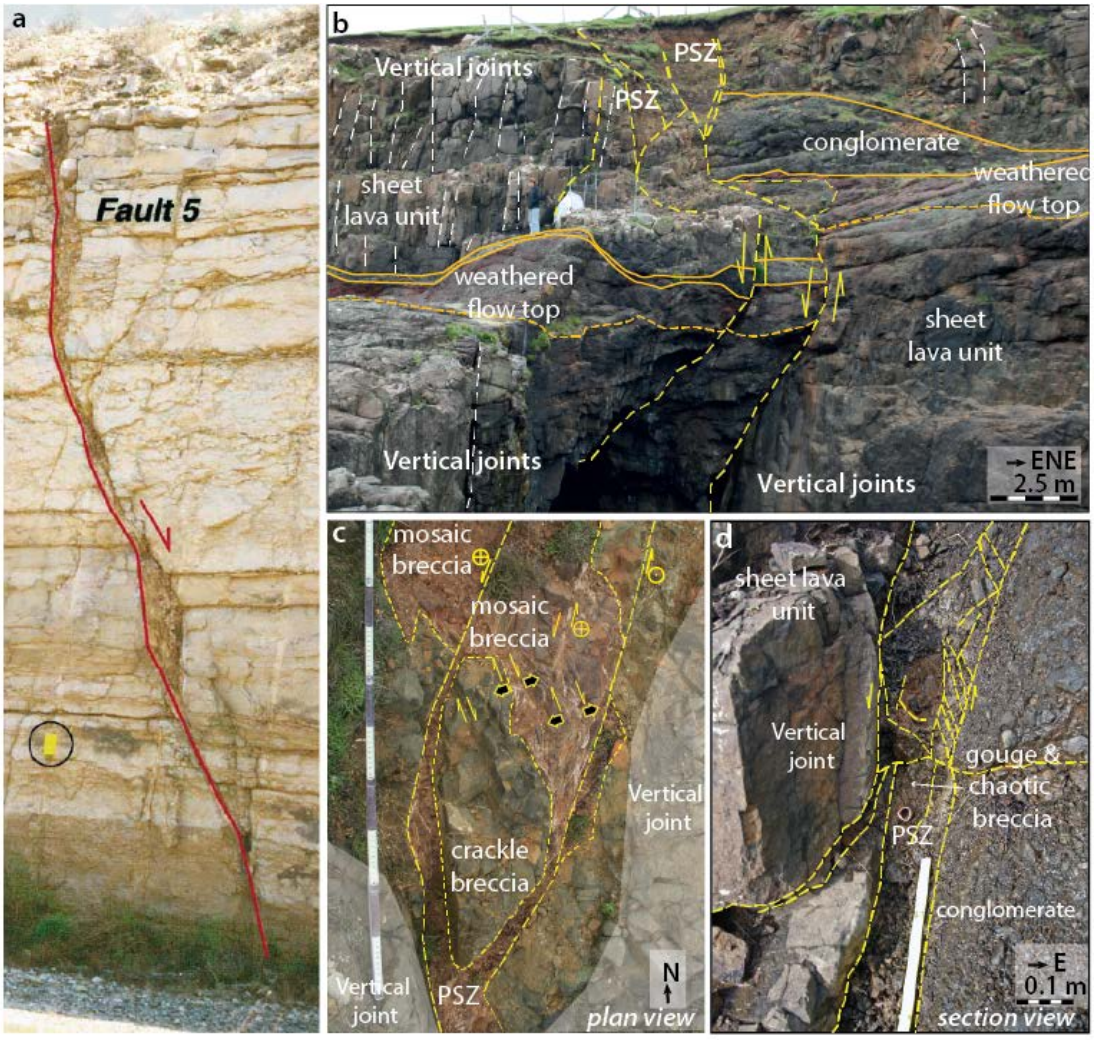

Figure 3.1. Examples of refracted fault traces in multi-layer sequences. a) Layered clastic sequences show steeply dipping fault segments in the stronger units and shallow dipping segments in weaker layers (from Ferrill and Morris, 2003). b) Volcaniclastic layers host inclined fault segments and ductile (non-localised) deformation, whereas fault segments are generally steeper, in the vertically jointed lava units. Inclined faults in the lava units consistently cut the vertical joint fabric at an

oblique angle in 3-dimensions. c) Plan view of a principal slip zone (PSZ). Some segments appear to follow the joint fabric but most of the deformation cuts obliquely to the adjacent, vertical joints. d) A PSZ cuts the joint fabric rather than following it. (Images in b-d modified from Walker et al., 2013)

At low strains, normal faults and/or extension fractures initiate in the mechanically stronger layers (e.g., sandstones) as steeply dipping extension fractures; mechanically weaker layers (e.g., mudstones) may initially deform by ductile flow. As the extensional strain increases, shear fractures develop within the weaker units, linking the steeply-dipping fracture segments to produce a through-going refracted fault (e.g. Schöpfer et al., 2006). More recent studies of fault propagation in volcanic systems show that faults undergo similar patterns of vertical segmentation and linkage through layered lava and volcaniclastic sequences (Walker et al., 2013: Figure 3.1b). Importantly, pre-existing cooling joint fabrics in these sequences *are not* ubiquitously reactivated; in many cases (refer to figures in Walker, 2010; Walker et al., 2013) natural basalt-hosted faults in the Faroe Islands are demonstrably oblique to vertical joint fabrics (e.g., Figure. 3.1) and show fracture densities that exceed the joint scaling, indicating that the intact rock strength was important during fault growth. In addition, volcano-tectonic studies of volcanic rift zones (e.g. Kilauea, Hawaii or Krafla, NE Iceland) highlight a dominance of double-couple earthquake focal mechanisms, associated with a range of shear displacements (i.e. normal, reverse and strike-slip) at depth (e.g. Brandsdottir and Einarsson, 1979; Thurber and Gripp, 1988; Arnott and Foulger, 1994; Wolfe et al., 2003; Lin and Okubo, 2016; Schuler et al., 2016). Universal opening and reactivation of pre-existing, open joint surfaces would not result in such a catalog.

Petrophysical analyses of flood basalt regions in the North Atlantic show significant variations in physical properties within individual lavas, particularly in terms of the volumes and geometries of pore space through the drilled sequence (e.g. Wilkens et al., 1991;

Planke, 1994; Planke et al., 1999). The variability of intact physical and mechanical properties has the potential to produce the effect of a multi-layered sequence within a single lava, and result in similar patterns of segmentation, fracture damage and linkage that we observe in clastic and crystalline-clastic sequences.

Here, I analyze the physical and intact mechanical properties of an individual pahoehoe lava from the Koa'e segmented rift system, to constrain a possible mechanical stratigraphy and consider the impact of this on the development of fault zones.

3.2. Background

Links have been made between the physical properties of brittle, porous solids (e.g. porosity and fracturing, both natural and man-made) and their elastic (mechanical) properties and strength. An increase in porosity has been shown, experimentally, to reduce the strength and the Young's modulus of the material (e.g. Rice, 1998; Al-Harthi et al., 1999; Palchik and Hatzor, 2004). The growth of faults through intact host rock is influenced by the mechanical response of a material to an applied stress, which is in turn controlled by the physical properties of the rock (e.g. Palchik and Hatzor, 2004). To fully characterise a rock's response to stress it is therefore important to examine its physical and mechanical properties.

3.2.1. Rock Strength

Traditional analysis of the strength and elastic properties of rocks involves the axial compression of cylindrical samples and the study of their stress-strain relationships, visualized on a stress-strain curve (e.g., Figure 3.2). Axial and lateral (circumferential or radial) strains, measured during the experiment using strain gauges attached to the sample, are plotted against stress to obtain the complete stress-strain curve (Jaeger and Cook,

1979). For tests where the lateral surface of the rock sample is tractionless, the experiment is considered unconfined and the sample undergoes uniaxial compression where $\sigma_1 > 0$ and $\sigma_2 = \sigma_3 = 1$ atm (0.1 MPa). When tractions are applied to the sample surfaces, the experiment is confined and stresses are applied in two orthogonal directions resulting in a stress state equal to $\sigma_1 > \sigma_2 = \sigma_3 > 0$.

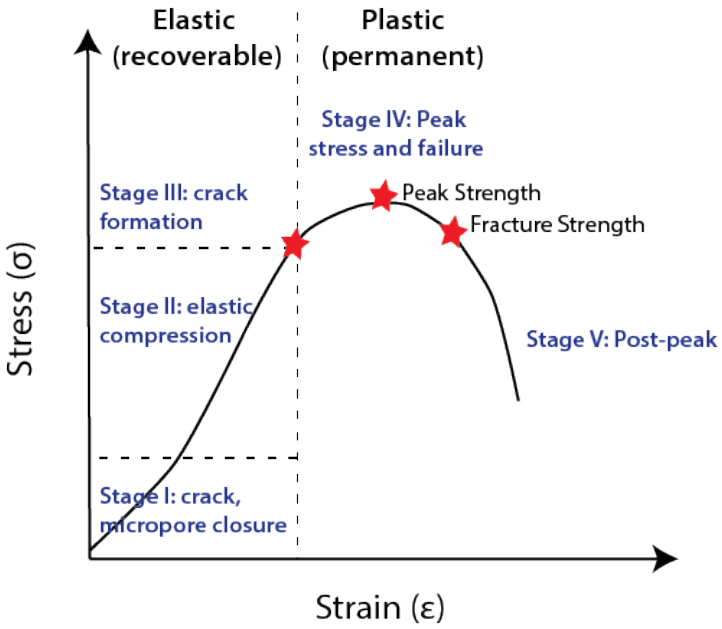

Figure 3.2. A typical stress-axial strain curve for rock materials demonstrating that stages of rock failure (after Jaeger and Cook, 1979).

Although two of these stresses are equal, the configuration is considered to be triaxial (Jaeger et al., 2007). During strain accumulation, the response of the rock is analysed using the complete stress-strain curve, which demonstrates 5 stages (e.g. Brady and Brown, 2004):

Stage I: Initial stress contact, "bedding down" and microcrack/pore closure (oriented normal to the applied compression). The resulting stress-strain curve shows an initial non-linearity.

Stage II: Period of linear elastic behaviour, reflected by a straight-line portion of the stress-strain curve. Strains during this stage are reversible.

Stage III: Strains become permanent as tensile cracking begins. Fracture initiation is reflected in the departure from the linear curve when the yield stress is attained; at this stage, lateral strain begins to increase with dilation related to crack opening. Crack propagation is stable but an increasing load is required to drive further growth (strain hardening).

Stage IV: Interaction and eventual linkage of microcracks lead to unstable crack growth without significant change in the energy of the system (strain weakening). Crack coalescence and the development of a localised through-going shear (or extensional-shear) fracture eventually results in catastrophic failure at the peak stress.

Stage V: At this stage, the rock has passed through the peak stress but the rock is still largely intact, although internally there is loss of cohesion. Strain localises onto the weaker elements and a constant residual stress is reached before the machine unloads the sample.

The curve describes the displacement of the samples from initial loading, through the linear elastic phase, the non-linear period of cracking to the peak stress and through the post-peak failure stage (Jaeger et al., 2007). The linear portion of the curve is used to derive the Young's modulus for samples; here the material shows identical stress-strain behaviour during loading and unloading. During post-processing, three values of Young's modulus (GPa) are calculated:

1) Secant Young's modulus: measured at 0-50% of the peak stress
2) Average Young's modulus at 20-80% of the peak stress
3) Tangent Young's modulus: measured at 25-75 % of the peak stress

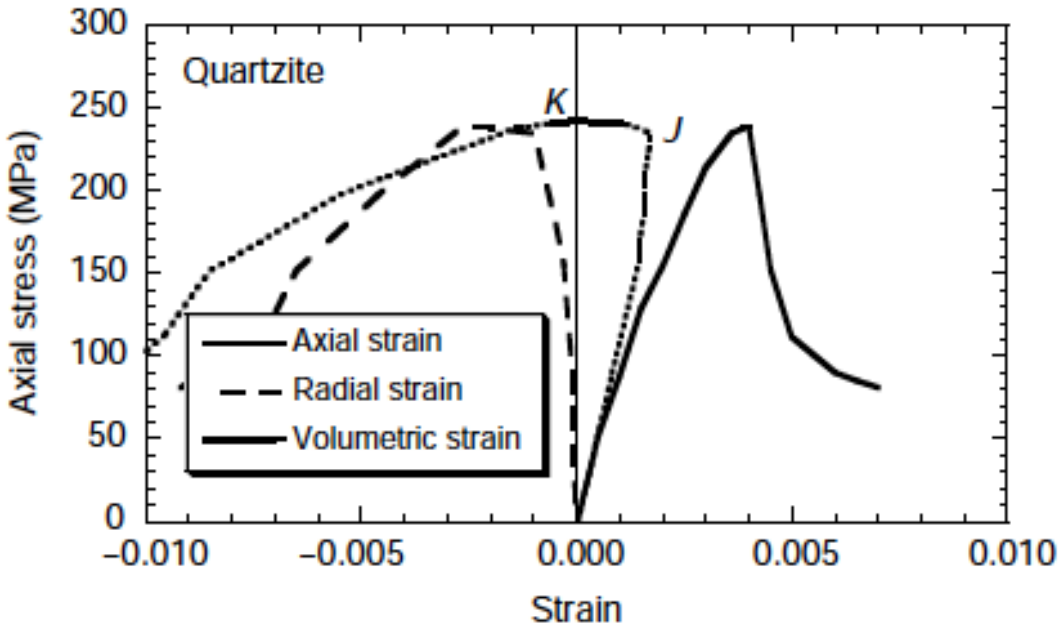

Figure 3.3. Example of a stress-strain curve for a quartzite, showing axial, lateral and volumetric strain plotted against axial stress in MPa. At point *J,* there is an initial loss of volume. At point *K,* radial/lateral strain is sufficiently negative that the total volumetric strain becomes negative and dilatancy takes place (from Jaeger et al., 2007).

Young's modulus is a property that defines how stiff a material is in response to an applied load: stiff elastic materials will demonstrate linear portions of the stress-strain curve that are steeper than less stiff materials (Pollard and Fletcher, 2005).

An elastic rock undergoing uniaxial stress will also shorten in the direction parallel to an applied axial compression (defined by the elastic modulus), whilst simultaneously extending in directions orthogonal to this. The negative ratio of lateral expansion to axial shortening forms an additional elastic constant known as the Poisson's ratio (v) (dotted line, J, Figure 3.3). For a linear elastic material, this property ranges from 0-0.5 and is independent of stress, with incompressible materials falling into the upper end of this range (Brady and Brown, 2004; Pollard and Fletcher, 2005; Jaeger et al., 2007). Uniaxial compression of cylindrical samples is used to determine these mechanical constants by measuring and recording the axial stress, axial strain, volumetric strain, and lateral strain

continuously until the material fails and stress is unloaded (e.g., Figure 3.3). Volumetric strain becomes the sum of axial and lateral (or radial) strain (dashed line, k, Figure 3.3), showing an initial decrease during loading associated with the phase of crack closure, and an increase with the development of microcrack volume (Jaeger et al., 2007).

Applying a confining pressure to samples under axial compression increases the stress required for failure and the rock is prone to more ductile (i.e. non-localised) behaviour. It has been shown that even minor increases in confining pressure at a constant differential stress result in significant increases in the amount of axial stress required to create a through-going shear fracture (Kranz, 1980; Costin, 1987).

3.2.2. Stress Concentrations

The mechanical properties of brittle rocks are sensitive to the nucleation and propagation of microcracks, which are in turn strongly influenced by the presence of void space, pores or pre-existing cracks in the material, which may behave as stress concentrators and nucleation sites. Inglis (1913) shows that local stresses concentrate around holes or corners in a plate subjected to an applied force and that those concentrations could be much greater than the remote stress. The magnitude of the stress amplification was shown, in elastic theory, to be controlled by the radius of curvature of the hole (e.g. Fischer-Cripps, 2007). Inglis found that a smaller radius of curvature resulted in a greater stress concentration and that the stress concentration factor (κ) for an elliptical hole was (Bagdahn et al., 2003; Fischer-Cripps, 2007):

Equation 3.1.

$$\kappa = 1 + 2\sqrt{\frac{a}{\rho}}$$

Where

a is the radius of the hole and ρ is the radius of curvature at the tip of the hole.

The scale of this amplification is dependent on the shape of the flaw, not the size; for an elliptical flaw the amplification is inversely proportional to the radius of curvature at the tip (e.g. Engelder, 1993). Studies of crack growth in glass and PMMA (acrylic glass) have suggested that inclusions or pores in rocks may act as stress concentrators, out of which microcracks will grow (Sammis and Ashby, 1986). For a spherical pore or void within an elastic body, tensile stresses are expected to localise around the north and south poles of the pore, equal to:

Equation 3.2.

$$\sigma_{\theta\theta} = -\frac{3}{2}\frac{(1+5\upsilon)}{(7-5\upsilon)}\,\sigma_1$$

According to the pore-emanating crack model of Sammis and Ashby (1986), microcracks are predicted to nucleate at the crowns of pores (Figure 3.4a) and if the ratio of length to radius (L/a) is <0.2, and local stresses exceed the fracture toughness of the intact material, self-sustaining (unstable) cracks will grow in a direction parallel to applied maximum compression. Progressive failure shifts the local stress maximum outward and elastic strain energy is released during increments of crack growth (Lajtai, 1974). An increasing load is required for microcracks to begin to link and coalesce. When the ratio exceeds 0.2, slow and stable crack growth dominates and microcracks reach a critical length where their stress fields begin to interfere, resulting in local stress increases that lower the required force for further crack propagation (strain-weakening behaviour) in the intact rock. Linkage and coalescence of individual pore-microcrack arrays lead to the formation of through-going fractures and, ultimately, brittle failure (Figure 3.4b).

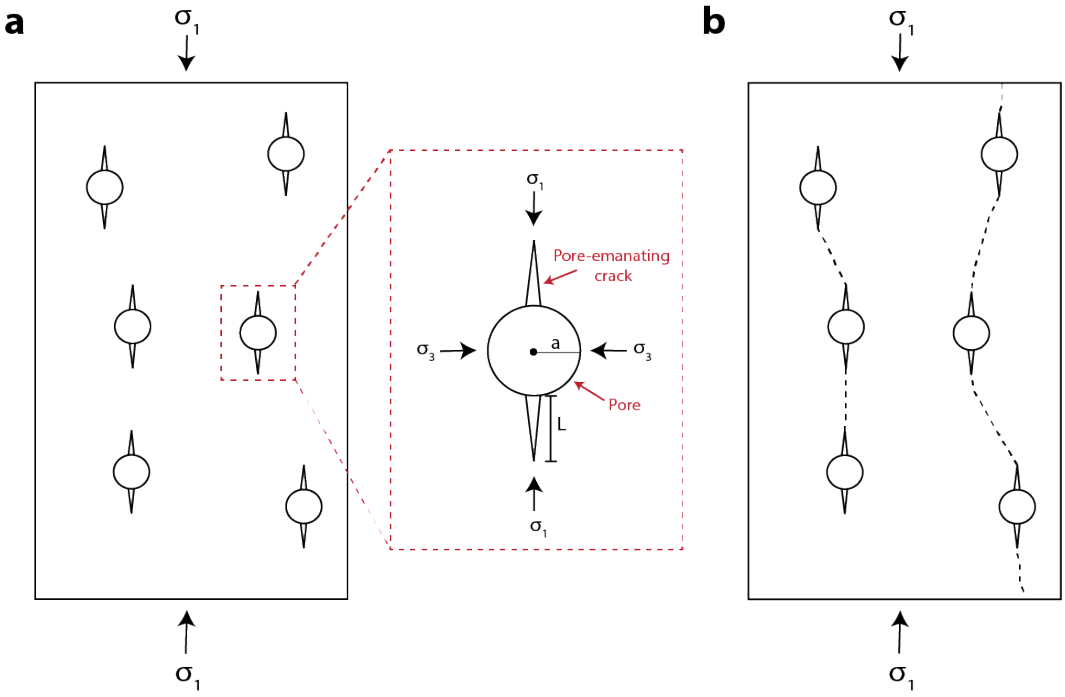

Figure 3.4. a) Tensile stresses are predicted at the intersection of a circular pore, or vesicle, with the maximum principal stress. In uniaxial compression, extension mode fractures will develop at the north and south poles of a pore, propagating parallel to the applied compressive stress direction. b) When L/a >0.2, crack growth becomes unstable (after Sammis and Ashby, 1986; Dresen and Gueguen, 2004; Heap et al., 2014).

For basaltic rocks, vesicles are thought to behave as stress concentrators and the initiation point for fractures in the same manner (Heap et al., 2014). Tensile stresses are predicted at the north and south poles of vesicles, where the applied compressive stress axis intersects the vesicle boundary (Figure 3.4). In the same way we expect stress concentrations at the tips of a crack to promote unstable microcracking and propagation, the stresses at the north and south pole of a vesicle should also drive the growth of cracks outwards from the edge of the vesicle (Dresen and Gueguen, 2004).

Brittle failure of rocks under uniaxial compression is attributed to localised tensile microcrack development, followed by progressive linkage and coalescence that produces a single macro-fracture. How the physical properties, i.e. the distribution of vesicles, vary in

basalts will tell us where, and under what stress conditions, a fracture will develop. Acquisition of this information will be used to test models of fault propagation and porosity maintenance in basaltic sequences.

3.2.3. Compound Lava Unit Characterisation

Large accumulations of lava flows, associated with large-scale, transient effusive volcanism, accompany the formation of volcanic passive margins during continental break-up (e.g. Planke et al., 2000). Such deposits do not demonstrate straightforward layer cake-like stratigraphy, but vary between tabular, jointed simple flow units (Figure 3.5a) and thinly layered compound units (Jerram, 2002; Walker et al., 2013; Figure 3.5b). Thicknesses of simple lavas in large igneous provinces, such as the North Atlantic Igneous Province, can range from 15-50 m and cover total areas of approximately 1.3 $x10^6$ km^2 (Planke and Eldholm, 1994; Jerram et al., 2009). Compound lava units comprise individual lobes with thicknesses varying from 0.5-5.0 m and lateral extents of a few metres to tens of metres (Jerram et al., 2009). Mechanical analyses in this chapter are conducted on subaerially emplaced intact olivine tholeiites or basaltic pahoehoe lavas (*henceforth, basaltic lava or lava unit*). Subaerial pahoehoe lavas are the most abundant volcanic rocks on Earth and are emplaced as channelized flows; this is the major characteristic that separates them from aa lava flows, large volume flood basalts and some submarine flows (e.g. Hon et al., 1994 and Self et al., 1998). A typical pahoehoe lava is characterised by smooth, ropey upper surfaces and flow takes place by the gradual inflation and impingement of separate lobes beneath a solid crust that become localised with time (e.g. Cashman and Kauahikaua, 1997). During this inflation-propagation process, the upper and lower surfaces of a lobe cool first, forming a glassy shell, and flow is focussed within the insulated flow front (core) of the lobe (e.g. Hon et al., 1994; Self et al., 1996, 1998; Cashman and Kauahikaua, 1997). The outer shell of a solidified, inflated lava shows a high proportion of glass and coarse vesicles, associated

with the rapid in situ exsolution of volatiles. During inflation of a lobe, the flow front experiences greater internal pressures that inhibit volatile exsolution. Instead, volatiles slowly rise leaving behind a dense, crystalline (low glass/vesicularity) core and resulting in a progressive increase in vesicularity and thickness of the upper outer shell (e.g. Fowler et al., 2015).

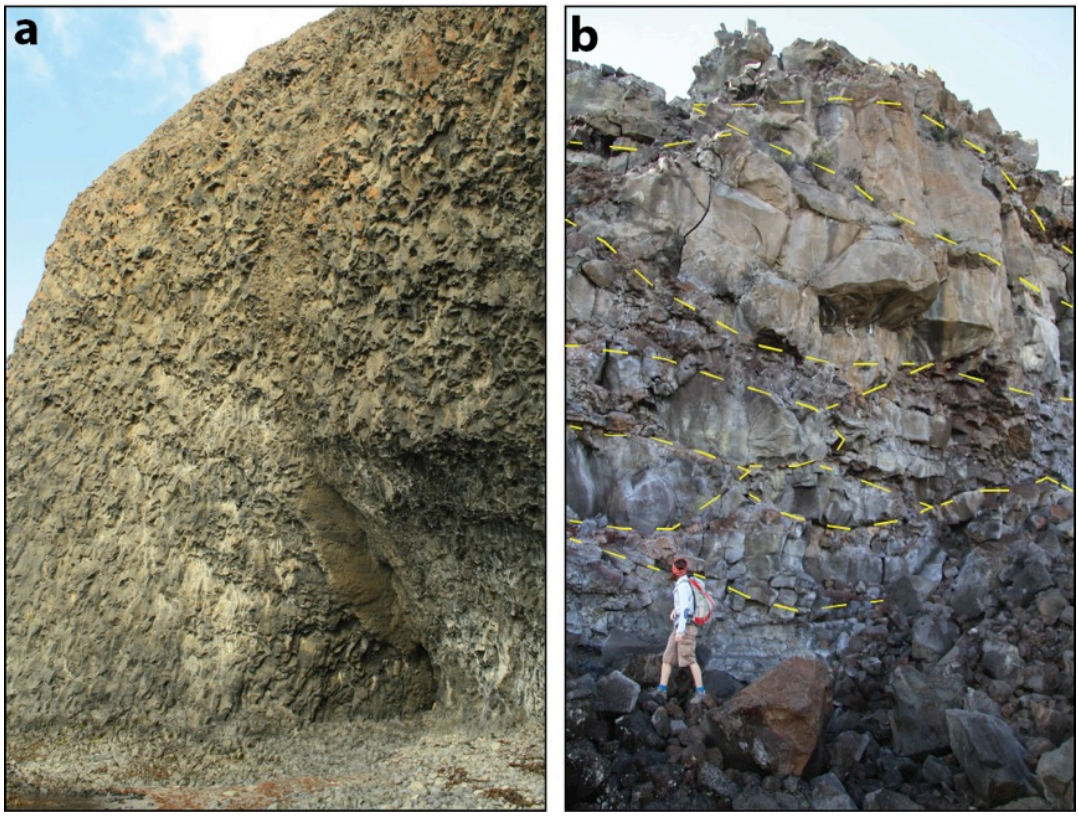

Figure 3.5. Examples of basaltic lavas. a) Thick, tabular, jointed *simple* lava (cliff height = 40-50 m) from NE Iceland. b) Thinly layered *compound* units comprise individual lobes with varying thicknesses (image from the Koa'e fault system, Hawai'i). Dashed yellow lines indicate individual lobes.

The amount of inflation within a lobe is a function of the lava viscosity, gas content and rate of magma supplying the basaltic lava flow; low supply rates result in lower flow velocity, smaller lobes and more rapid cooling (Hon et al., 1994).

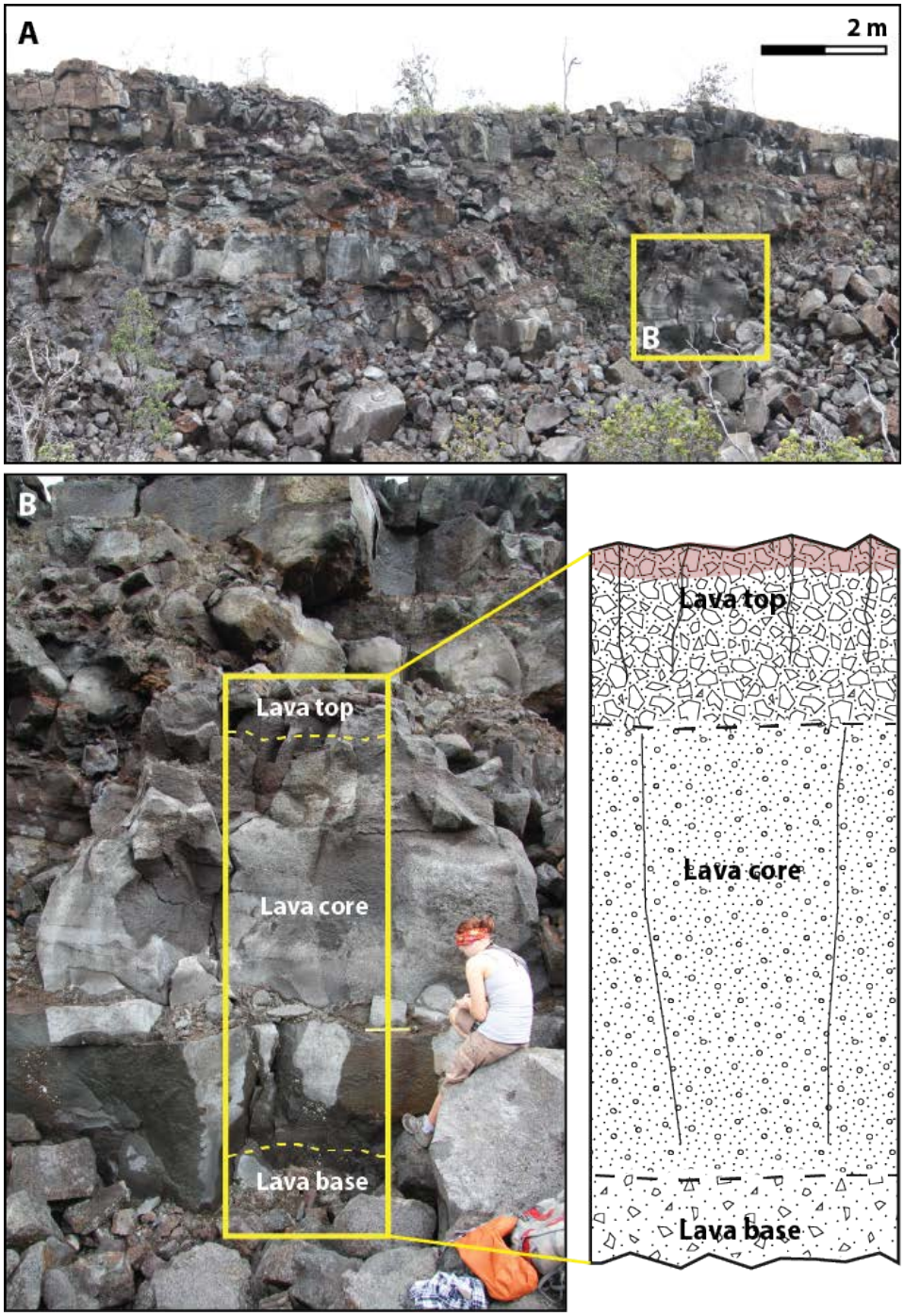

Figure 3.6. (a) A ~6 m high scarp exposing a series of lobate basaltic lava units. (b) Internal structure of a single basaltic lava unit highlighting three components shown schematically. (c) A weathered and vesicular unit top, massive unit core, and rubbly unit base.

Internal to an individual unit are three components (Figure 3.6) that scale with lava thickness and are defined by varying vesicle size, distribution and shape (e.g. Planke, 1994; Self et al., 1998; Planke et al., 1999; Petford, 2003; Walker et al., 2013):

1) Highly vesicular, glassy (low crystallinity) lava tops that are commonly weathered and reddened, reflecting the dominance of alteration clays such as smectite and iron hydroxides.

2) Dense, high crystallinity (low glass content) lava cores, characterised by low vesicle concentrations and larger scale joint-related porosity.

3) Rubbly lava bases that show similar glass contents to the top and intermediate porosities.

The characteristics of each of these components (top, core, and base facies) is ubiquitous in basaltic lavas and the proportions of each one scales with flow thickness (e.g. Self et al., 1998, 2015; Jerram et al., 2009).

As a basaltic lava cools and solidifies, stress due to thermal contraction accumulates to a level where the tensile strength of the material is reached, resulting in the formation of internal columnar cooling joints (e.g. Lyle, 2000). For lava that cools from above, joints are predicted to propagate downwards, in increments, with column diameters that are controlled by the cooling rate and thermal gradient of the lava (Phillips et al., 2013). For lobate extrusion, the outer portions cool more rapidly and joints are correspondingly smaller then the insulated core. The variable rates of magma supply produce varying lobe thicknesses and therefore juxtapose units with varying joint scales. Consequently, planar, in-plane discontinuities rarely exist in basaltic lavas.

At seismic scale thicknesses (40-50 m), seismic reflection techniques are able to image the thickness of lavas, which are well-expressed in low velocity sediments, and detect high and low velocity zones. Thinner basaltic lavas (or vertical dikes) are, however,

challenging or impossible to detect; internal architectures are especially difficult to resolve (Schutter, 2003). To characterise the internal characteristics and physical properties of lavas, detailed petrophysical analyses of drilled samples have been necessary. However, issues regarding core recovery and questions over the resolution of lava-scale variations in both porosity and P-wave velocity measurements have raised doubts on the reliability of interpretations based on these (Planke, 1994). A characterisation of the brittle strength of lavas, and the growth and propagation of fractures within them, is fundamentally important to our understanding of fault growth in basaltic lava-hosted volumes, and especially where fault development may not be controlled by the reactivation of pre-existing joint surfaces.

3.3. Datasets

This study involves detailed physical and mechanical characterization of naturally exposed fault plane surfaces within compound lavas in the Koa'e fault system, located on the south flank of Kilauea Volcano on Hawaii's Big Island (Figure 3.7a). In addition to measurements of porosity, density, and unconfined compressive strength, this characterisation includes measurement of the lava thicknesses, as well as careful classification of the internal architectures of the lavas.

3.3.1. Sample Collection: The Kulanaokuaiki Fault Trace

Rock samples were collected from the exposed natural fault surface of the Kulanaokuaiki fault, located at the eastern end of the Koa'e fault system, 7-8 km south of Kilauea's summit caldera (Figure 3.7a and b). Normal faults in the Koa'e fault system develop at shallow depths (0.5-4.0 km: Denlinger and Okubo, 1995; Lin and Okubo, 2016) with the early stages of fault propagation associated with the formation of extension fractures at the

free surface ahead of upward propagating normal fault tips (e.g. Martel and Langley, 2006). Eventual linkage of faults and extension fractures has resulted in surface traces that demonstrate both vertical and horizontal components of displacement (for more details, see Chapter 4).

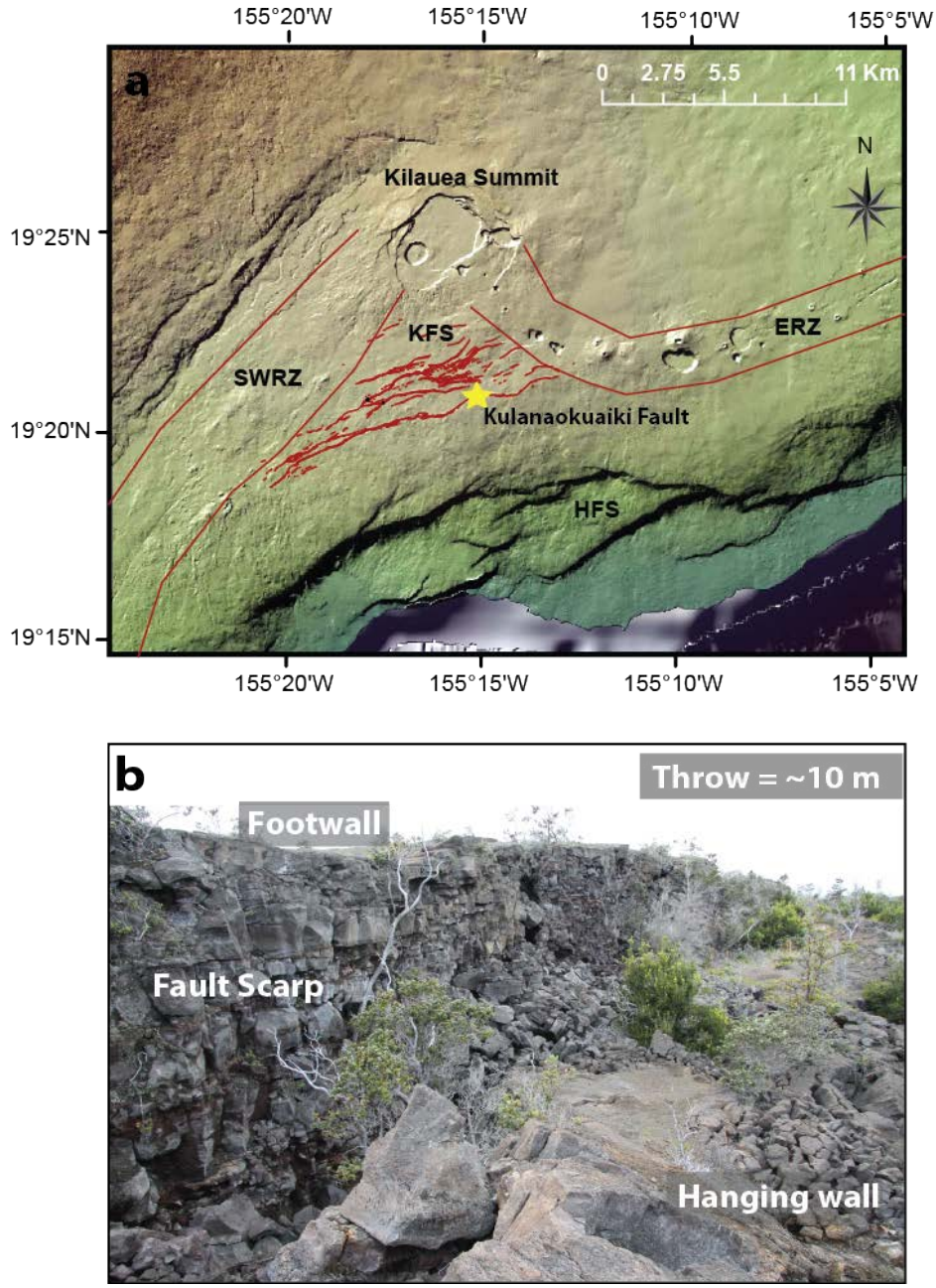

Figure 3.7. (a) Location of the Kulanaokuaiki Fault in the Koa'e Fault System, Hawai'i highlighting the major tectonic elements on the south flank of Kilauea Volcano: the southwest rift zone (SWRZ), east rift zone (ERZ), the Koa'e fault system (KFS) and the Hilina fault system (HFS). (b) Footwall and hanging wall surfaces are offset across subvertical scarps up to 12-15 m that are characterised by

open fractures at their base. Maps produced using GeoMapApp version 3.4.0. For more information on the geological setting of this fault see Chapter 4.

The Kulanaokuaiki fault is an ENE-WSW striking normal fault, comprised of a series of linked en echelon segments, forming a segmented single fault structure 4-5 km long. Footwall and hanging wall surfaces are offset across a sub-vertical fault scarp by up to 15 m. The fault was most recently active during the December 1965 eruption of Kilauea (Fiske and Koyanagi, 1968). Mapping of ground cracks and faults that developed during this activity revealed substantial damage along the Kulanaokuaiki fault, which formed the southern-most extent of ground cracking (Fiske and Koyanagi, 1968).

Sample cores were drilled from blocks of minimally weathered 750-1500 year old basaltic lava (Wolfe and Morris, 1996), exposed along the Kulanaokuaiki Fault. Samples are fine grained with porphyritic textures and dominated by phenocrysts of olivine and plagioclase, set in a matrix of granular plagioclase and pyroxene. Olivine phenocrysts are typically euhedral, up to 1-1.25 mm in size. XRF (X-ray fluorescence) major element analysis of samples reveals high silica content of ~50% and lower MgO and CaO contents of ~7% and ~10% respectively. Comparison with lavas from the Hawaiian Scientific Drilling Project (HSDP) show a strong correlation (Table 3.1).

Element	Kulanaokuaiki Sample	Kilauea (HSDP) Standard*
SiO2	50.72%	50%
TiO2	2.55%	2.76%
Al2O3	13.46%	13.74%
Fe2O3	12.35%	12.09%
MnO	0.164%	0.18%
MgO	7.42%	6.88%
CaO	10.93%	11.42%
Na2O	2.31%	1.78%

Table 3.1. Major elements of the Kulanaokuaiki basalts and Kilauea standard (* Rhodes and Vollinger, 2004).

Samples obtained in this thesis are vesicular with open, non-mineralised voids ranging from 2 mm to 20 mm, depending on the location within the unit. Vesicles in the unit tops show average diameters of 3-5mm but voids of up to 20 mm are not uncommon. In the core zone, vesicles are more homogenous, with diameters of 0.5-1.0 mm, and 2-3 mm in the base of the lava. Vesicles also vary in shape, being rounded to sub-rounded with no preferred orientation in the unit top and core, and flattened ellipsoids aligned parallel to the flow direction in the unit base. To identify whether lavas exhibit similarly variable mechanical profiles as we observe in compositionally variable clastic or crystalline-clastic sequences, four blocks were collected from vertical transects through two separate lava units, which provided 18 samples to test. Multiple samples were taken from each component (top, core, base), based on their morphological characteristics (Figure 3.8), to determine the physical and mechanical properties of each one.

Careful characterisation of basaltic lavas exposed along the length of the fault trace reveals a physical stratigraphy based on the total volume and geometry of vesicles and the scale of joint patterns along a vertical profile through the lavas. Examples of the three components are summarised in Figures 3.8 and 3.9, which show three units at the m-scale and one at the cm-scale. Lavas with thicknesses >2 m were present but difficult to access to conduct detailed logging. Vesicularity and joint scaling, however, shows internally consistent characteristics at a range of lava unit thicknesses from tens of cm to >2 m (Figures 3.8 and Figure 3.9), consistent with published studies of pahoehoe lava units (e.g. Planke et al., 1994; Self et al., 1998). Mechanical analysis required samples to be representative of the internal structure of a lava unit, hence samples did not need to be taken as a continuous transect from a single lava.

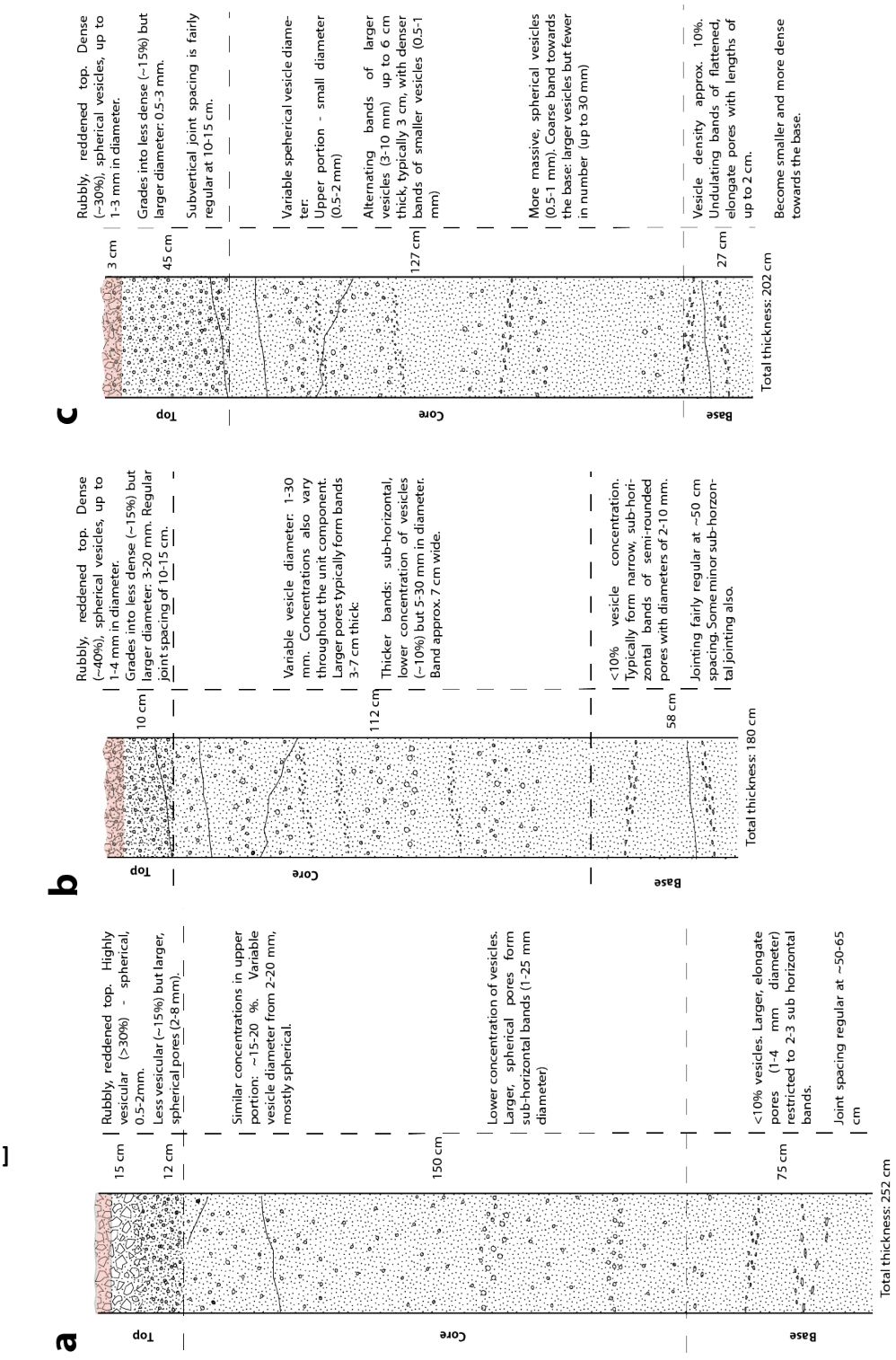

Figure 3.8. Examples lava stratigraphy of units exposed along the Kulanaokuaiki Fault in the Koa'e fault system, Hawai'i. Cores show the lowest vesicle concentrations. Unit tops are variable in thickness, but thinner than core components with weathered tops and the largest vesicle concentrations. Unit bases are typically approximately half the thickness of the cores. Vesicle distributions are variable and geometries are often flattened, and elongate rather than spherical.

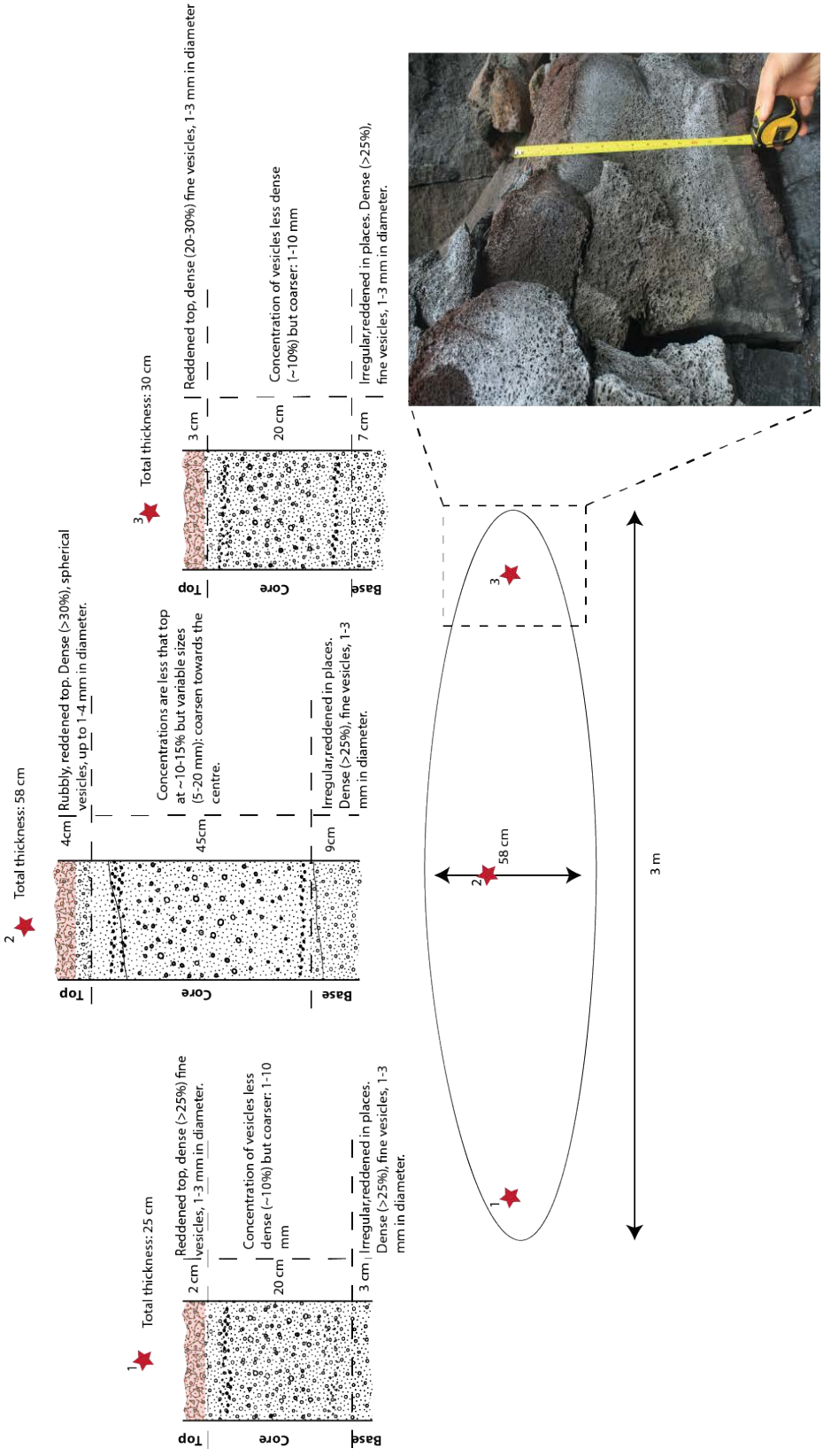

Figure 3.9. Example of lava stratigraphy. Characteristics for each component are comparable to lava units with thicknesses of 1-2 m (Figure 3.8) and pahoehoe lavas from other basalt provinces, such as Iceland or the Columbia river where thicknesses exceed 10-20 m (Self et al., 1998).

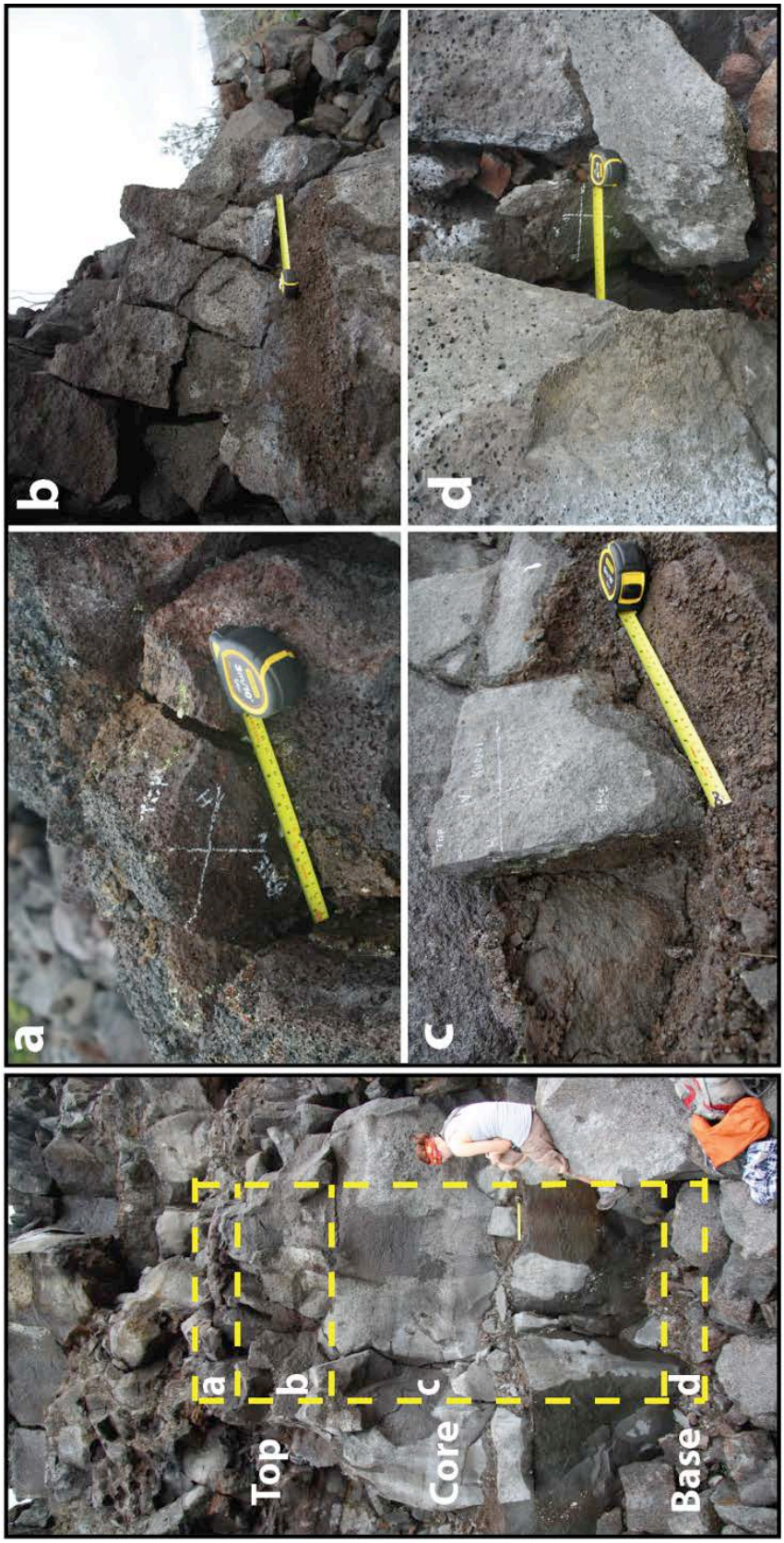

Figure 3.10. Example of lava unit demonstrating the three components: top, core, base. Images a-b show the location of samples within the unit. a) Rubbly, oxidised upper unit top surface. b) Unit top. c) Dense unit core. d) Unit base.

To avoid inducing any microfracturing during the sampling process, blocks that could be lifted free from the rock face by exploiting natural rock fractures or joints were sampled, rather than hammering samples out. Due to research permit restrictions, sample collection was limited to 40 kg, which provided four blocks from the targeted units: (1) one from the upper part of the unit top; 2) one from the lower part of the flow top; (3) one from the core of the flow unit, and (4) a block from the base of the flow unit (Figure 3.10).

3.3.2. Sample Preparation

To experimentally reproduce the stress conditions required to nucleate and propagate fractures through a dry, near-surface intact solidified basaltic lava unit, the unconfined compressive strengths of 18 samples (sourced from 4 blocks) were measured: 8 from the upper unit top, 4 from the lower unit top, 4 from the unit core and 2 from the unit base. Samples are considered to be comparable to subaerially quenched lava samples retrieved from depths of 740-1200 m in boreholes that were drilled to a depth of ~2 km in Kilauea's East Rift Zone (Quane et al., 2000).

Uniaxial compressive strength testing requires test samples with a length approximately two times the diameter to avoid the build up of pressure at either end that is in contact with the apparatus, and thus to ensure the even distribution of stress throughout the sample (ASTM, 2008). Samples should also be prepared so that the diameter is ten times the diameter of the largest grain or pore to remove the risk of edge effects and related failure (Fairhurst and Hudson, 1999). Lava samples for these tests have an average diameter of 37 mm and an average length of 74 mm, giving a length to diameter ratio of 2:1. Average pore diameter in the highest porosity samples (unit top) of 2.5-3.0 mm. Due to permit-enforced limitations on sample collection, a choice between a greater number of

small cores or a small number of large cores had to be made. For the purposes of reproducibility, 38 mm diameter cores were selected to increase the number of tests possible. A diameter less than this would produce a greater number of samples to test but larger vesicles in some of the samples would exceed the 10:1 ratio of diameter to vesicle size.

To identify and characterise any three-dimensional mechanical anisotropy, samples were cored in two orthogonal orientations (Figure 3.11): (1) a vertical core, oriented normal to the bedding contacts between lava units and, (2) a horizontal core, oriented parallel to the bedding contacts direction.

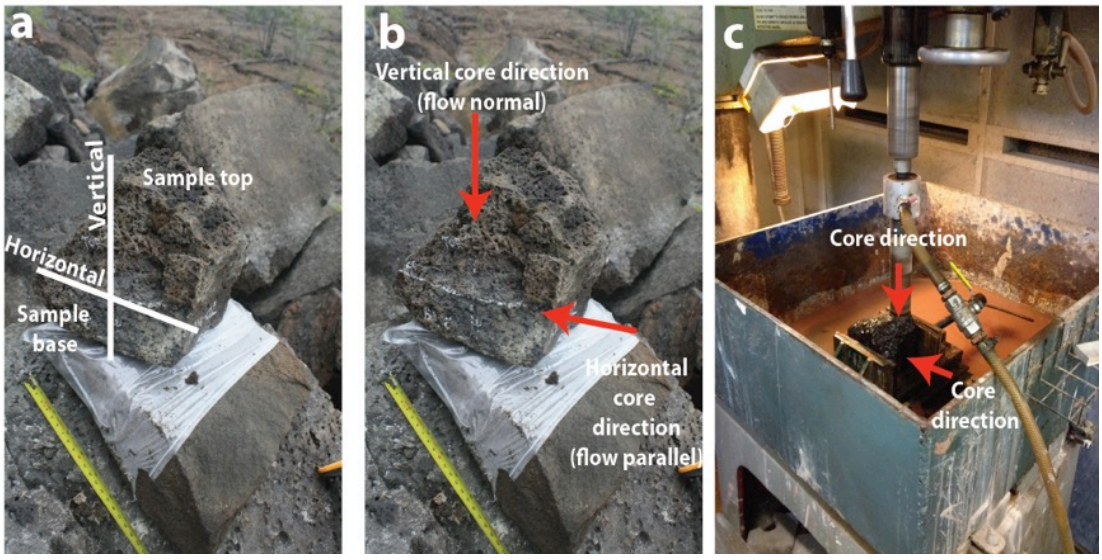

Figure 3.11. Sample orientations. a) Horizontal and vertical directions are measured and marked on each rock sample along with top and base positions before they are removed. b) Vertical directions represent the planes oriented normal to the orientation of bedding surfaces. Horizontal directions represent planes parallel to bedding surfaces. c) Each sample was cored along these orthogonal planes to fully characterise any strength anisotropy.

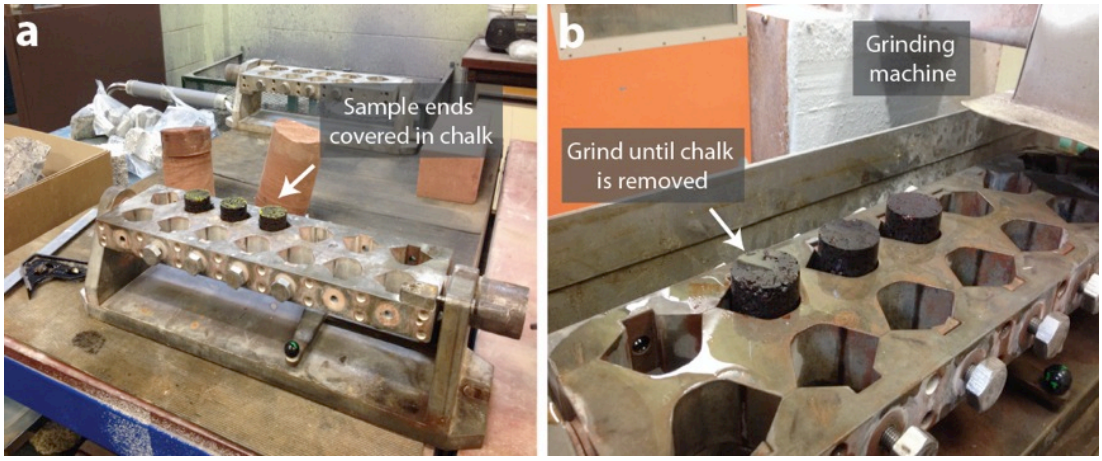

Figure 3.12. Machine grinding of sample ends. a) Ends are covered in chalk, levelled and placed in a vice. b) Two stages of grinding takes place: a coarse and fine pass. The first pass is complete when the chalk is removed. Surfaces are then re-chalked and the second, fine pass begins.

For samples to fit the tolerance of ASTM (2008) method requirements for straightness, flatness and perpendicularity, each of the cored cylinders was smoothed using grinding machinery (Figure 3.12), which produces surfaces that are flat to within 0.002 mm and perpendicular to the cylinder axis by no more than 0.001 radians. Precision grinding of sample surfaces limits potential stress concentrations and ensures even distribution of stress through the sample.

3.3.3. Measuring Porosity and Density

The physical characteristics of a rock (e.g. porosity and density) have significant implications for the strength and deformability of the material. In basaltic lavas the principal porosity comes from their vesicularity, therefore, prior to measuring the unconfined compressive strength, each sample was tested for porosity and density. These properties were measured using the ISRM suggested methodology (Bieniawski and Bernede, 1979b). Since density is related to the grain mass, volume, and porosity, it is possible to calculate one parameter if the others are known. For full procedure details, see Appendix I.

Effective porosity (P), or the proportion of voids per unit of total volume becomes:

Equation 3.3:

$$\boldsymbol{P = \frac{V_v}{V} \times 100}$$

Where

$\boldsymbol{V_v}$ = Pore volume
$\boldsymbol{V}$ **=** Bulk volume

In soil mechanics, it is assumed that all of the pore space in the material is interconnected. This is not the case for rocks, therefore the resulting figure is measurement of the interconnected pores only and represents an effective porosity rather than a total porosity, which would also include isolated voids.

3.3.4. Unconfined Compressive Strength

Uniaxial compression of cylindrical samples provides a measurement of the unconfined compressive strength (measured in MPa), and elastic properties: Young's modulus (GPa) and Poisson's ratio (dimensionless) for each flow unit component (Figure 3.13). Rocks were experimentally taken to failure under analogous near-surface stress conditions to those inducing failure in the Koa'e fault system in the upper 0.5-4 km of Kilauea's south flank (Lin and Okubo, 2016), using an MTS 815 servo-controlled hydraulic rock mechanics testing system with a 4600kN loading frame.

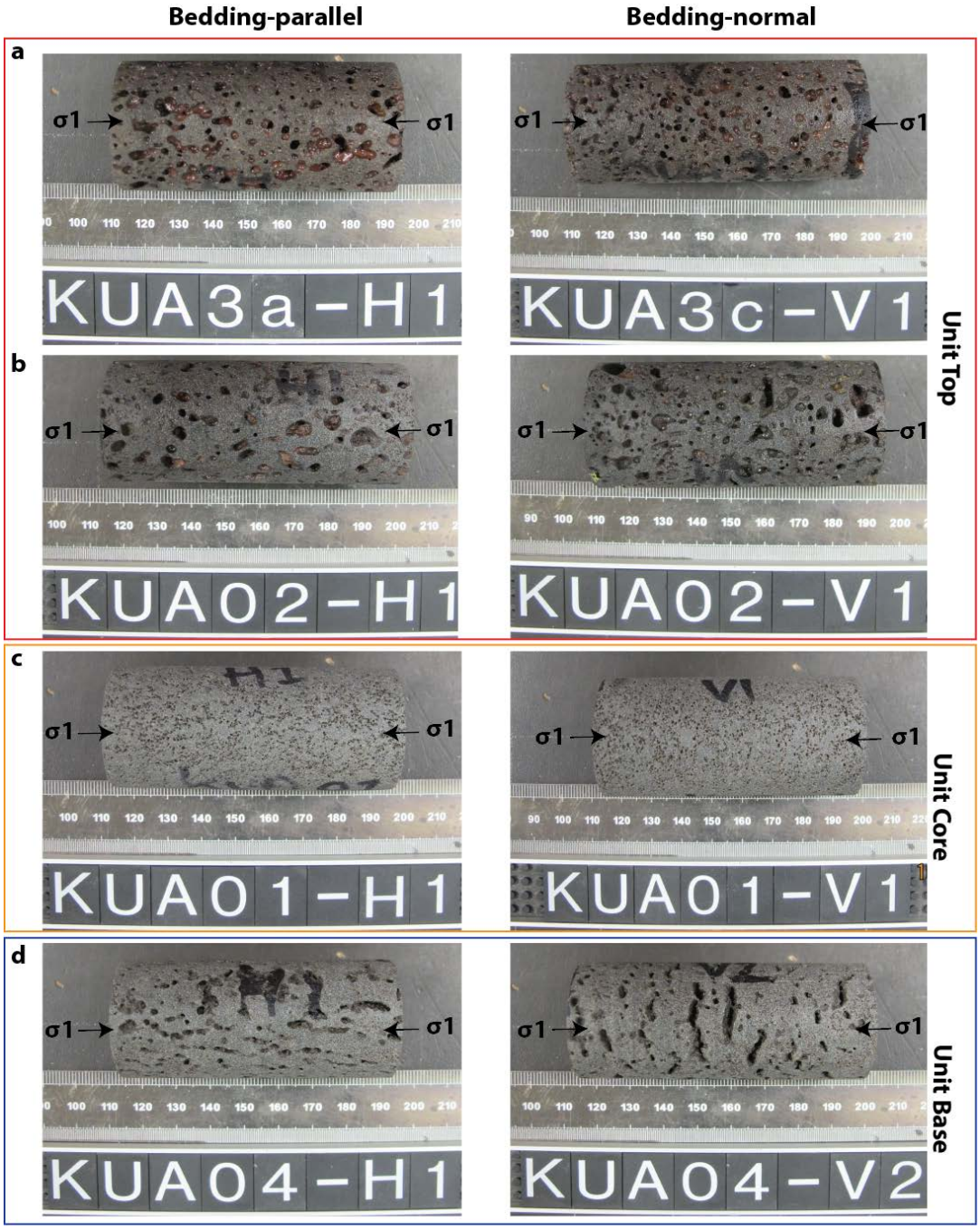

Figure 3.13. Prepared samples from each lava unit component in each sample orientation and the applied stress direction. a) Upper unit top. b) Lower unit top. c) Unit core. d) Unit base.

The measurement of unconfined compressive strength was conducted in accordance with the ISRM suggested methodology (Bieniawski and Bernede, 1979a, Fairhurst and Hudson, 1999). Following coring and precision grinding, axial and lateral strain gauges were

attached to the samples (Figure 3.14) to obtain a complete stress-strain curve. To reduce the effects of specimen non-parallelism, a spherical seated upper loading platen was used, the radius of which was slightly larger than the radius of the samples being tested. Samples were positioned so that their top surface coincided with the centre point of the spherical seat.

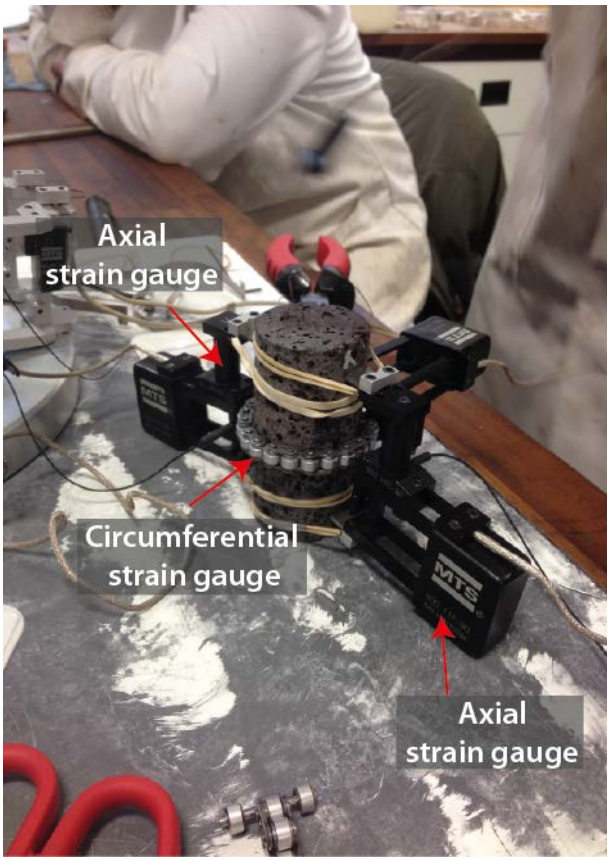

Figure 3.14. Preparing samples for uniaxial compressive strength testing: Samples are cored and precision ground to produce cylinders 36 mm in diameter and 70-73 mm in length, resulting in a length: diameter ratio of 2:1. A 104 mm chain is wrapped around the centre of each sample to measure lateral strain throughout the test. On opposite sides of the samples, two 50 mm axial gauges are attached.

Direct contact extensometers were employed to measure axial and lateral strain: axial gauges had a length of 50 mm and lateral chains were 104.4 mm long. Axial gauges of this length covered more of the sample but potentially recorded deformations pertaining to edge effects. A smaller axial gauge could have been attached to the sample but this would have collected readings from a smaller area that may not have been representative of the whole sample. During each test, a constant strain rate control mode was used where the machine adjusts axial stress accordingly throughout the test. For the duration of each test,

axial and lateral strain were measured and recorded continuously using these gauges. Testing of brittle materials under axial compression has shown that the use of axial strain control is often insufficient in bringing rock to failure at a controlled rate once the peak stress has been attained (Bieniawski and Bernede, 1979a, Fairhurst and Hudson, 1999). This is related to the characteristics of the stress-strain curve following peak stress: samples that behave in a more ductile manner will display a class I curve, whereas a class II curve is typical for materials that respond in a more brittle manner (Figure 3.15).

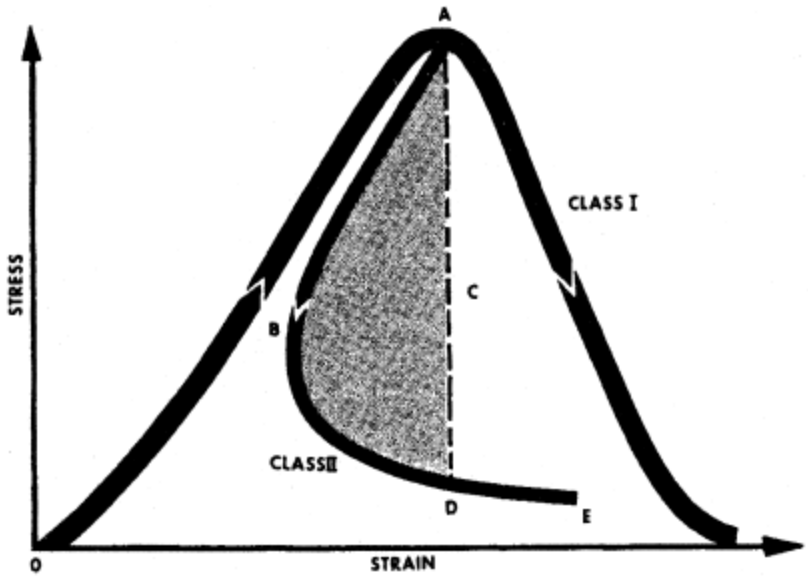

Figure 3.15. Characteristic stress-strain curves depicting class I and class II behaviour of rock failure during uniaxial compression (from Fairhurst and Hudson, 1999).

For class II behaviour, the corresponding curve does not monotonically increase in strain and the machine is unable to respond efficiently to the unloading in axial strain control. It is therefore recommended that lateral strain control be used. Accordingly, testing began in axial strain control at a continuous strain rate of 5 $x10^{-6}$ mm/s; swapping, manually, to lateral strain control at approximately 70% of the peak stress, when strain rate equals ~ 0.001 mm per 2.5 secs, to a rate of 5 $x10^{-4}$ mm/s.

Measurement of the applied load is obtained from the built-in load cell, and strain is recorded from the strain gauges throughout the procedure. Compressive stress is calculated as the applied compressive load divided by the initial cross-sectional area of each sample. Axial and lateral strain are calculated as follows:

Equation 3.4:

$$\epsilon_{axial} = \frac{\Delta \iota}{\iota_o}$$

Where

l_o = Original length
Δ_l = Change in length

Equation 3.5:

$$\boldsymbol{\epsilon_{circumferential}} = \frac{\Delta_c}{c_o}$$

Where

c_o = Original circumference
Δ_c = Change in diameter

The results of equations 3.4 and 3.5 are plotted against compressive stress to give complete stress-strain curves, which are used to characterise the response of each component of the lava, in orthogonal orientations, to the applied stress in unconfined and dry conditions.

3.4. Results

3.4.1. Porosity and Density

The porosity and density of 50 specimens were tested: 18 of these specimens were 36 mm diameter cylinders that were tested prior to UCS testing and the remaining 32 specimens were ~8 cm^3 pieces of off-cut material. The upper portion of the lava unit top demonstrates

the highest effective porosities, with an average of 27.04% and a maximum of 30.81%. Dry densities show the lowest values for this component at 2.1 g/cm^3. The lower portion of the lava unit top show slightly lower effective porosities, with an average of 20.15% and an average dry density of 2.32 g/cm^3. The core of the lava unit shows the lowest effective porosities, with an average of 12.91% and the highest average dry densities of 2.63 g/cm^3. The base of the lava unit has intermediate values for both effective porosity (average 16.31 %) and dry density (average 2.54 g/cm^3). Overall, there is a good linear correlation between effective porosity and density for each sample orientation (Figure 3.16). All measurements of density and effective porosity for each lava unit component are shown in Appendix I.

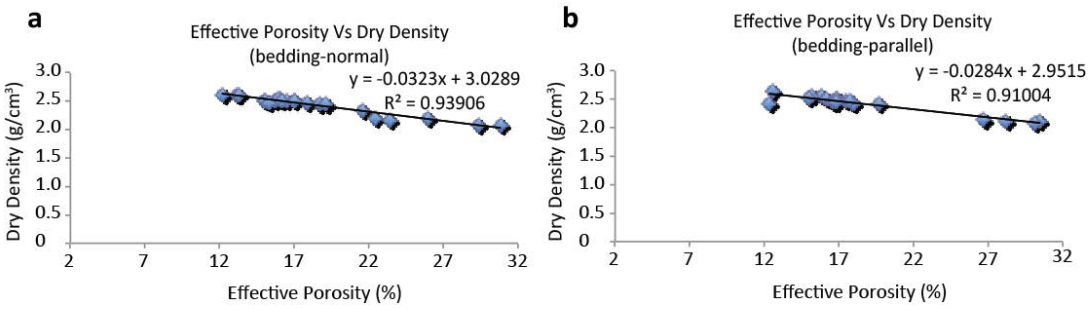

Figure 3.16. Variation of dry density with porosity for each sample orientation. a) bedding-normal. b) bedding-parallel.

There are systematic increases in porosity outwards from the core of the lava unit, increasing to a maximum in the unit tops (Figure 3.17). As expected, these correlate strongly with variations in dry density.

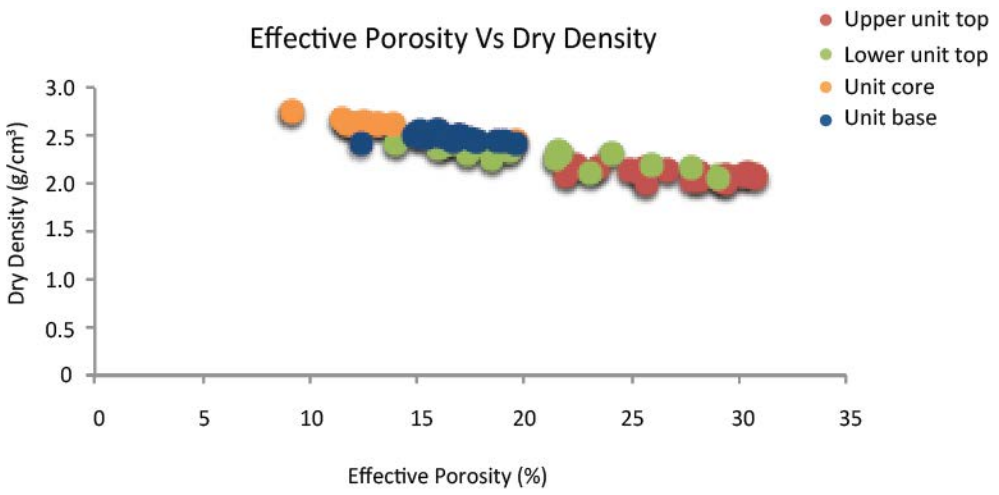

Figure 3.17. Variation of effective porosity with density for each component of the lava unit in both sample orientations.

Any internal variations of porosity and density within these components may be related to the amount of interconnected pore space or the presence of macropores in each sample.

3.4.2. Unconfined Rock Strength

Uniaxial compression tests were conducted on 18 cylindrical samples: 10 of these were oriented normal to the bedding contacts and 8 were oriented parallel to the bedding contacts. Failure of each sample was associated with the initial development of multiple vertical mode-I fractures that coalesce to form conjugate, or partial conjugate, extensional-shear fractures (Figure 3.18). There is a broadly inverse linear relationship between porosity and unconfined compressive (UC) strength in both bedding-parallel and bedding-normal sample orientations (Figure 3.19a and b) and an approximately linear increase in UC strength with dry density (Figure 3.19c and d).

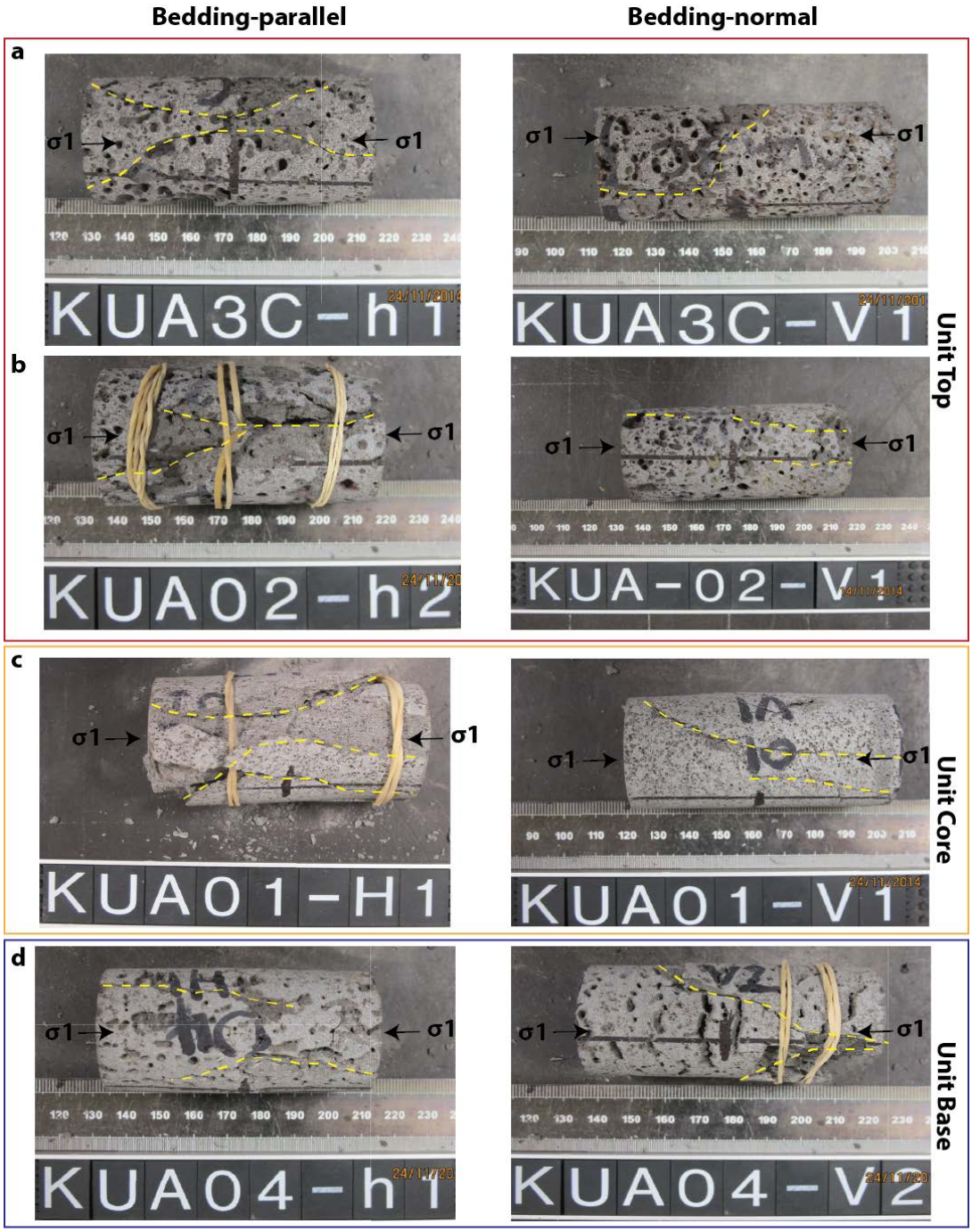

Figure 3.18. Examples of tested samples from each lava unit component in each sample orientation and the applied stress direction: a) Upper unit top. b) Lower unit top. c) Unit core. d) Unit base. In each case, samples exhibit numerous vertical extension (mode I) fractures, that linked to form subvertical through going, and partial, conjugate shear fracture sets, highlighted by the dotted yellow lines.

The highest UC strengths, and lowest porosities are found in the lava unit core in both sample orientations. In the bedding-parallel orientation the lava core is 30% stronger than the lower lava unit top, which shows a relative porosity increase of 5%, and the unit core is ~52% stronger than the upper portion of the lava unit top, which shows a relative 16% increase in porosity. From the lava unit core to the base there is a 46% decrease in UC strength with a 4% increase in porosity.

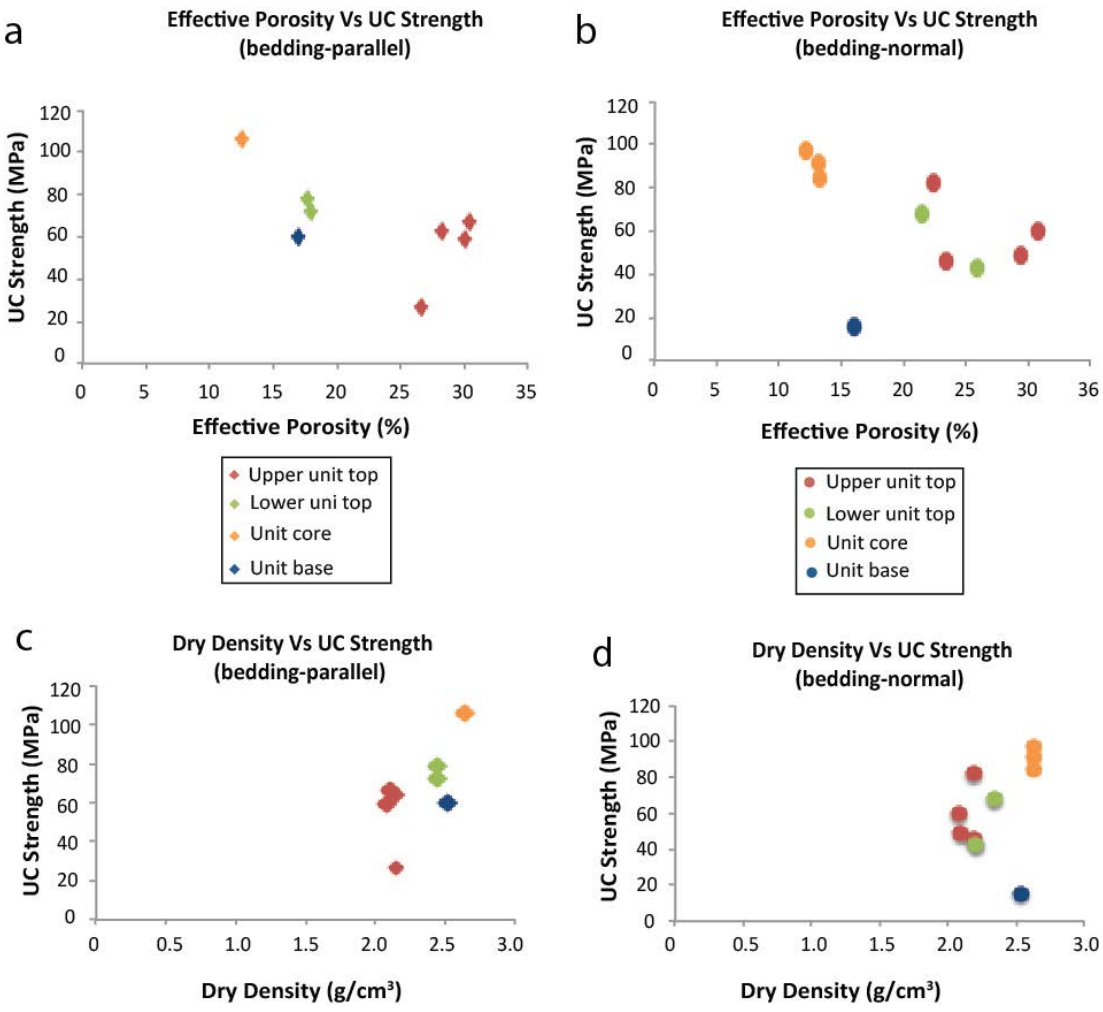

Figure 3.19. Variation in unconfined compressive strength with effective porosity for each lava component (red: upper top; green: lower top; orange: core; blue: base). a) Bedding-parallel orientations. b) Bedding-normal. c) Variations in unconfined compressive strength with density for bedding-parallel samples. d) Bedding-normal samples.

There is a UC strength reduction of 35%, with a porosity increase of 11% between the lava unit core and lower lava unit top in *bedding-normal orientations* and a reduction of 32% in the upper portion of the unit top, with a 13% increase in porosity. There is a 75% increase (30% more than the bedding-parallel orientation) in UC strength from the lava unit base to the core, but only a 3% decrease in porosity. These results highlight that even small increases in porosity will have a significant effect on the resulting UC strength of the rock.

Complete stress-strain curves for each unit component (Figures 3.20-23; summary plot: Figure 3.24) in both orientations, can all be divided into the 5 stress-strain stages and highlight pronounced variations in unconfined compressive strength (for full plots, of all samples tested, see Appendix I). Unit core samples are the strongest, irrespective of compression direction, with peak strengths of 106 MPa (bedding-parallel) and 91 MPa (bedding-normal). Samples from the unit top show some variability in UC strengths but values are consistently lower than the unit core at 45-80 MPa. Lava unit bases, however, show a more complicated relationship: the sample that was cored parallel to bedding demonstrates a UC strength of 60 MPa, similar to those of the unit top. The sample that was cored normal to bedding, however, shows a UC strength of 16 MPa, substantially lower than the rest of the basaltic lava. These strength patterns are summarised in Figure 3.24.

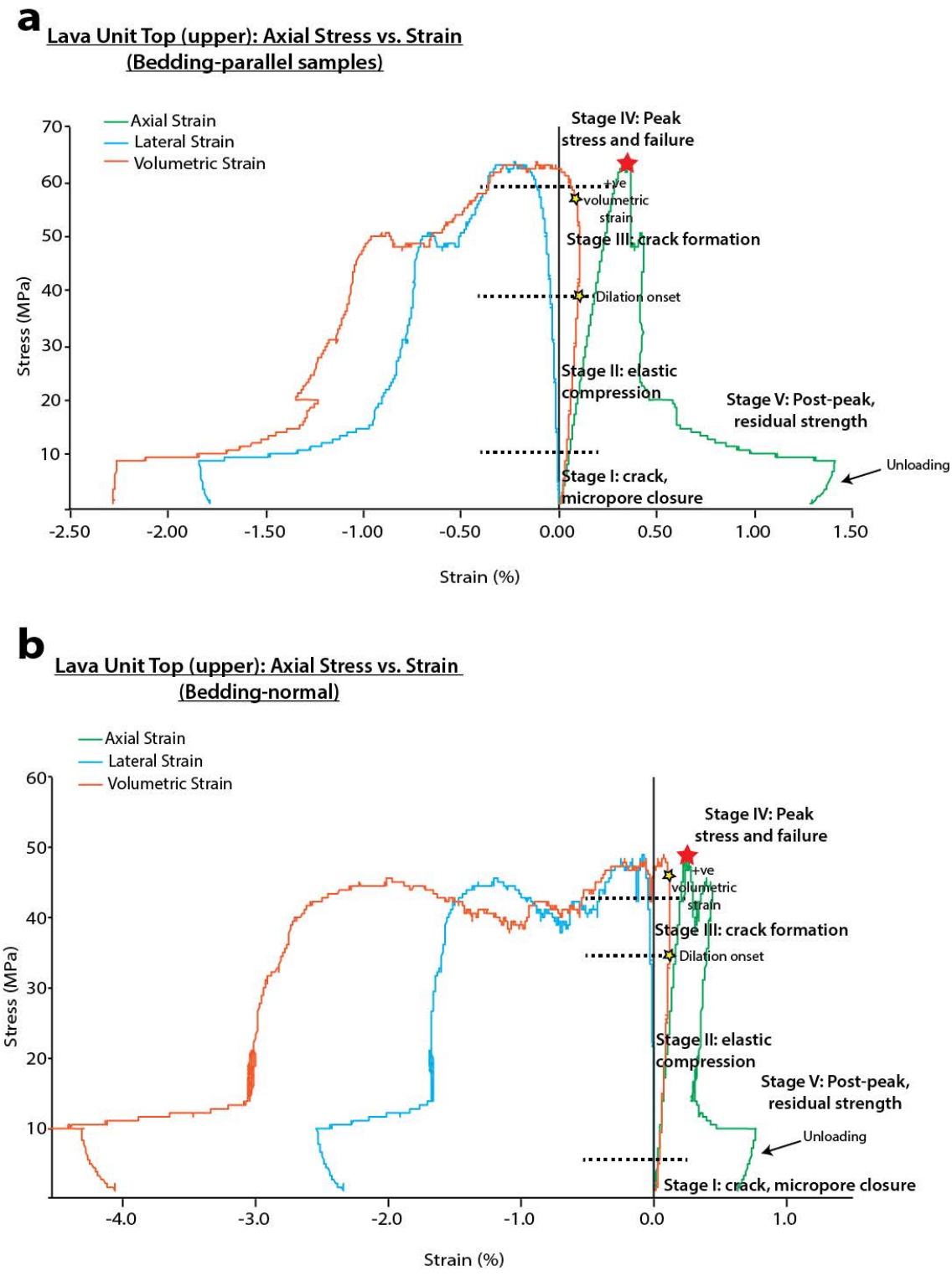

Figure 3.20. Example of axial stress Vs strain curves for (upper) top lava samples. a) Bedding-parallel. b) Bedding-normal orientations. Both graphs show axial strain, lateral strain and volumetric strain curves (for all stress-strain curves, please see Appendix I).

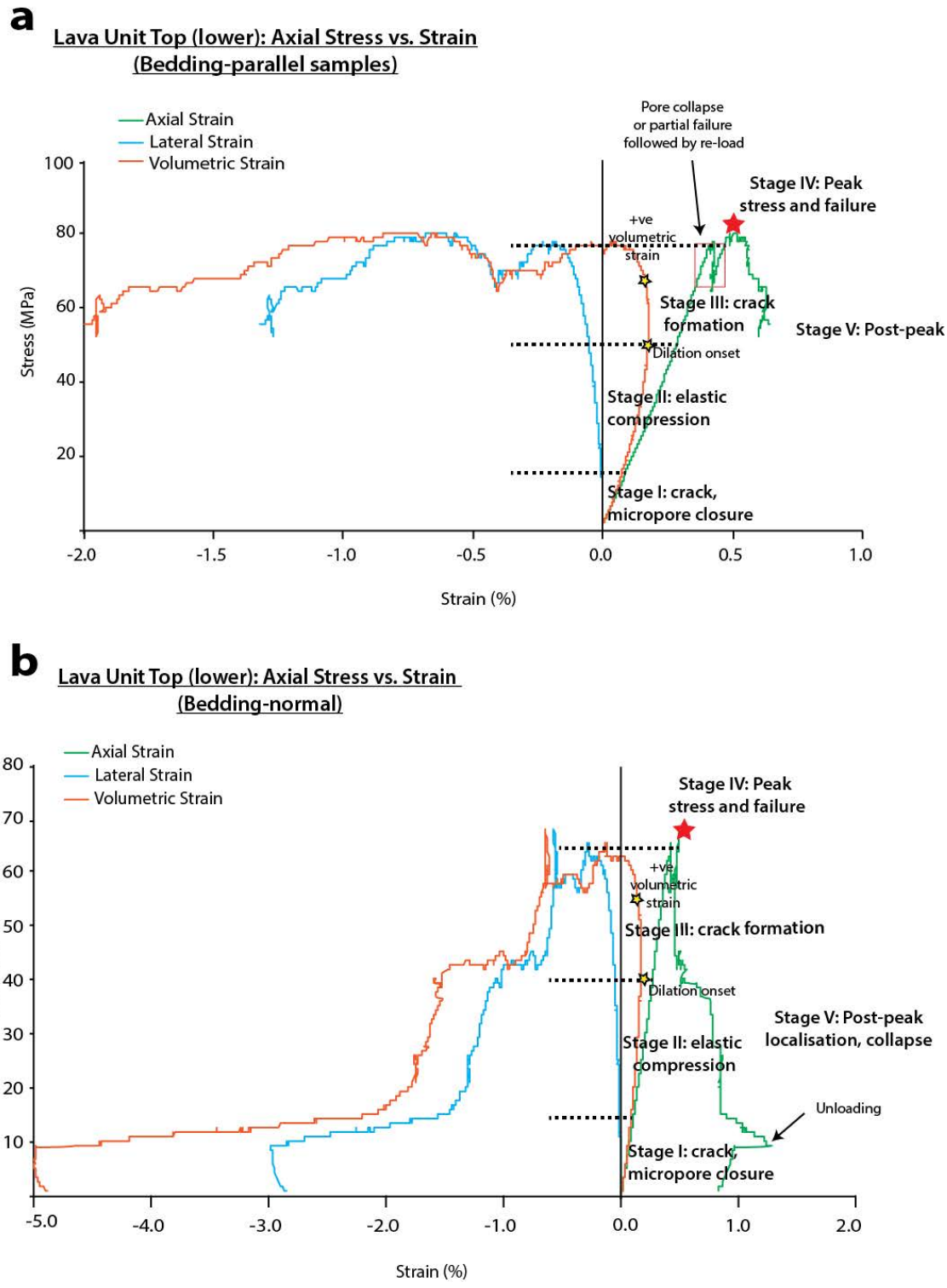

Figure 3.21. Example of axial stress Vs strain curves for (lower) top lava samples. a) Bedding-parallel. b) Bedding-normal orientations. All graphs show axial strain, lateral strain and volumetric strain curves (for all stress-strain curves, please see Appendix I).

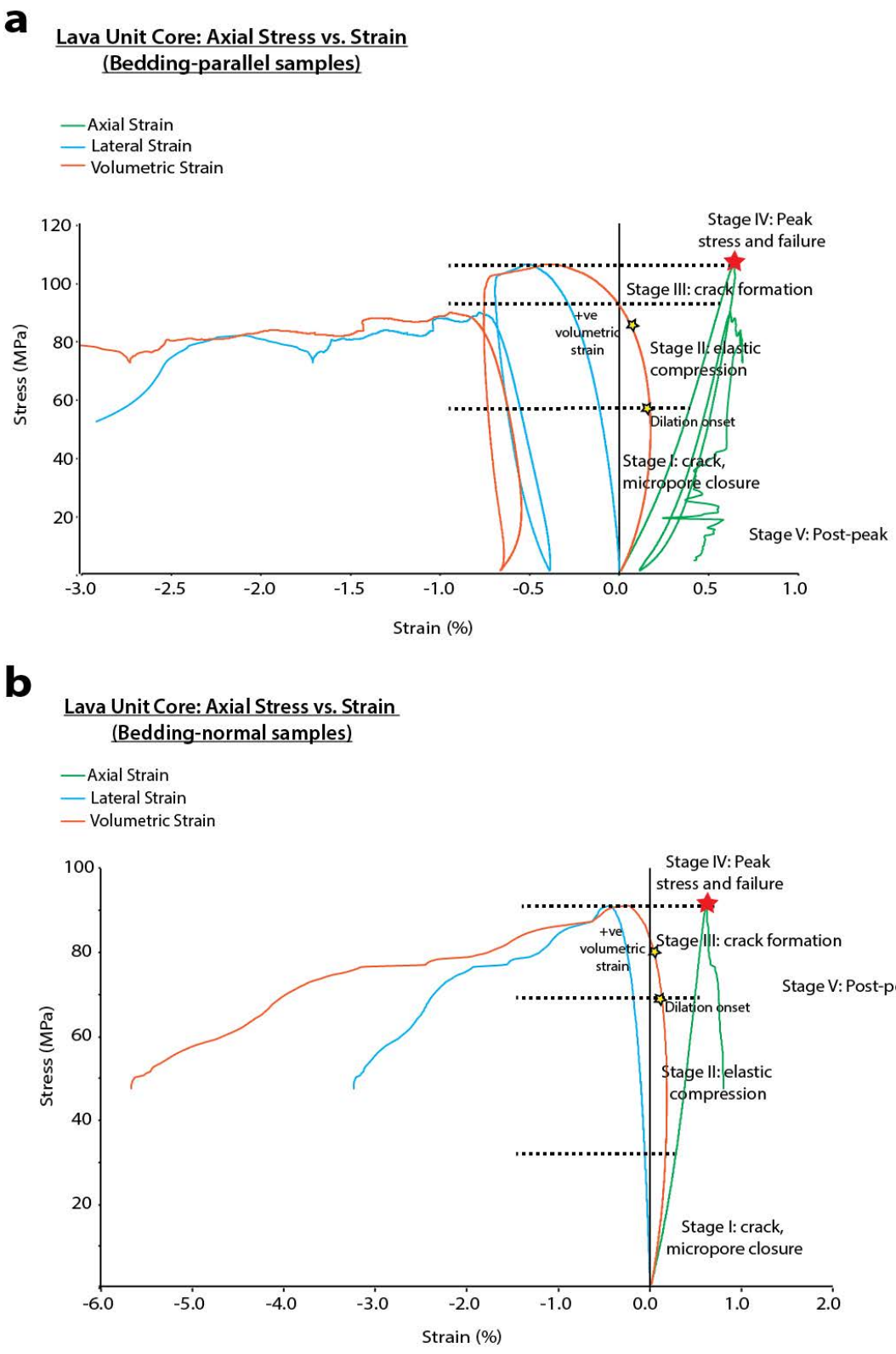

Figure 3.22. Example of axial stress Vs strain curves for lava core samples. a) Bedding-parallel. b) Bedding-normal orientations. All graphs show axial strain, lateral strain and volumetric strain curves (for all stress-strain curves, please see Appendix I).

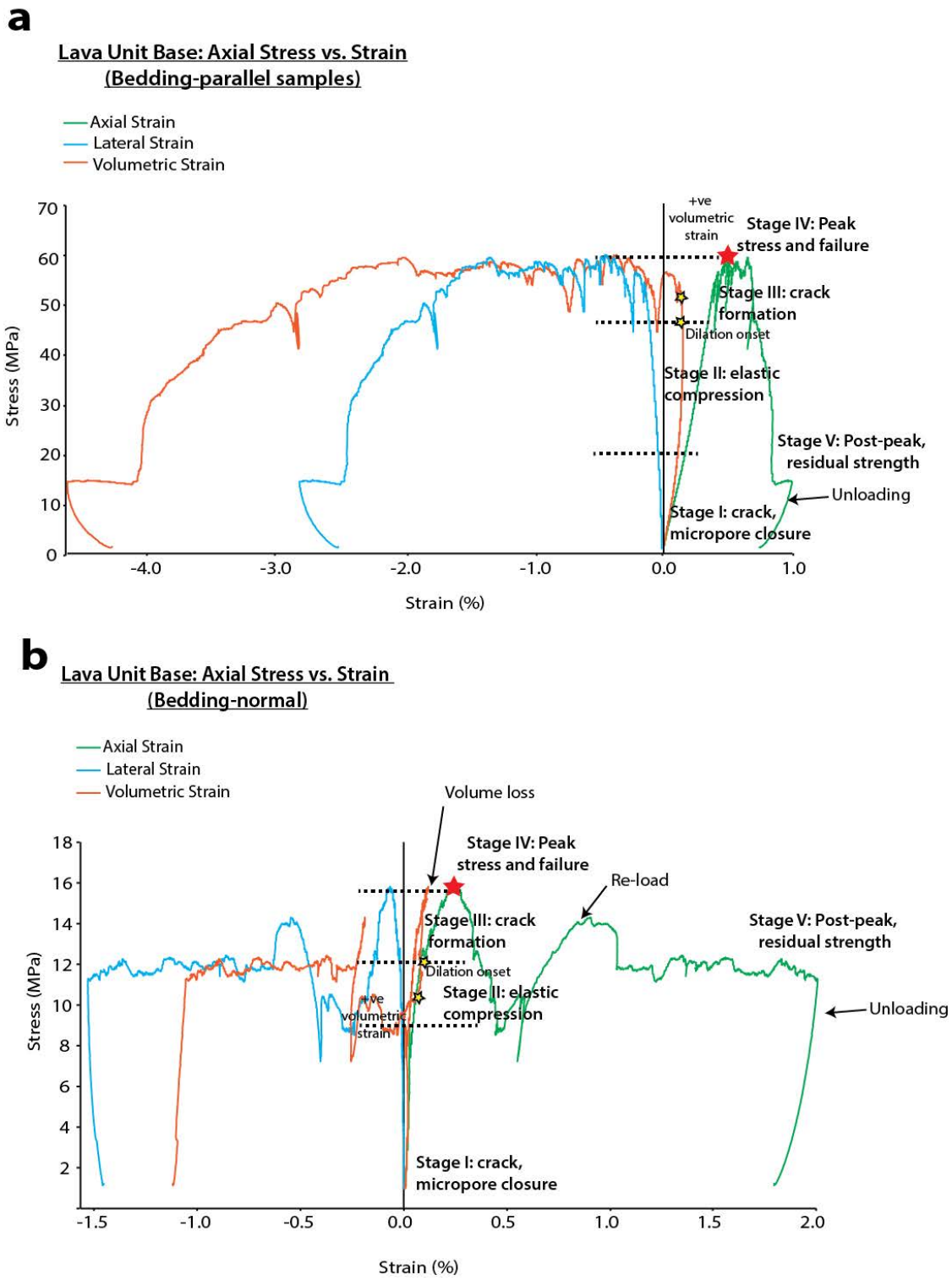

Figure 3.23. Example of axial stress Vs strain curves for lava base samples. a) Bedding-parallel b) Bedding-normal orientations. All graphs show axial strain, lateral strain and volumetric strain curves (for all stress-strain curves, please see Appendix I).

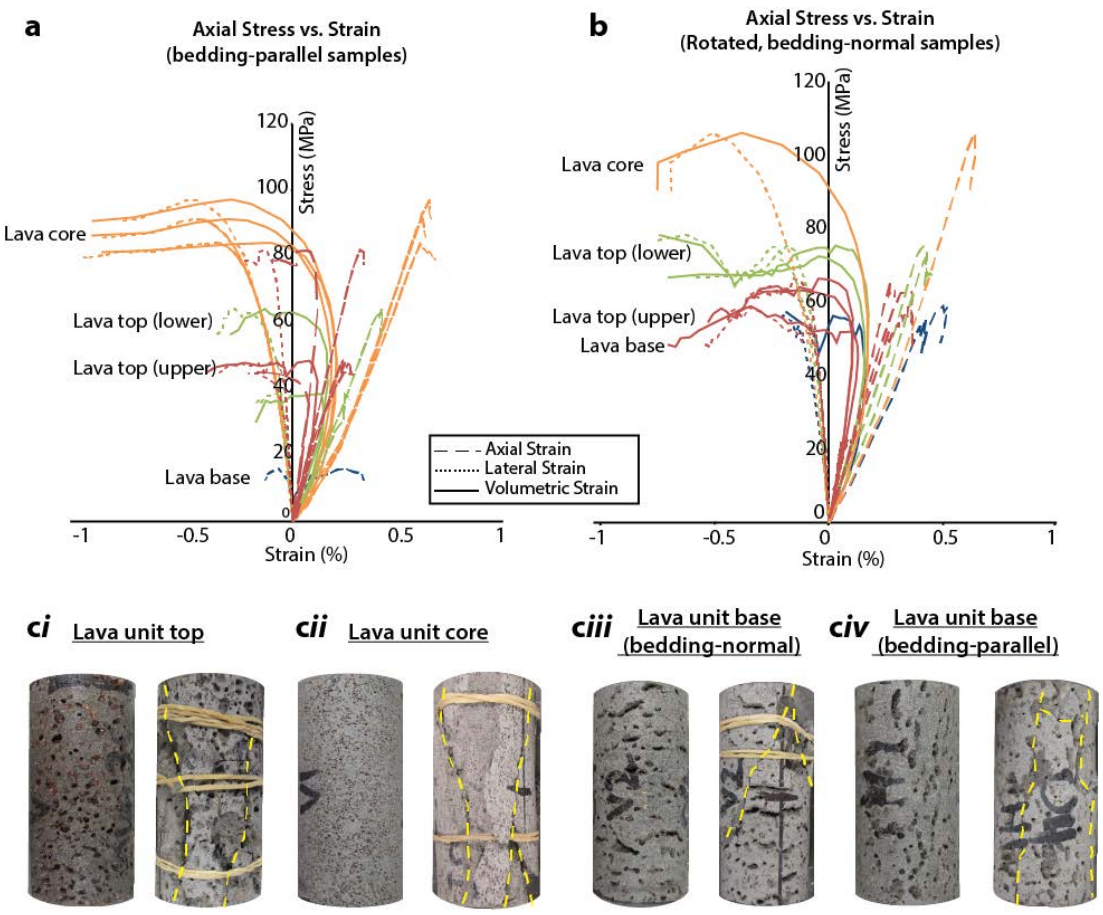

Figure 3.24. A comparison of full stress-strain curves for all samples. a) Bedding-parallel. b) Bedding-normal. Dashed lines represent axial strain, dotted lines show lateral strain and solid lines demonstrate variations in volumetric strain with stress. Orange lines are unit core results; green are unit top (lower); red are unit top (upper); and blue are data from unit bases. (*ci-iv*) Examples of pre- and post-failure samples. Major fractures are highlighted by yellow dashed lines. Cylinders have diameters of 36 mm.

3.4.3. Young's Modulus

In addition to having a profound influence on the UC strength of materials, there is a positive correlation between porosity (and density) and the calculated Young's modulus for the samples.

Data from the top of the upper portion of the lava top shows a large amount of variability in elastic modulus, and results are broadly anomalous compared to the rest of the unit. Samples from this component range from 15-23 GPa with an average of 21.3 GPa. Results from the both sample orientations from the lower portion of the lava top show less variability, with values of 15-18 GPa and an average of 17.2 GPa. Results from the core zone are also relatively uniform, in both orientations, with values ranging from 18-20 GPa with an average of 19.4 GPa. Samples from the unit base show markedly different values in each of the sample orientations. The sample in the bedding-parallel orientation shows a Young's modulus of 16.1 GPa (and UCS of 60 MPa) whereas the bedding-normal orientation demonstrates a Young's modulus of 5.4 GPa (and UCS of 16 MPa). There is a positive correlation between UC strength and Young's modulus for all samples, except those from the upper lava unit top (Figure 3.25a and b).

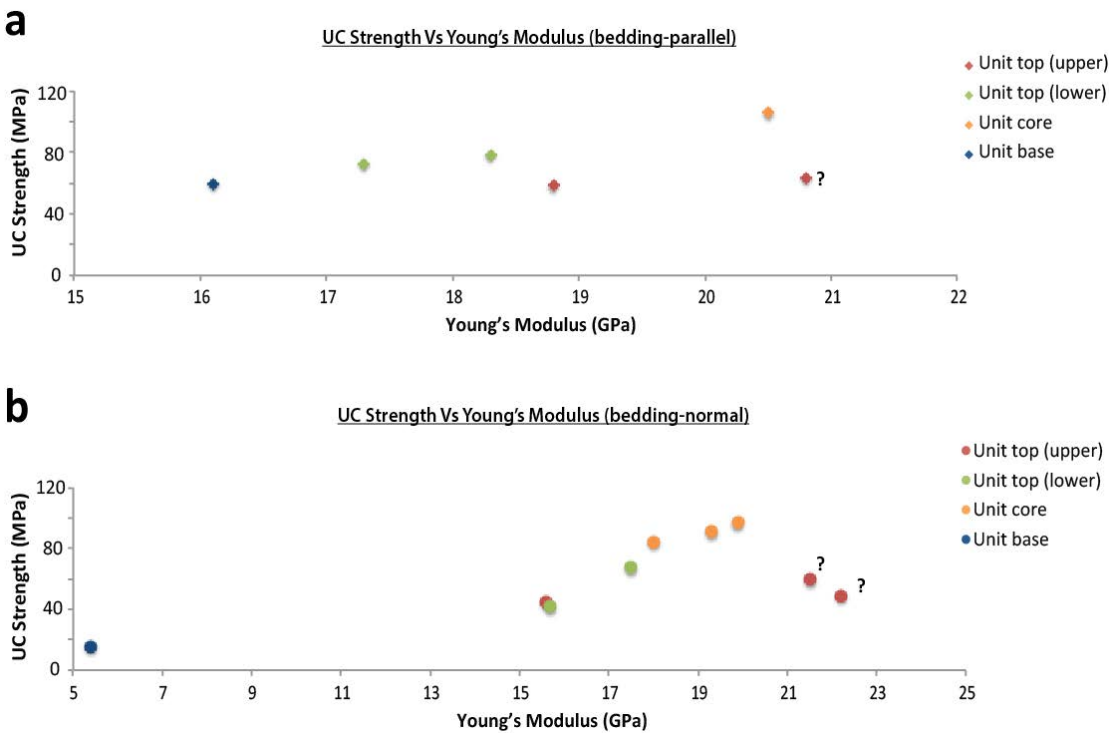

Figure 3.25. Comparison of Young's modulus with varying UC strength for each of the basaltic lava components in (a) bedding-parallel and (b) bedding-normal orientations.

3.5. Discussion

For a vertical transect through a solidified basaltic lava, the upper portions of the lava unit top shows the greatest effective porosities (~30%), but intermediate UC strengths of ~60MPa and highly variable values of Young's modulus (15-23 GPa: Figure 3.26a and b). This variability is not unexpected and may be a function of heterogeneous and anisotropic pore space: samples from this part of the lava show a range of vesicles diameters (mm-cm in scale) and a non-uniform distribution.

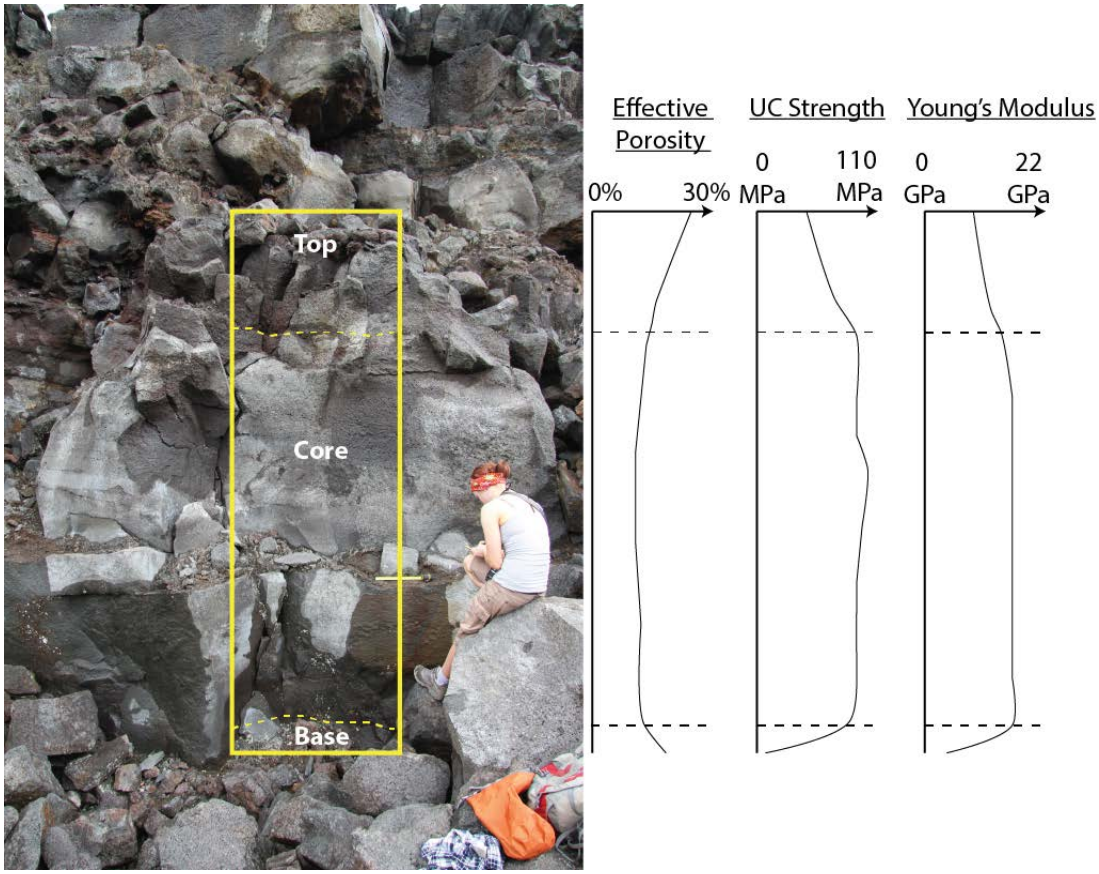

Figure 3.26. Vertical mechanical stratigraphy through a basaltic lava. The lava core zone is the stiffest and strongest, followed by the lava top. Lava bases are the softest and least strong component.

Experimental characterisation of the elastic modulus for such highly anisotropic materials is known to be challenging (Jaeger et al., 2007). A more homogenous porosity may result in

more uniform measurements of UC strength and Young's modulus. A reduction in the porosity of unit core samples (12-13%) increases both the stiffness of the material (Figure 3.27a and b) to ~20 GPa, and the UC strength (90-110 MPa), in both sample orientations. The base component (in both sample orientations) is characterised by an intermediate effective porosity (~16%), much of which is associated with flattened, oblate vesicles. Samples from the unit base however, show markedly different values for UC strength and Young's modulus for each sample orientations, despite similar porosities (16%: see figure 3.27a and b). The sample in the bedding-parallel orientation shows a Young's modulus of 16.1 GPa and a UCS of 60 MPa, whereas the bedding-normal orientation demonstrates a Young's modulus of 5.4 GPa and UCS of 16 MPa, thereby defining "stiff and strong" orientation and a "soft and weak" orientation. Rotating the sample by 90° into the bedding-parallel orientation increases the Young's modulus by 10%; this increase appears to be associated with a change in pore geometry alone.

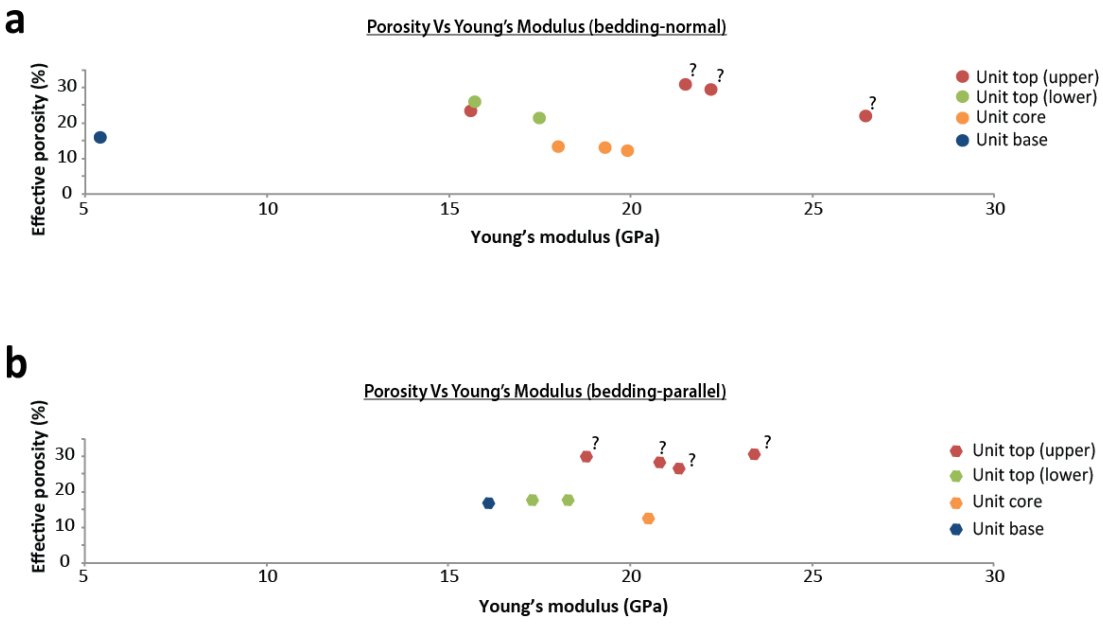

Figure 3.27. Comparison of porosity and Young's modulus for each of the lava components in (a) bedding-normal, and (b) bedding-parallel orientations.

Studies of porous ceramics and metals show that materials with the highest porosities have the lowest UC strength (e.g. Fleck and Smith, 1981; Rice, 1998; Nakamura et al., 2000). Notably this is not the case for the Hawaiian basalt samples, with the lava base showing intermediate porosities, but either substantially lower UC strengths (16.8 MPa) or similar UC strengths to the higher porosity components (59.67 MPa).

Vesicle geometry and distribution appears to be the more significant factor in controlling the brittle response of the rock than total porosity: the porosity difference between the core and base is ~3%, but compressive strength decreases by 75%. The difference in effective porosity between the core and the lava top is about 11%, yet the decrease in strength (32%) is only minor (Figure 3.26).

It is common for crystalline rocks to contain flaws that have the potential to behave as mechanical inclusions that exert a strong influence on the response of these rocks to an applied load. For porous solids, this has been shown even when total porosities are low (Jaeger et al., 2007). Data presented in this chapter supports this hypothesis, but suggests that total porosity, a scalar quantity, on it's own does not account for variations in rock strength. Pore *geometry* and *orientation* with respect to an applied stress may also be important.

3.5.1. Mechanical Properties of Porous Solids

Experimental analyses of porous materials have recognised a link between porosity and density with brittle strength and fracture toughness (e.g. Li et al., 2004; Nakajima, 2007). The mechanical properties of ceramics are also strongly influenced by physical attributes of the material, including grain/pore size, shape, and orientation. It has been shown numerically and experimentally that there is an inverse relationship between porosity and strength, and grain or pore size and strength for a range of man-made and natural materials, including: (1) ceramic materials (Rice, 1998; Boccaccini, 1999; Nakamura et al.,

2000; Leguillon and Piat, 2008); (2) sintered steel (Fleck and Smith, 1981); (3) lotus copper (Nakajima, 2007); (4) sandstone (Dunn et al., 1973; Palchik, 1999; Tuğrul, 2004; Chang et al., 2006; Sabatakakis et al., 2008; Heidari et al., 2013); (5) limestone (Palchik and Hatzor, 2002, 2004; Tuğrul, 2004; Sabatakakis et al., 2008); (6) dolomite (Hatzor and Palchik, 1998) and (7) marls (Sabatakakis et al., 2008). In all of these examples, reduction in porosity, and a corresponding increase in density, is associated with an increase in brittle strength, or fracture toughness (Figure 3.28a). In addition to brittle strength, a porosity (and density) dependence of Young's modulus also exists for these materials. Studies of lotus copper has further identified directional anisotropies; pores oriented with their long axes normal to the applied compressive stress were more easily deformed (open circles, Figure 3.28b: Nakajima, 2007).

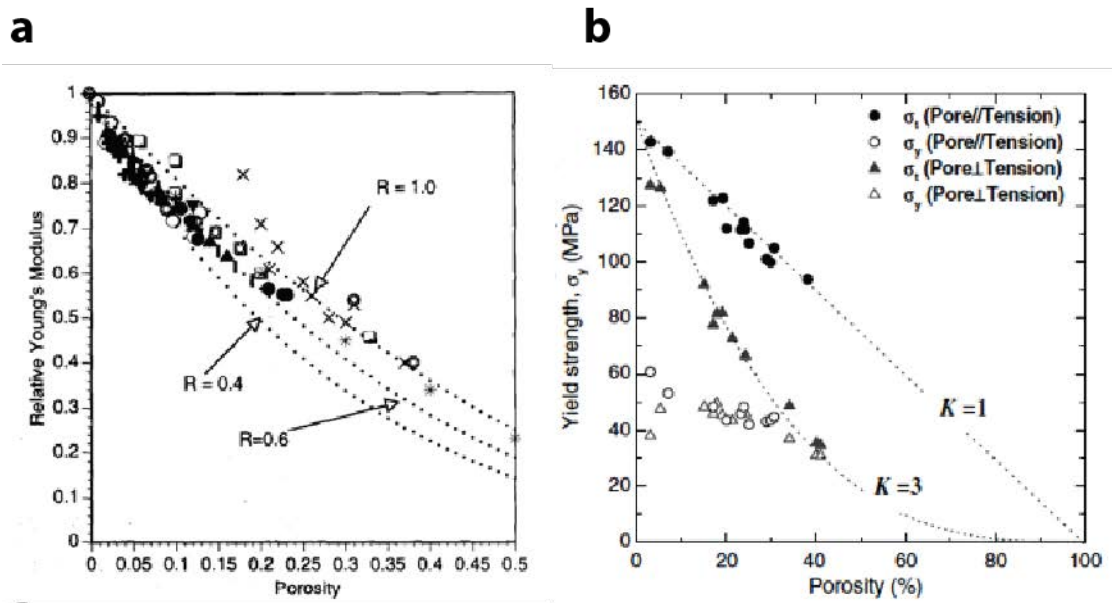

Figure 3.28. a) Comparison of experimental Young's modulus results for porous ceramics with different porosities (From Boccaccini and Fan, 1997). b) Measurements of yield strength for lotus copper with varying porosities, in two applied stress orientations (From Nakajima, 2007).

3.5.1.1. Mechanical Properties of Basalt

A small number of investigations have been conducted on basaltic lava samples with varying porosities and densities. Primary porosities in basalts are associated with non-connected vesicles, and micro-cracks related to cooling (Petford, 2003; Gates, 2008). The scale and amount of either type of porosity has been shown to vary through individual lava units, despite negligible compositional variation. Existing studies of the mechanical properties of basalts, however, have not investigated the existence of a mechanical stratigraphy, despite the presence of physical property variation (e.g. Cashman and Kauahikaua, 1997; Planke et al., 1999). Compressive strength demonstrates a strong correlation with dry density (Figure 3.19). This sits well with the findings of Tuğrul and Gurpinar (1997) who found that strength values decreased from 136 MPa to 3.69 MPa at densities of 2.6-2.0 g/cm^3. It has also been shown experimentally that the compressive strength of basalt increases when vesicularity, and therefore porosity, is lower (Al-Harthi et al., 1999; Gates, 2008). Experimental data in these studies show that larger increases in compressive strength take place for porosities <10% and above this, the effect is less. Data presented here show that changes in compressive strength are significant at effective porosities of 15%. Al-Harthi et al., (1999) compared the ratio of Young's modulus to Poisson's ratio against UC strength for a range of different porosities (Figure 3.29a).

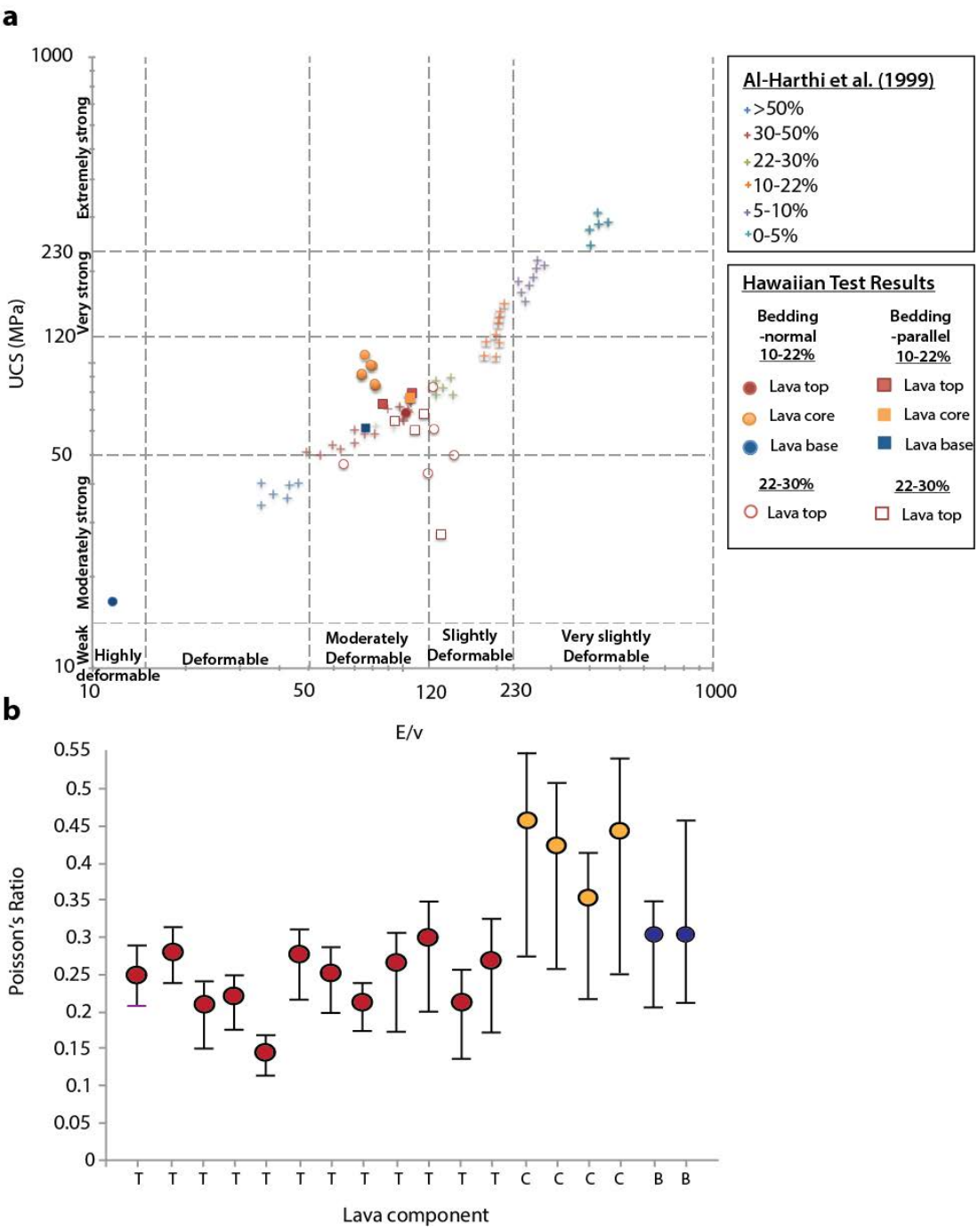

Figure 3.29. a) Plot of the engineering classification of vesicular basalts: cross symbols represent different porosities and demonstrate the relationship between UC strength and deformability from Al-Harthi et al., 1999 (based on Turk and Dearman, 1983). Deformability of lava components from this thesis in bedding-parallel (circles) and bedding-normal (squares) orientations is plotted for comparison. Using the deformability range of Al-Harthi et al., 1999 and Turk and Dearman, 1983, it is shown that the base unit of lavas (in bedding-normal orientations: filled blue circle) are highly

deformable relative to the rest of the lava. The other samples lie in the moderately deformable-strong field. b) Poisson's ratio for each sample with upper and lower error bars to represent the tangent and secant Poisson's ratio respectively. Values vary by up to 0.2-0.25 GPa depending on the portion of the stress-strain curve that is used to calculate it. Averages are used in this study.

For high porosities, they recorded low compressive strength and low deformability ratios (Young's modulus to Poisson's ratio). Results are similar for the unit top (red open circles and squares) implying that samples from this component fall into the moderately-slightly deformable and strong range of Turk and Dearman (1983) and Al-Haarthi et al. (1999). Samples from the unit base (filled blue circle and square in Figure 3.29a) lie in two separate fields of the deformability graph. The bedding-normal sample (with the lowest UCS of 16 MPa) lies in the highly deformable portion, and the bedding-parallel sample, with the same effective porosity, lies in the moderately deformable field. At lower porosities, and higher UC strengths higher E/v ratios are expected, however large error bars associated with the Poisson's Ratio for these samples (Figure 3.29b) place them in the moderately deformable field with unit top samples. Unit cores exhibit the greatest UC strengths, lowest porosities, and highest Young's modulus, implying they should be much less deformable than the rest of the unit (Figure 3.29a).

Results presented in this thesis show some similarities with previous numerical and experimental results but the directional strength anisotropy of lava unit base samples is significantly anomalous. The relationship between total porosity, and pore geometry on porous rock strength will have important implications for the long-term strength of materials but it remains poorly documented in geological literature. For basaltic lavas, porosity has a profound effect on the development of fractures but further study would identify whether pore geometry plays a greater role.

3.5.2. Effect of Porosity on Fracture Growth

Based on models of brittle failure in porous solids (e.g. ceramics, sintered steel) under compression, circular holes or pores in rocks are expected to show concentrations of tensile stresses at the north and south poles, which induces microcracking and redistributes stresses into the surrounding intact rock (Sammis and Ashby, 1986; Ingraffea, 1989). Vesicles in basalts are expected to behave in the same manner by concentrating tensile stresses at the north and south poles and lowering the differential stress required to cause catastrophic failure (Heap et al., 2014, 2016 ; Vasseur et al., 2015). Macrofractures should propagate out from and link individual vesicles, parallel to the applied compressive stress direction. Tested samples, however, exhibit a range of fracture propagation pathways: crack-pore (Figure 3.30a), crack-crack (Figure 3.30b) and a combination of these modes (Figure 3.30c). No instances of cracks propagating out from the north and south poles of vesicles are observed. Where cracks are associated with a vesicle, they typically propagate from the edges as an apparent tangent, usually towards another neighbouring pore (Figure 3.30a). Elsewhere, they by-pass pores entirely and propagate through the intact rock between pores or they diverge in the vicinity of a pore (Figure 3.30b). The inconsistency in propagation pathways implies that the process is more complicated than presented previously (e.g. Heap et al., 2014, 2016) and that the nature of mechanical inclusions - vesicles in this instance - and locally amplified stresses may be more influential in crack propagation than the mechanical properties of the intact rock.

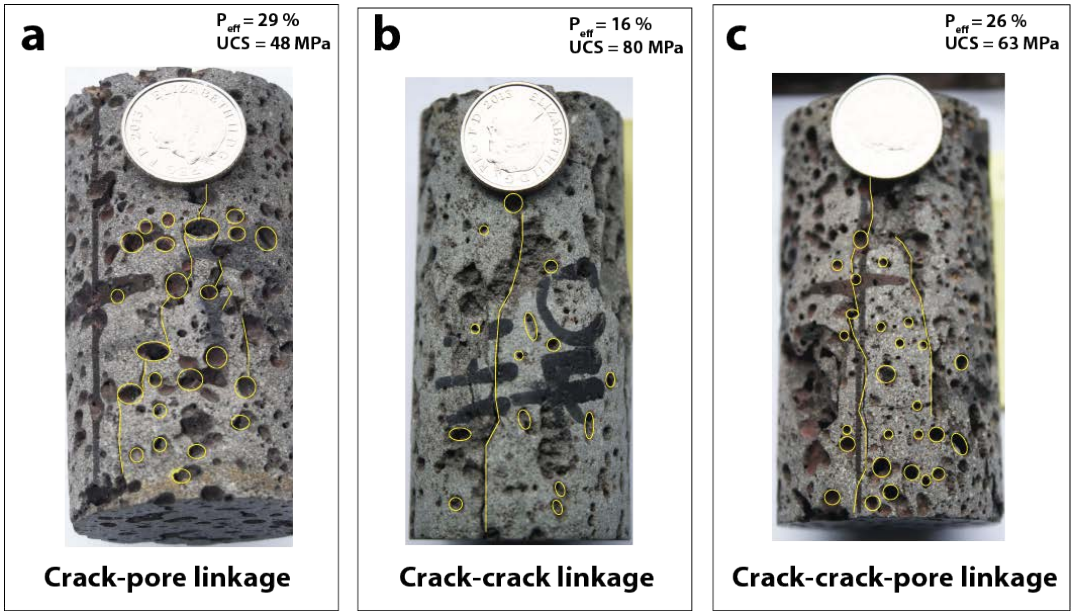

Figure 3.30. Examples of crack propagation pathways in tested samples. a) Vesicles are linked by a series of subvertical fractures that connect with pores at their "east" and "west" margins. b) Vesicles are unconnected, and unbreached. A through-going fracture has developed through the linkage and coalescence of microcracks. c) A proportion of vesicles show fracture linkages (again, at the east and west margins) and elsewhere fractures have propagated through the intact material between vesicles.

St. Venants principle (e.g. Gudmundsson, 2011) states that stress perturbations are local effects and at distances that are great relative to the size of the discontinuity, the stress field is unaffected. For faults, the separation distance at which stress field interaction occurs is thought to be less than twice the depth of faults (e.g. for faults that penetrate 10-15 km, interaction will be significant if they are separated by less than 20-30 km: Segall and Pollard, 1980). Within this zone of interaction, stresses are thought to be 40-50% higher than the remote value (Crider and Pollard, 1998). At the porosities measured for the samples in this study (12-31%), the pore-pore distance between isotropic vesicles is less than twice their diameter, therefore pore-interaction and compressibility is likely to exert a stronger influence on the nucleation and propagation of fractures within the samples than direct intersection and coalescence (Jaeger et al., 2007). The fracture paths observed in

samples in this study may therefore reflect the competition between applied and local stresses (i.e. stress field interaction-induced effects).

Finite element models have shown that stresses will concentrate in the neck areas between pores, resulting in stress magnitudes that are considerably higher despite the same applied stress (Li et al., 2004). Microcracking may be localised initially by the presence of a vesicle, but they will nucleate in the high stress intensity zones between them, and propagate outwards from there. Depending on the induced stress field trajectories in these zones, some fractures will propagate along modified trajectories towards, and link with, cohesionless vesicles, while others will diverge away from them. This implies that at moderate to high porosities (and small pore-pore distances) the stress concentrations associated with vesicles are less critical in the nucleation of microcracks than the stress field interaction and resulting stress amplification in the neck regions between neighbouring vesicles. This fits well with observations of pore-stress concentrations in porous ceramic materials (under tensile loading) where it is suggested that stress concentration from pores has a limited effect on the mechanical behaviour of the material. Pores that are considered isolated still exhibit stress gradients around them but with increasing porosities, and decreasing pore-pore distances, the load-bearing ability of the material is reduced and a smaller stress is transmitted through the material. Interactions between pores may become significant at porosities as low as 5-10% and significantly reduce the effect of pore-induced stress concentrations (Rice, 1997). For lava top and base samples (20-30% porosity) load-bearing surface area in the rock is small and vesicles behave like mechanical inclusions affecting the distribution and magnitude of stresses within the samples. Local stress perturbations, coupled with the failure of fewer elements will result in failure at lower applied stresses.

In addition to low UC strengths, Young's modulus is also lower. An increase in pores per unit volume will result in stress field interactions and amplified stress intensity factors

surrounding the pores, which promotes cracking. These crack displacements will cause substantial reductions in Young's modulus. For the lower porosity flow core (12-13%) where load-bearing surface area is greater and vesicles are smaller with greater pore-pore distances, Young's modulus is greater. Here, the influence of pore interaction stresses is less, and local increases in fracture toughness associated with pore blunting may be more important (e.g., Leguillon and Piat, 2008). When a crack encounters a pore, the tip becomes blunt as the energy dissipates, reducing the stress intensity and producing an effective increase in fracture toughness locally. To propagate the crack further, an increase in applied load is necessary to overcome this induced toughness (Deng et al., 2004). At low porosities, therefore, vesicles will only lead to localised microcracking where applied stresses are sufficiently high to overcome the elastic limit and strength of the intact rock. For intermediate porosities or irregularly distributed vesicles, non-uniform stress concentrations (pores vs cracks) will occur and stresses at the tip of a crack will be high as a function of the applied force across a small surface area, and stress concentrations around vesicles will be small in comparison. In such instances, crack-related stresses dominate any pore-induced stresses.

3.5.3. Effect of Pore Geometry

Though the progressive development of fractures is still uncertain, the amount of open pore space in the rock demonstrably impacts elastic properties, and the ultimate strength of the material. Previously, the brittle strength of basaltic lavas has been attributed to mineralogical variations and pre-existing microcracks, but more recent studies of heterogeneous volcanic edifice materials have also recognises a link between emplacement-induced vesicularity and mechanical strength (Schaefer et al., 2015; Vasseur et al., 2015). Porosity, however, does not account for the significant strength contrast in lava base samples observed here, and such directional anisotropy has not been recognised in existing

studies of porous rocks. In these samples, porosities are all ~16% yet show significant variations in compressive strength: ~60 MPa for the flow-parallel orientation and ~16 MPa for the flow-normal orientation. The principal difference between samples in this orientation is the geometry of vesicles and their orientation relative to the applied compression (Figure 3.31). Consequently, in addition to the amount and distribution of pore space, or load-bearing surface area, the shape of vesicles relative to the orientation of applied stress has a significant influence on the brittle strength of basalts.

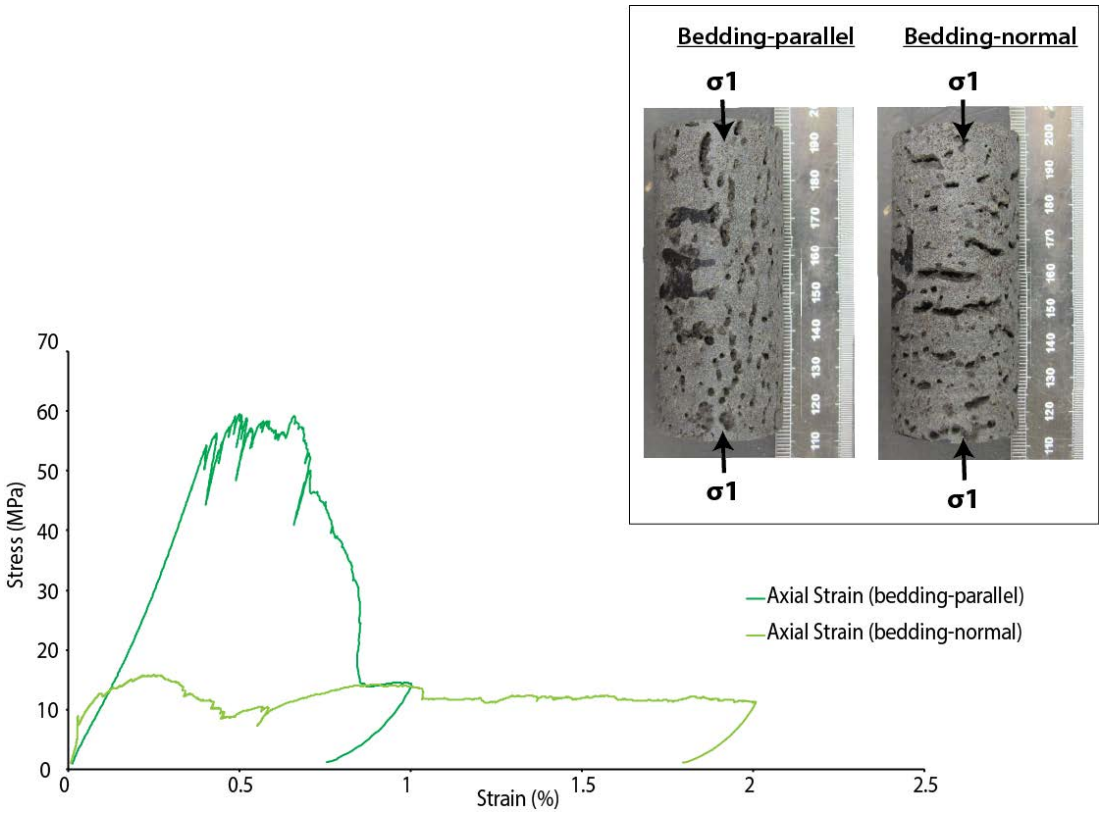

Figure 3.31. Summary of tested samples from the lava unit base. Combined stress Vs. axial strain curves for both bedding-parallel and bedding-normal orientations from the unit base. The key morphological difference between these samples is the orientation of ellipsoidal pores (see inset). The axial stress-strain curve for the bedding-normal sample (light green**)** shows relatively ductile behaviour. The sample in a bedding-parallel orientation is 73% stronger in compression than the sample oriented normal to the bedding contacts.

Density measurements for the base component of the lava are consistent for both orientations at 2.45-2.5 g/cm^3. A chemical homogeneity is supported by thin section analysis, which reveals that the samples do not vary mineralogically and the proportion of glass is also uniform. Mechanical variations are therefore attributed to heterogeneous and anisotropic porosity that is intrinsic to the lava. Effective porosities at the base of the unit show intermediate values of ~20% but this porosity is dominantly associated with flattened amalgamations of individual pores, producing ellipsoidal pores, up to, 5-10 mm in diameter. Flattened pores in the base of the lava, when oriented orthogonally to the applied stress, produce a lower Young's Modulus (~5 GPa vs. ~16 GPa) and brittle strengths are correspondingly lower (15.83 MPa: Figure 3.30). Lava base samples have similar values of effective porosity (16-17%) in both of the cored orientations, but samples with vesicles aligned with the long axis parallel to the applied stress are significantly stronger than vesicles aligned with the long axis normal to the applied stress direction.

The mechanical response of a curved surface to an applied stress, and the relationship with geometry, has long been of interest in engineering and material sciences. This response is thought to be governed by their geometry and driven by a need to deform in the most energetically efficient manner, resulting in a mechanical response that differs to those of other solid materials (Vaziri, 2009). Numerical-based studies have shown that curved surfaces gain significant strength when they are compressed along their major axis due to *geometry-induced strength* (Lazarus et al., 2012; Vella et al., 2012). Studies have recently focussed on the biomechanics of eggshells to explain this. When a load is applied to the tip of a shell, the radius of curvature is small and considered axi-symmetric; stresses are distributed across the surface in such a way that no single part of the shell accommodates the entire applied load. Conversely, the side of the shell has a large radius of curvature, and this curvature varies in three-dimensions. Consequently, the load is distributed over a broader surface area. Through the use of finite element

simulations and indentation tests it was shown that an egg is significantly stronger in compression than in tension.

Lazarus et al. (2012) conclude that the strength of eggshells is controlled by: 1) the local load curvature, 2) the material properties and, 3) the tip-wall differential stress. They further concluded that the response is scale invariant, and influenced by the shell's aspect ratio alone. A similar conclusion was made by Perdigou (2010), who found that a shell twice as high as a sphere was twice as stiff: the defining parameter is the aspect ratio for the radial stress. These analyses of ellipsoidal shell structures are also applied to account for the apparent strength of other natural and man-made curved surfaces, including domes and bridges. The induced strength is a function of the local radius of surface curvature alone. By applying the same analyses and concept of geometry induced stiffness to flattened, ellipsoidal vesicles in the base of a lava unit, I propose that the directional strength anisotropy observed is the result of an induced effective strength that is governed by the geometry, or load radius of the vesicles. The ends of the vesicles are equivalent to a highly vaulted dome with a small radius of curvature, and the edges equivalent to a flat dome with a large radius of curvature. This correlates well with the results of Jaeger et al., (2007) who describe spherical holes as the stiffest geometry, where their compressibility increases with decreasing aspect ratio, and Nakajima (2007), who found that cylindrical pores were more prone to buckling when compressed along their minor axis; they attribute this to concentration of stresses around the pore.

The strength profile identified here is significant, indicating that studies using only very low porosity lava components will not be representative of the whole unit. Low porosity values represent an endmember parameter, not an average, and are therefore unrepresentative of the entire rock type. This is especially relevant for models of volcanic flank stability, where parameters are typically derived from tests on isotropic basalts (porosities of 1-4%)

under isotropic loads (Vinciguerra et al., 2005; Becker et al., 2007; Heap et al., 2010). In addition to the amount of pore space and the orientation, continuity and frictional strength of pre-existing joint fabrics, the geometry of pores must also be considered when analysing the strength characteristics of basaltic lavas. As a consequence of the varying physical characteristics within a lava unit, each component will respond differently to an applied stress. The resulting mechanical stratigraphy is a product of the intrinsic porosity of the material. The presence of such a distinctive strength anisotropy has important implications for any study of the long-term maintenance of porosity, the permeability structure of layered basaltic sequences, and the accommodation of strain.

3.5.4. Fault Propagation in Basaltic Sequences

The three-dimensional segmentation and propagation of faults has been shown to be strongly influenced by the mechanical response of the layers they develop in (e.g. Bürgmann and Pollard, 1994; Cowie, 1998; Crider and Peacock, 2004). A mechanical stratigraphy will have a significant influence on the geometry of fault zones and the deformation mechanisms taking place (e.g. Ferrill and Morris, 2003; Schöpfer et al., 2007). In clastic sequences, the strength and elastic properties of the materials are governed by the porosity, grain size, and matrix type within the primary facies (e.g. Palchik and Hatzor, 2004; Sabatakakis et al., 2008). Current models of fault development in clastic multilayer (e.g. Ferrill and Morris, 2003; Schöpfer et al., 2006, 2007, 2009) and crystalline-clastic multilayer (Walker et al., 2013) sequences predict that strain is dominantly accommodated in the stronger layers during the initial increments of strain (Figure 3.32a). Simultaneously, weaker layers (such as a mudstones or clay-rich volcaniclastic sediments) relieve stress by deforming in a ductile manner via grain sliding (Figure 3.32b). In the following strain increments, brittle fractures in the strong layers extend and eventually the weaker, ductile layers also develop fractures. A lower angle of internal friction within these weaker layers

produces more inclined fracturing and with increasing extension, linkage of these steep and inclined segments takes place (Figure 3.32c), removing surface asperities and producing a through-going fault structure with a prominent refracted geometry. Critically, both layers are deforming: one by elastic-brittle deformation, and the other by ductile-brittle deformation.

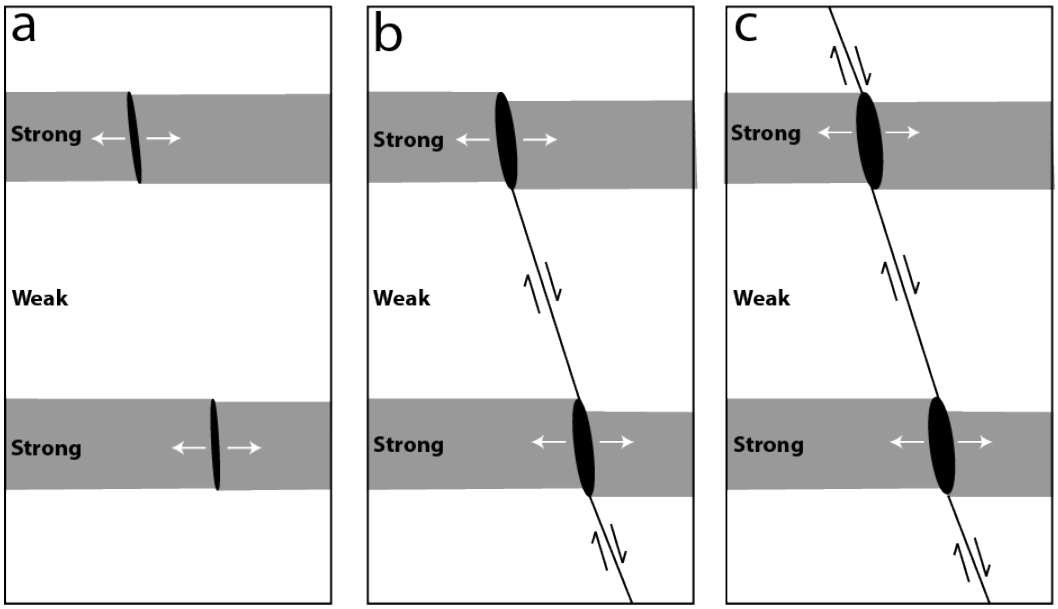

Figure 3.32. Existing model of vertical segmentation of fractures in multilayer sequence, based on examples in clastic and crystalline-clastic sequences. a) Localisation of sub-vertical fractures in mechanically strong layers. b) Linkage along inclined shear fractures in weaker layers. c) A through-going fault develops (after Schöpfer et al., 2006).

Common to these models is the mechanical classification of different layers as “strong” and “weak”: fracturing initially localises in the strong layers, followed by brittle failure of the weaker layer with increasing extension. All of the basalt samples that were tested here for their UC strength, however, show elastic-brittle failure: the “weaker” layers display localised failure at low differential stresses (15.83 MPa). As such, fracture toughness

classification may be a more precise description of compressive strength as it considers the amount and geometry of initial flaws in the material (see Engelder, 1993).

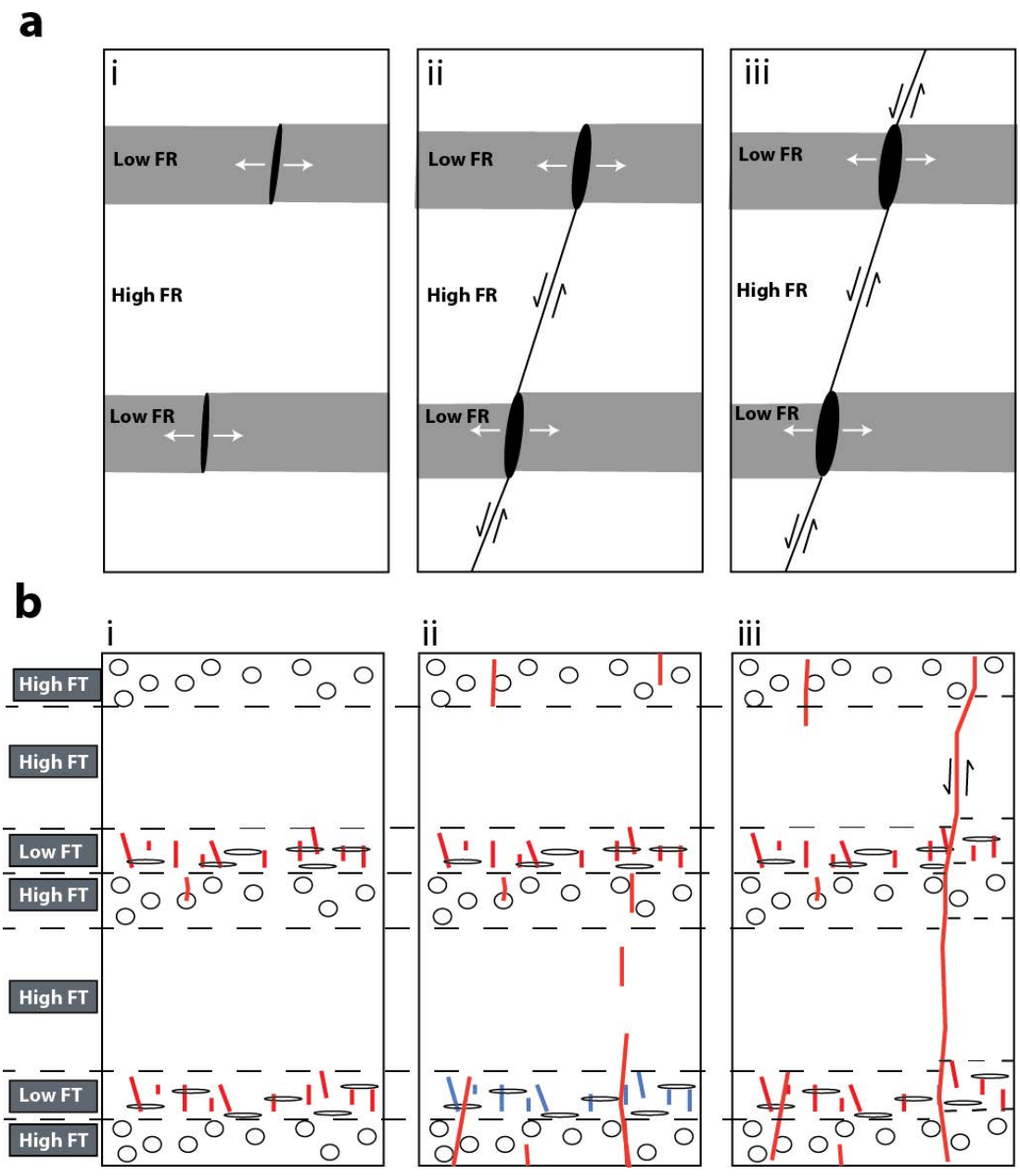

Figure 3.33. a) Fault propagation through multilayer sequences (modified after Schöpfer et al., 2006). i) Localisation of sub-vertical normal faults in layers with a low resistance to fracture. ii) Linkage of fault segments through layers with a higher resistance to fracture (FT). iii) Eventually, a through-going fault structure develop (iii). b) Fault propagation in layered basaltic sequences. i) initial localisation of extension fractures in the base component of lava flows. ii) Eventual linkage of extension fractures through the lava top and core. iii) Formation of a through-going normal fault.

Based on this classification, initial brittle failure will occur in layers with low resistance to fracture, followed by progressive failure in the layers with a high resistance. For a horizontal sequence of lavas, with a vertical σ_1, initial fracture growth would occur in the lava base, where UC strengths and Young's modulus are the lowest as a result of high effective porosities associated with flattened vesicles (Figure 3.33a). In the next increment of strain, the top of the lava begins to fracture and a segmented sequence of subvertical extension fractures develops (Figure 3.33b). Eventually, when differential stresses approach 90 MPa, the core of the lava begins to fracture and a through-going extensional-shear fracture forms (Figure 3.33c).

The role of the intact basaltic lava strength will be critical when any pre-existing anisotropy (e.g. cooling joints) is not the primary control on fault development. This is discussed further in Chapter 4. During emplacement, the lavas advanced as a series of interconnected lobes, spreading radially from a flow or point source and resulting in a series of laterally discontinuous lobes or channels, of varying thicknesses. The vertical and lateral juxtaposition of these mechanically variable layers have the potential to have a substantial influence on the nucleation of cracks and the vertical and lateral segmentation of fractures as they propagate through the sequence.

3.6. Summary

- The mechanical response of basaltic rocks to uniaxial compression is governed by the amount, and geometry, of the intrinsic porosity within the rock.
- Basaltic lava units show three components defined by the relative distribution and geometry of vesicles: (1) flow tops, characterised by effective porosities of 22-31%, associated with isotropic pores 2-20 mm in diameter, with Young's moduli of ~23 GPa and uniaxial compressive strengths of ~60 MPa; (2) flow cores, with effective porosities

of 12-13% associated with small (1-2 mm) rounded pores, and Young's moduli of ~17 GPa and uniaxial compressive strengths of ~91 MPa; (3) flow bases, with effective porosities of ~16%, associated with bands of flattened, elliptical pores with long axis up to 15 mm in length. Flow bases exhibit Young's moduli of ~12 GPa and uniaxial compressive strengths of ~16 MPa. The relative proportions of each of these components scale with flow unit thickness.

- Densities are consistent within each component and vary from: 2.1 g/cm^3 in the top (upper portion) and 2.4 g/cm^3 (lower portions), 2.6 g/cm^3 in the core and 2.45-5 g/cm^3 in the base. Thin section analysis reveals that each unit component is mineralogically homogenous. Mechanical variations are therefore attributed to changes in the volume and geometry of vesicles.
- An increase in porosity through the lava unit lowers the stiffness and the UC strength and reduces the vesicle-vesicle distances, promoting local stress amplification and fracture development in the throat regions between neighbouring vesicles. These interaction-induced stresses further weaken the material.
- Ellipsoidal vesicles in the base of flow units show a defined strength anisotropy that is controlled solely by their geometry and the relative orientation of the applied compressive stress: ellipsoidal vesicles with their major axis oriented normal to the load are very weak. The same vesicles become significantly stronger when the load is applied parallel to their major axis.
- Whilst total porosity, as a scalar quantity, exerts a strong influence on the strength of intact basalt, it is the geometric anisotropy associated with the shape of vesicles and their orientation with respect to applied stresses that appear to be the primary control of brittle strength in basalts. The directional strength anisotropy is the result of an induced effective strength produced by the effect of their radius of curvature and how stresses are distributed across them.

- In instances where the intact strength of the lava sequence is more influential in fault growth than the reactivation of pre-existing joint fabrics (e.g. at depth in rift zones), the distinctive mechanical stratigraphy produced by heterogeneous and anisotropic pore space is likely to have significant implications on the 3D segmentation and geometry of propagating faults, as is observed in clastic sequences and for the maintenance of porosity with burial.

Chapter 4

Rift-Fault Segmentation: the Koa'e Fault System, Hawai'i

4.1 Introduction

An improved understanding of the evolution of normal faults in basaltic sequences, and the controls on their distribution and geometry, has important implications for existing models of normal fault growth in cohesive sequences on Earth, as well as those on other planets. Existing studies of normal fault development in layered basaltic sequences at low confining pressures identify three principal characteristics: (1) sinuous zones of vertical extension fractures; (2) monoclinal flexure of the ground surface and; (3) sub-vertical fault scarps that show components of dilation (Duffield, 1975; Acocella et al., 2000; Acocella et al., 2003; Grant and Kattenhorn, 2004; Martel and Langley, 2006; Holland et al., 2006, 2011; Kaven and Martel, 2007; Villemin and Bergerat, 2013).

Two models have been proposed for the propagation of normal faults in shallow depth systems: (1) shallow nucleation and downward propagation; and (2) nucleation at depth, and upward propagation. Proponents for model 1 propose that faults initiate as open fractures at the surface and propagate downwards to a critical depth where, according to Griffith criterion, they become shear fractures (Opheim and Gudmundsson, 1989; Gudmundsson and Backstrom, 1991; Gudmundsson, 1992; Acocella et al., 2003; Gudmundsson 2011). For tensile failure to prevail, the minimum principal compressive effective stress must be negative, the maximum principal compressive stress should be vertical, and the differential stress must be less than four times the tensile strength of the

host rock; conditions that are most easily maintained in very shallow (<1 km) portions of the crust (Gudmundsson 2011). The failure criterion dictates that, in the absence of elevated pore fluid pressures, the maximum depth (D_{max}) that a tensile fracture may reach is determined by:

$$D_{max} = \frac{3T}{\rho g}$$

Where *T* is the tensile strength of the host rock, ρ is the host rock density and *g* is the constant for gravitational acceleration. For a range of tensile strengths and crustal densities, this maximum depth was found to lie in the range of 400-900 m (Gudmundsson, 1992; Gudmundsson 2006); below this depth, downward propagating fractures will show shear displacements. The model assumes that extension fractures exploit pre-existing cooling joints at the free surface and propagate downwards by reactivating continuous, vertical, planar joint surfaces. Natural joints in rocks such as basaltic lavas, however, are non-planar, vary in scale depending on lava thickness, and lava component. They are also commonly tilted away from vertical either at the individual lava lobe scale or at a local-sub-regional scale due to tectonic subsidence or the pre-existing topography that the lava has filled. These factors will have a pronounced effect on their shear strength at depth (e.g. Barton, 2013, 2014). The process is therefore likely to be more complex, and the role of the intact rock properties are may be more important than is currently assumed. This is consistent with seismicity records from rifting episodes in Kilauea's south flank where records of over 30,000 focal mechanisms are populated by double-couple mechanisms, associated with normal faulting (49%), strike-slip faulting (26%) and thrust faulting (25%) (Lin and Okubo, 2016).

The alternative model is that the formation of extension fractures at the free surface is associated with local concentrations of tensile stress surrounding the tip of an upward-propagating normal fault. Flexure of the surface into monoclines accommodates displacement on the fault at depth and is expected to induces additional tensile

fracturing along the crest. Downward propagation and eventual linkage of surface extension fractures with normal fault tips at depth lead to breaching of surface monoclines and the development of sub-vertical, surface-breaching fault segments that display horizontal and vertical components of displacement (Grant and Kattenhorn, 2004; Holland et al., 2006; Martel and Langley, 2006; Kaven and Martel, 2007).

Common to the downward and upward propagating models of fault development is the *a priori* assumption that deforming basaltic sequences behave as a mechanically homogenous unit undergoing homogenous and isotropic applied stresses. Detailed laboratory-based mechanical transects through Hawaiian basalts presented in Chapter 3, have demonstrated that basaltic lavas have irregular geometries and demonstrate a distinctive mechanical stratigraphy attributed to varying physical properties, related to the total porosity and void geometry through an individual lava. The resulting lateral and vertical variation in strength and elastic properties can effect fracture nucleation and growth at depth in the absence of continuous and planar joints, and hence control the initial segmentation of a fault as it propagates.

In this chapter I aim to characterise fault segmentation and interaction at a range of scales (cm- to km-scale) to constrain normal fault evolution in basaltic rocks. Based on previous numerical studies of segmented fault growth (e.g. Segall and Pollard, 1980), interaction and linkage of adjacent structures will result in local rotations in the regional stress within an inter-fault (relay zone) with interaction-induced stress amplifications leading to the develop of ancillary deformation. I will therefore identify the geometry, distribution and kinematics of ancillary deformation at a range of scales using remote- and field-based measurements of surface strains associated with the propagation of normal faults in a layered basaltic sequence in a low strain (<1%), evolving rift system. The presence of variably oriented and kinematically heterogeneous ancillary strains will

have an important influence on later rift geometry, as well as facilitating increased fluid flow.

4.2 Background

This study uses a combination of high-resolution field and remote mapping of faults, and fault-related strain in the Koa'e fault system; a system of developing normal faults located on the south flank of Kilauea volcano, Hawai'i that connect the Southwest and East Rift Zones.

4.2.1 Geological Setting

Kilauea is the youngest and southernmost subaerial volcano in the Hawaiian-Emperor chain (Figure 4.1) and one of five intraplate volcanic systems on Hawaii's Big Island. Kilauea forms a highly active basaltic shield volcano with a 3 km x 5 km collapsed caldera at its summit (Swanson et al., 1976; Neal and Lockwood, 2003). Geodetic, geophysical, and geological data imply that magma ascends along a sub-vertical conduit from the mantle to a storage reservoir 2-5 km below the summit caldera (e.g. Wright and Klein, 2006; Poland et al., 2012).

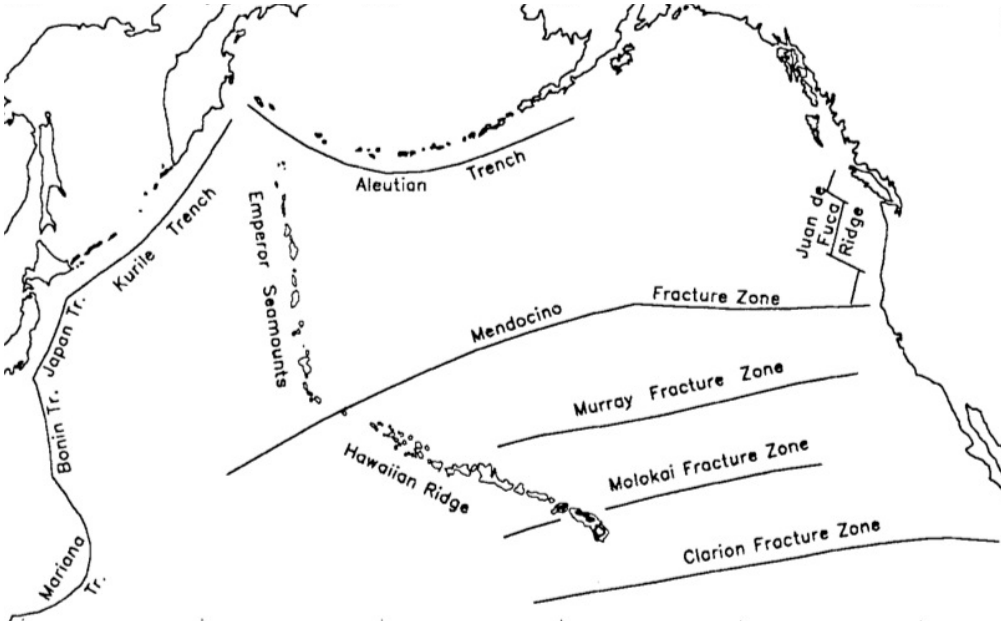

Figure 4.1. The Hawaiian-Emperor Chain extends ~6000 km across the Pacific Ocean, and consists of more than 107 individual volcanoes that have developed over the last ~70 Ma, as the Pacific plate moves north and west over the Hawaiian hotspot (image from Rubin 1990).

Based on lava accumulation rates, Kilauea is estimated to have formed 150-300 Ka (Quane et al., 2000). A 2 km deep borehole into Kilauea's south flank has revealed that subaerially emplaced lavas comprise approximately 60% of the volcanic sequence, with dikes comprising ~30% of the core below 1200 m and hyaloclastite comprising ~10% (Quane et al., 2000). Periodic influx of magma into the storage reservoir beneath Kilauea's summit typically results in eruption either at the summit, or shallow intrusions and eruption within two pronounced rift zones (Figure 4.2) that radiate eastward and south-westward from the summit (Duffield et al., 1982a; Dzurisin et al., 1984).

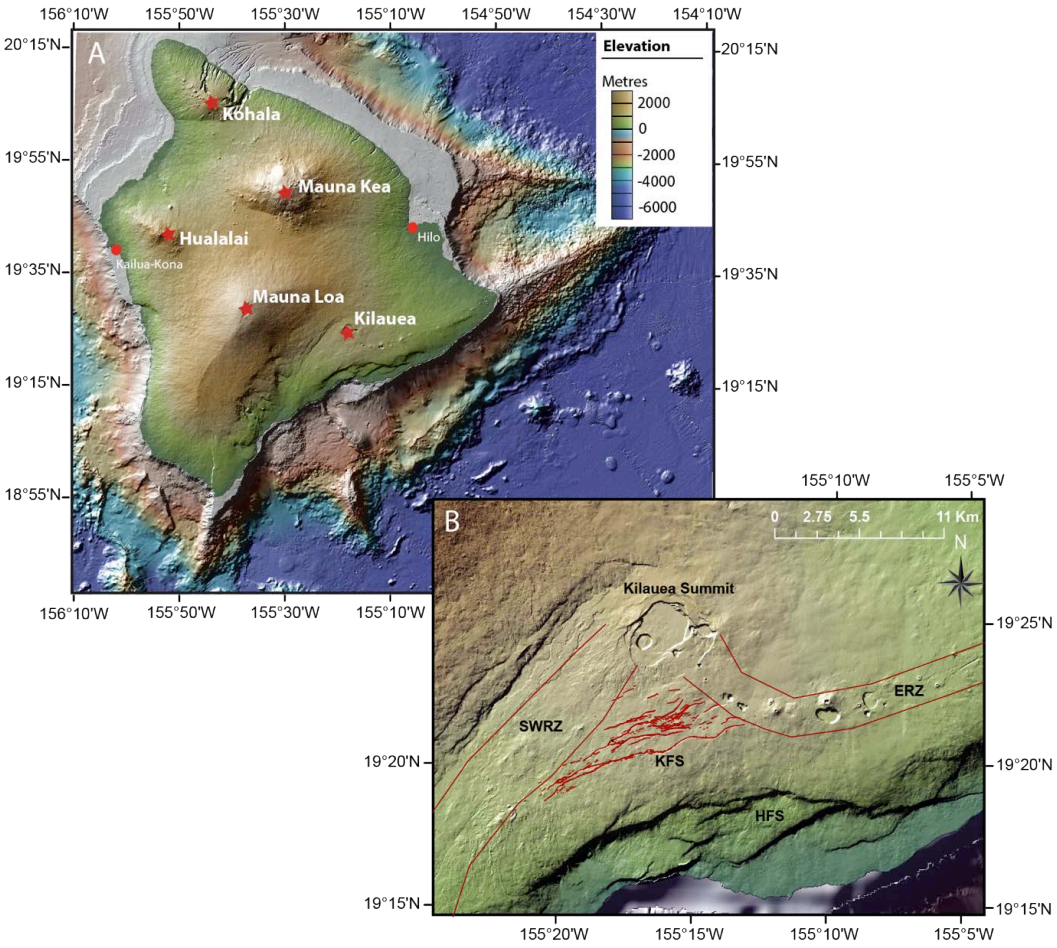

Figure 4.2. Topographic and bathymetric image of Hawai'i showing five volcanic systems: Kohala, Hualailai, Mauna Kea, Mauna Loa, and Kilauea. B) Topographic image of Kilauea Volcano highlighting the tectonic elements comprising the mobile south flank: the southwest rift zone (SWRZ), east rift zone (ERZ), the Koa'e fault system (KFS) and the Hilina fault system (HFS).

Forceful intrusion of magma into these rift zones has resulted in the uplift of the flank and is closely associated with the southward displacement of the entire south flank of Kilauea (Figure 4.3) (e.g. Swanson et al., 1976). Extension in these rift zones is accommodated by subsurface diking, elongated zones of extensional faults and fractures at shallow levels that vary in length from a few kilometres to many tens of kilometres (Swanson et al., 1976; Duffield et al., 1982a; Peacock and Parfitt, 2002; Neal and Lockwood, 2003; Le Corvec and Walter, 2009).

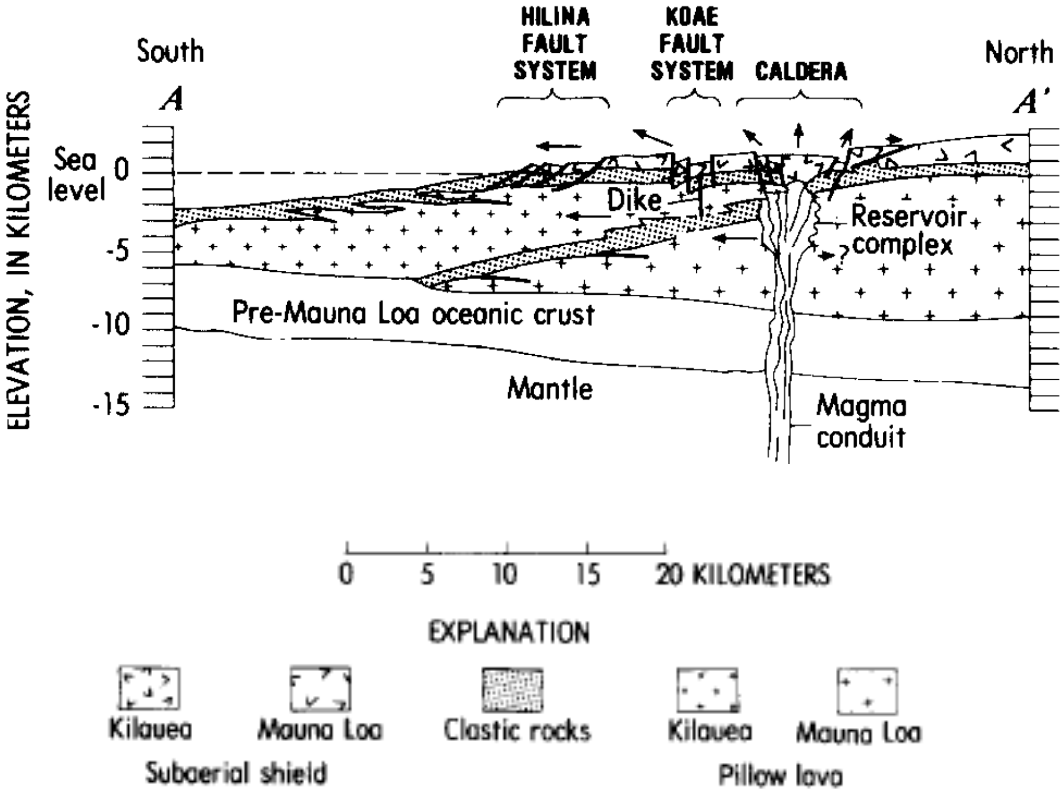

Figure 4.3. A cross-section across Kilauea. The south flank is decoupled from the north flank and Mauna Loa by the east and southwest rift zones and the Koa'e fault system (from Duffield et al., 1982b).

The subaerial portion of the east rift zone (ERZ) is 3-6 km wide and extends ~60 km with a prominent bend attributed to the maintenance of the magma supply from the summit reservoir during flank displacement (Holcombe, 1987; Moore and Trusdell, 1993; Le Corvec and Walter, 2009). The southwest rift zone (SWRZ) is 4 km wide and ~30 km long, and separated into 3 strands or sections that converge down-rift. Volcanism in the SWRZ is much less active than the ERZ, with only five historic eruptions recorded compared to more than twenty since 1950 in the ERZ (Holcombe, 1987; Moore and Trusdell, 1993). A well-known inflation-deflation cycle of ground deformation at the summit is attributed to the repeated transfer of magma from the reservoir into these rift zones (Duffield et al., 1982a; Delaney et al., 1998; Poland et al., 2008). Episodes of inflation and ground tilting at

the summit are commonly associated with periods of minor swarm seismicity in the ERZ, whereas deflation is typically accompanied by increasing swarm seismicity in the ERZ.

Based on several decades of continuous and campaign GPS measurements, seismicity data, and more recently, interferometric synthetic aperture radar (InSAR) techniques, 2.75 m of seaward displacement of the south flank of Kilauea has occurred since 1976, at an initial rate of ~25 cm/year and < 5 cm/year since 1983 (Delaney et al., 1990, 1998; Denlinger and Okubo, 1995; Owen et al., 2000; Jung et al., 2010; Poland et al., 2012). Flank motion is attributed to slip on a basal detachment at ~9 km depth, identified from the focal mechanisms of approximately 70,000 earthquakes, recorded during the period between 1962 and 1983 (Klein et al., 1987). The south flank is idealised in many studies as being laterally unconstrained, while the north flank is buttressed by the presence of Mauna Loa (e.g. Kaven and Martel, 2007). Ambient horizontal stresses normal to the rift strike are set to zero and predicted to be perturbed by one, or a combination of, two competing models that are currently proposed to account for the observed extension of Kilauea's south flank: (1) shallow, and repeated emplacement of dikes in two rift zones at ~2-4 km depth (e.g. Swanson et al., 1976; Rubin, 1990; Morgan et al., 2000); or (2) gravitational instability of the volcanic pile, facilitated by the presence of hot, weak material within the edifice (i.e. deformation is unrelated to seismicity: e.g. Clague and Denlinger, 1994; Delaney et al., 1998; Plattner et al., 2013). Numerical studies of the flank have proposed that periods of magmatic quiescence are accompanied by pure gravitational spreading, with rift-dominated extension occurring when magmatic activity increases (Le Corvec and Walter, 2009). To facilitate outward pushing, two systems of faults propagate from the top of the intrusion to the surface (Le Corvec and Walter, 2009). The fault structures predicted in these models may be analogous to two fault systems located on the south flank of Kilauea: the Koa'e and Hilina fault systems.

4.2.2 The Hilina Fault System

The Hilina Fault System (HFS: Figures 4.2b and 4.3) comprises a 5 km wide zone of south-dipping, en echelon normal fault segments with surface offsets up to ~500 m, recorded since the last resurfacing by lava flows 1500-750 years ago (Swanson et al., 1976; Wolfe and Morris, 1996; Parfitt and Peacock, 2001, 2002). The origins and 3-dimensional extent of the fault system, however, remains unclear. Swanson et al. (1976) propose that the exposed scarps represent lava-covered headwalls of large landslide blocks that are episodically reactivated, resulting in destructive earthquakes (e.g. the November 1975 M7.2 Kalapana earthquake). The fault system may represent shallow listric faults that extend through lavas and hyaloclastites, and terminate at 1-3 km depth (Duffield et al., 1982b). Alternatively, the fault system may penetrate to greater depths and bottom out at the base of the volcanic pile along the detachment at 9-11 km depth (Denlinger and Okubo, 1995; Okubo et al., 1997; Morgan et al., 2000; Parfitt and Peacock, 2001).

4.2.3 The Koa'e Fault System

The Koa'e fault system (Figure 4.2) is a 20 km long and ~3 km wide region of dominantly north-dipping normal fault segments that extends between the ERZ and SWRZ to produce a continuous zone of extension (Duffield, 1975; Swanson et al., 1976; Duffield et al., 1982b; Martel and Langley, 2006; Podolsky and Roberts, 2008). The fault system is interpreted to be the result of the forceful emplacement of dikes in the east rift zone, the cumulative effect of which has been ~25-30 m of extension since the last resurfacing event 400-750 years ago (Duffield et al., 1975; 1982b; Swanson et al 1976; Wolfe and Morris, 1996; Peacock and Parfitt, 2002). This is inferred from spatial relationships with the most recent lavas: there is no evidence for ponding of southward flowing lavas below north-facing fault scarps, as would be expected for pre-existing fault scarps. The observed

throw across faults in the Koa'e has therefore developed since the most recent lavas cooled, accumulating at a rate of 2-3 cm per year (Martel and Langley, 2006).

The principal structures that have previously been identified in the Koa'e fault system (e.g. Duffield et al., 1982b; Swanson et al., 1976; Peacock and Parfitt, 2002) include: (1) early-forming footwall fractures that strike sub-parallel to the fault tip line (Figure 4.4, stage 1); (2) gentle monoclines ahead of fault tips at depth, that steepen with increasing displacement on the fault (Figure 4.4, stage 1 and 2); (3) hanging wall buckles associated with overlapping fractures and faults at depth (Figure 4.4, stage 3); and (4) Sub-vertical fault scarps with maximum throws of ~15 m that are predicted to breach monoclines, transferring them to the hanging wall (Figure 4.4, stage 4). Based on their characteristic zig-zag appearance footwall fractures are thought to exploit pre-existing cooling joints in the basalt at the free surface (e.g. Holland et al., 2006). Apertures of ~ 2m are common, but only where scarp heights exceed 1 m (Martel and Langley, 2006). In such instances, it is common for angular, collapsed blocks to fill the fracture and obscure true depths. Hanging wall buckles, or moletracks, are sharp anticlinal folds with fractured crests along the base of fault scarps, indicating a substantial local component of horizontal compression (Martel and Langley, 2006). Generally these folds are not greater than 1 m high but may have surface trace lengths of ~20 m (Martel and Langley, 2006).

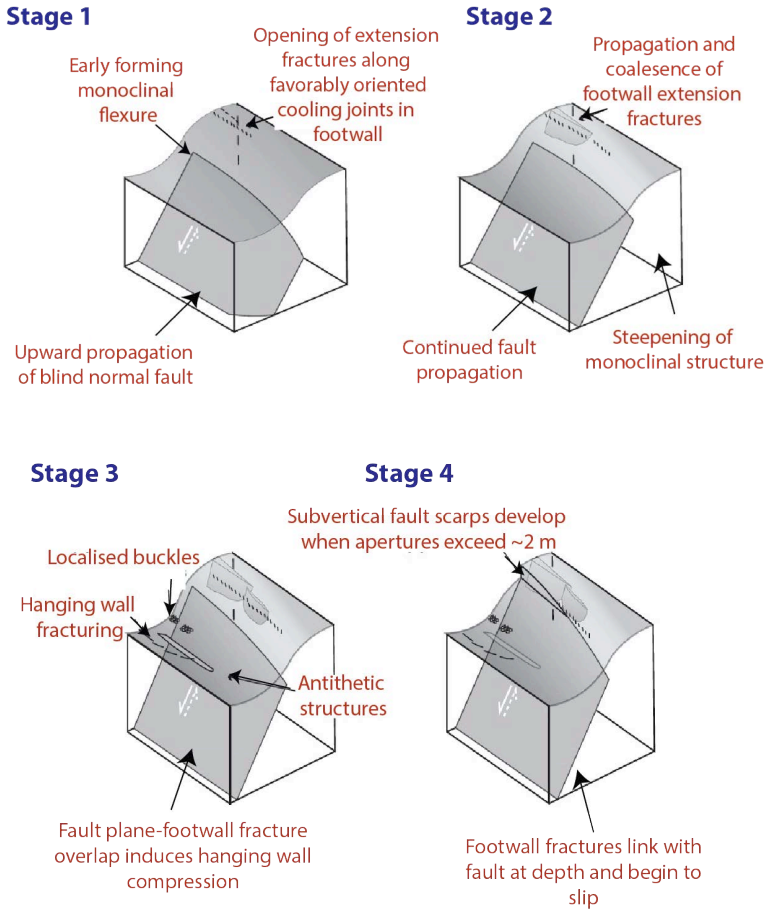

Figure 4.4. Model of fault development in the Koa'e fault system (after Kaven and Martel, 2007). Stage 1: an upward propagating blind normal fault induces extension fractures ahead of the tip (parallel to the tip line) and causes flexure of the surface. Stage 2: continued growth of the fault at depth causes monocline steepening and fractures interact and coalesce. Stage 3: with further growth, localised buckles and extension fractures (ahead of subsurface, antithetic fractures) develop on the adjacent hanging wall. Stage 4: normal faults link with extension fractures at depth, resulting in surface-breaching faults with opening and vertical components of displacement. Surface monoclines are breached and transferred to the hanging wall.

The origins and penetration depths of Koa'e faults are still debated, with some proposing that deformation is related to dike emplacement (e.g. Le Corvec and Walter, 2009) or accommodation of footwall uplift north of the HFS (Parfitt and Peacock, 2001) and others suggesting that it represents a "tear-away zone", related to extension in the ERZ and

forms an incipient link between the SWRZ and ERZ segments, producing a continuous zone of extension (Duffield, 1975). The trend of the upper ERZ lies between the surface expression of the rift and the strike of the Koa'e (90-102^{o}); this has been used as evidence for opening at depth across a broad region between the Koa'e fault system and the upper ERZ (Owen et al., 2000). There is good evidence for diking within the Koa'e fault system, including the absence of a negative gravity anomaly in the area (Swanson et al., 2012), seismicity propagation from the ERZ (Fiske and Koyanagi, 1968; Duffield, 1975) and spatter derived from pre-existing ground cracks (Swanson et al., 2012). There are also instances of closely spaced, antithetic faults that are separated by a narrow trough; such a pattern has previously been attributed to diking at depth in Iceland (e.g. Tentler, 2005), and thought to have similar origins in the Koa'e fault system (D. Swanson, Pers. Comms. 2014). The Koa'e fault system may therefore be strongly influenced by dike emplacement, though not necessarily induced solely by forceful intrusion.

4.3 Datasets

Initial mapping of faults and extension fractures within the Koa'e fault system was conducted using a range of two-dimensional Landsat ETM+ and World-View2 satellite (14.25 and 0.5 m resolution, respectively) and three-dimensional remote sensing datasets (aerial LiDAR with 0.5 m resolution). Faults and extension fractures were cross-referenced in each dataset to ensure lineaments corresponded to fault-related deformation, avoiding any possible artefacts, noise or man-made features in the images.

4.3.1 Data Analysis

The combination of LiDAR-derived datasets and high-resolution satellite imagery allowed first pass mapping of faults and fractures throughout the Koa'e fault system before field-

based ground-truthing took place. Extension fractures with apertures exceeding the resolution of the remote datasets (0.5-1 m) were picked and traced in ArcGIS; aperture was measured at multiple points each of the fracture traces (Figure 4.5). In addition to fracture geometry, and distribution, the wavelength and amplitude of surface folding and fault throw (where present in the datasets) could be assessed (Figure 4.5: cross-sections a and b; Figure 4.6: cross-sections a-c). Total fracture lengths and maximum apertures were thus obtained for 1,849 extension fractures in the fault system (Figure 4.7).

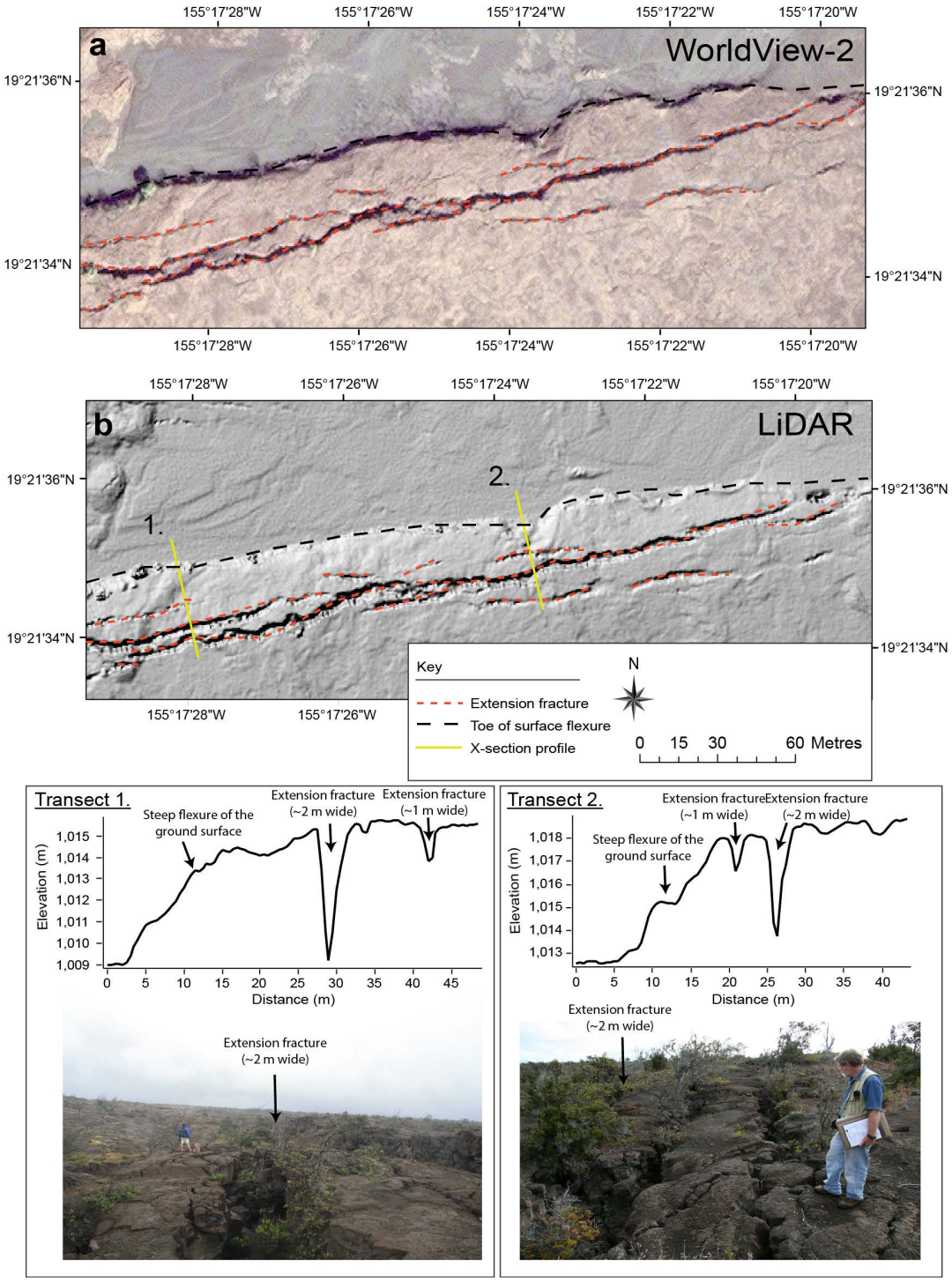

Figure 4.5. Examples of picking structures from satellite and aerial LiDAR-derived hillshade images with a resolution of ~0.5 m and at a scale of 1:1000. Transects 1 and 2 demonstrate the morphology of surface flexures in the Koa'e fault system, and the distribution of extension fractures along their crest. N.B. Extension fractures do not always correspond to the outer arc of the folds.

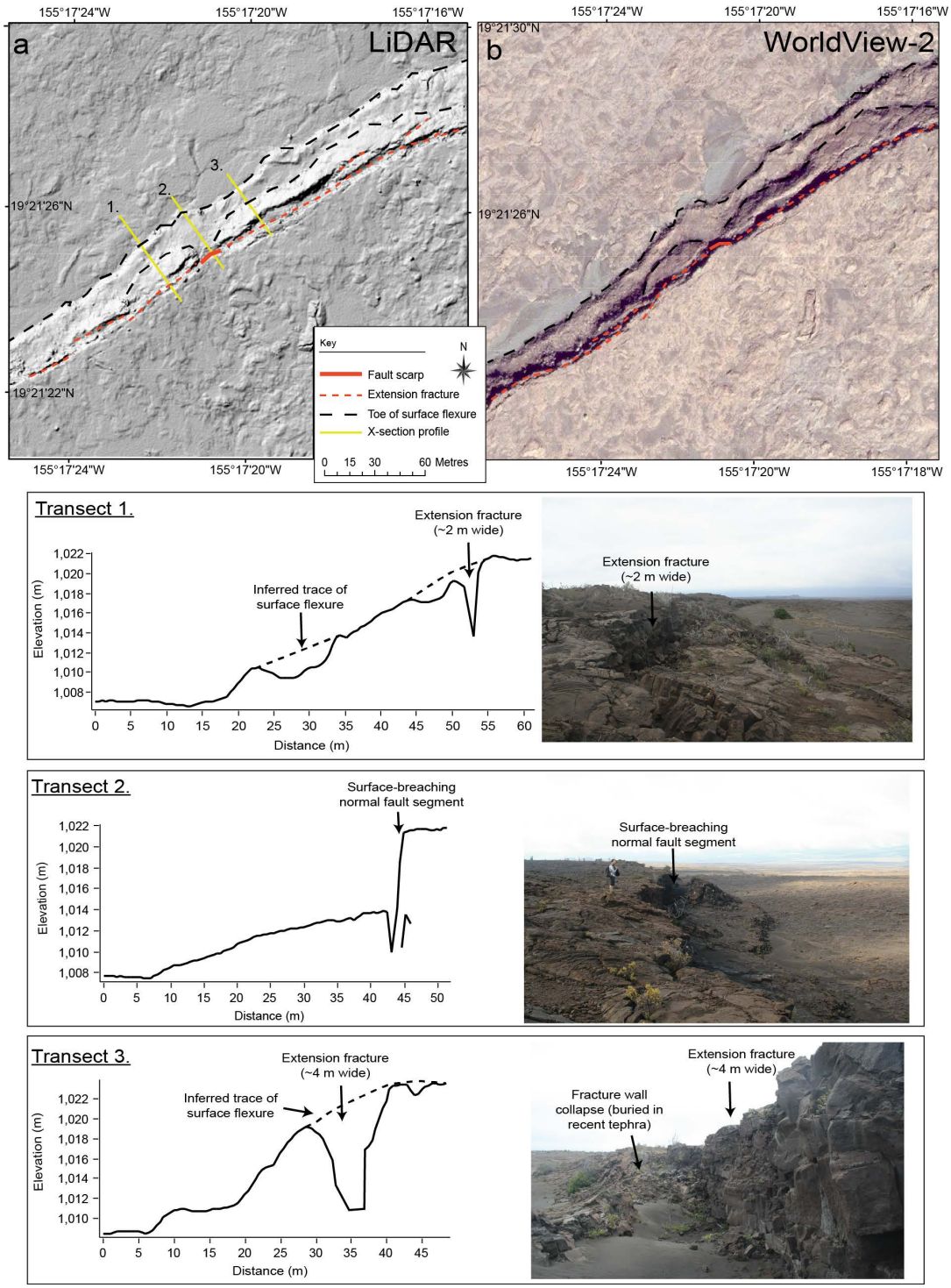

Figure 4.6. Examples of picking structures from (a) aerial LiDAR-derived hillshade images and (b) satellite images with a resolution of ~0.5 m and at a scale of 1:1000. Transects 1-3 and photo insets demonstrate lateral variations in surface flexure morphology and extension accommodation. Transects 1 and 3 show rounded surface flexures, cut by extension fractures. Transect 2 shows a surface-breaching normal fault segment with clearly offset footwall-hanging wall surfaces. Surface flexure is minor or non-existent along this fault segment.

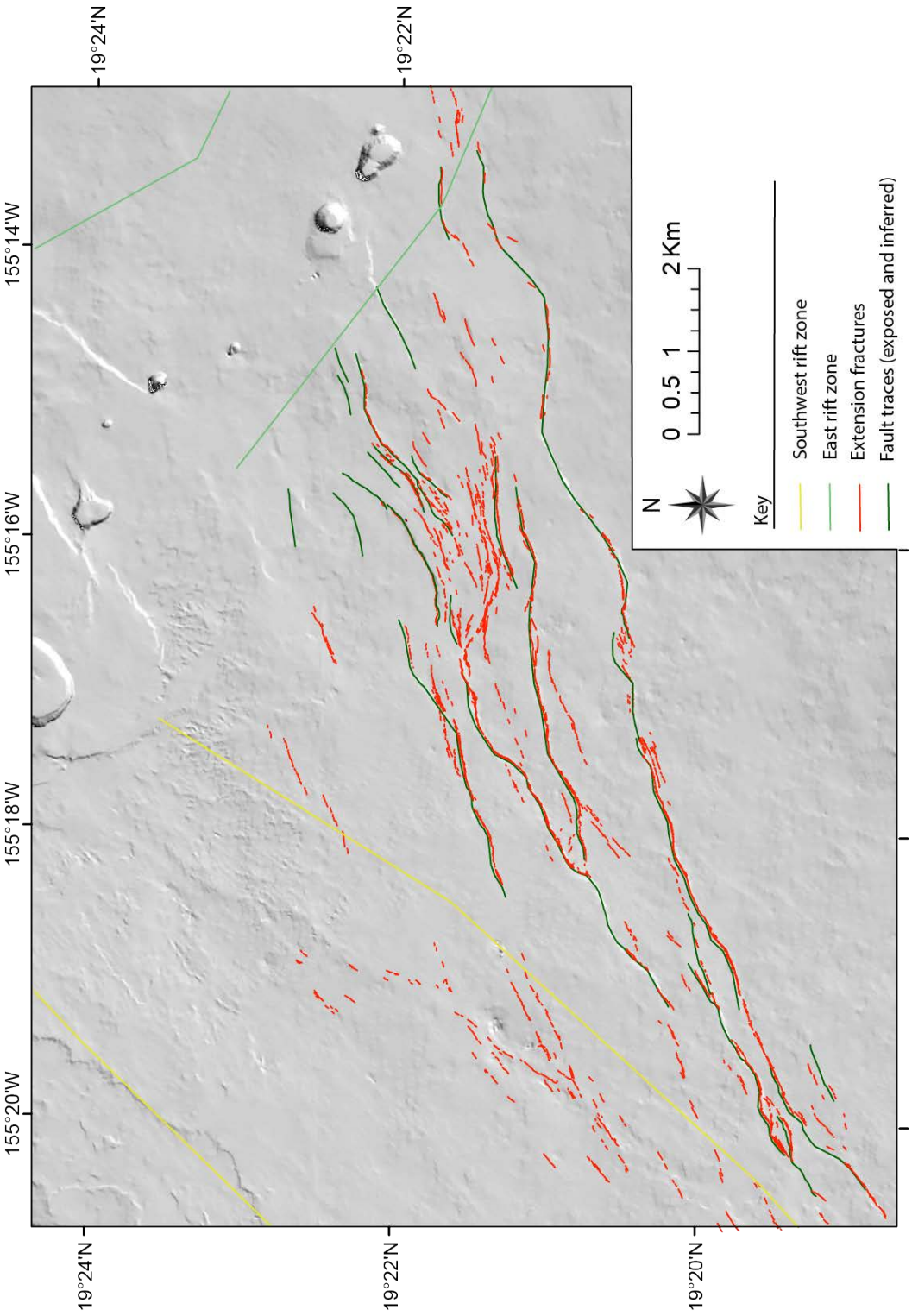

Figure 4.7. Fault and extension fracture map of the Koa'e fault system, consisting of 1,875 separate polylines. Extension fractures commonly form en echelon arrays that are dominantly located in the footwall of blind normal faults. Fault traces are inferred based on exposed fault

scarps or areas of surface flexure, which are interpreted to represent deformation above a restricted blind normal fault tip. Outline of SWRZ and ERZ taken from Holcombe, 1987.

Initial remote mapping in the fault system provides a first order observation of the extension fracture and fault distributions in the region. This has been used as a basis for selecting a smaller area of interest for high-resolution field data collection with an aim to: (1) better constrain the distribution of strains in the Koa'e fault system; and (2) determine the geometry and the three-dimensional segmentation of fault structures in an evolving rift zone.

4.3.2 Field Mapping

Remotely produced structural maps were ground-truthed during intensive field mapping using Leica differential GPS (dGPS), to characterise extension fracture and fault geometries and distributions to sub-metre precision and accuracy. Geometry and length data were obtained for approximately 350 individual extension fractures with apertures ranging from 0.1-2.0 m and lengths between ~0.18-150 m in a 3 km^2 area of the Koa'e fault system. Above apertures of 2 m, extension fractures commonly start to accumulate throw or show collapsed walls, making rapid and accurate measurement of extension direction difficult. At this scale, fracture aperture is estimated from satellite and LiDAR datasets, and derivative datasets.

Figure 4.8. a) Manual collection of fracture kinematic data: aperture, extension/opening direction and azimuth. b) Differential GPS measurements were collected at multiple points, including the extension fracture's tips, and where any significant kinks or eroded portions occur along each extension fracture. c) Extension fractures were given an ID number with additional values denoting individual sites along each extension fracture where kinematic measurements were recorded. Measurements and ID numbers were recorded in a field notebook.

In addition to geometrical characterisation, the following kinematic measurements were collected along each extension fracture: (1) extension direction; (2) opening style (e.g. purely tensile or extensional-shear); (3) fracture azimuth; and (4) vertical offset (if present) (Figure 4.8a). Measurements were taken at the start and end of each fracture (or as close as exposure allowed) as well as at a series of regularly spaced points along each fracture trace (Figure 4.8b and c). The resulting combined (remote and field) dataset of over 2,000 measurements covers 3 orders of magnitude of fracture length data and provides high-resolution documentation of the distribution of strains in an evolving system of normal faults.

4.4 Results

Structural characterisation of brittle deformation in the Koa'e fault system is separated into two types: (1) extension fractures that demonstrate an opening and no throw, and (2) normal faults that demonstrate an opening and a vertical offset (throw). In the Koa'e fault system, faults scarps show significant horizontal components of displacement in addition to their throw.

4.4.1 Fracture Geometry and Distribution

Due to the limited number of surface-breaching fault segments in the areas of interest (AOI), the displacements and distribution of extension fractures at the surface are used as a proxy to the slip distribution and kinematics of underlying fault segments, on the assumption that extension fractures developing within the process zone of blind normal faults scale linearly with the size of the process zone (see Chapter 2, section 2.1.2 for definition of this term). In this case, larger fracture apertures may reflect greater stress intensities ahead of larger faults at depth and the location of displacement maxima in a set of extension fractures coincides with the displacement maxima on the fault at depth.

4.4.1.1 Fracture Distribution and Scaling

Extension fractures in the Koa'e fault system form zones up to 3-5 km in length and 30-50 wide, most commonly in the footwalls of blind, or surface-breaching faults, which die out laterally into linear sets of extension fractures. At the free surface, extension fractures initiate along pre-existing cooling joints in the lavas that are favourably oriented to the regional minimum compressive stress direction. The reactivation of pre-existing

(cohesionless) cooling joints appears to exert the primary control, at a local scale, and at near-surface depths, on the geometry of the fractures, producing their characteristic zigzag traces (Figure 4.9). At greater depths, joints, which have healed, been sealed or are characterised by high effective shear strengths, may not present the primary control. For instance, shear-dominated seismicity is common at 2-5 km depth beneath the Koa'e fault system, but also occurs at ~0.5-1 km depth (Lin and Okubo, 2016).

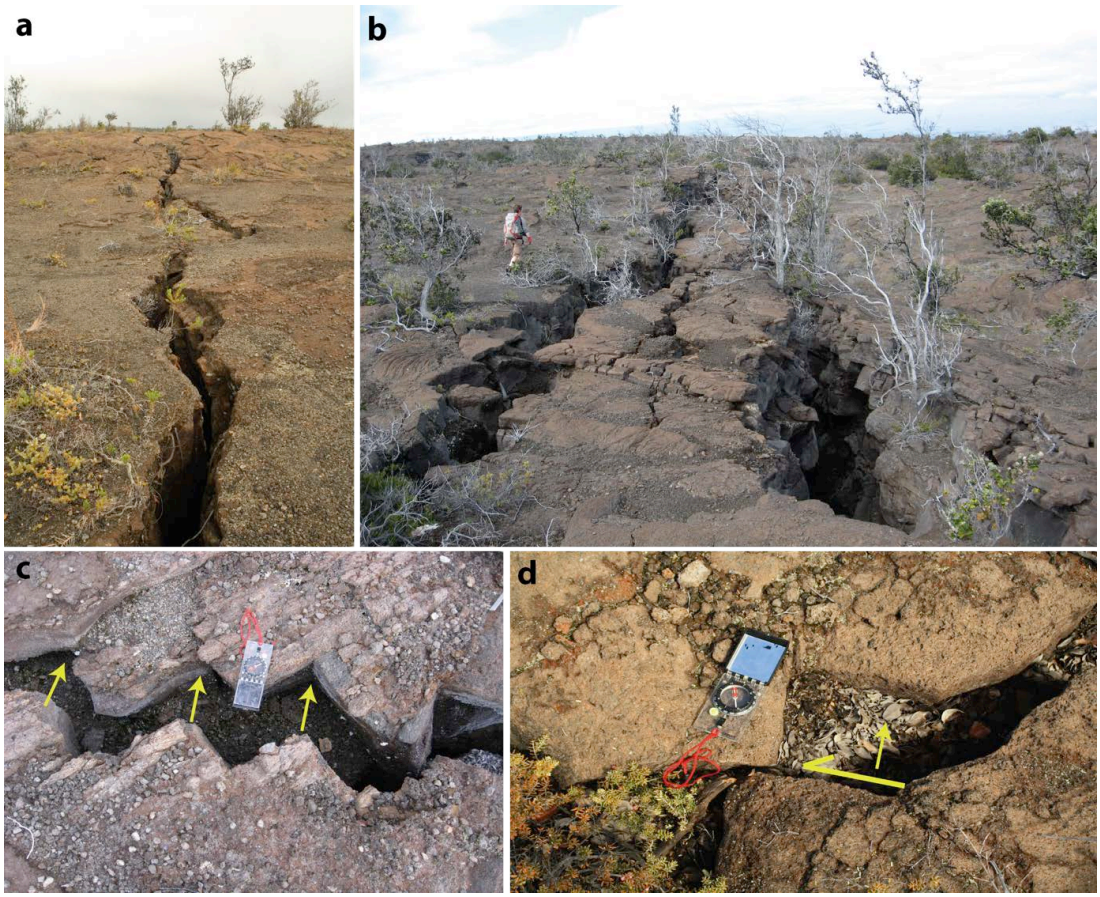

Figure 4.9. Examples of extension fractures in the Koa'e fault system, which show a variety of path geometries. a) Underlapping, curved. b) Overlapping, straight. c) Extension fracture openings show wall displacement in a direction orthogonal to their strike dimension. ~ 90% of fractures in the Koa'e are purely open-mode (extensional). (d) There are four instances of fractures that demonstrate mixed-mode (extensional-shear) opening.

Mapping of subvertical extension fracture networks show them to be parallel to surface-breaching fault scarps or the long axes of surface flexures, and to vary in length from a few metres to more than 200 m (Figure 4.10a) with apertures most commonly of 0.3-0.6 m (Figure 4.10b).

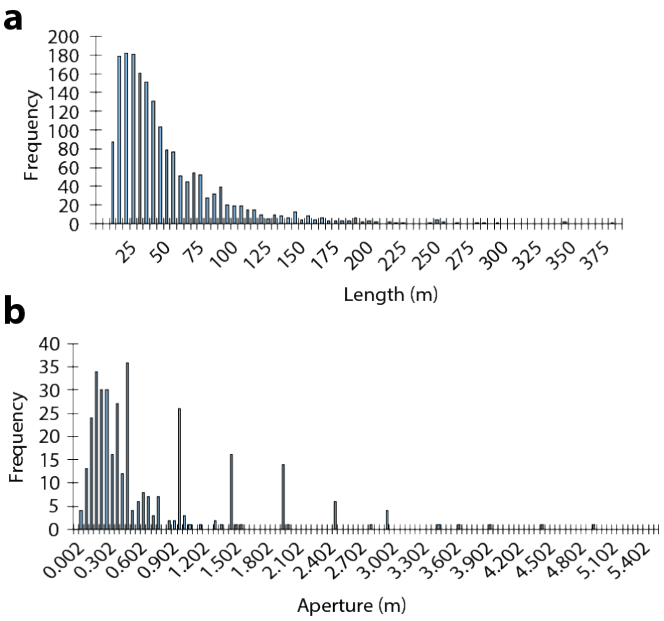

Figure 4.10. Distribution of fracture lengths and maximum apertures. a) Histogram of frequency as a function of fracture length in metres. b) Histogram of frequency as a function of fracture aperture in metres.

Log-log graphs of cumulative number plot against length (Figure 4.11a, b) and against maximum aperture (Figure 4.11c, d) indicate exponential scaling distributions. Such a distribution has been recognised in both oceanic fault populations (e.g. Cowie, 1998) and continental fault populations (e.g. Gupta and Scholz, 2000b). It has been suggested that non-power law scaling may be a short-term characteristic of interacting populations or an indicator of different processes or controls operating at different scales (e.g. Cartwright et al., 1995; Nicol et al., 1996b).

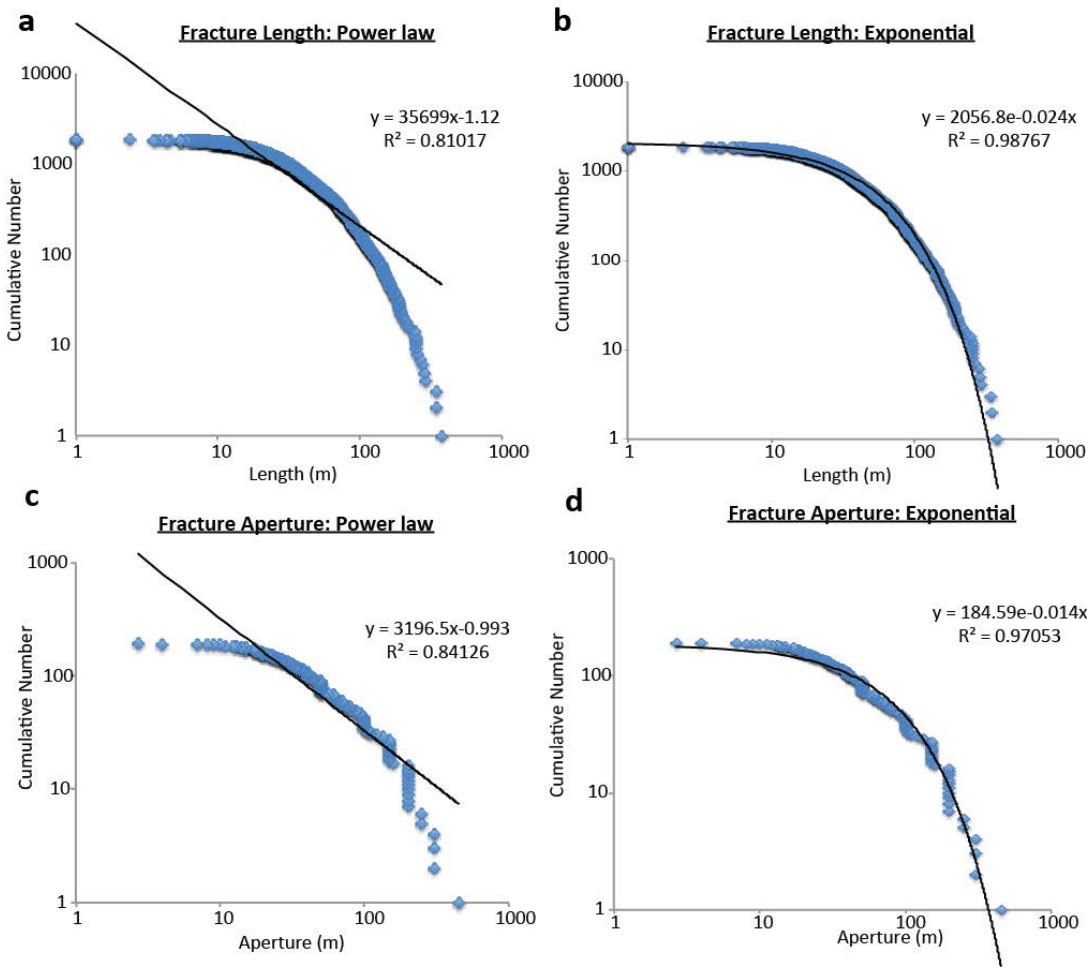

Figure 4.11. Population distribution plots. a) Power law distribution for extension fracture length. b) Exponential distribution for extension fracture length. c) Power law distribution for maximum extension fracture aperture. d) Exponential distribution for maximum extension fracture aperture. Plots suggest fracture scaling in the Koa'e fault system is best described using an exponential function.

Scatter in the graphs in Figure 4.11 may be related to exposure or local variations in aperture associated with non-tectonic opening, such as wall collapse and subsidence, which would lead to underestimate lengths and overestimated apertures, respectively. Interaction between neighbouring fractures may also lead to higher than expected aspect ratios and skewed scaling patterns (maximum aperture divided by the fracture length).

4.4.1.2 Fracture Kinematics and Segmentation

Detailed fracture mapping in the AOI has revealed a series of fracture networks that follow two dominant orientations: (1) a rift-parallel 080° (ENE) set (Figure 4.12, sets A and C); and (2) a rift-oblique 110° (ESE) set (Figure 4.12, set B). Both fracture sets display purely extensional openings (Figure 4.12, rose plots). Rift-parallel (ENE) fracture sets in the AOI represent the surface expression of two en echelon, rift zone-parallel blind normal fault segments, separated by approximately 700 m (Figure 4.12). The estimated fault trace length based on the map view extent of extension fractures of set A is ~3 km and the estimated length of C is 1-1.5 km. Based on their surface expression (interpreted using extension fracture distributions), the two faults appear to be underlapping, however, it is noted this may not be true in the sub-surface. Between these two segments, is the rift-oblique, ESE, set of fractures that appear to be developing ahead of a separate, obliquely striking fault segment at depth, or a tip-to-plane linkage of fault C. A total displacement (aperture) profile has been measured using the summed apertures of fractures along the array. This profile (Figure 4.13) does not exhibit a centrally located displacement maxima, implying that the extension fracture networks are not developing as geometrically and kinematically coherent segments of a single structure at depth, but are rather interacting initially isolated faults.

Figure 4.12. An aerial LiDAR-derived DEM for the mapped area of the Koa'e fault system showing fracture distributions, orientations and kinematics. Two main extension fracture sets are identified: ENE-WSW (A and B), and ESE-WNW. Small black (precise) and orange (larger fracture estimates) arrows on individual polylines indicate opening directions at multiple points along each fracture. These are summarised by the inset rose diagrams of opening direction and average strike (red line on rose plots). The results show that fractures in each set show purely extensional openings.

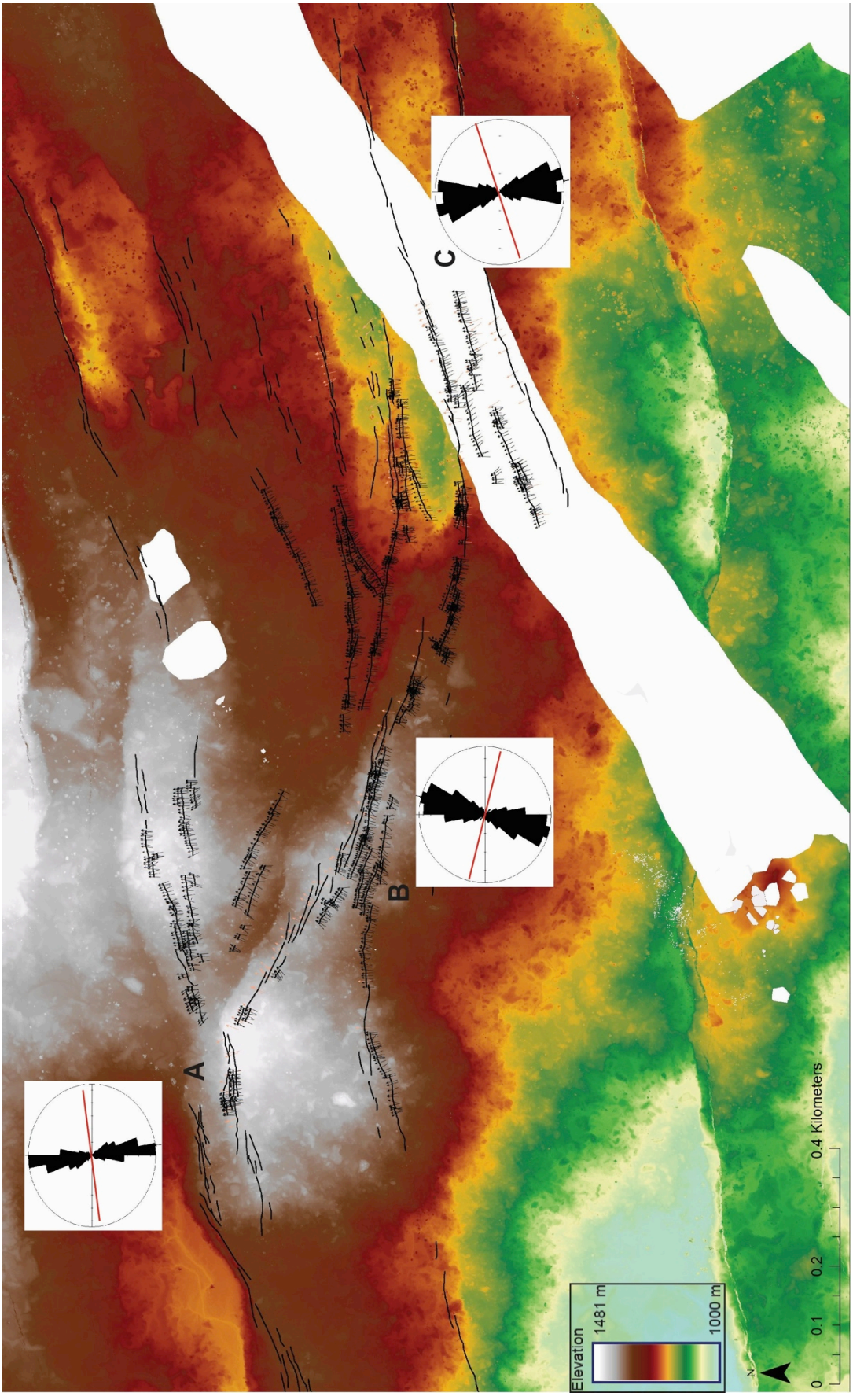
A
B
C
Elevation
1481 m
1000 m
0
0.1
0.2
0.4 Kilometers
N

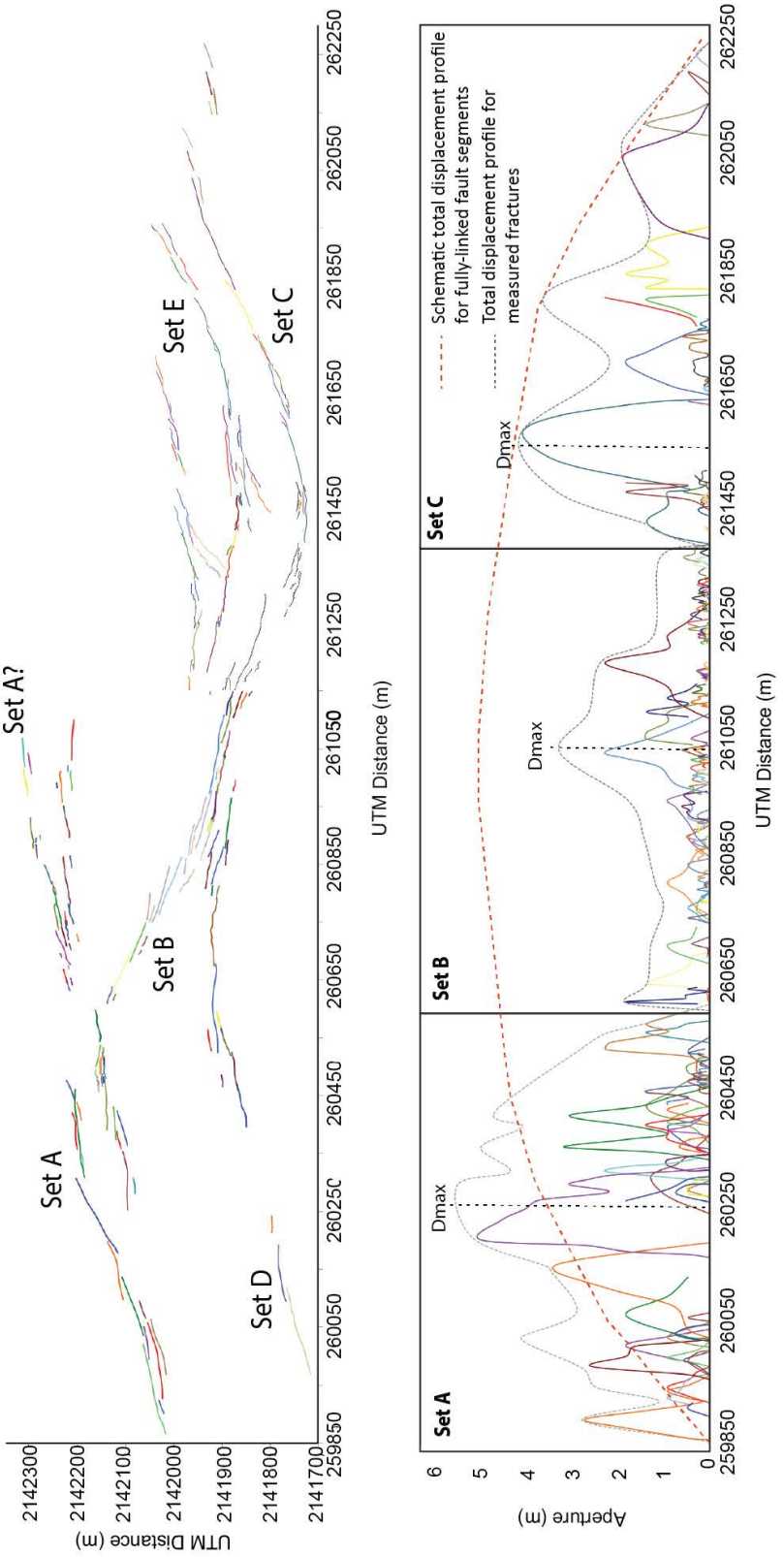

Figure 4.13. Total displacement profiles for the extension fracture array, which is interpreted to parallel blind fault sets A and C, show asymmetric displacement profiles with high gradients approaching set B. Set B shows a slightly asymmetric, with a minor gradient developing towards set C and aperture deficits at each tip.

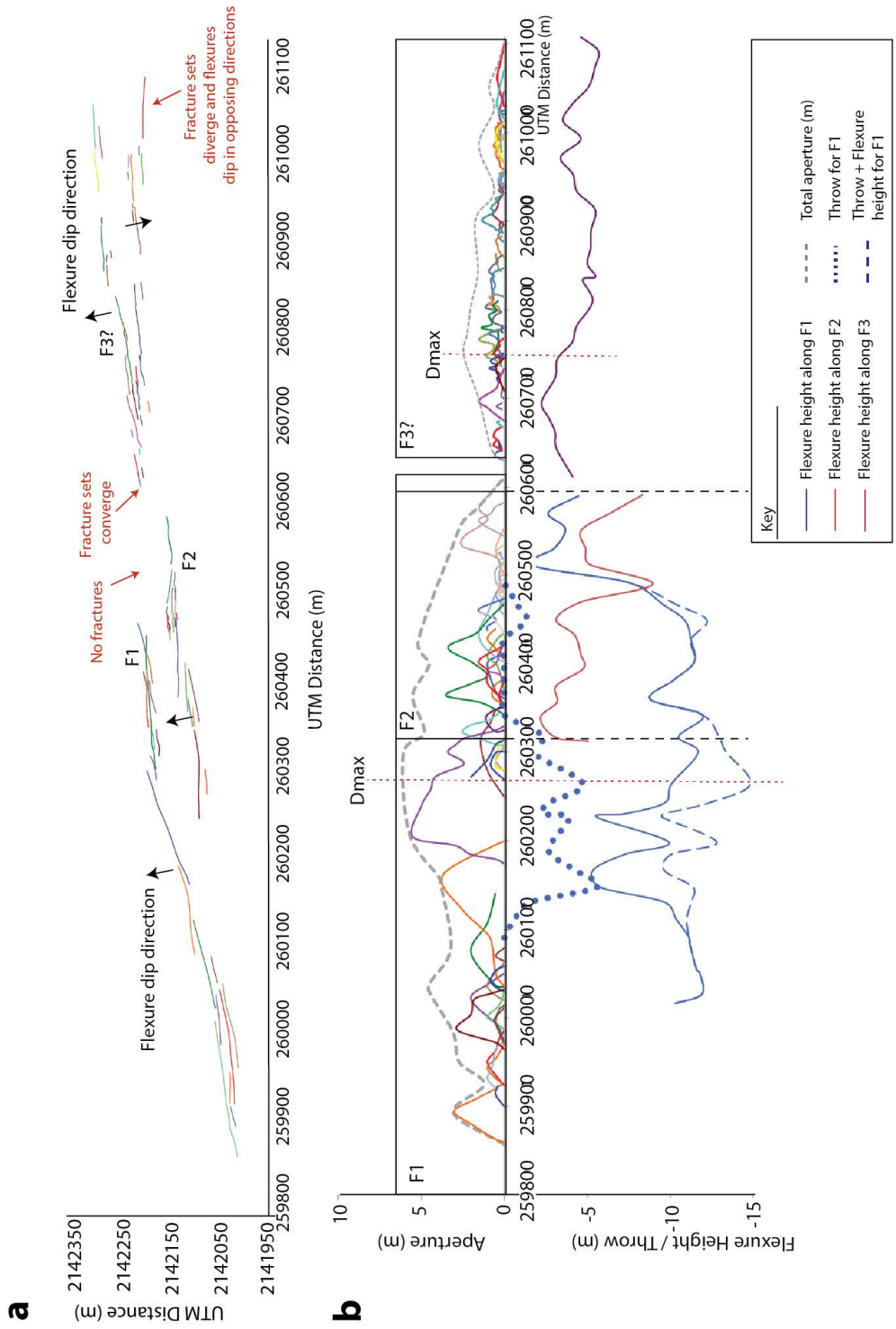

Figure 4.14. a) Distribution of extension fractures at the tip of set A. b) A combined displacement-length profile showing extension fracture aperture (coloured polylines), total aperture (dotted grey profile), fault throw (where present: dotted blue line), flexure height (solid blue line) and combined flexure-throw (dashed blue line). Arrows indicate the dip-direction of faults or surface flexures (a proxy for fault dip direction at depth). Points of maximum fracture aperture also approximately correspond to the locations of surface-breaking fault segments.

SET A: Extension fractures show a symmetrical total aperture profile with a displacement maximum in the centre of the array (Figure 4.14). The set is composed of two parallel strands of primarily composite, hard-linked extension fractures up to 150 m long with apertures of up to 5 m. The two sets are interpreted to be surface expressions of blind normal fault splays (F1 and F2). Surface flexure amplitude is high (~15 m) and the greatest fracture apertures coincide with the areas of highest flexure amplitude or segments of surface-breaching fault (F1). Though unconnected in map view, there is a set of short fractures at the tip of A (≤10 m in length), showing relatively minor apertures of up to 1m, that are included in the same set. The timing of their development remains unclear; it is unknown if these represent the abandoned tip of fault A, or reflect a more recent stage of post-breach fault propagation. Extension fractures form two sets that converge near the tip of set A and parallel the crest of surface flexures that dip in opposing directions.

Set B: Fractures show a defined displacement gradient with a point of maximum displacement that is shifted slightly towards the tip of bounding set C (Figure 4.15,). The lateral tips taper towards zero, with a steep displacement gradient proximally to either bounding set.

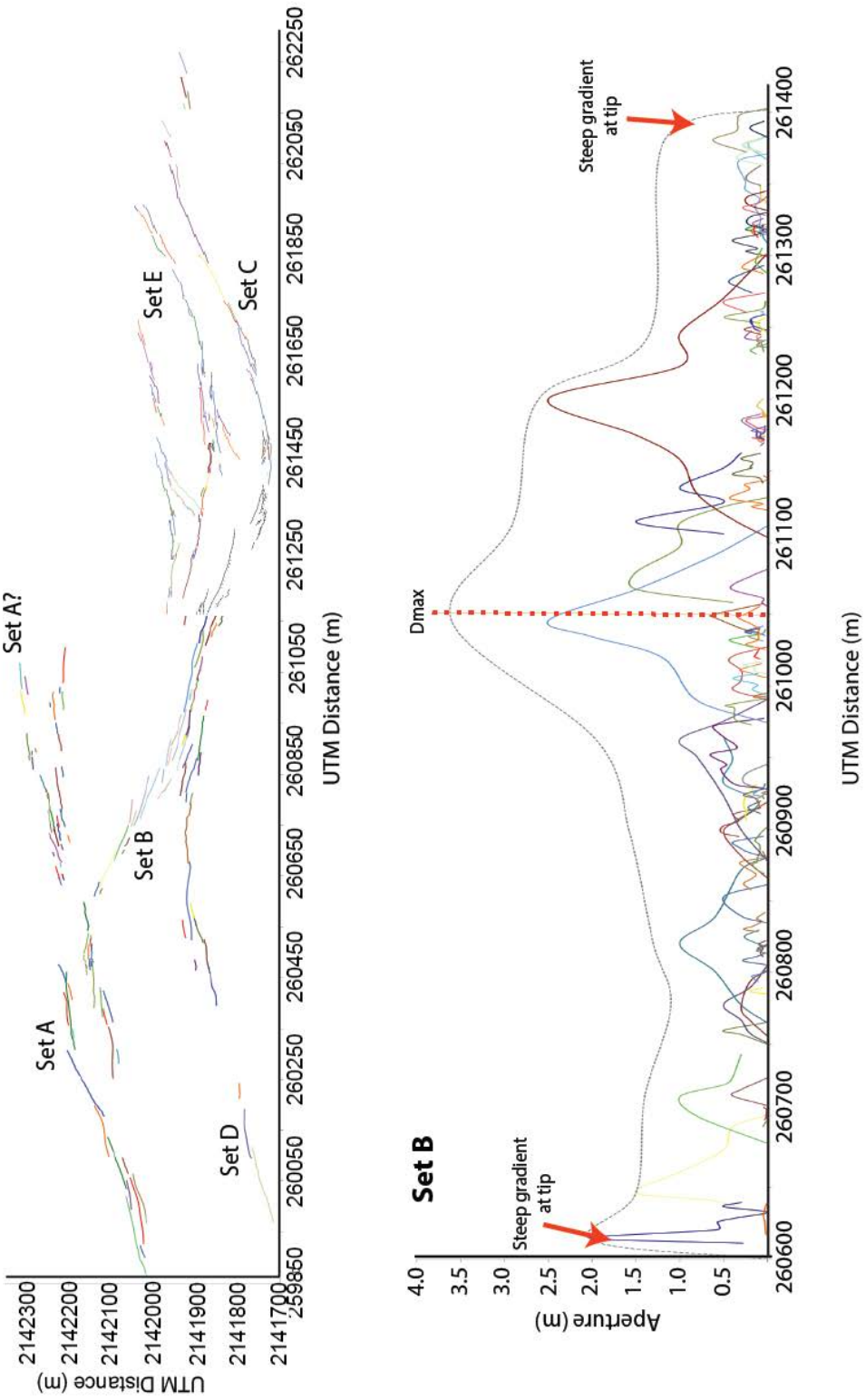

Figure 4.15. a) Distribution of extension fractures in the AOI. b) Displacement (aperture)-length profiles for fracture set B. Total displacement profile (dotted, grey line) is asymmetric with the maximum aperture shifted slightly off-centre, towards the tip of set C.

SET C: Fractures are associated with a single north-dipping fault that forms the southern bounding fault of the relay zone (Figure 4.16). Displacement-length profiles show a highly asymmetrical aperture gradient with the greatest apertures located at the western tip of the array. Approaching the tip there is a surface-breaching fault segment, indicating significantly higher elastic strains exist at the tip of this structure.

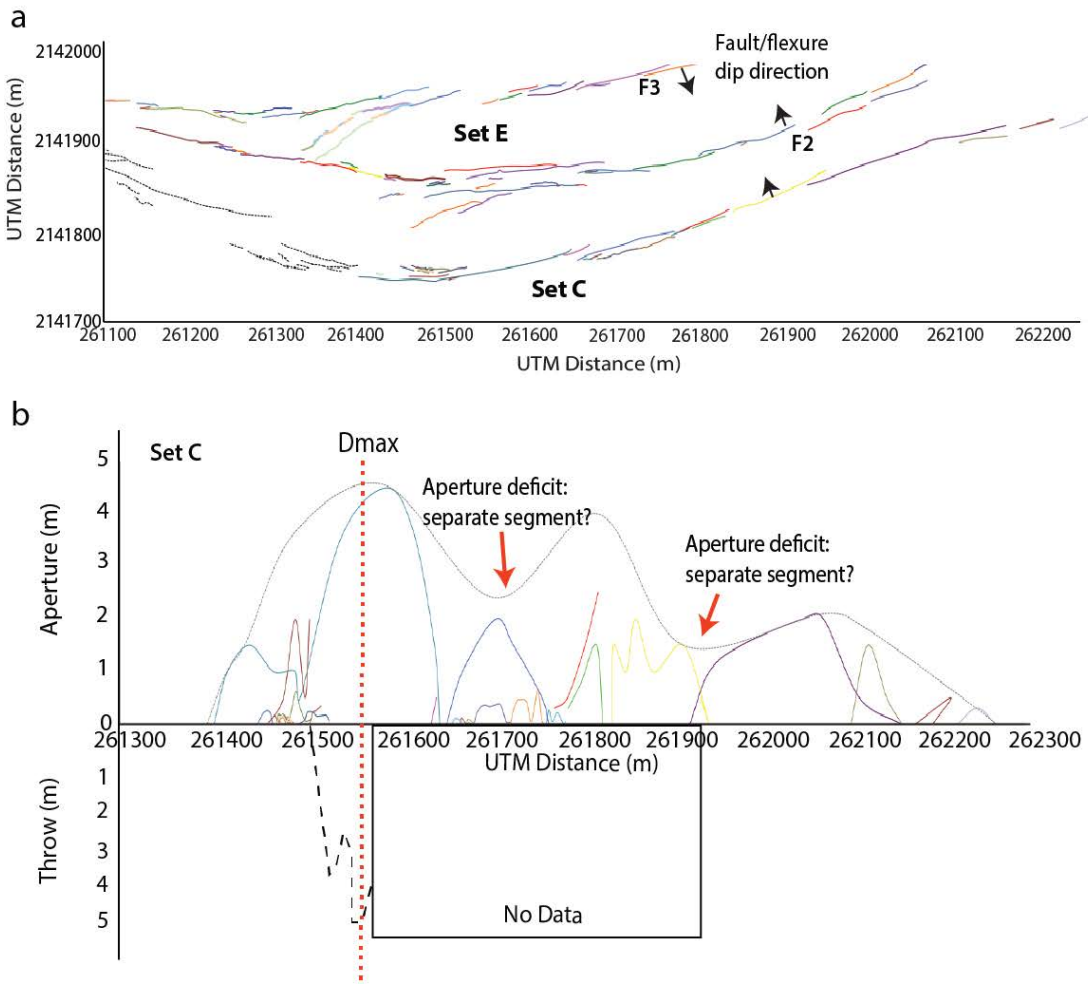

Figure 4.16. (a) Distribution of fractures in set C. b) Displacement-length profiles for extension fractures in set C. A total displacement profile (dotted, grey line) is strongly asymmetric, with the steepest gradient towards the western tip, close to the junction with set B.

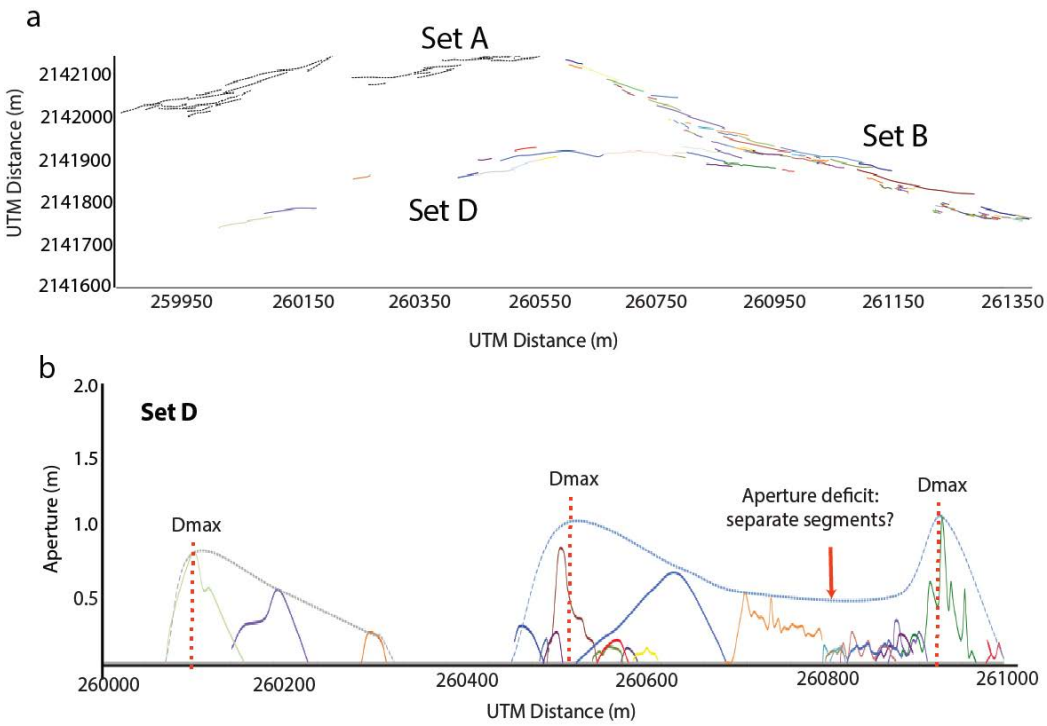

Figure 4.17. (a) Distribution of fractures in set D. b) Displacement-length profiles for extension fractures in set D. Total displacement profiles (dotted, grey line) are strongly asymmetric.

SET D: Fractures of set D show the smallest apertures and lengths in the dataset (Figure 4.17), and unlike the other sets, are not associated with any surface flexure. Displacement-length profiles show dominantly asymmetrical profiles with a maximum located halfway along the array. Set D may represent an along-strike continuation of F1 and F2 of set E (see Figure 4.18), implying the propagation of a new rift-parallel fault that cuts set B.

SET E: Extension fractures form two separate linear arrays, associated with two fault structures: F1 and F2 that are separated by 50 m and dip in opposite directions, forming a small graben (Figure 4.18a). Three segments of surface-breaking fault are identified along F1 (Figure 4.18b), although it is not possible to trace this further east due to a gap in the aerial LiDAR dataset. Fault segments are located approximately mid-way along the inferred trace of the structure and coincide with the maximum apertures for fractures.

Fracture apertures decrease towards the oblique (ESE) fracture trend of set B. Fractures that form the surface trace of F2 show smaller apertures than those of F1 (<2 m for F2 fractures and up to 4 m for fractures of F1) but the total displacement profile exhibits three points of displacement deficits, implying the fault is comprised of approximately four components (Figure 4.18c).

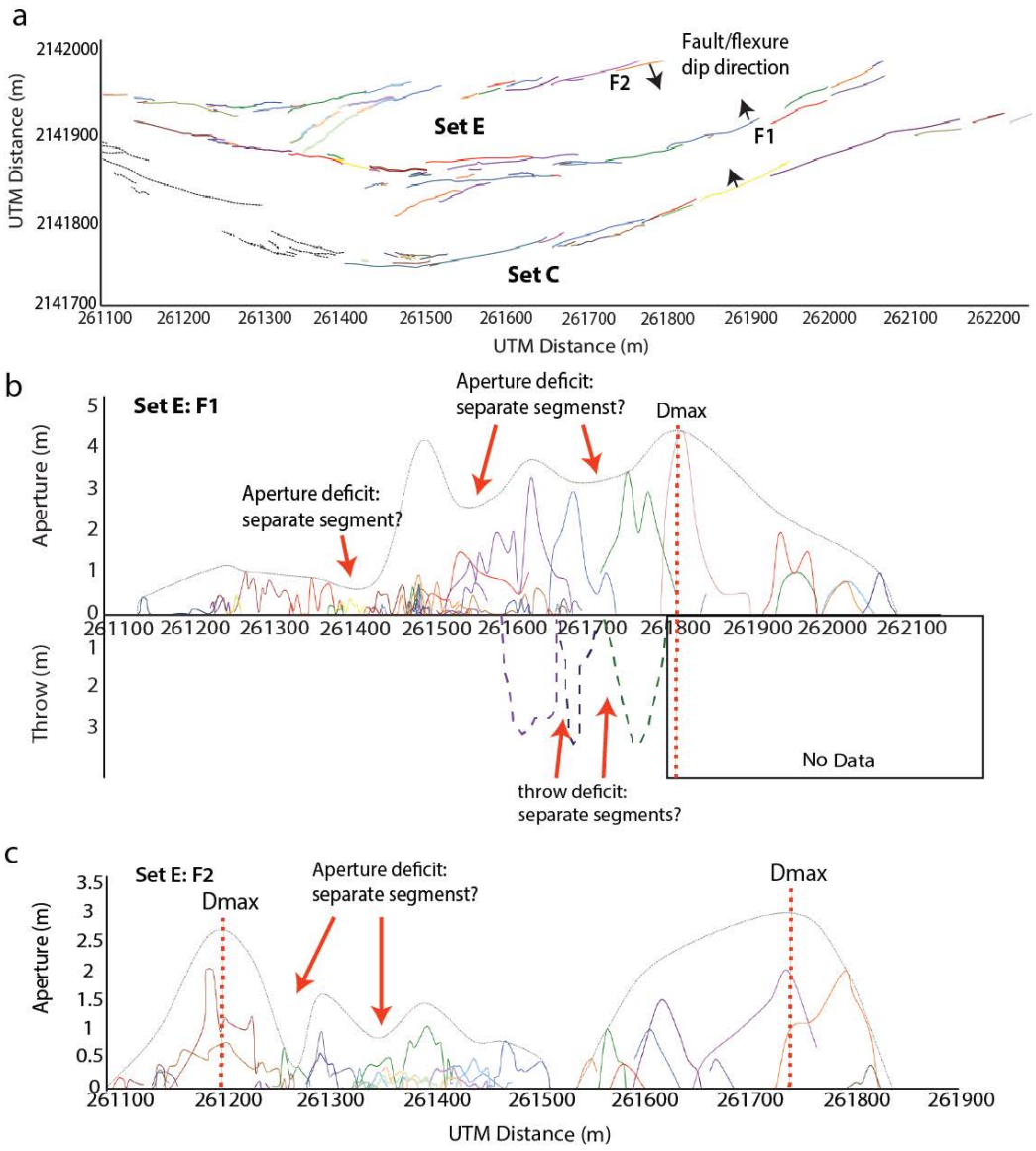

Figure 4.18. (a) Distribution of fractures in set E. b) A combined throw-aperture-length profile for fault segment F2. c) A combined throw-aperture-length profile for fault segment F3. Points of maximum fracture aperture also correspond to the locations of surface-breaking fault segments. Arrows indicate the dip-direction of faults or flexed ground surface (a proxy for fault dip direction at depth).

4.4.1.3 Fracture Interaction

To attempt to define the relative role of fracture interaction within the AOI, displacement gradients are quantified here using a value of asymmetry that is normalised to fracture length. This allows direct comparison of fractures across the fault system, and identification of the amount of displacement asymmetry and thus, the relative degree of tip restriction effecting individual fractures. The method assumes that an isolated fracture that is unrestricted by free surfaces will propagate with an elliptical tip line, to produce a symmetric displacement gradient through its centre. Displacements that do not show a centralised displacement (aperture) maximum (D_{max}) can be described as asymmetric, and the amount of asymmetry can be defined as the displacement asymmetry: values approaching 0 indicate a symmetrical profile and values approaching 1/-1 indicate an asymmetrical profile. The distance from each fracture tip to the point of maximum displacement (D_{max}) is measured to find how far from either tip D_{max} is located (Figure 4.19a). The proximity of this point to either tip is taken to reflect inhibited propagation in that direction. Negative or positive values indicate the direction (Figure 4.19b) of the steepest displacement gradient, which reflects the direction and magnitude of interaction and tip restriction (to the left or right of D_{max}).

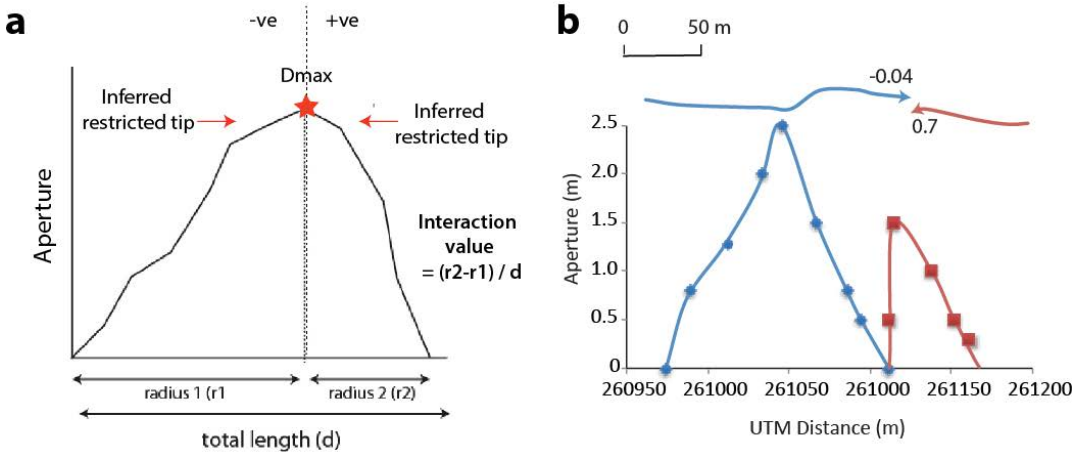

Figure 4.19. The method used to estimate the amount of interaction experienced by individual fractures. The distance from each extension fracture tip to the point of maximum aperture is measured, this value is then normalised by extension fracture length (a). An example of two en echelon extension fractures: the blue fracture shows a low interaction value (0.04) and a symmetrical displacement-length profile, while the red fracture shows a higher value (0.7) and a steeper, asymmetrical aperture-length profile. Maxima located to the left of centre will give negative values, and positive for maxima to the right of centre.

For instance, a negative value of 0.2 has the same magnitude as a positive 0.2 but reflects an opposite polarity of interaction. Of the extension fractures within the AOI, 65% show steep displacement gradients and asymmetry values that are greater than 0.2; examples of symmetrical (or near-symmetrical) displacement profiles with values approaching zero (values of 0-0.2), account for approximately 35% of the dataset.

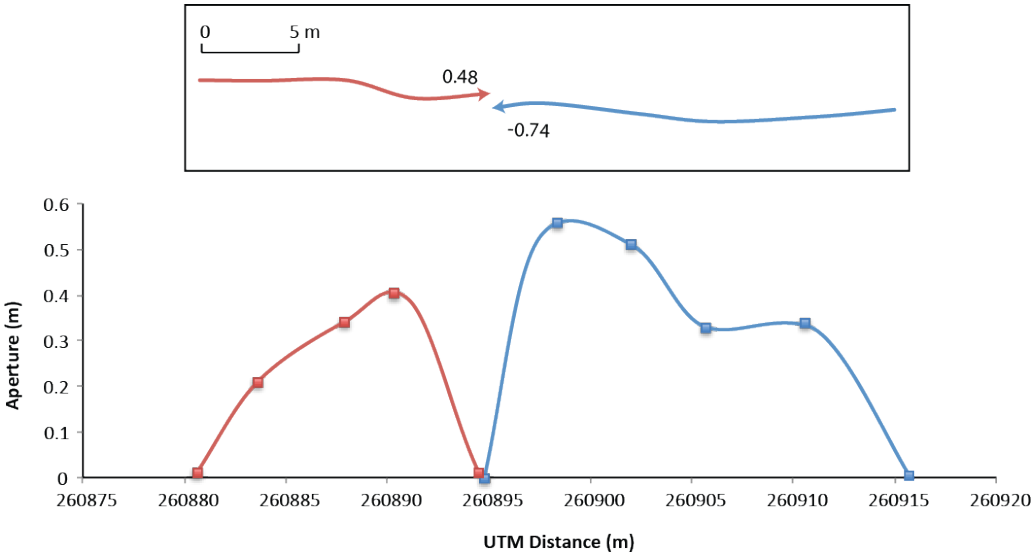

Figure 4.20. Displacement -length graph for two en echelon extension fractures in the AOI demonstrating profile asymmetry, and therefore lateral tip restriction and continued extension. Measurements for the blue fracture produce a higher relative displacement gradient than the shorter red fracture.

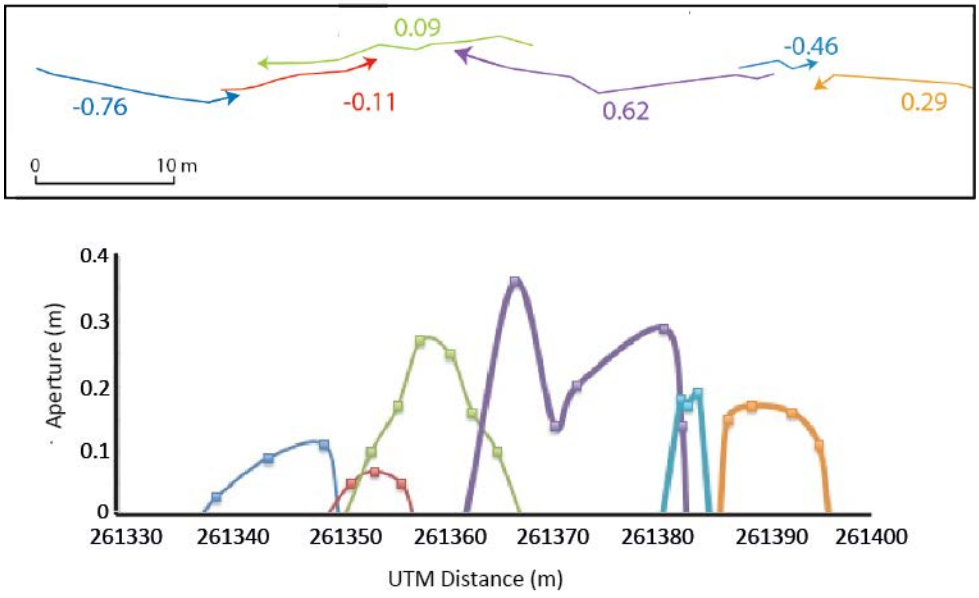

Figure 4.21. Example of pathways and asymmetry values of an array of fractures with a centrally located composite aperture maxima.

Asymmetric displacement-length profiles do not typically show equal values on opposing fractures, and in some instances larger fractures show greater interaction values than adjacent smaller fractures (Figure 4.20). It is also common for profiles to show symmetrical displacement gradients, with little evidence for increased displacement gradients at fracture tips, despite a close spatial proximity between neighbouring fractures (e.g the green fracture in Figure 4.21). In other examples, profiles demonstrate asymmetrical profiles despite relatively large distances to neighbouring fractures.

4.4.2 Surface Flexure

Sets of interacting, segmented extension fractures are most commonly associated with areas of surface flexure, the crests of which parallel the extension fracture trend (Figure 4.22). These flexures are generally low-amplitude folds that are commonly heavily fractured. Existing models for fault propagation in the Koa'e predict the existence of "monoclinal" surface flexures above the tips of blind normal faults during the early stages of fault growth (e.g. Martel and Langley, 2006). Field mapping, however, suggests that this model may not account for all instances.

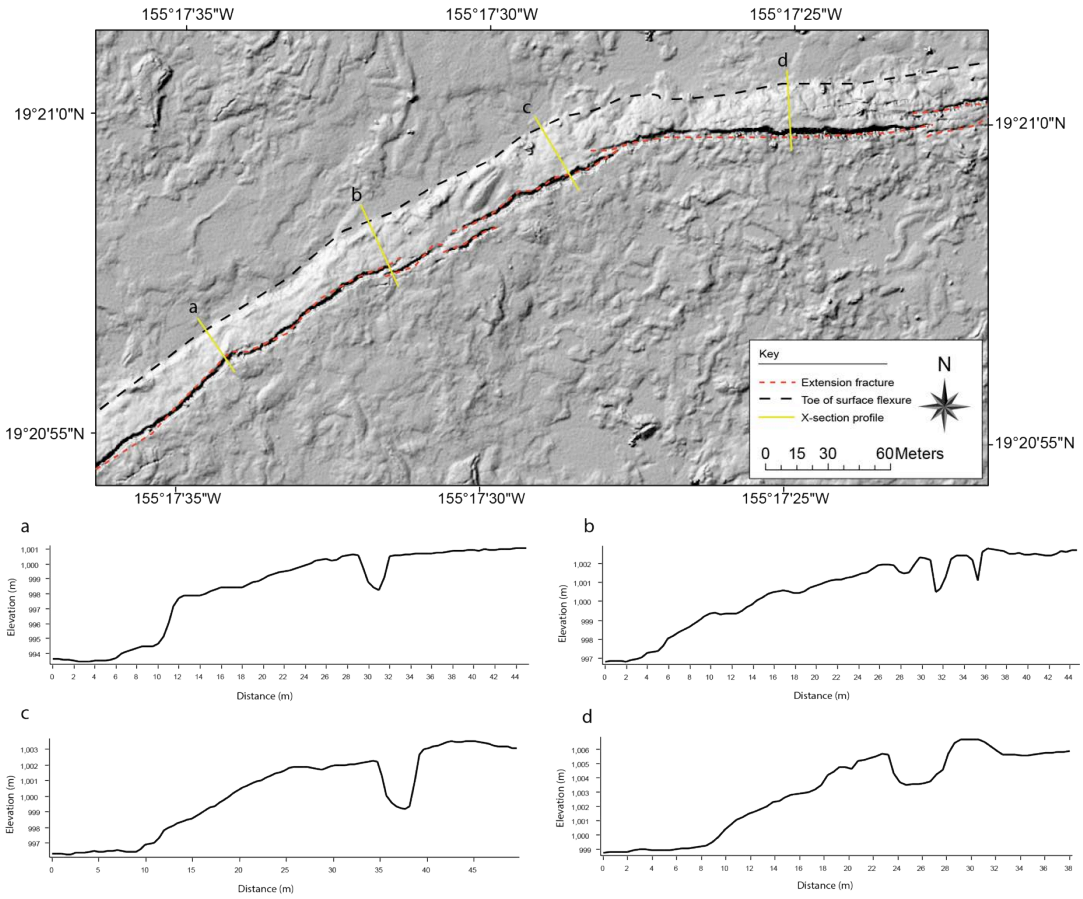

Figure 4.22. Aerial and cross-sectional view of a typical surface flexure in the Koa'e. The longitudinal axis of the flexure follows the trend of extension fractures, and presumably, an underlying fault. LiDAR-derived cross-sections show that flexures are gently dipping with amplitudes here of 6-10 m and wavelengths of a few tens of metres.

Surface flexures in the Koa'e may be split into two types based on their spatial extent and associated fracture density:

1) **Laterally continuous flexure** (Figure 4.22 and 4.23): In western and central-western areas of the Koa'e, gently dipping flexures that parallel the trend of inferred fault traces and extension fracture networks are observed as continuous structures for distances of up to ~3 km. Flexures of this type are rarely breached and show amplitudes of up to ~10-12 m, comparable to throw values for surface-breaking fault segments.

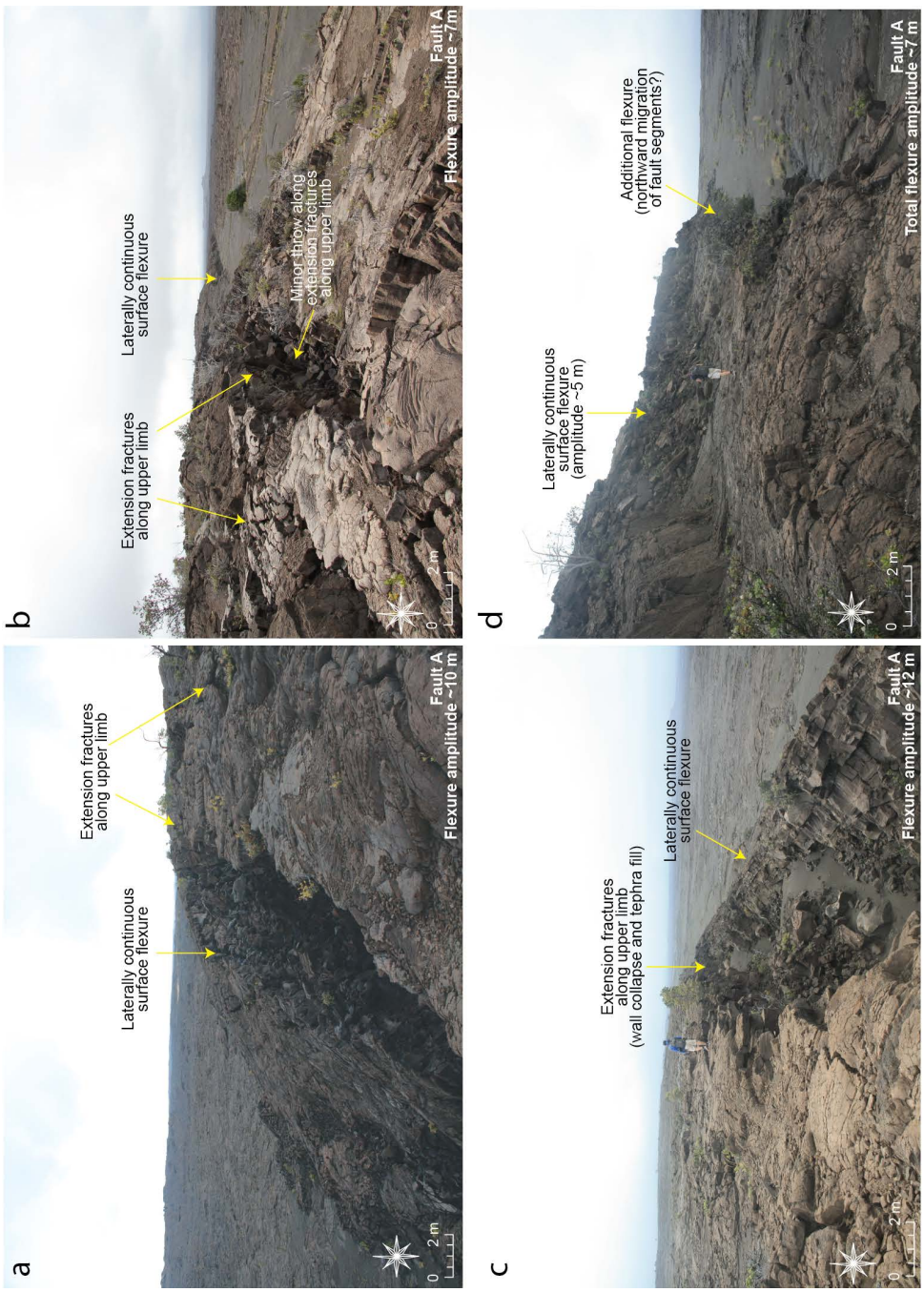

Figure 4.23. Examples of laterally continuous surface flexures. a) Flexures dip gently and vary from a 2 m to ~ 10 m in amplitude. (b) Laterally continuous traces for over 1 km, and commonly, steep and rubbly toes. (c) Extension fractures often show extensive wall collapse (here buried in recent tephra from Kilauea Volcano) and show the appearance of a breached monocline. (d) Forward migration of flexures is apparent on one fault in the fault system, with uplift of ~15 m accommodated by two flexed structures that are stacked on top of each other.

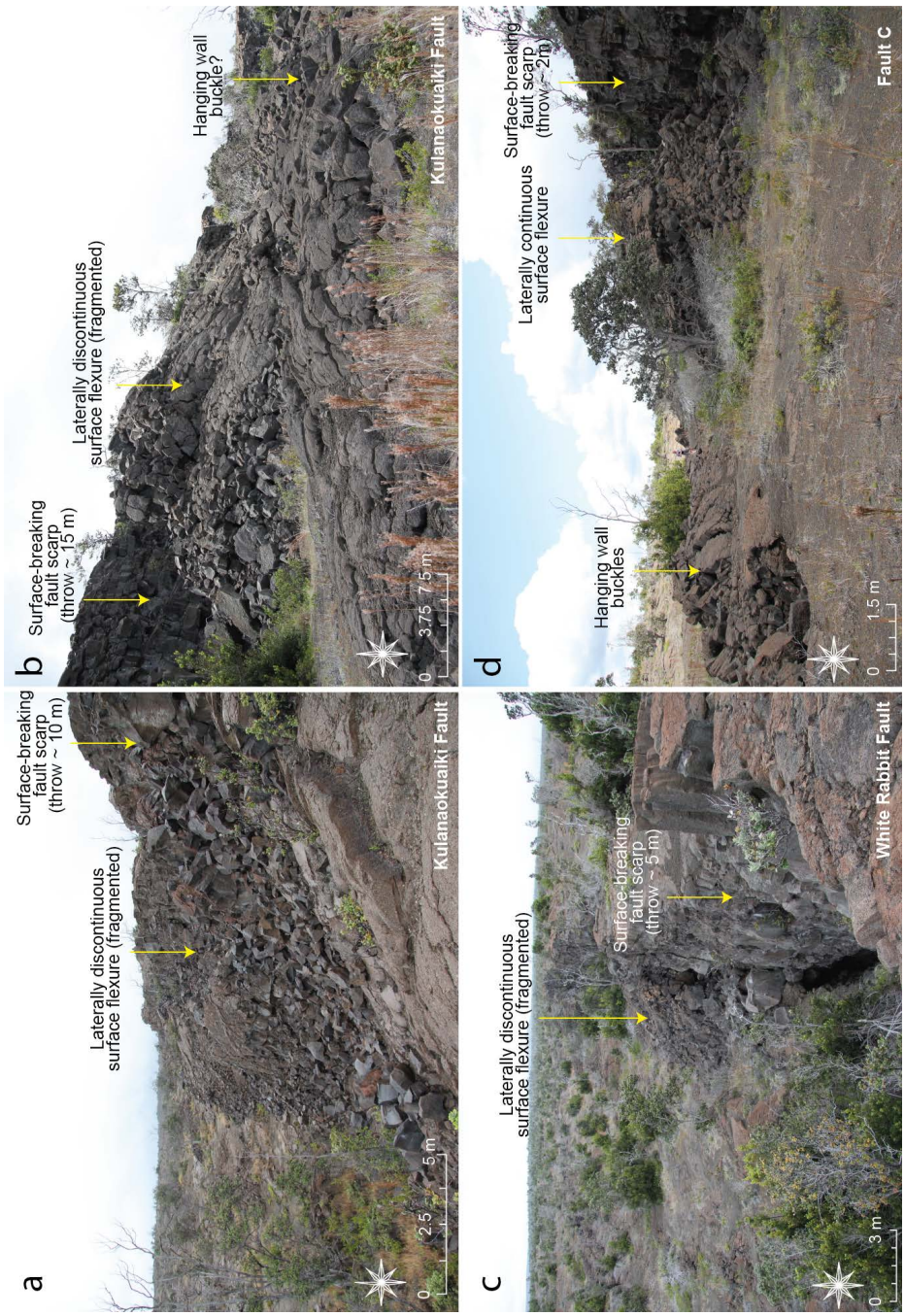

Figure 4.24. Examples of laterally discontinuous surface flexures. a) Flexures form densely fractured, often disintegrated blocks in the hanging wall of faults. b) Lengths vary from 10 m to 70 m and amplitudes from 2 m to 15 m (image shows ~12 m vertical offset). c) Areas of discontinuous flexure are separated by co-linear surface-breaking fault segments and match the vertical offset of adjacent surface-breaking fault segments. d) Planar hanging wall and footwall surfaces are offset (here, by ~ 2.5 m) across discontinuous sections of fractured and rotated hanging wall and normal fault segments.

Extension fracture sets are occasionally located along the crest of the limbs of the flexures, where outer arc extension may contribute to their opening. Elsewhere, however, zones of extension fracturing occurs without any evidence for surface flexure (e.g. set D or the eastern lateral tip of fault C), which implies that additional arc-tension is a local effect rather than a driving process behind extension fracture growth.

2) **Laterally discontinuous flexure** (Figure 4.24): In eastern and central-eastern areas of the Koa'e fault system (e.g. the Kulanaokuaiki fault in the eastern Koa'e) we observe discontinuous, highly fractured or disintegrated hanging wall blocks that are located between co-linear or partially overlapping, surface-breaking normal fault segments with throws of 10-15 m. These isolated blocks demonstrate limited lateral extents (30 m to ~150 m) with very steeply dipping surfaces.

The mapped flexures (or rotations) are never breached by faults, despite being parallel to the trend of adjacent fault segments (Figure 4.25); instead they match the vertical offset on either side and form isolated blocks, connected to the fault segments by co-linear extension fractures, at various points along some main fault traces. Their limited lateral extent, fragmented appearance and steep dip give the appearance of a rotation rather than a fault-propagation fold. Such rotational features have been predicted in analogue models of fault propagation in brittle sequences (Holland et al., 2006; Michie et al., 2014).

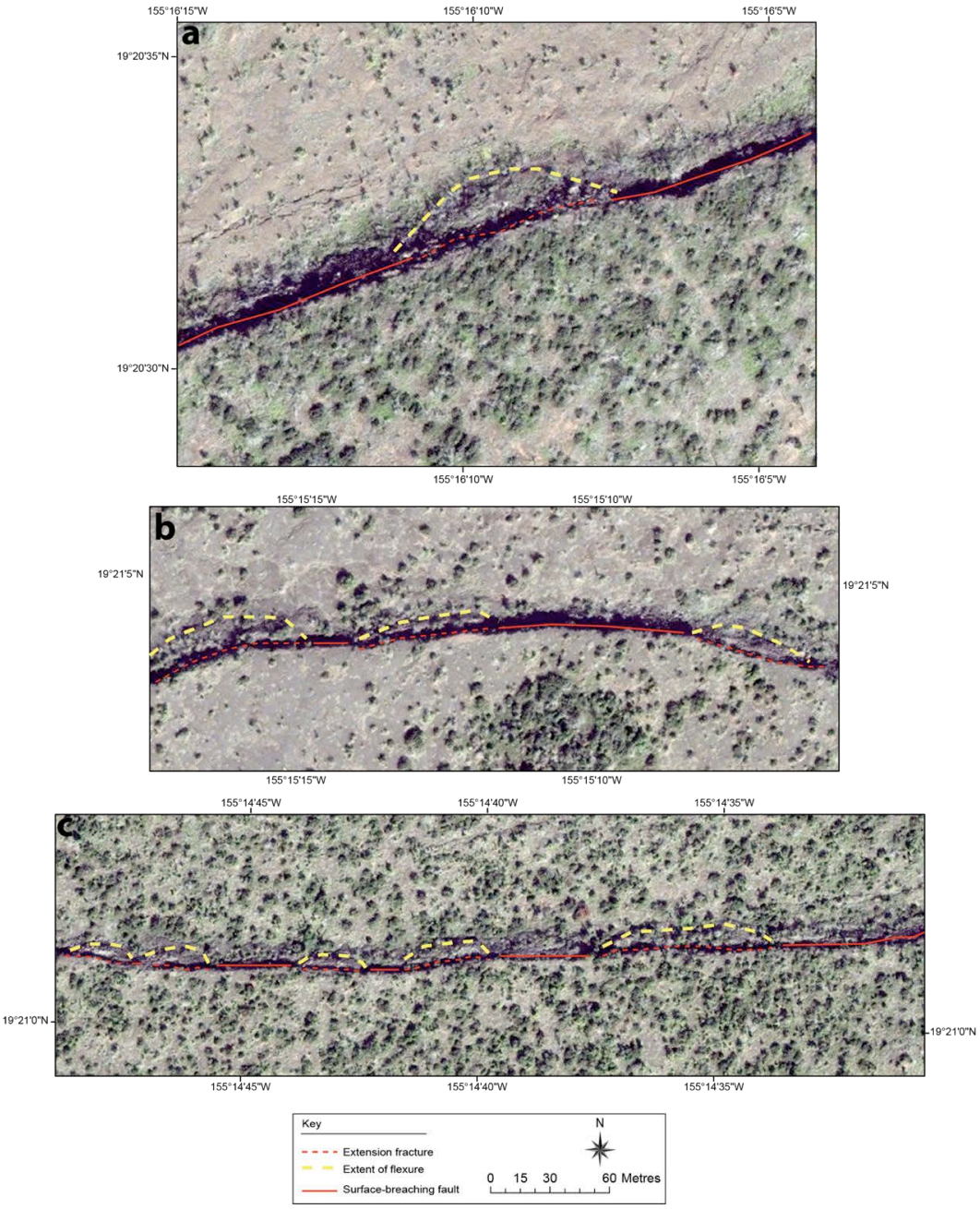

Figure 4.25. Map view of discontinuous surface flexures along a major fault in the Koa'e fault system. In all three examples, we identify a series of fractured hanging wall blocks (dotted, yellow lines) that appear to be isolated between segments of surface-breaching normal faults (heavy red line). None of the blocks are breached by faults.

Areas of continuous flexure are characteristic of the central-western and western portions of the fault system where magmatic activity is known to be low (e.g. Holcombe, 1987;

Moore and Trusdell, 1993). Elsewhere discontinuous surface flexure and surface-breaching faults are observed in the magmatically more active eastern Koa'e. Magmatism at depth may therefore have a strong influence on strain rates and the propagation of faults in the Koa'e fault system.

4.4.3 Fault Geometry and Distribution

Faults form parallel arrays of N to NNW dipping, sub-vertical strands that follow the ENE (080^{o}) trend of the east rift zone and comprise approximately 20% of inferred fault traces in the Koa'e fault system. Fault scarps form discontinuous segments of inferred fault traces in eastern and central-eastern portions of the fault system. In addition to a vertical component of displacement, all surface-breaching fault segments demonstrate significant horizontal openings along composite extension fracture traces up to 200 m in length (Figure 4.25). Faults scarps have not lost their inherited joint surface irregularities and we find no evidence for slickenlines or slickensides on fracture surfaces to indicate initial shear displacement, agreeing with previous authors that *surface* faulting in the Koa'e develops through linkage with early forming extension fractures that have reactivated joints at the free surface (e.g. Peacock and Parfitt, 2002; Holland et al., 2006). Where present, fault scarps offset planar footwall and hanging wall ground surfaces by up to ~20 m and do not breach areas of surface flexure, contrary to the expectations of previous studies of fault propagation in basaltic sequences, which argue that they are precursors (e.g. Grant and Kattenhorn, 2004; Martel and Langley, 2006).

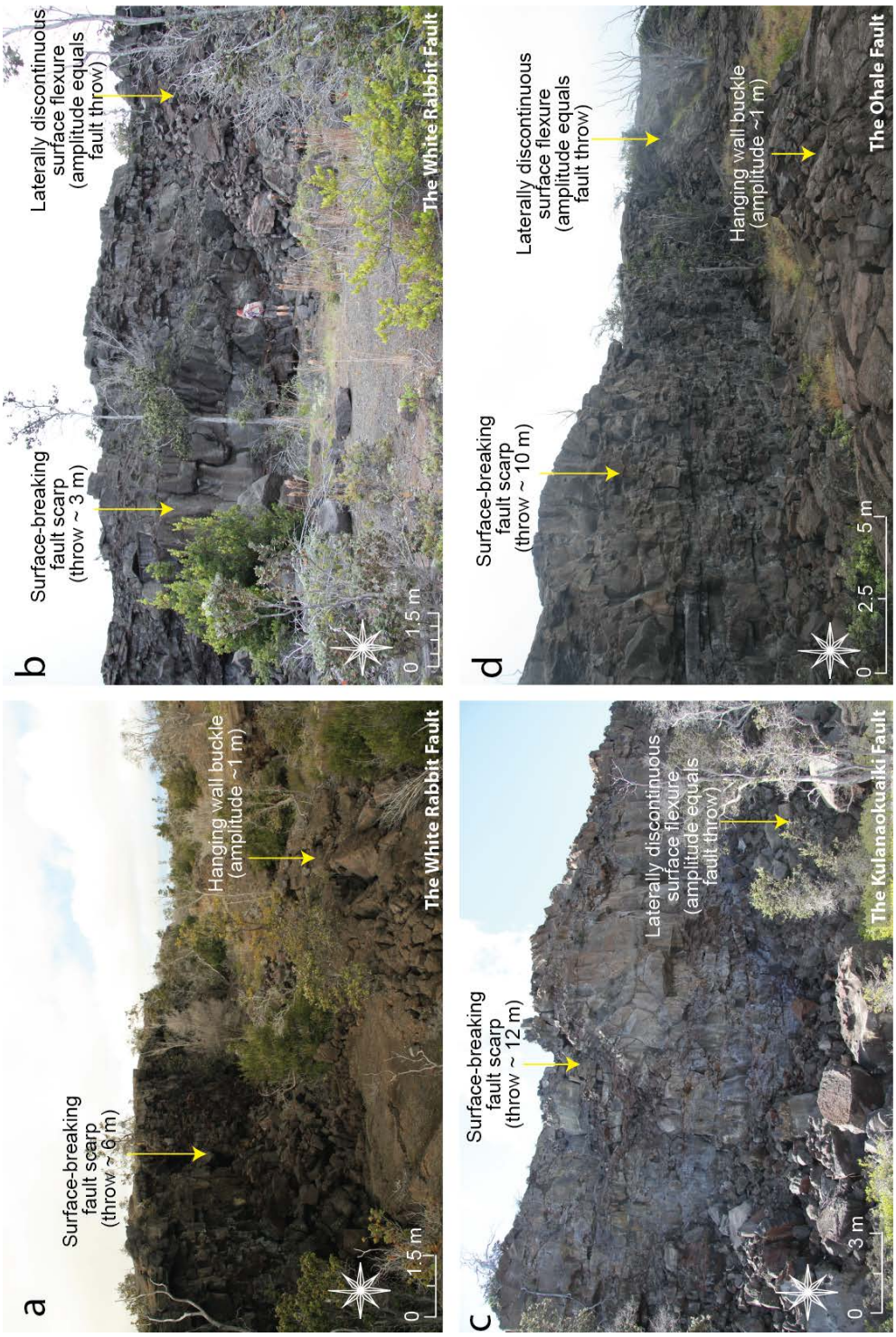

Figure 4.26. Examples of surface-breaching fault segments along three fault traces in the Koa'e fault system. a-b) The White Rabbit fault. c) The Kulanaokuaiki fault (see Figure 4.35 for locations). d) The Ohale Fault. All scarps show a significant component of horizontal opening and offset planar footwall and hanging wall ground surfaces. The largest vertical offsets (up to ~15m) and greatest proportion of breaching fault segments are found on the Kulanaokuaiki ("Shaking Spine") fault.

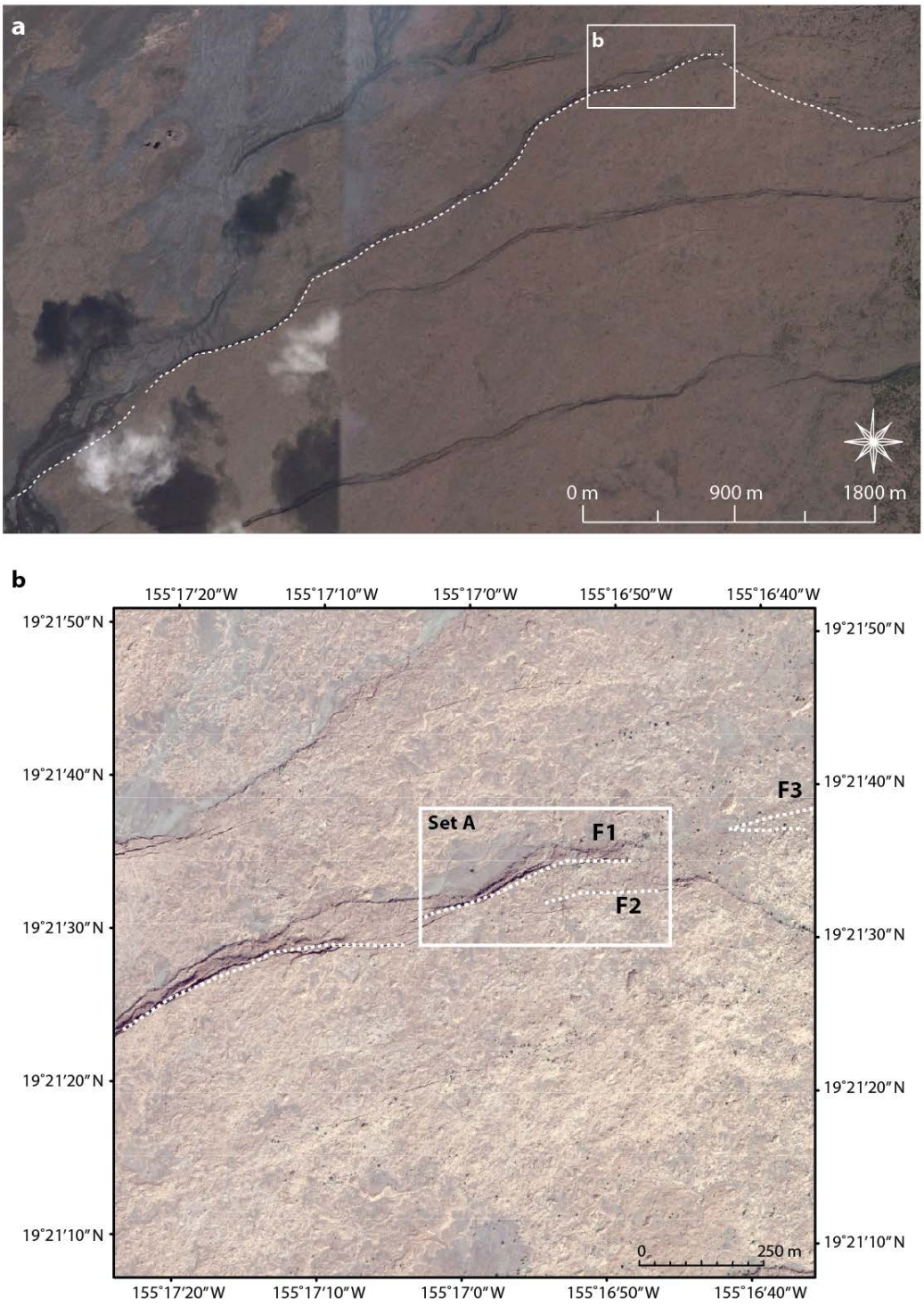

Figure 4.27. a) WorldView satellite image of the full extent of Fault A. The total length of this structure is ~5 km. The map traces is characterised by numerous steps or bends, which are interpreted to represent individual segments that initiated in isolated but linked to form the composite fault structure. b) Analysis in this chapter focuses on the eastern-most segment of this fault (which comprises 3 segments: F1, F2 and F3).

Fault A: The total trace length of this fault is ~5 km and forms the eastern most segment of a 5.3 km long fault (Figure 4.27)a. In map view, this structure has a sinuous appearance, suggesting it comprises 5-6 north-dipping segments and a continuous surface flexure, of up to 10 m in amplitude, is also present for much of its composite length. The tip area of the eastern most fault segment is considered here (Figure 4.27b). F1 represents the primary fault and F2 and F3 are likely to be splays from this structure that have not yet breached the surface (Figure 4.28a). Despite hosting the largest extension fracture apertures (5-7 m) and flexure heights (~10 m) in the fault system (Figure 4.28b and Figure 4.30a), only 3 segments of surface-breaking faults are observed. Extensional strain on this structure appears to be accommodated at the surface by gaping fissures and flexure.

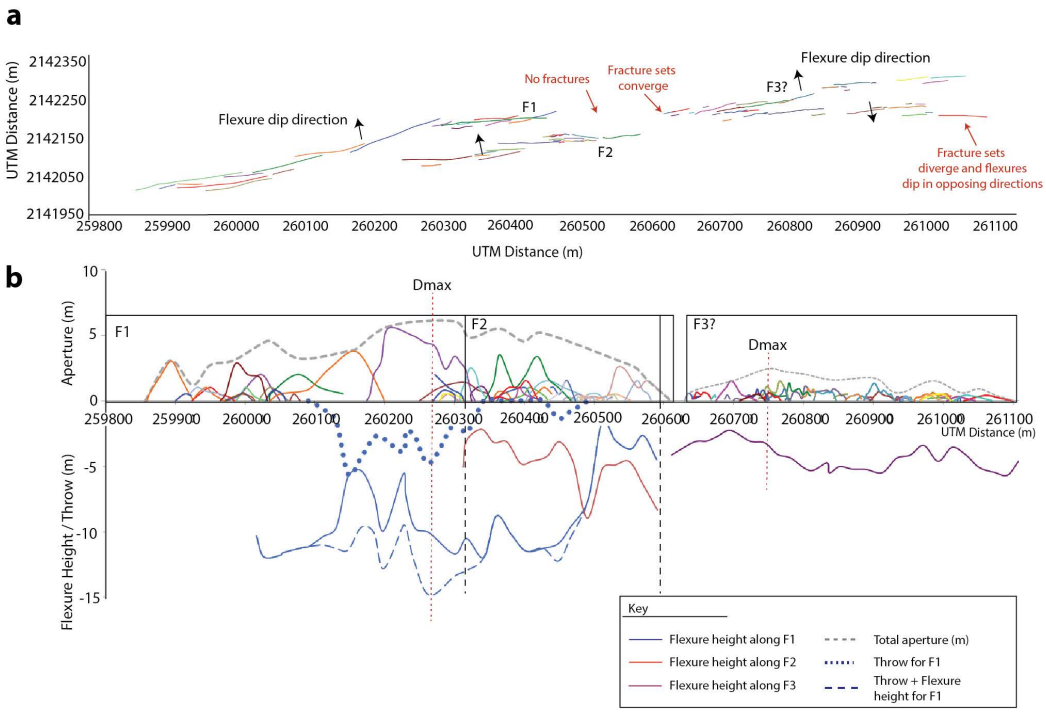

Figure 4.28. a) Distribution of **e**xtension fractures that form set A. b) Associated profiles of displacement-length, flexure height and fault throw (b). Fault A may be separated into 3 north-dipping segments. Fractures of F1 have the largest apertures in the AOI and are associated with the greatest surface flexure (up to ~10m). Despite large apertures, only small sections of surface-breaking faults are present, towards the eastern tip. Fractures of F2 and F3 may represent a splays of the primary fault (F1), but have not yet breached the surface.

Fault C: This fault is expressed principally as a network of ENE-WSW trending interacting (based on the shape of their displacement-length profiles) extension fractures and a broad area of surface flexure that parallels the fracture trend, and presumably, the trend of the fault tipline at depth. This flexure and network of extension fractures accounts for ~90 % of the total inferred trace length (Figure 4.29a, b), with the remaining 10% characterised by throw across a subvertical, surface-breaking fault segment (Figure 4.29b, c). This segment of surface-breaking fault is located at the western tip of the inferred trace of fault C, close to where it meets the oblique 110° set of fractures (fault B). Here, the ground surface is offset by 2-3 m with no evidence for surface flexure (Figure 4.30b).

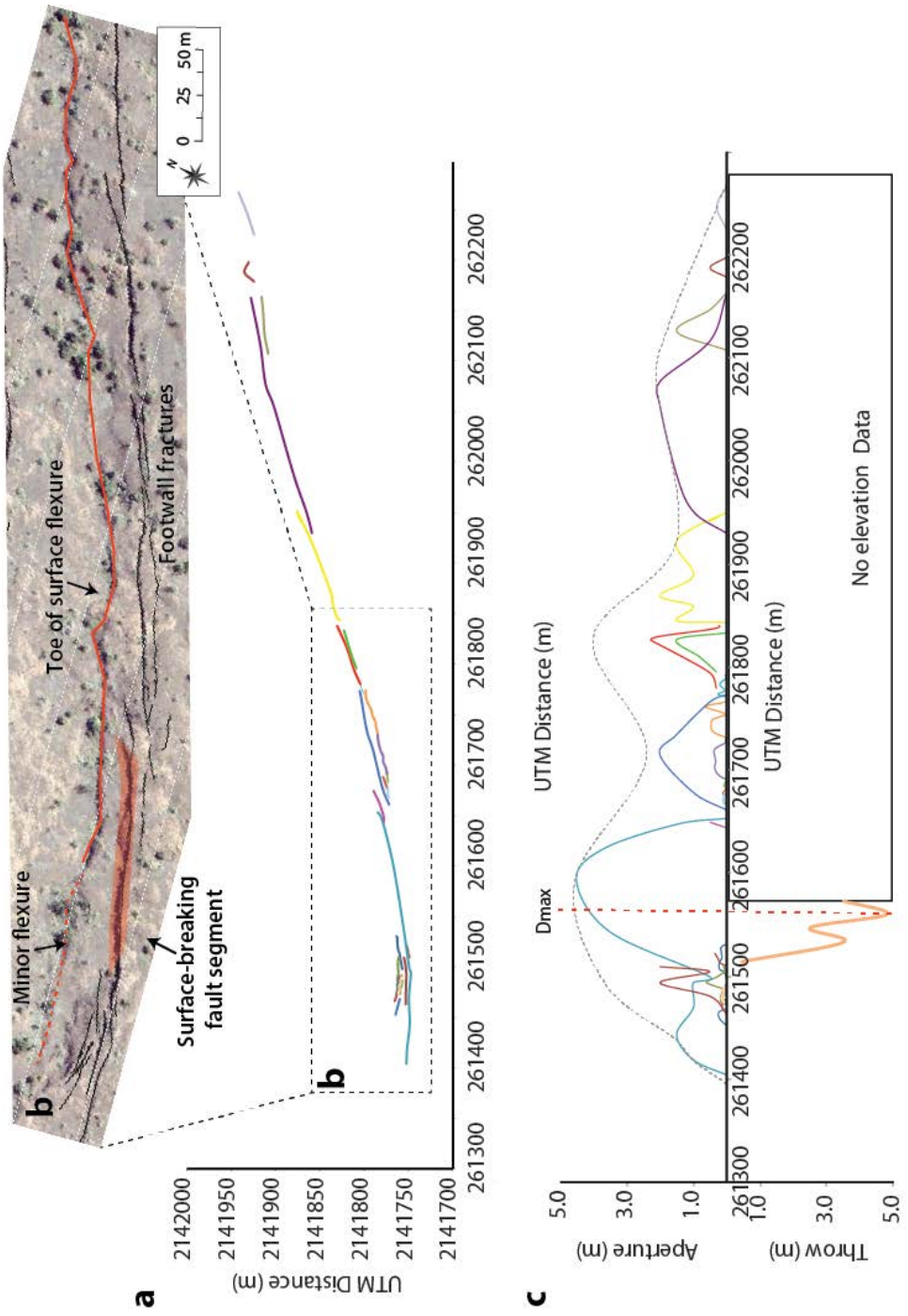

Figure 4.29. a) Distribution of extension fractures that form set C. b) WorldView satellite view of inset box shown, which highlights visible topographic features. c) Profiles of displacement-length for extension fractures of set C showing location and magnitude of fault throw. At the western tip of Fault C is a surface-breaking fault segment, coinciding with the widest fracture apertures in the set. There is no elevation data for this area due to a gap in the LiDAR dataset that follows this fault.

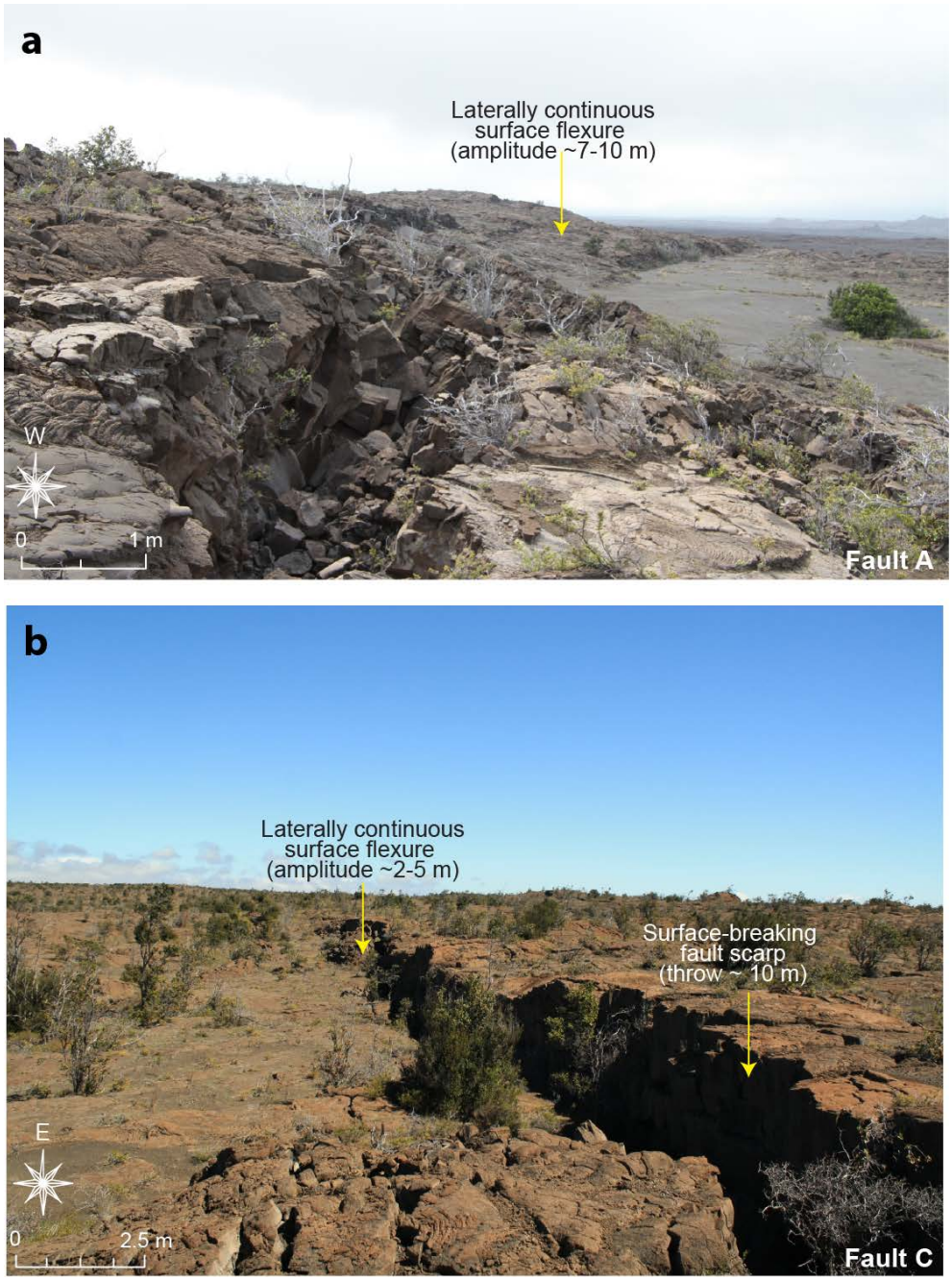

Figure 4.30. Characteristic views of the relay bounding faults in the AOI. (a) Fault A is characterised by en echelon extension fractures and surface flexure for much of it's 5 km length. Small sections of surface breaking fault segments exist near the eastern tip. (b) The total inferred trace of fault C is characterised by ~1 km of laterally continuous surface flexure and en echelon extension fractures with apertures <2 m. The westernmost 80-90 m features two segments of surface breaking fault with up to 2 m of throw. The displacement at this tip drops to zero near to the intersection with the fractures of fault B (see Figure 4.29c).

Eastward from the surface-breaking tip of fault C, footwall and hanging wall surfaces are offset across a laterally continuous surface flexure (Figure 4.29). The distribution of extensional strains along this structure may be evidence for higher elastic strains and lateral inhibition at this tip. The ENE-WSW fracture trend associated with fault C, curves gently into the 110° trend (set B), which may imply the continued propagation of this tip into the ramp, eventually producing a through-going fault with a bend in the trace that trends 110°. However, this is incompatible with the displacement deficit present in the aperture-length profile for fractures at the southern tip of fault B. Alternatively, the steep gradient of fault C, demonstrated by a fault throw of ~2m that decreases to zero over a distance of 70 m (Figure 4.29c), may represent the restricted tip of this fault and a separate fault is developing in the zone between.

Estimating the combined influence of continuous and discontinuous strains, i.e. horizontal and vertical components, is challenging. The uneven terrain, and 0.5 m resolution elevation data makes accurate measurement of the continuous component of strain in the AOI very difficult. In general, we find the greatest flexure heights (or throw, where present) alongside the widest fractures, and presumably the greatest fault slip at depth. Consideration of surface flexure for faults A and B could smooth the displacement deficit evident in the fracture apertures at the northern end of set B, but it does not smooth the profile between sets B and C.

4.5 Discussion

Existing models of upward propagating fault growth in basaltic sequences (e.g. Iceland and Hawai'i), which are commonly are based on 2D analytical solutions (e.g. Grant and Kattenhorn, 2004; Martel and Langley, 2006) use the governing equations of linear elastic fracture mechanics for isotropic rocks under isotropic loading. These models treat the

host volume as a linear elastic, isotropic, isothermal, semi-infinite continuum and faults are modelled as isolated, planar and frictionless structures that are infinite in their lateral dimensions (e.g. Grant and Kattenhorn, 2004; Martel and Langley, 2006; Kaven and Martel, 2007; Abe et al., 2011). Faults are represented by a series of discrete triangular elements and slip is induced by applying a shear stress to these elements. Analysis of the displacements and resulting stress field surrounding the isolated fault is then used to predict surface flexures and the location, and kinematics of fractures. Modelling of faults as upward propagating discrete planes (with fixed dimensions) in this way have been able to produce some of the features the above authors have observed in the field, including footwall fractures and monoclinal flexure (e.g. Kaven and Martel, 2007).

Scaled analogue models have also been used to reproduce near-surface faulting in basalts using hemihydrate powder with a finite and measured tensile strength (Holland et al., 2006, 2011). The models use a symmetrical graben system with a rigid central block that lowers during the experiment to produce isolated, pre-existing blind normal faults that dip at ~60° with fixed lateral dimensions. The experiments replicate many of the features observed in the field, including initial development of vertical extension fractures at the surface and rotated, disintegrated hanging wall blocks. However, although they are good approximations for the processes responsible for fault growth in cohesive sequence and local stress distributions they cannot reproduce natural conditions; i.e. the deforming material is mechanically homogenous, and temporally and/or spatially variable applied stresses are not accounted for.

Based on existing published numerical simulations, analogue experiments and field observations, the development of normal faults in basaltic sequences is expected to follow a systematic growth path. However, such studies are unable to account for (1) the effects of a mechanically anisotropic sequence; (2) syn-tectonic, cyclic and heterogeneous volume change; or (3) local interaction-induced inelastic deformation. High resolution,

and extensive field mapping in the Koa'e fault system suggests that these models predict certain geometries, but do not reproduce the same natural variability visible in the field.

4.5.1 Segmentation and Interaction in the Koa'e Fault System

Extension fractures in the Koa'e fault system may be separated into three types: (1) isolated, non-interacting; (2) interacting, segmented (apertures < 1.5 m); and (3) linked, composite fractures with apertures > 1.5 m. There are few instances of (1) isolated, single fractures; mapped fractures fall principally into the second category (>60%) and demonstrate asymmetric aperture profiles with high displacement gradients at their lateral tips, consistent with previous interpretations of high elastic strains, restricted propagation, and displacement transfer for normal faults (e.g. Childs et al., 1995; Huggins et al., 1995; Gupta et al., 1998; Gupta and Scholz, 2000; Hus et al., 2006). Based on the analysis of the distribution, geometry and displacement characteristics of extension fractures, surface flexures and normal fault segments in the study area, strain is interpreted to be transferred between faults A and C and the zone between them is therefore interpreted to be a *relay zone*. For geometrically and kinematically coherent fault arrays, continuous (ductile) and discontinuous (brittle) components of fault-related deformation are expected to show systematic geometries and strain accumulation from their initiation, which should be reflected in a symmetrical aggregate displacement profile throughout their evolution (e.g. Walsh et al., 2003, Long and Imber, 2010). Continuous rotation in the zone between sets A and C is broad (up to 6-7 m across an area 40-90 m wide) but does bridge the topography between the two bounding fault structures (see Figure 4.12 and section 4.4.2). Aperture-length profiles for the linking set of fractures (set B) show pronounced displacement deficits at their tips and maximum apertures are found on the northern bounding fault, not in the centre of the array. This may suggest that faults A and C grew in isolation and an evolving link is developing as a result of their interaction.

In addition to describing segmentation and linkage at multiple scales, this chapter also identifies a hitherto unnoticed spatial distribution of extensional strains in the Koa'e fault system. Extension in the eastern portion of the study area is expressed dominantly as surface-breaking normal faults with throws of 5-10 m, whereas the western portion features networks of interacting extension fractures and surface flexures with amplitudes of up to ~10 m. The pattern of deformation implies that total strains are comparable across the fault system, but strain rates may vary: high rates in the east facilitate fault segment linkage, and lower rates in the west prevent through-going fault development. Instead, segments slip slowly at depth and irregular lava lobes slide and fold rather than fracture ahead of the tip line.

4.5.1.1 Evidence for Segmentation and Interaction: Path Geometry

Evidence for extension fracture and fault segment interaction is observed at a range of scales based on: (1) the geometry of observed fracture and fault traces, at their individual length scale; (2) the shape of aperture-length profiles and; (3) the magnitude of displacement asymmetry in aperture-length profiles.

It has been shown that an isolated tensile crack will propagate in the direction perpendicular to the orientation of minimum compressive stress. However, at the tips of overlapping fractures, mechanical interaction of their opposing stress fields leads to: (1) locally increased stress intensity factors, which promotes local cracking by lowering the required crack extension force for propagation; and (2) the local reorientation of the minimum compressive stress (Pollard et al., 1982; Olson and Pollard, 1989; Engelder, 1993). Fracture tips follow these modified trajectories, controlled by the distribution of tensile stress, producing the characteristic hook-shaped fracture pathway (Gudmundsson et al., 1993; Acocella et al., 2000). Examination of the geometry of propagation pathways

can therefore provide a first order interpretation of the *in situ* stress responsible for extension fracture development and of their relative timings.

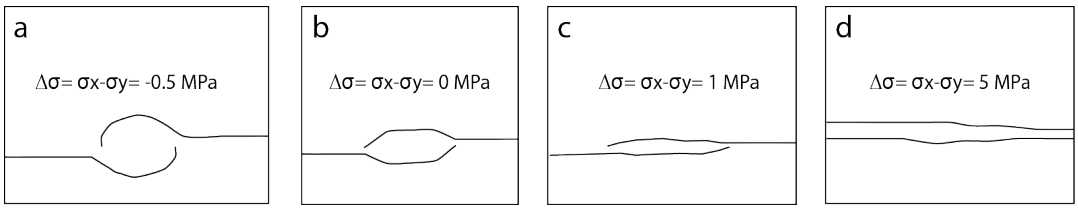

Figure 4.31. Theoretical fracture propagation pathways (adapted from Engelder, 1993 and based on Olson and Pollard, 1989). The amount of curvature is thought to be controlled by the remote differential stress magnitude and the surface roughness: a) crack-parallel remote stress (σy) is less than the crack-normal remote stress (σx). b) Crack-parallel and crack-normal remote stresses are equal. c) Crack-parallel remote stress is greater than the crack-normal remote stress. d) Crack-parallel remote stress is much greater than the crack-normal remote stress.

Curving paths may suggest the predominance of local, interaction-induced stress concentrations over remote stresses during propagation, whereas straight pathways suggest that remote stresses exert a greater control (Pollard et al., 1982; Olson and Pollard, 1989; Thomas and Pollard, 1993; Engelder, 1993; Figure 4.31). Fractures in the Koa'e fault system display a range of crack pathways, reflecting a complex relationship between remotely applied stress and the local stress distributions surrounding the tips of en echelon fractures (Figure 4.32).

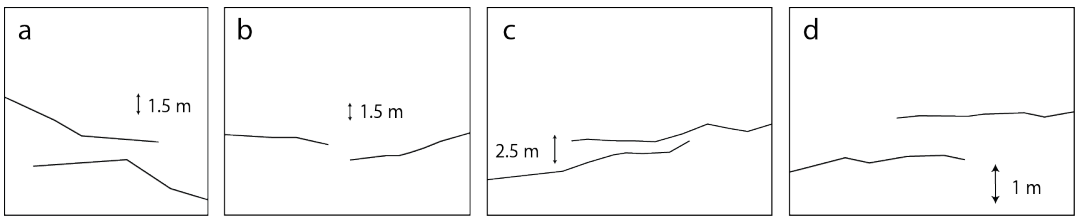

Figure 4.32. Example of fracture pathways from the Koa'e fault system. a) Mutually divergent, or possible future hook-shape. b) Mutually convergent where the convergence angle is variable

fracture to fracture. c) Convergence of one fracture with an existing fracture. d) Straight, overlapping reflecting the dominance of regional stress over local.

In the Koa'e fault system there are few examples of the classic hook-shaped fracture pathway, with crack-crack interactions resulting in fractures that exhibit dominantly straight (~60%) or convergent (~30%) fracture pathways. These path geometries are investigated at the length scale of individual extension fractures to observe the preferred propagation path of the entire extension fracture, rather than joint-scale irregularities. Convergence curvature on fractures in the Koa'e fault system is relatively broad, and commonly only on one fracture within a pair, implying separate stages of fracture propagation. Mutually convergent and divergent fracture pathways are interpreted to represent contemporaneous fracture growth (Figure 4.30a, b). Fractures demonstrating straight path geometries are interpreted to represent early-forming fractures that have propagated in isolation. Their presence will perturb the local stress field when new fractures initiate. These younger fractures curve towards the existing fracture during their propagation (Figure 4.32c), eventually abutting with the earlier fracture and forming a composite fracture with a bend along the trace. Adjacent fractures exhibiting straight pathways may imply that local stress intensity factors were not great enough to overcome the remote stress field (Figure 4.32d). En echelon fractures demonstrate propagation along modified trajectories that are oriented obliquely to the regional extension; kinematics of these fractures are consistently open-mode, regardless of the degree of obliquity. The range of fracture pathways, developing contemporaneously, under the same remote stress regime demonstrates the heterogeneity of stress fields surrounding the tips of en echelon fractures.

4.5.1.2 Evidence for Segmentation and Interaction: D-L Profiles

D-L profiles for composite, aggregate extension fractures show the greatest lengths and apertures in the Koa'e fault system. Examples of kinematically coherent fractures are expected to show symmetric displacement profiles throughout their evolution, with a displacement profile that resembles that of an isolated fault, despite comprising multiple linked segments (e.g. Gupta and Scholz, 2000; Walsh et al., 2003). The profiles presented in this chapter for both individual fractures and arrays of fractures do not exhibit this relationship. Instead displacement profiles show multiple points of displacement minima, which represent former linkage sites of previously en echelon or co-linear single fractures, and the displacement maxima is commonly off-centre (Figure 4.33). Results from this study indicate that fractures initiate as isolated, segmented structures that interact when they approach one another, growing progressively through segment linkage to produce composite fractures (e.g. Peacock and Sanderson, 1991; Gupta and Scholz, 2000).

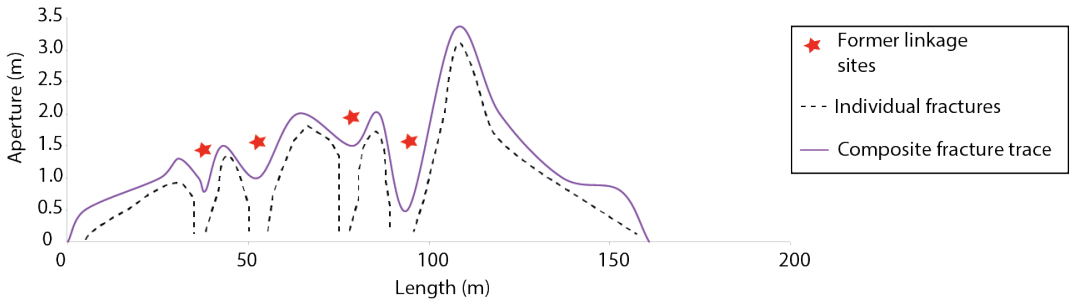

Figure 4.33. An example of a ~150 m long extension fracture showing multiple points of displacement minima and maxima. The purple line represents the composite, mapped fracture trace with aperture minima highlighted by red stars. The black dotted lines represent the locations of inferred former single fractures that interacted and linked to form the composite trace.

Extension fractures that show symmetrical D-L profiles are interpreted as the earliest forming fully coalesced fractures in the fault system with later fractures showing

asymmetry polarities that are influenced by the earlier generation (e.g. Figure 4.34a). Similar degrees of asymmetry on adjacent fractures may indicate that propagation of both tips is mutually inhibited and that the stress fields surrounding them are of equal magnitude. Centrally located displacement maxima and straight pathways on one fracture and asymmetrical displacement on a second, curved structure is interpreted as unencumbered growth of one fracture, followed by later impingement of the second fracture. However, on the whole, asymmetry values for en echelon fractures are highly variable, regardless of fracture size and stress distribution (interpreted based on the relative steepness of displacement gradients) does not appear to scale with fracture length; a shorter fracture can exert a greater inhibiting influence, resulting in a higher displacement gradient, on a longer fracture than vice versa (e.g. blue fracture, Figure 4.34b). The cause of this range of fracture tip displacements is difficult to isolate and may be symptomatic of a highly anisotropic deforming volume.

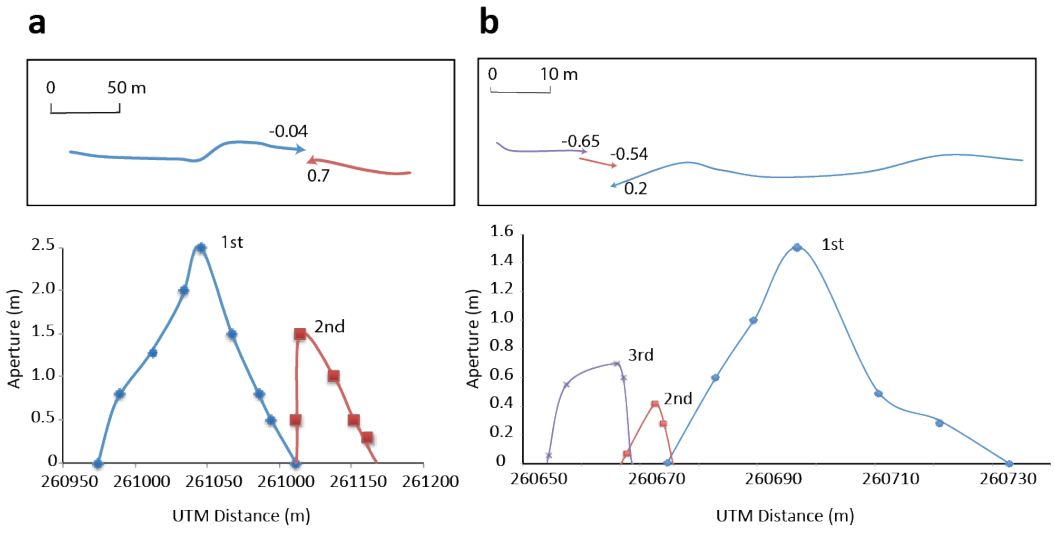

Figure 4.34. Examples of displacement asymmetry on individual fractures: a) Blue fracture shows a nearly symmetrical profile whereas the red fracture shows a relatively steep displacement gradient, suggesting the blue fracture formed earlier in isolation and perturbs local stresses as the red fracture nucleated. b) The blue fracture shows a nearly symmetrical profile whereas the other two show steep displacement gradients, in the direction of the blue fractures. The blue fracture may have formed first, followed by the red and purple fractures.

When linear elastic and isotropic conditions are no longer assumed, displacement analysis of extension fractures and normal faults is challenging. For instance, displacement profile symmetry does not necessarily imply isolation or non-interaction. Restricted growth of a fracture at both lateral tips could produce a symmetrical profile despite actively interacting with adjacent structures. Meanwhile, seemingly isolated fractures that demonstrate asymmetrical displacement profiles may be indicative of interaction with subsurface fractures or with local joints, which result in stress perturbations in the idealised isotropic medium.

Evidence for varying degrees of tip restriction, and a poor correlation with fracture length, suggests highly heterogeneous stress distributions exist at the tips of fractures and imply that en echelon fractures do not develop in a perfectly isotropic, homogenous volume. However, three key observations may be summarised at this stage: (1) extension fractures appear to reactivate pre-existing joints at the free surface, but not all joint orientations show evidence for reactivation; (2) extension fractures show organised distributions in narrow zones that parallel the trend of the ERZ and exposed normal faults; and (3) at the cm-scale up to the km-scale, extension fractures and faults do not form isolated, single structures throughout their evolution but show evidence for interaction, local stress rotation and linkage. Therefore, the initial growth and segmentation of brittle structures will be controlled by the mechanical anisotropy of the deforming sequence: i.e. the pre-existing joint fabric and shear strength of joints at depth, and the mechanical stratigraphy of the intact lava sequence.

4.5.2. Mechanical Layering

It has been demonstrated in Chapter 3 that basaltic lavas are not mechanically homogenous and isotropic materials and cannot therefore, be modelled as such. In

addition to pre-existing joint fabrics, naturally varying physical attributes induce a distinctive mechanical stratigraphy and directional strength anisotropy.

4.5.2.1. Pre-existing Cooling Joints

Faults in the Koa'e fault system are predicted to exploit pre-existing, suitably oriented cooling joints in the lava pile. At shallow depths (i.e. low mean stress) where joints are near vertical, and therefore orthogonal to the axis of minimum compressive stress, extensional opening is predicted while the differential stress is $<4T_o$ (when T_o is the tensile strength of the lava (Figure 4.35a*iii*). At greater depths (i.e. increasing differential stress) where $\sigma_1 - \sigma_3 > 4T_o$, and joints are typically tilted away from horizontal, shear failure is predicted to take place (Figure 4.35a*iv,* Figure 4.36a). This may occur through the downward propagation of surface extension fracturing, with compressional shear occurring when (e.g. Gudmundsson and Backstrom, 1991):

$$\sigma_1 = \rho g z$$

Where p is the average host rock density

g is the acceleration due to gravity

z is the fracture depth

The maximum depth of tensile fracturing is predicted to be approximately 800 m depth using a density of 2300 kg m^{-3} (Gudmundsson and Backstrom, 1991; Gudmundsson, 2011).

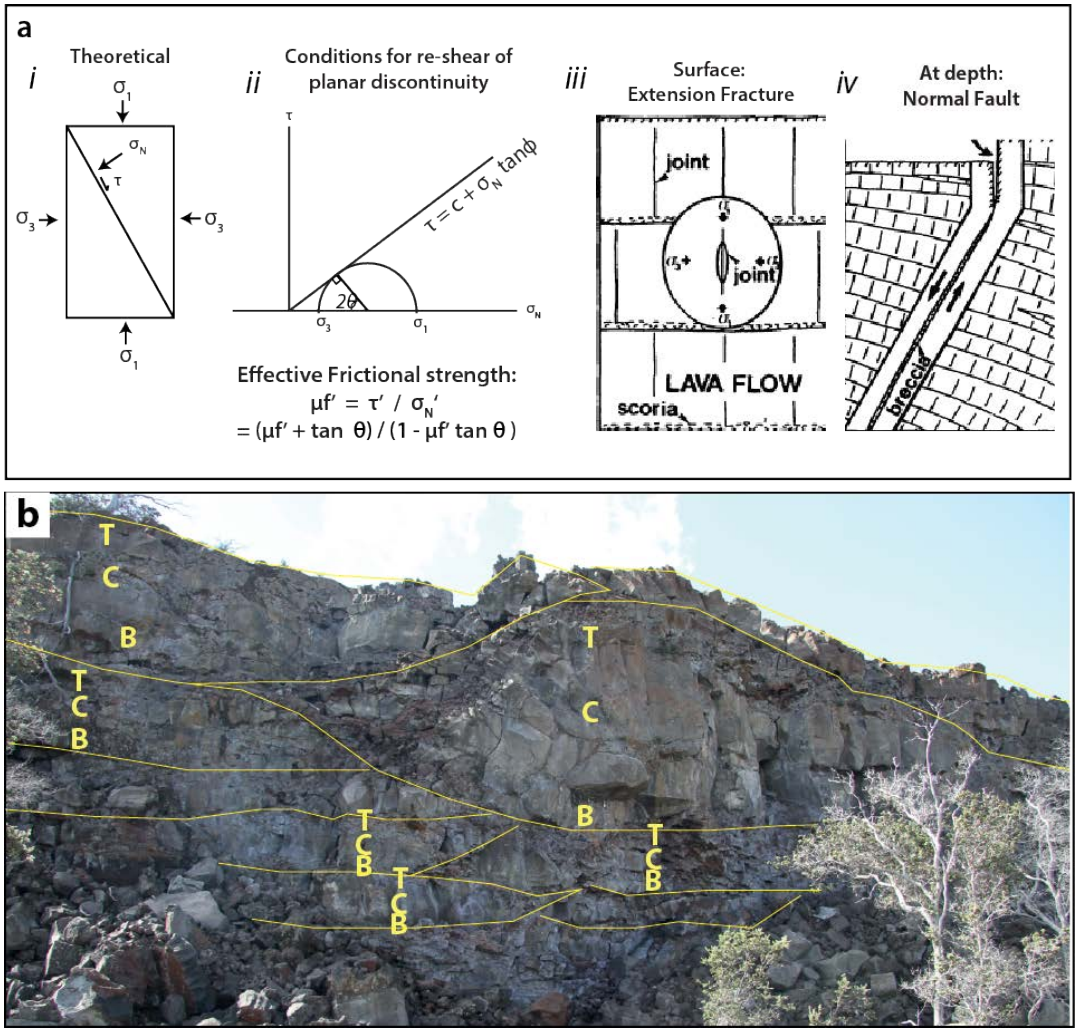

Figure 4.35. During the theoretical reactivation of an optimally oriented existing discontinuity, the shear stress (τ) required to initiate shear failure is equal to the normal stress confining the surfaces (σ_N) times the co-efficient of friction for that material (a*i ,ii*). Existing models for the exploitation of joints in a lava pile (e.g. Gudmundsson and Backstrom, 1991; Gudmundsson, 1992) predict extensional opening of vertical joints near the surface (a*iii*) and extensional shear on inclined joints at depth (a*iv*: from Gudmundsson, 1992. b) An exposed fault scarp along the Kulanaokuaiki fault shows the varying thickness and lobate unit morphologies, which are comprised of scalable portions of lava top component (T); lava core component (C); and lava base component (B). See Chapter 3 for more detail.

Below this depth, two components of shear strength define the conditions under which a discontinuity will fail in shear (e.g. Sibson, 1998): (1) strength of chemical and physical

bonds and, (2) the effective frictional strength (for a dry system) associated with the micro- or macroscopic interaction of asperity interfaces that make up the area of contact (Hencher, 1995). Alternatively, normal faults may develop from inclined cooling joints at depth. Assuming that lava is extruded across a subhorizontal surface, the cooling joint fabric can become tilted from vertical with increasing loading due to burial or horizontal axis rotation with progressive slip of major normal faults; such morphology has been observed in regions of Iceland where older sequences are exposed (e.g. Gudmundsson and Backstrom, 1991). When joint surfaces become non-parallel to the maximum principal stress (Figure 4.35a*iv*), they are subject to shear stresses and normal faults initiate (e.g. Gudmunsson, 2011).

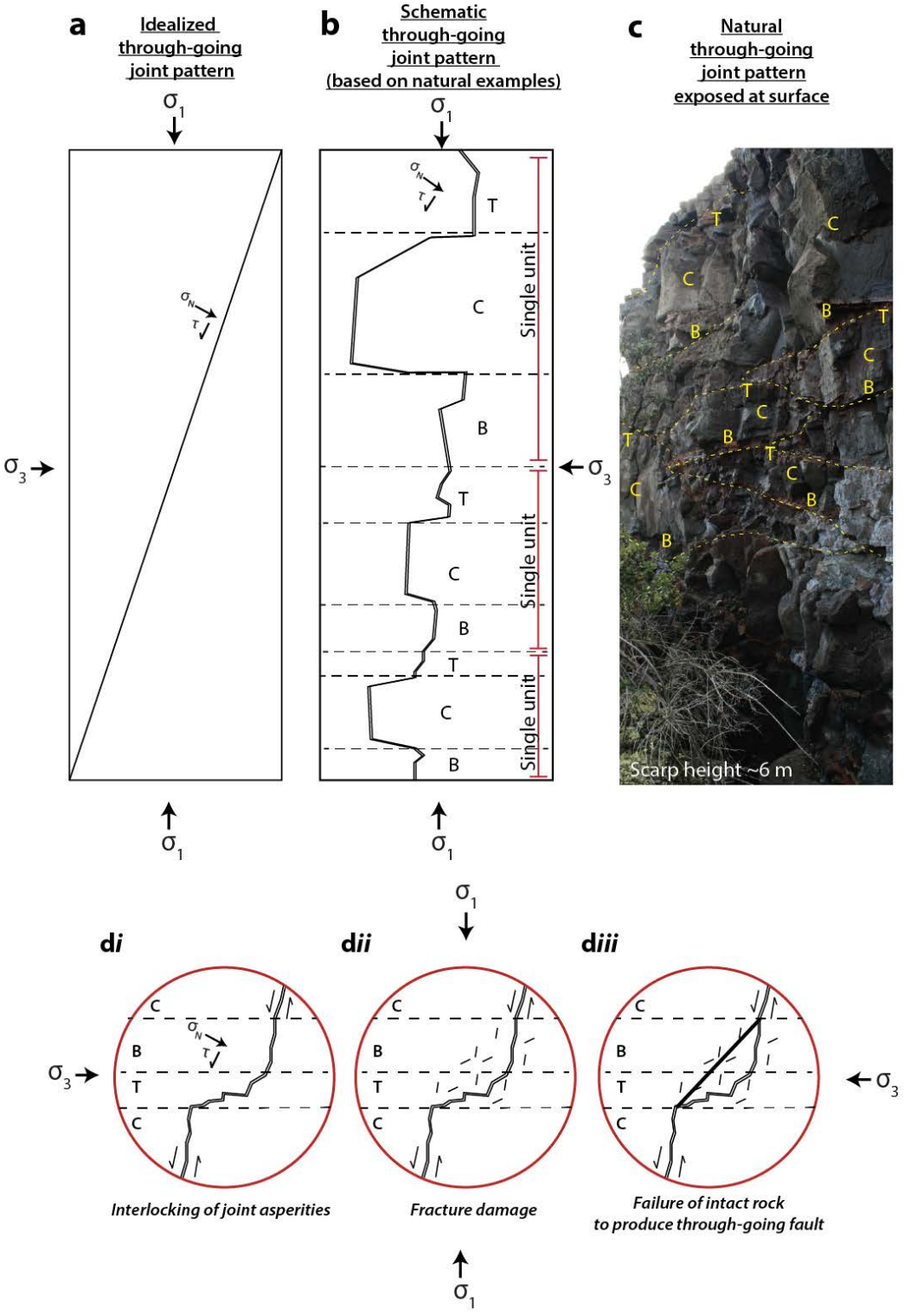

Figure 4.36. (a) In numerical-based models, joints are idealised as inclined planar discontinuities. b) Natural joints however show variable scales and orientations (inclined, sub-vertical and subhorizontal planes) and surfaces tend to be weathered, which produces highly irregular joint patterns. c) At depth, joint surfaces are in contact and the intact strength of asperities becomes important. Where joint planes are irregular and non-vertical (ci) shearing resistance is

correspondingly high and fracture damage can develop where the intact rock strength is lower (c*ii*). New through-going shear fractures may develop in weaker lava components to produce linked structures (c*iii*).

Growth of normal faults through the reactivation of pre-existing cooling joints is problematic. Assuming that joints remain open and are not sealed by mineralising fluids, the variable shape and size of lava lobes, and thus the variable scale of both horizontal and vertical joints within them (Figures 4.35b and 4.36b, c) mean that no planar, in-plane discontinuity exists. The propagation of a through-going plane therefore requires tensile failure of the intact rock to connect offset joint segments (e.g. Gudmundsson and Backstrom, 1991). Thus, the formation of a normal fault is strongly influenced by the strength of the intact lava. Furthermore, to drive repeated slip on an incipient normal fault, normal and shear stresses acting on the plane must satisfy the Mohr Coulomb failure criterion (Figure 4.35a*i*, *ii*). At depths where $\sigma_1 - \sigma_3 > 4T_o$ (>~800 m depth), cooling joint surfaces are in contact and the shear strength of the fault is governed by the shearing resistance, or co-efficient of friction of intact asperities in contact on the joint planes (e.g. Savage et al., 1996). The shear stress required to induce repeated slip on natural cooling joints is therefore a function of the surface roughness and the induced friction, which produce heterogeneous increases in normal and shear stress for horizontal or inclined joint surfaces that must be overcome for through-going failure (e.g. Dieterich, 1978; Sibson, 1985; Scholz, 1998; Barton, 2013; Walker et al., 2013. Figure 4.36b). As a result, local sites of stress concentration may occur throughout the lava pile where shearing resistance is high, producing a segmented sequence of fractures. Regions of fracture damage will develop to accommodate extensional strains (Figure 4.36c*i-iii*). In lower compressive strength lava components (base, top) overcoming the intact rock strength will require lower shear stresses and faults may propagate through failure of the

intact host rock, rather than by joint reactivation (Figure 4.36c*iii*). In locations (e.g. proximally to the ERZ) where magmatic pressures are high, joint surfaces may be forced apart as they are intruded and asperity-induced effective shear strength will be less critical.

The style and distribution of deformation in the Koa'e fault system show that the deforming host volume is highly heterogeneous and anisotropic. The *a priori* assumption that is made in existing models of fault growth in basaltic sequences that the volume is mechanically homogenous and isotropic is therefore invalid. Mechanical anisotropy related to the variable intact strength of lavas and networks of irregular and discontinuous cooling joints, exert a strong influence on fracture and normal fault growth and segmentation across a range of scales. In addition to a mechanically anisotropic host, the assumption of homogenous and isotropic stress is also questioned here.

4.5.2.2. Magmatic Influence

The distribution of strain in the Koa'e fault system highlights a distinctive east-west strain gradient: large through-going, surface-breaking faults and rotated, disintegrated blocks in the east, and extensive zones of en echelon extension fractures and flexure of the surface above segmented faults at depth in the west (Figure 4.37). This may be evidence for higher strain rates in the eastern portion of the Koa'e than the west. The inferred strain rate gradient also coincides with a decrease in magmatic activity from the east to west. Calculations of magma supply into Kilauea's rift system from 1956-1983 suggest that 35% of the net magma supply was erupted during this interval and the remaining 65% is stored within the ERZ (55%) and SWRZ (10%) (Dzurisin et al., 1984). Tilt records from the same period also demonstrate that the ERZ may be acting as a repository and supplying magma

to the summit (Dzurisin et al., 1984). Between 1840-1950, eight eruptions have been recorded in the ERZ, and more than 20 since 1950.

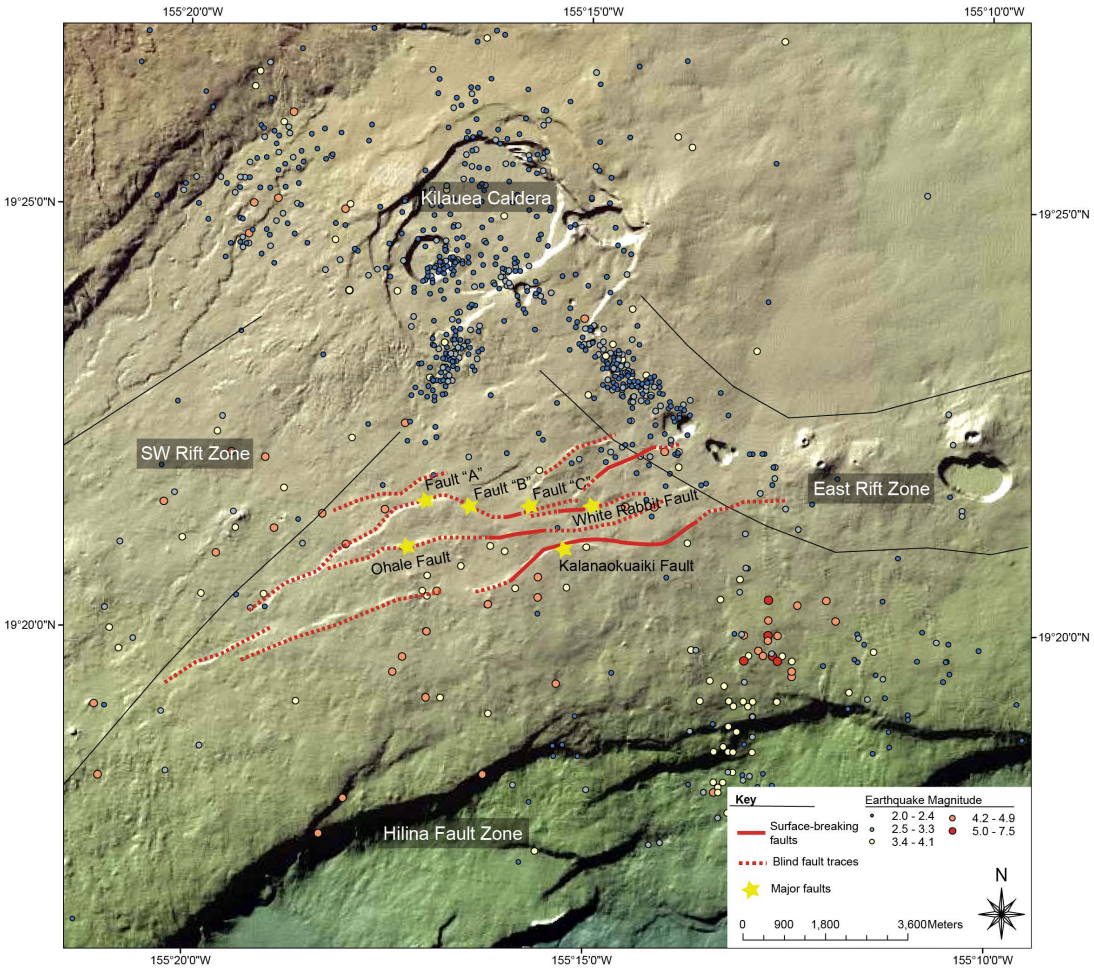

Figure 4.37. Map of the distribution of earthquakes with magnitudes of 2.0-7.5 covering the period 1973-2014. Surface-breaching fault segments of the Koa'e fault system are shown as solid red lines and regions of surface flexure as dotted red lines. Fault scarps are found in central-eastern and eastern portions of the fault system where we find the greatest amount of seismic activity. (Earthquake data from the USGS Earthquake Archives).

In contrast, only two eruptions are recorded for the SWRZ since 1956 (Dzurisin et al., 1984; Dvorak and Dzurisin, 1993). This implies that magma is periodically held in the SWRZ, but less extensively than in the ERZ. The result is locally higher compressive stress associated with the storage and emplacement of magma, as dikes, in the ERZ. A magma-

driven strain rate gradient should therefore show a progressive change from fully linked surface faulting in the east to segmented, blind faulting in the west. This may be seen at the scale of the whole fault system, which is wider at the eastern end than the west, increasing from ~ 1 km near the SWRZ to ~3.5 km at the upper ERZ. It is also evident in the AOI within the centre of the Koa'e fault system, which marks a transition from dominantly surface-breaching faults in the east to laterally continuous traces of un-breached surface flexure in the west.

4.5.3. Lateral fault propagation

The distribution, geometry and kinematics of brittle structures (Figures 4.38a and 4.38b) at the scale of individual fractures (centimetre to tens of metre long) and at the fault scale (hundreds of metres to kilometres long) show similarities with predicted geometries based on analogue models (Figure 4.38c*i*, c*ii*) and analytical solutions of en echelon structures (e.g. Martel and Langley, 2006; Kaven and Martel, 2007). Structural mapping has revealed two dominant fault and fracture sets (Figure 4.38a): (1) a set of ENE-WSW trending extension fractures and normal faults, that parallel the trend of the ERZ and accommodate a NNW-SSE extension direction (Figure 4.38a, b*i,* b*iii*); and (2) an oblique set of NW-SE trending extension fractures that are associated with the tip regions of en echelon rift-parallel fault sets (Figure 4.38a, b*ii*). There are no observed instances of rift-normal strike-slip faults within the AOI; both sets accommodate a unique extension direction that may indicate a local counter-clockwise reorientation of the regional extension direction (Figure 4.38b*iv*). Obliquely oriented fractures have only been identified in the areas surrounding en echelon rift-parallel faults, or the regions where previously en echelon faults have coalesced, leaving an obliquely oriented step in the trace. On the basis that oblique orientations are associated with relay zones between en

echelon rift faults, it is inferred that stress field interaction controls the formation of obliquely oriented fracture sets and the following lateral propagation history is proposed:

Stage 1: ENE-WSW trending, rift-parallel blind normal faults A and C (Figure 4.36d*i*) nucleate and propagate towards each other. Except for some isolated areas, we see the formation and growth of ENE-WSW trending extension fractures and surface flexure that accommodate a NNW-SSE extension direction (Figure 4.36b*i*).

Stage 2: Continued lateral propagation of faults A and C, and mechanical interference of their opposing stress fields result in locally high elastic strains in the overlap (relay) zone between them (Figure 4.38d*ii*). At the western tip of fault C is a segment of surface-breaking fault where throw decreases from 5 m to zero over a distance of ~70 m (Figure 4.29b, Figure 4.30b); this indicates either that the fault has propagated into a softer sediment, or that strains are considerably higher at the tip of this fault. East of the surface-breaking fault segment, vertical displacement is accommodated in flexure, ahead of a blind fault segment suggesting this portion of the fault has so far been unable to breach the surface. Locally elevated stresses could be induced by interaction-related stresses within the relay zone. A new NW-SE striking (110°) fault (fault B), expressed as interacting extension fractures (accommodating a NE-SW extension direction: Figure 4.38b*ii*) and minor flexure at the surface, developed to relieve internal strains and initiate a hard-linkage (Figure 4.38d*ii*). Extension fractures that developed in the NW-SE trend do not show any oblique component to their opening, implying that rift-normal and rift-oblique extension may be taking place simultaneously. Displacement deficits at the north and south tips of extensions fractures in this set suggest a separate connecting fault, behaving as a single structure (showing centrally located displacement maxima), is developing within the ramp to transfer strains between the bounding structures.

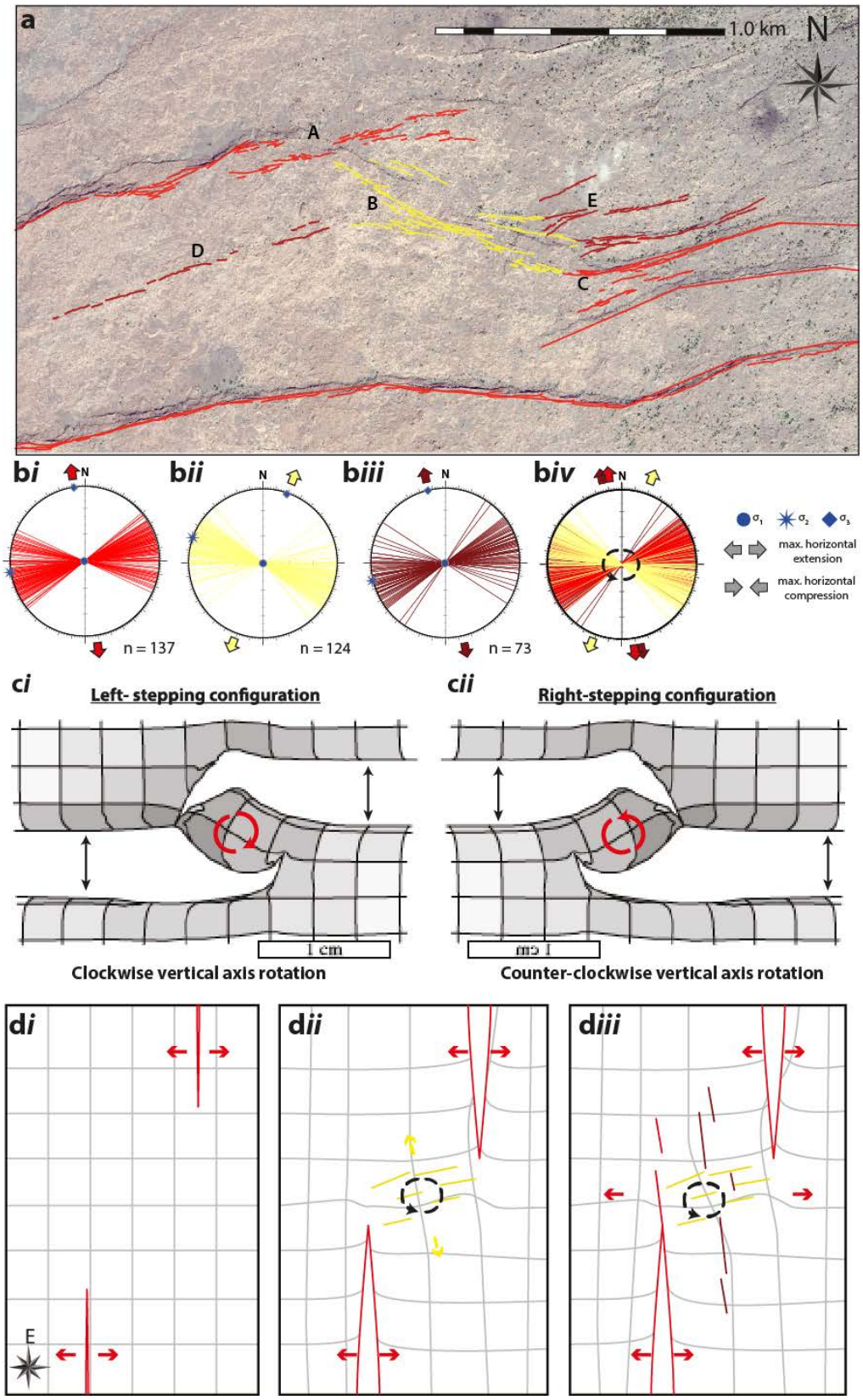

Figure 4.38. (a) Mapped faults and extension fractures in the AOI. Red polylines represent the dominant rift-parallel fault and fracture set that accommodate the regional NNW-SSE extension direction. Additional oblique fracture and fault sets (fault B) have developed at the tips of en

echelon rift faults (faults A and C), which appear to be cut by further rift-parallel structures. b) Individual stereographic projections for each structural set show measured fault/fractures as planes and measured extension directions (b*i-iii*) and a combined stereographic projection summarizes a proposed counter-clockwise rotation in extension direction from the regional NNW-SSE-WNW, to NNE-SSW, to NNW-SSE with the cutting of the relay zone (b*iv*). c) Modelled strain fields surrounding two interacting fractures (darker grey is higher strain intensity) based on the analogue models of Tentler and Acocella (2010) showing a left-stepping fracture configuration, resulting in a clockwise vertical axis rotation (i) and a right-stepping fracture configuration that produces a counter-clockwise vertical axis rotation (c*ii*). d) Proposed evolution of fault sets: (d*i*) Propagation of the main rift-fault set. d*ii*) Interaction between the main right-stepping rift faults leads to clockwise vertical axis block rotation in the relay zone, and induced local reorientation of extension direction accommodated on ESE-WNW trending fractures. d*iii*) Propagation of new rift-parallel faults in the footwall and hanging wall of fault B leads to an effective straightening out of the relay zone**.**

Stage 3: In the latest stage, new fault structures (set D and E) that follow the ENE-WSW (rift-parallel) trend, accommodating the same NNW-SSE extension direction as the bounding fault structures have developed (Figure 4.38b*iii*, d*iii*).

There are no clear cross-cutting relationships between fractures developing in the oblique set (set B) and rift-parallel sets in the footwall and hanging wall of the relay (set D and set E, respectively) so it is unclear which fracture sets developed first. However, unpublished measurements of ground cracks following the last major cracking event in the Koa'e during the December 1965, however, which identified fresh extension fractures in the ENE-WSW trend in the footwall of the relay zone, suggest they are a later set (set D: Figure 4.39; unpublished data from Don Swanson, Hawaii Volcano Observatory).

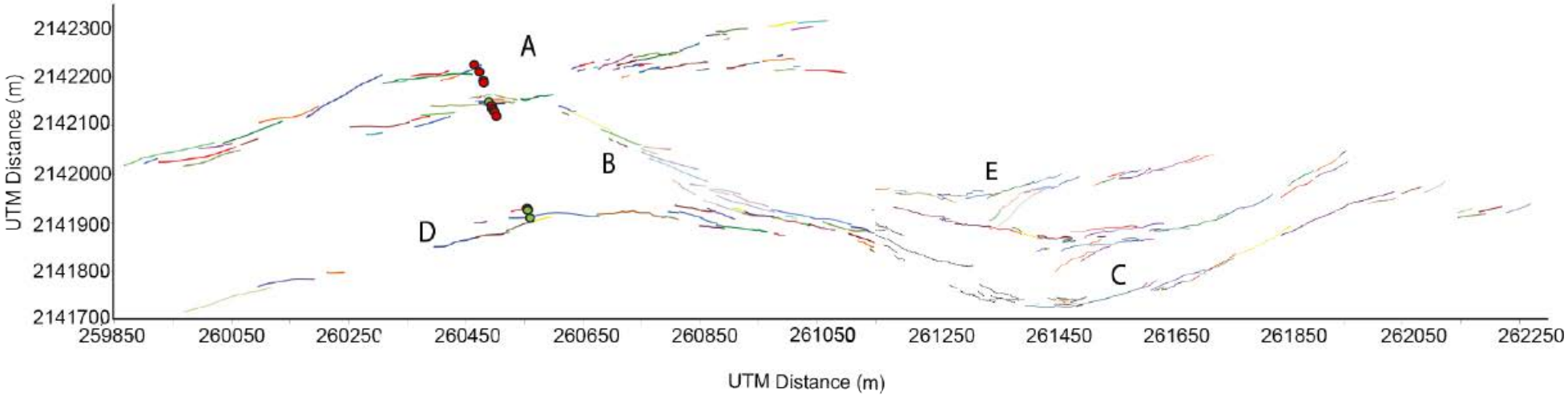

Figure 4.39. Map of the main structural sets in the mapped area of the Koa'e and data from fracture mapping in October-November 1966. Red circles represent older fractures and green are thought to be new fractures that developed during the 1965 eruption and cracking event (D. Swanson, D. Fiske, Pers. Comms).

The effect of the recent development of sets D and E is an overall straightening out of the relay zone, implying either (or a combination of the following) that: (1) the ramp is unable to accommodate the internal strains efficiently and a post-breach stage of fault development is taking place; or (2) a new dike (s) have been emplaced at depth and fault and fracture segments are localising ahead of this. Observations of propagation and linkage in the strike dimension of surface extension fractures are interpreted to also take place in their vertical dimension; this is discussed further in Chapter 6.

4.6. Summary

- Using the geometry of fracture traces and their displacement characteristics, it is shown that mechanical interaction of opposing fracture tip stress fields results in, asymmetrical displacement profiles and variable path geometries, implying local stress perturbations.
- At both the fracture and fault scale, extensional strains in the Koa'e fault system have developed as a result of two stress components: (1) a regional stress associated with the dynamics of the volcanic flank; and (2) local interaction induced strains that result in the reorientation of stress trajectories and deviation in the regional extension vector.
- The process of fault interaction and linkage is not an instantaneous process but a progressive inelastic process, which results in multiple fault sets and complex non co-axial strains.
- The deforming lava sequence contains significant mechanical anisotropies due to the presence of networks of cooling joints and the mechanical stratigraphy that was identified in Chapter 3.

- Records of the temporal and spatial emplacement of magma at depth suggest driving stresses are neither isotropic nor homogenous (constant in time and magnitude, and uniformly distributed) and strain rates may vary across a rift zone, which in-turn controls the distribution and style of deformation
- Current models involving the in-plane propagation of a fault in a linear elastic, isotropic, homogenous deforming volume are therefore unable to predict the natural, scale-invariant and intrinsic segmentation, progressive interaction and linkage that occurs in the study area.
- Segmentation may be a function of one, or a combination, of an anisotropic deforming sequence and the distribution and magnitude of syn-tectonic volcanism, which results in primary and secondary scales of segmentation.

Chapter 5

Rift-Fault Segmentation: the Krafla Fissure Swarm, NE Iceland

5.1. Introduction

Evolving rift systems comprise large-scale structural domains that are characterised as segments, with heterogeneous populations of discontinuous normal faults that show lengths of tens to hundreds of kilometres, accommodating the regional extension vector (e.g. Bosworth, 1985; Rosendahl et al., 1986; Faulds and Varga, 1998). Rift segments requires inter-fault transitional zones at their terminations, where extension is conserved and transferred (Gibbs, 1984; Ebinger, 1989; Ebinger et al., 1989; Morley et al., 1990; Nelson et al., 1992; Gawthorpe and Hurst, 1993; Hayward and Ebinger, 1996). First order segmentation is associated with one of two types of inter-fault transitional zone: (1) zones that are hard linked by subvertical, transtensional or strike-slip "transfer" faults that strike parallel or sub-parallel to the regional extension direction; and (2) soft-linked belts (accommodation zones) of ductile strain between overlapping synthetic or antithetic fault tip lines (e.g. Morley et al., 1990; Faulds and Varga, 1998; Peacock et al., 2000).

Much of our understanding of the segmentation within rift systems has developed as a result of greater access to commercial and academic seismic reflection and gravity datasets, as well as field mapping in areas such as the East Africa Rift (EAR). Limitations regarding the resolution of these datasets (e.g. Doré et al., 1997; Planke et al., 1999; Schutter, 2003; Moy and Imber, 2009), however, make it challenging to resolve both the temporal and kinematic evolution of inter-fault transfer and accommodation zones and their sub-seismic-scale

distribution and geometries. Field based studies of overlapping individual rift faults and rift segments in areas such as the EAR have drawn attention to segmented and curvilinear fault geometries that show similarities to: (1) faults in Iceland (Gudmundsson et al., 1993; Acocella et al., 2000); (2) the geometries exhibited by overlapping oceanic ridge segments (Macdonald et al., 1987; Pollard and Aydin, 1984; Tentler, 2003); (3) dike segments (Delaney and Pollard, 1981; Pollard et al., 1982); and (4) extension-mode fractures, e.g. joints, veins or dikes (Olson and Pollard, 1989). These geometries have also been predicted in scaled analogue (McClay and White, 1995; Acocella et al., 1999; Clifton et al., 2000; Acocella et al., 2005; Van Gent et al., 2010) and numerical models of fracture propagation in isotropic, homogenous media based on theoretical fracture mechanics (Segall and Pollard, 1980; Thomas and Pollard, 1993; Crider and Pollard, 1998; Maerten et al., 2002). In these linear elastic analogues, progressive mechanical interference of stress fields surrounding the terminations of en echelon fractures are shown to control fracture and fault geometry during propagation, and generate locally elevated stress concentrations in the overlap zone during their formation. The predicted stresses in this region can be great enough to overcome the propagation criterion, resulting in the out-of-plane failure beyond the fault tip and the formation of multiple sets of ancillary faults and fractures (Segall and Pollard, 1980; Atkinson, 1987; Engelder, 1993; Maerten et al., 2002).

Natural examples of triaxial strains surrounding the tips of en echelon rift faults have been found in areas of the EAR where deformation is partitioned onto multiple sets of minor, ancillary fault sets (Griffiths, 1980; Morley et al., 1990). These types of strain are traditionally explained by one of three models: (1) multiple tectonic episodes, conserving an inherently plane-strain extension (e.g. Angelier et al., 2000); (2) perturbations of the applied and local stress field by local fault development, where faulting predates additional deformation (Rotevatn et al., 2007); or (3) basement lineament control (e.g. Maerten et al., 2002). Understanding the architecture of these inter-fault areas, or *relay zones*, and the distribution of extensional strains within them is important not only to our understanding of crustal extension

but it has vital implications for the exploration of fluid-related resources, including hydrocarbons, in rift settings (e.g. Gawthorpe et al., 1993; Moy and Imber, 2009; Rippington et al., 2015; Fossen and Rotevatn, 2016). Internal complexities associated with local stress perturbations can result in more distributed or increased fault rock volumes which may act as barriers or conduits to fluids.

It has been shown in the preceding chapters that segmentation is an intrinsic and transient feature of fault and fracture development from the scale of initial crack nucleation to a tens of cm to hundreds of metre-scale in an incipient rift zone. This segmentation, and the resultant local stress variation, is partly controlled by the natural mechanical anisotropy (e.g. joints and intact rock strength variations) within the deforming host rock and the distribution of magmatic overpressures, and hence, strain rates (e.g. large, surface-breaking faults proximally to the magmatically active ERZ and blind faults distally). In this chapter, high-resolution structural mapping of the distribution and geometry of rift-faults and ancillary strains surrounding their tips is used to study the role of inheritance and kinematics during fault coalescence and localisation.

5.2. Geological Setting

Iceland is located on the divergent plate boundary between the North American and Eurasian tectonic plates, and represents a subaerially exposed segment of the Mid-Atlantic Ridge. Interaction between the Mid Atlantic Ridge and a mantle plume located beneath Iceland have led to anomalously high crustal thicknesses (10-15 km), approximately double that of typical oceanic crust. This interaction has generated an active rift zone that accommodates WNW-ESE (103°) extension of ~19 mm/year (Sæmundsson, 1974; Angelier and Bergerat, 1997; Gudmundsson, 2007; Wright et al., 2012).

Iceland can be divided into three major domains, based on the age of rift zone material: (1) the current axial rift zone, comprising Holocene lavas and Upper Pleistocene

(0.001-0.070 My) rocks; (2) the lower Pleistocene rift axis (0.07-0.31 My) and (3) the original rift axis, comprising Tertiary lavas (3.1-16.0 My) and acidic intrusive volcanic centres (Opheim and Gudmundsson, 1989; Gudmundsson, 1992; Gudmundsson et al., 1996). The present day neovolcanic zone (NVZ) marks the onshore continuation of the Reykjanes Ridge in the south and the Kolbeinsey Ridge in the north, with present-day extension accommodated in a series of volcanic rift zones centred above the hotspot beneath the Vatnajökull icecap (Garcia et al., 2003; Bergerat and Angelier, 2008; Figure 5.1).

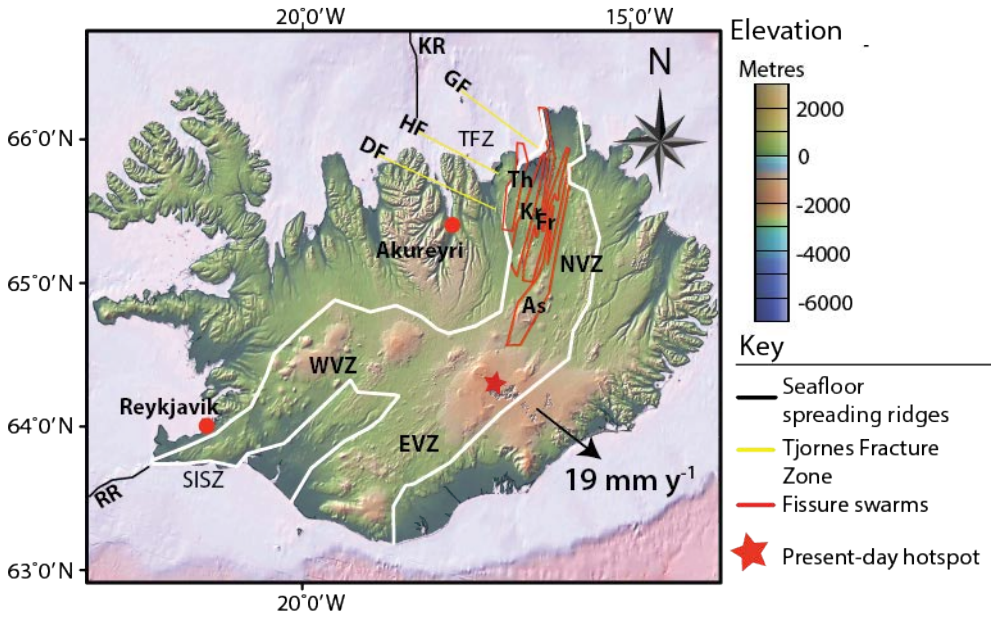

Figure 5.1. Map of Iceland highlighting the major tectonic elements: Reykjanes Ridge (RR); the Kolbeinsey Ridge (KR); South Iceland Seismic Zone (SISZ); West Volcanic Zone (WVZ); East Volcanic Zone (EVZ); Neo-Volcanic Zone (NVZ: the axial rift zone); Askja volcanic centre (As); Fremri-Namur volcanic centre (Fr); Krafla volcanic centre (Kr); Theistareykir volcanic centre (Th); the Tjornes Fracture Zone (TFZ) comprising the Dalvik lineament (DF), the Husavik-Flatey Fault (HF) and the Grimsey lineament (GF).

The dynamic nature of the plate boundary is such that the neovolcanic zone is inherently unstable and rift jumps have previously taken place at intervals of 5-10 My (Pedersen et al., 2009). The neovolcanic rift zone has shifted more than 100 km eastward with respect to the Mid Atlantic Ridge from the former axial rift, the West Volcanic Zone (Sæmundsson, 1974). Dating of

the rift jumps reveals a diachronous pattern from north to south: in northern Iceland, the latest rift jump took place at 8.0-8.5 Ma, whereas in southern Iceland the jump occurred at 2-3 Ma (Garcia et al., 2003; Bergerat and Angelier, 2008). To accommodate the migration of the plate boundary, two major transform fault zones have developed: the South Iceland Seismic Zone (SISZ), linking the Reykjanes Ridge and the neovolcanic zone, and the Tjornes Fracture Zone (TFZ), which connects the neovolcanic zone to the Kolbeinsey Ridge (Figure 5.1). Much of the seismicity in Iceland is recorded in these transform zones (e.g. Bergerat and Angelier, 2008). Seismicity in the TFZ is concentrated in a 120 km long and 70 km wide, WNW-ESE striking zone, which has cumulative right-lateral displacements of up to 60 km. Focal mechanisms from within this zone reveal three primary seismogenic features, accommodating right-lateral displacements: the Grimsey lineament, the Husavik-Flatey lineament, and the Dalvik lineament (Figure 5.2a; Gudmundsson et al., 1993; Rognvaldsson et al., 1998; Bergerat and Angelier, 2008). The SISZ is an east-west striking zone of seismicity, 70-80 km long and 20-30 km wide, that represents the onshore continuation of the Reykjanes Ridge, linking this segment with the western (WVZ) and eastern (EVZ) volcanic zones. A general left-lateral displacement is identified across this zone, although it is dominated by north-south striking normal faults and ENE-WSW left- and right-lateral strike-slip faults (Bergerat and Angelier, 1999, 2008). Unlike the TFZ, however, the SISZ lacks the tectonic components consistent with an oceanic transform fault, including transform-parallel strike-slip faults and grabens (Gudmundsson, 2007).

Within the present day neovolcanic zone are 4 sub-parallel NNE-SSW striking en echelon volcanic systems and associated fissure swarms, a term used to describe the rift zones in Iceland, which are characterised by large open normal faults and extension fractures (i.e. fissures) (e.g. Gudmundsson, 2011). From NW to SE these are: Theistareykir, Krafla, Fremri-Namur, Askja, and Kverkfjöll (Figure 5.2b). Krafla and Askja feature well-developed central volcanoes and calderas, whereas Theistareykir and Fremri-Namur show a less developed morphology (i.e. no central caldera).

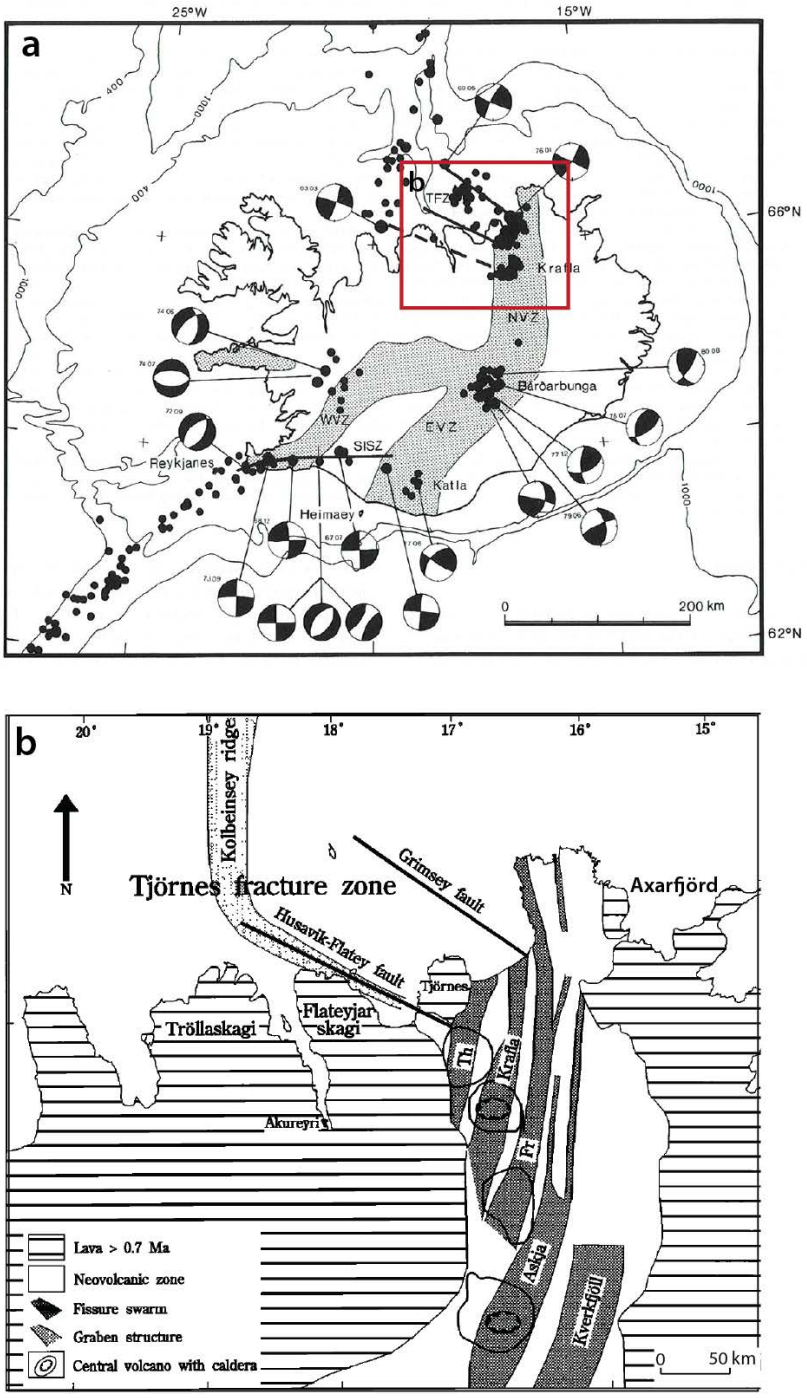

Figure 5.2. (a) Map highlighting epicentres and focal mechanisms of earthquakes in Iceland during the interval 1963-1987 (map from Einarsson, 1991). b) Rifting since the upper Pleistocene has taken place in the neovolcanic zone, comprising five en echelon volcanic systems: Theistareykir, Krafla, Fremri-Namur, Askja and Kverkfjöll (map from Langbacka and Gudmundsson, 1995).

Crustal extension in each of these zones is accommodated by sub-parallel systems of normal faults, eruptive fissures and extension mode fractures that are associated with an axial volcano that forms the locus of activity (Sæmundsson, 1974; Brandsdóttir and Einarsson, 1979). Historical records imply that only one of these volcanic systems is active during any rifting episode (Gudmundsson and Backstrom, 1991).

5.2.1. The Krafla Fissure Swarm

The Krafla central volcano, and associated fault and fracture networks has dominated recent volcanic activity in the neovolcanic zone with approximately 35 Holocene basaltic eruptions identified (Brandsdóttir and Einarsson, 1979; Opheim and Gudmundsson, 1989). The Krafla volcanic rift zone extends 80-100 km from the south of Myvatn Lake to the coast at Axarfjörd (Figure 5.2b), with a width of 4-10 km (Bjornsson et al., 2007). Magma is stored beneath the central caldera ~10 km north of Myvatn, in a reservoir at approximately 2.5-3.0 km depth (Dauteuil et al., 2001). When a critical level of inflation is reached, magma migrates laterally north and south, and a rifting event takes place (e.g. Rubin, 1990; Angelier and Bergerat, 1997). Recurrence intervals for rifting events in northern Iceland are reported to be ~100-150 years (Bjornsson et al., 1978). Regional WNW-ESE extension during each rifting episode is characterised by slip on NNE-SSW striking normal faults and opening along both new, and existing extension fractures (Tryggvason, 1984; Opheim and Gudmundsson, 1989; Angelier and Bergerat, 1997). Published records of repeated geodetic measurements have shown that during a single episode, extension is dominantly localised in a 1-2 km wide zone where faults accumulate an average of 1-2 m of displacement and extension fractures dilate by 1.5-2.0 m (Bjornsson et al., 1978; Tryggvason, 1984; Forslund and Gudmundsson, 1991; Tryggvason, 1994). Extension in the Krafla fissure swarm is accommodated on surface-breaking normal faults with maximum throws of up to ~30 m, and fractures with openings of up to ~4 m, suggesting that

extension in the region is characterised by the repeated reactivation of a smaller number of major structures (i.e. faults have accumulated displacement rather than forming new faults during each rifting event). The observed deformation in the Krafla fissure swarm has developed since 10 Ka, based on ages for lavas and erosional surfaces. Extension of approximately 30 m across the 3 km wide rift gives total strains of ~1% since that time (Dauteuil et al., 2001).

During the most recent episode of rift activity, between 1975-1984, multiple inflation-deflation cycles were identified, associated with 21 individual rifting events that culminated in crustal extension of approximately 9-10 m in central and southern portions of the rift, and 3-4 m in the north. Initial rifting during this period was characterised by the emplacement of dikes into the rift zone, which propagated 70-80 km along the rift (Hollingsworth et al., 2013). Inflation is thought to be the result of magma accumulation in the reservoir approximately 3 km below the centre of the volcano (e.g. Tryggvason, 1984; Hollingsworth et al., 2013). Deflation events are associated with lateral dike emplacement and earthquake seismicity that migrates from the central volcano outwards during a rifting event (Brandsdóttir and Einarsson, 1979; Tryggvason, 1984; Angelier and Bergerat, 1997). The latest rifting episode took place in 1984 with the extrusion of 0.25 km^3 of fresh lava during individual events (Opheim and Gudmundsson, 1989).

5.3. Datasets

The focus of this chapter is the segmentation, distribution, and kinematics of normal fault structures, and their associated extension fracture networks, within an area of segmented rift faults in the Gjastykki Valley, ~10 km north of Krafla volcano (Figure 5.3). Regional WNW-ESE extensional strain in the Gjastykki Valley is accommodated by NNE-SSW striking normal faults and extension fractures. The area offers the opportunity to constrain the progressive development of through-going extensional faults in a higher strain, more evolved rift zone by characterising the relative timing, geometric relationships, and kinematics of ancillary strains

surrounding segmented faults. This is achieved through remote and field-based structural mapping.

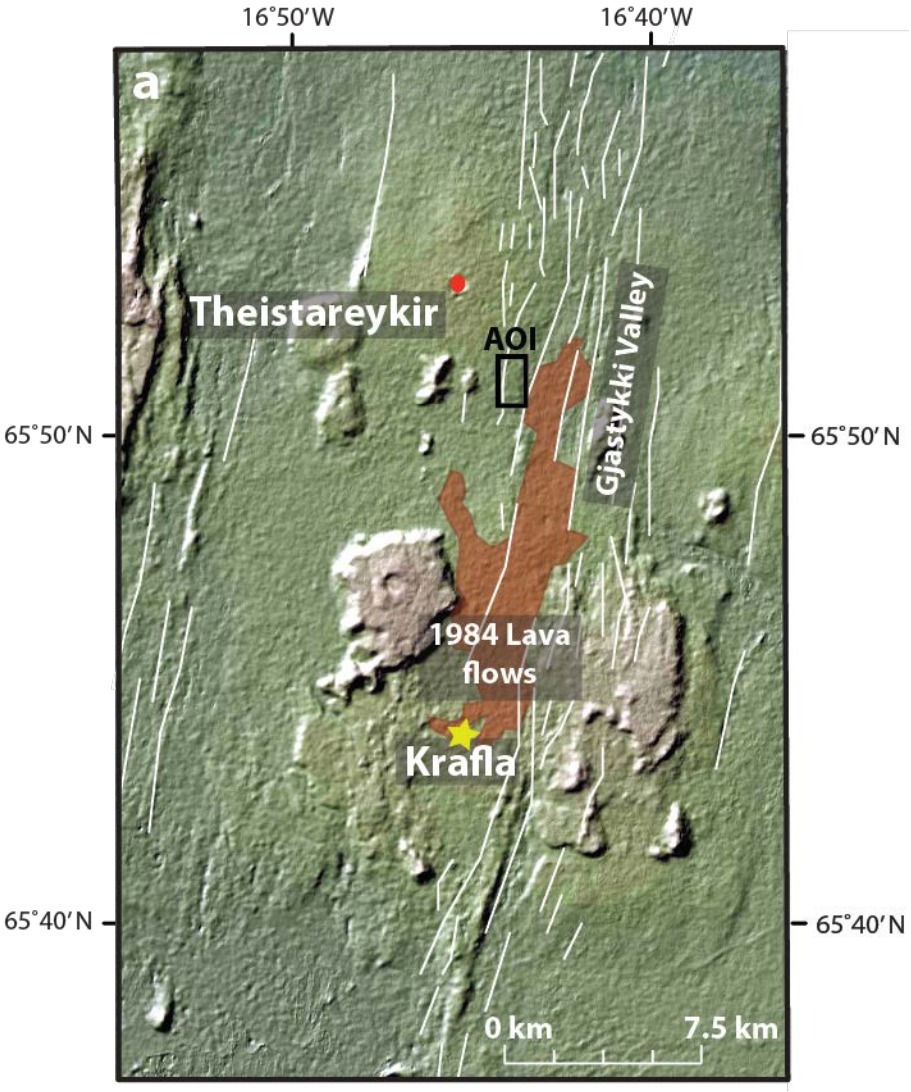

Figure 5.3. Map highlighting the Krafla and Theistareykir volcanic centres and the orientation of major rift faults (white lines) in the neovolcanic zone and the extent of the most recent lava flows erupted from Krafla in 1984. The area of interest (AOI) for this chapter in highlighted. Base image topography taken from GeoMapApp.

5.3.1. Field Mapping

Extension fracture measurements were collected at the start and end of the surface trace for each fracture (or as close as exposure allowed) as well as at a series of regular points along each fracture trace (Figure 5.4). Measurement of extension direction and style of opening within the area of interest (AOI) is made possible by the characteristic zig-zag geometry of fracture traces, which allows displaced walls to be matched across the crack aperture, and show either extension (mode-I) or extensional-shear (mixed-mode) openings. Data collection was focussed in an area of the Gjastykki Valley along a series of rift-parallel (NNW-SSW) normal faults and extension fractures. Mapping included measurement of the following: (1) extension direction and mode; (2) fracture aperture; (3) fracture azimuth; and (4) vertical offset, where present (Figure 5.4). Measurements were collected in the AOI (Figure 5.5) at the tips and a series of locations along fracture (and fault) traces. An average azimuth was also taken for fractures from one tip, looking towards the other.

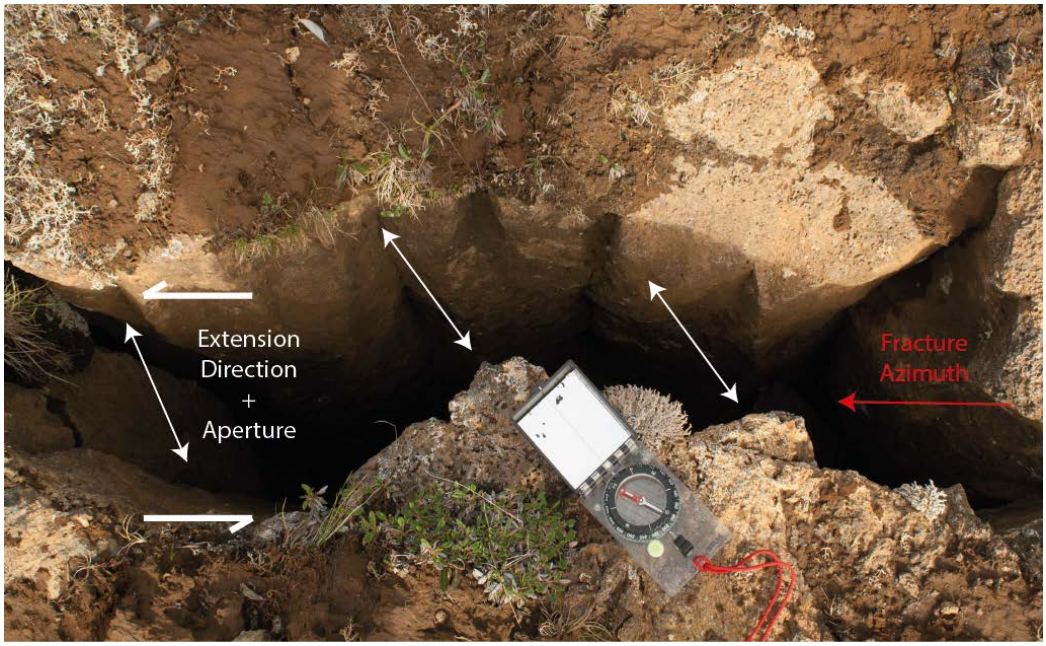

Figure 5.4. Measurement of fracture geometry and kinematics: extension-mode opening across pre-existing cooling joint surfaces allows the traditional measurement of opening direction, aperture, azimuth

and vertical offset. The fracture in the image shows an aperture of ~0.3 m, and an opening direction of 9°, oblique to the azimuth of the fracture (~330°), indicating a component of left-lateral shear.

Surface-breaching, sub-vertical normal faults demonstrate components of horizontal and vertical displacement, and are inferred to reflect linkage of surface extension fractures with blind normal fault tips at depth. Exposed normal fault surfaces in the Krafla fissure swarm have been subject to erosion or collapse, therefore the extensional opening history (i.e. dip slip Vs dip-oblique slip) could not be constrained. It was possible, however to observe and record fault azimuth, approximate throw and geometry.

Field data were collected digitally, using a Windows Surface Pro 2 tablet computer running a Windows 8 operating system and ArcGIS 10.2. Fracture measurements were recorded directly into a shapefile in ArcGIS using a Bluetooth Garmin Glo GPS device. The intermediary, open source program *Fransom GPSGate* was used to generate a virtual COM port, with location data from the Garmin receiver translated into a NMEA protocol that is used by ArcGIS to obtain live spatial reference data. Fracture measurements were digitally plotted directly onto a satellite image or base map for the area. Digital data, as points within the shapefile, were exported and input into Microsoft Excel for further analysis. Traces for faults and fractures located outside the AOI in Figure 5.5 are mapped remotely using Google Earth™ imagery and geometric measurements (length/azimuth) are derived using lineament analysis functions in ArcGIS. The resulting dataset contains ~430 kinematic measurements of faults and fractures in the AOI and provides high-resolution documentation of the distribution and kinematics of primary and ancillary deformation within a relay zone.

5.4. Results

Structural characterisation of extensional strains in the Krafla fissure swarm is separated into two types: (1) extension fractures that demonstrate horizontal openings but no throw and (2) normal faults that demonstrate a horizontal and vertical (throw) component of displacement.

5.4.1. Fracture Distribution and Scaling

Extension fractures in the Krafla fissure swarm form linear zones that are up to 5 km long and 5-15 m wide. These zones are dominantly located in the footwalls of NNE-SSW striking surface-breaking normal fault segments that form the bounding structures of a NNE-SSW striking graben approximately 1 km wide, ~ 10 km north of Krafla volcano (Figure 5.5).

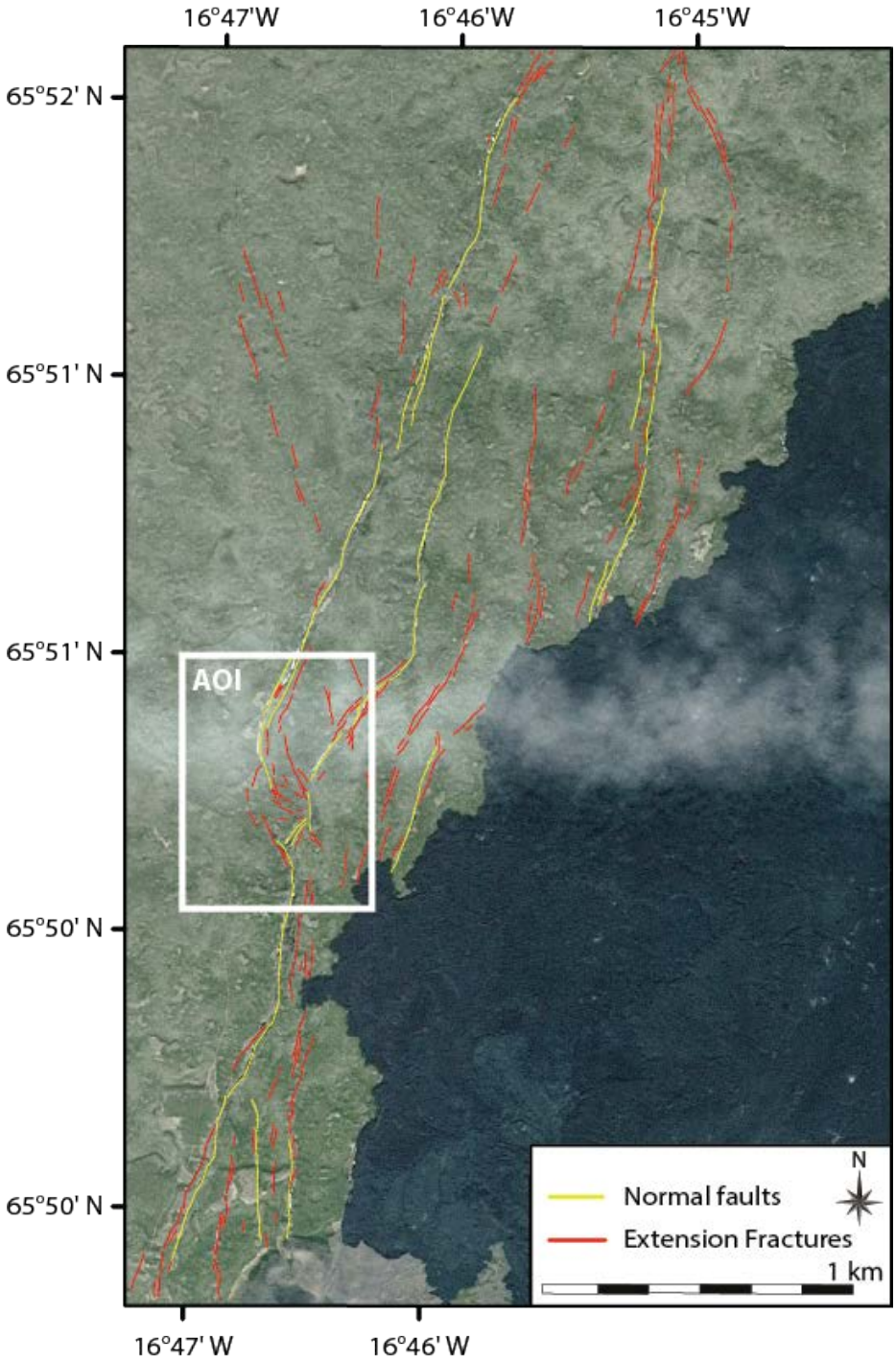

Figure 5.5. Mapped extension fractures (red polylines) and normal faults (yellow polylines) in the Gjastykki valley within the Krafla fissure swarm (remote and field-derived data). Faults form a NNE-SSW striking graben approximately 1 km wide. White box highlights the AOI shown in Figure 5.8. Satellite imagery from Google Earth™.

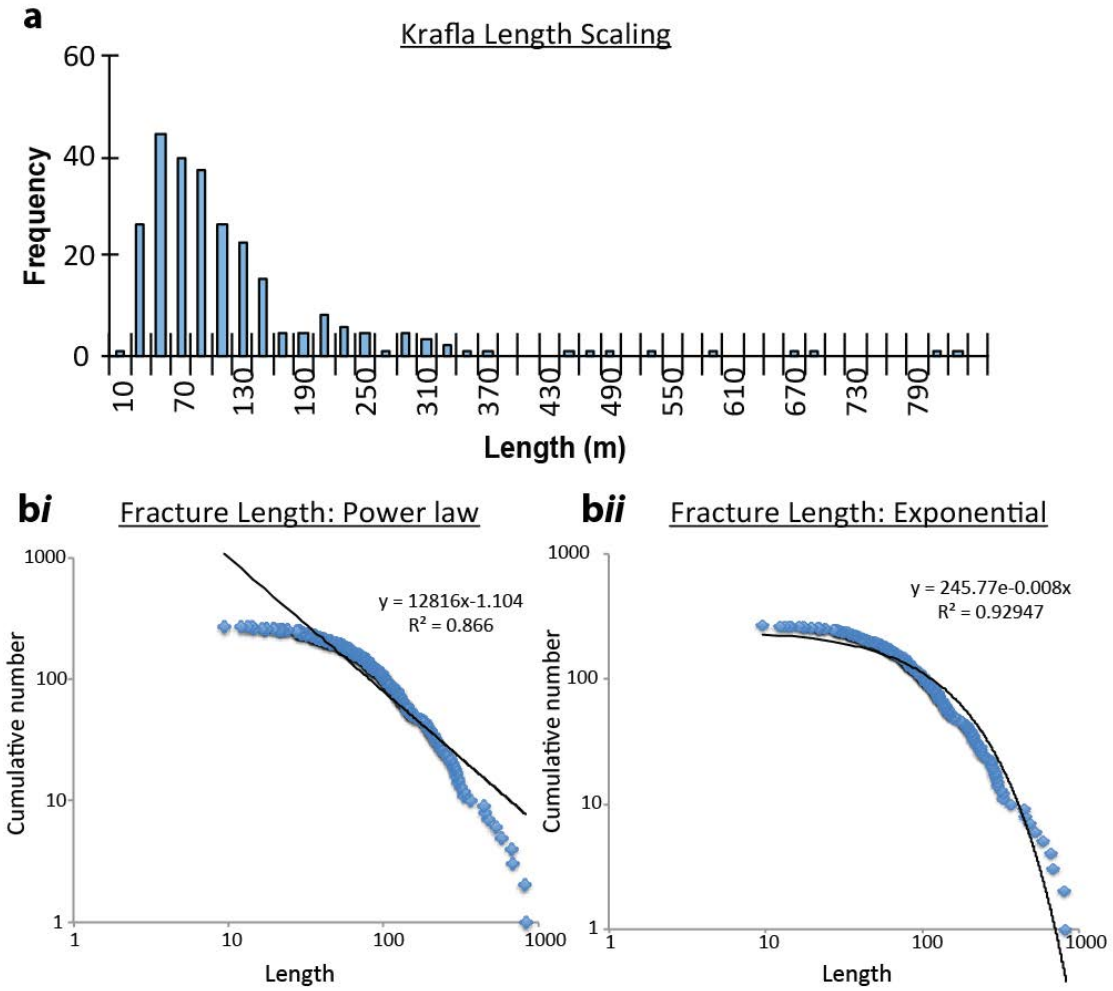

Figure 5.6. (a) Distribution of fracture lengths in the Gjastykki valley in the Krafla fissure swarm. b) Population distribution plots. *i*) Power law distribution for extension fracture length. *ii*) Exponential distribution for extension fracture length. Plots suggest fracture scaling in the Krafla fissure swarm is best described using an exponential function.

Zones of footwall extension fracturing most commonly comprise extension fractures up to ~800 m long (Figure 5.6a) and up to 4 m wide. At the metre-scale, these fractures demonstrate steps or undulations locally that are indicative of earlier linkage of smaller segments, but at the scale of the whole fracture (tens-hundreds of m-scale), traces are linear and considered composite structures: single fractures that develop through the interaction and linkage of smaller fractures. Log-log graphs of cumulative number plot against length (Figure 5.6b) indicate exponential scaling distributions. Such a distribution is consistent with extension

fracture data from the Koa'e fault system (Chapter 4) and published data from oceanic fault populations (Cowie, 1998) or vertically constrained faults (Ackermann et al., 2001). It has also been suggested that non-power law scaling may be an indicator of different processes or controls operating at different scales (Nicol et al., 1996b).

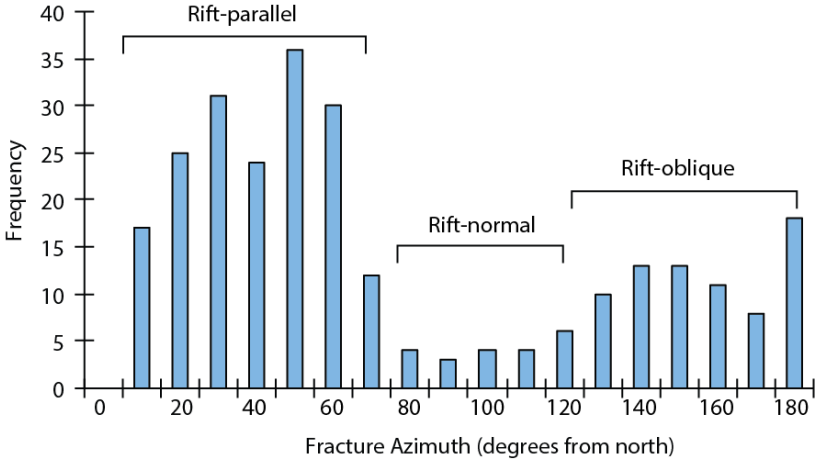

Figure 5.7. Frequency of fault and extension fracture strike orientations for traces shown in Figure 5.5.

The dominant fracture orientation in the Gjastykki Valley is NNE-SSW to NE-SW (Figure 5.7), with individual fractures extending up to 800 m in length with apertures of 2-4 m. Approximately 60% of faults and extension fractures fall into the NNE-NE to SSW-SW main rift trend, with oblique, or rift-normal structures comprising 30% and 10% of the population, respectively (Figure 5.7). Fractures outside of the main rift trend (NNE-SSW) are neither pervasive nor randomly distributed but show a close spatial association with the tip regions of en echelon rift-parallel faults.

5.4.1.1. Fracture Kinematics and Segmentation

Remote and field mapping of extension fractures in the Krafla system reveal three structural sets, which are separated based on their kinematics and orientations:

(1) **Rift-parallel** (NNE-SSW striking) sets of fractures show purely extensional openings and accommodate the regional WNW-ESE extension (red polylines, Figure 5.8).

(2) **Rift-oblique** (NW-SE striking) fractures that demonstrate a component of left- and right-lateral shear, in addition to extensional openings, accommodating a NE-SW extension (green polylines, Figure 5.8).

(3) **Rift-normal** (WNW-ESE striking) fractures that also show purely extensional openings, accommodating N-S to NNE-SSW extension (yellow polylines, Figure 5.8).

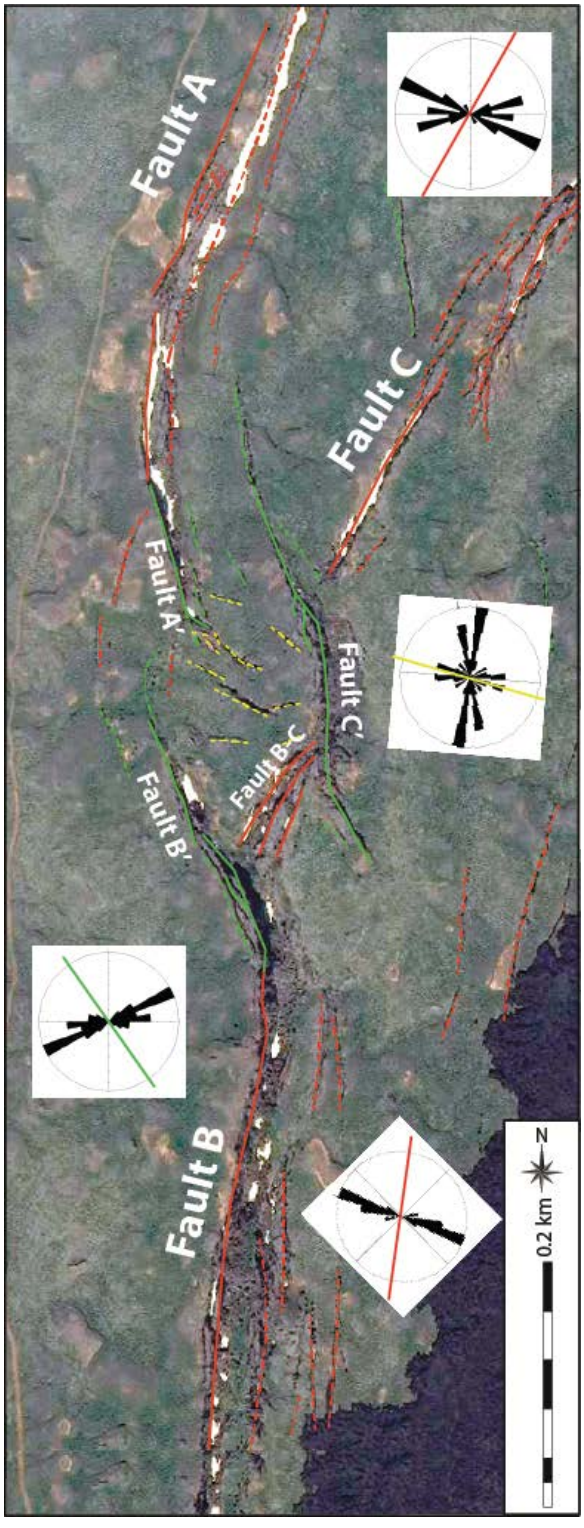

Figure 5.8. Mapped faults and fractures of the Gjastykki Valley in the AOI highlighted in Figure 6. Field mapping revealed three dominant orientations: (1) rift-parallel (NNE-SSW striking) sets of extension mode fractures (dashed red polylines) and normal faults (solid red polylines, Faults A, B, C), that accommodate WNW-ESE extension; (2) rift-oblique NW-SE striking extensional-shear fractures (dashed green polylines) and normal faults (solid green polylines) that accommodate NE-SW extension; and (3) rift-normal WNW-ESE striking extension mode fractures (dashed yellow polylines), accommodating N-S to NNE-SSW extension. Rift-oblique and rift-normal sets are localised features found at the terminations of en echelon rift-parallel faults A, B and C. Inset rose diagrams demonstrate the opening directions for each fracture set across the AOI. Satellite imagery from Google Earth™.

Rift-parallel (NNE-SSW) striking extension fractures most commonly lie in the footwall of and parallel the trend of surface-breaking normal faults throughout the Gjastykki Valley. Rift-oblique extension fractures, located in the footwall of NW-SE striking normal faults, and rift-normal extension fractures are discontinuous, local features that are identified at the terminations of en echelon rift-parallel normal faults, rather than representing rift-wide features (e.g. Figure 5.8).

Displacement-length profiles for extension fractures in the study area commonly show one or more points of displacement minima that represent former fracture linkage sites of previously en echelon or co-linear single fractures (e.g. Figure 5.9). Extension fractures may have developed initially as isolated structures that propagated towards each other with increasing extension, resulting in interaction and linkage to produce single, composite fractures.

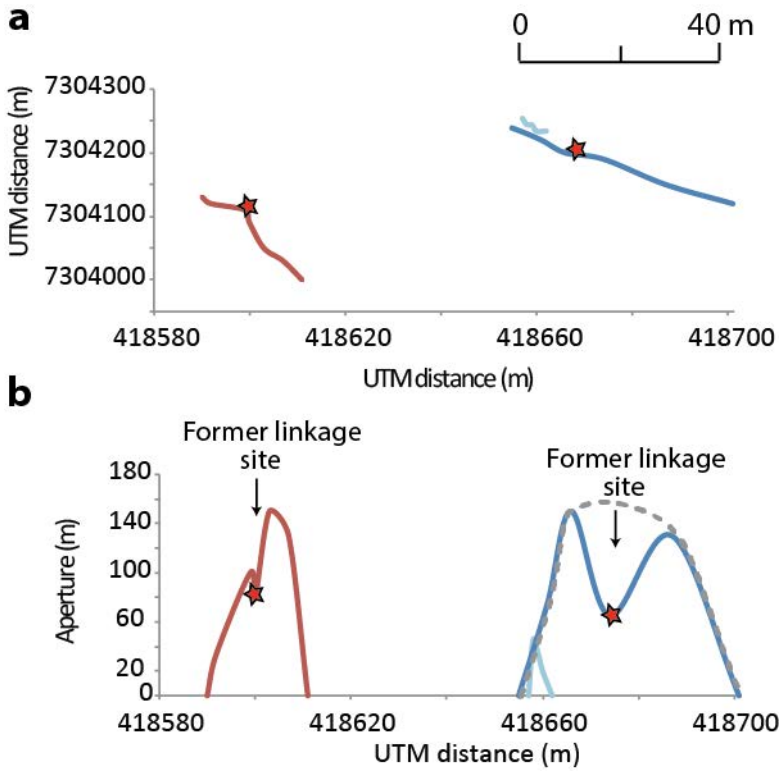

Figure 5.9. (a) An example of two composite fractures showing points of displacement minima, highlighted by red stars. b) Fracture traces show prominent bends corresponding to sites of linkage of former single fractures.

Displacement -length profiles most commonly demonstrate symmetrical displacement gradients with centrally located displacement maxima that taper towards the lateral tips of the fracture (e.g. Figure 5.9, red fracture). Sets of rift-parallel extension fractures most commonly show total displacement profiles with centrally located maxima that decrease to zero towards the lateral tips of the array, indicating that fractures comprise fully linked sets of fractures (Figure 5.10b). There are a few instances displacement-length profile asymmetry and high displacement gradients at the tips of fractures, which are an indication of fracture interaction. The greatest proportion of mapped extension fractures (70%) show centrally located displacement maxima.

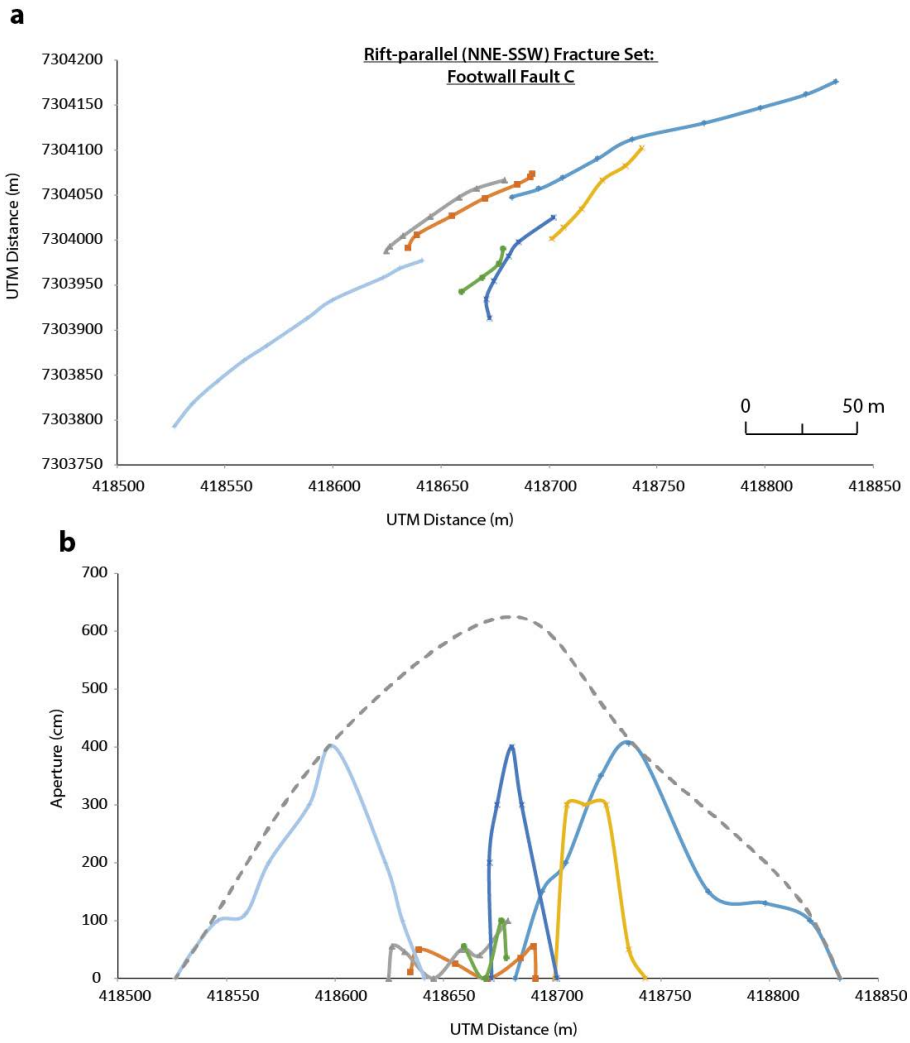

Figure 5.10. (a) Map traces for rift-parallel (WNW-ESE) extension-mode fractures located in the footwall of fault C. b) Displacement-length profiles for these fractures. Dotted grey line shows total aperture across the fracture set and indicates a centrally located aperture maxima.

Total displacement profiles for sets of rift-parallel extension fractures also show displacement maxima that are located close to the centre of the array (Figure 5.10), implying fractures are fully linked.

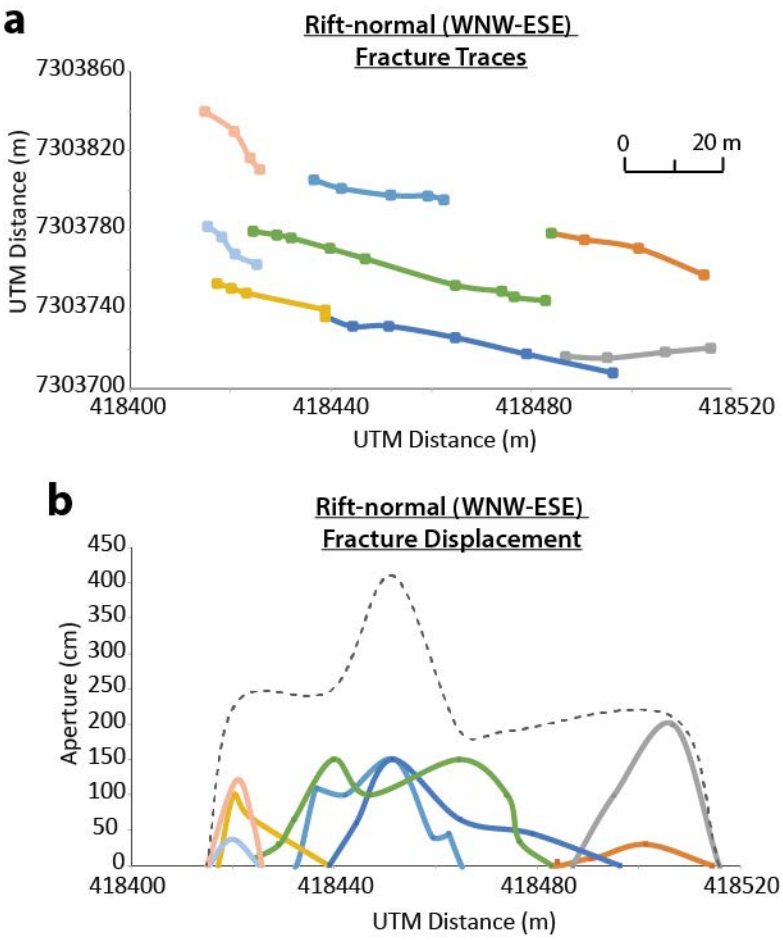

Figure 5.11. Map traces for rift-normal (WNW-ESE) extension-mode fractures (a) and (b) D-L profiles for these fractures. Dotted grey line shows total aperture across the fracture set.

Displacement-length profiles for sets of rift-normal extension fractures are more asymmetrical, and show steeper displacement gradients than rift-parallel extension fracture sets. A total aperture profile for rift-normal extension fractures is also asymmetrical, with steep gradients at both ends (Figure 5.11). This may imply that fractures in this set have not linked fully.

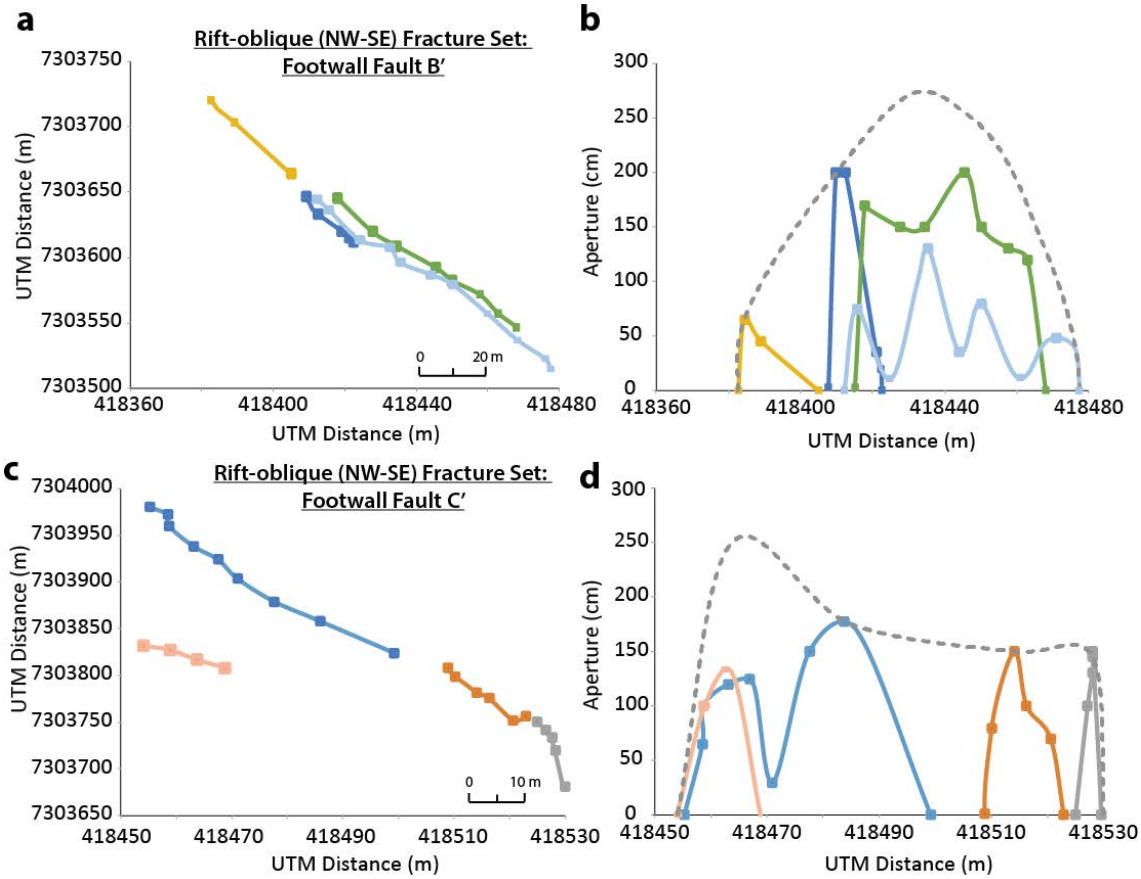

Figure 5.12. (a) Mapped traces for rift-oblique (NW-SE) extension-mode fractures located in the footwall of fault C'. b) Displacement -length profiles for fractures in the footwall of C'. c) Mapped traces for rift-oblique (NW-SE) extension-mode fractures located in the footwall of fault B'. d) Displacement -length profiles for fractures in the footwall of B'. Dotted grey lines on displacement-length profiles (b and d) show total aperture across the fracture sets.

Both individual, and total displacement-length profiles for sets of rift-oblique extension fractures show symmetrical profiles, with centrally located maximum apertures (Figure 5.12a, b). There are also examples of more asymmetrical, steep displacement gradients (Figure 5.12c, d), implying that this set have also not linked fully.

Rift-parallel (NNE-SSW) striking fractures are the most frequently observed set and show the greatest lengths (up to 800 m) in the Gjastykki Valley. Recorded apertures commonly exceed 3 m. Rift-normal (WNW-ESE striking) fractures have the smallest lengths (less than ~40

m) and apertures (up to ~ 1m) in the AOI (Figure 5.11a and b). Rift-oblique (NW-SE) striking fractures accommodate greater openings of up to 4 m (across open fault scarps), but more typically 2.0-2.5 m with lengths up to ~50 m (Figure 5.12a-d).

5.4.2. Fault Geometry and Distribution

Extensional strains in the Krafla fissure swarm are dominated by large (>15 m throw), sub-vertical surface-breaking faults that are continuous in length for 1.0-1.5 km and follow the NNE (018^{o}) strike of the NVZ. In addition to a component of throw, all surface-breaching fault segments demonstrate significant horizontal openings (up to ~4 m) along composite fracture traces, commonly between 50-100 m long but up to ~800 m long. Observable heave on these faults is negligible due to their subvertical nature. Surface-breaching fault scarps in the Krafla fissure swarm offset planar footwall and hanging wall surfaces by up to ~30 m and seldom breach areas of surface flexure (Figure 5.13a-d). Two types of fault are identified in the Gjastykki valley: (1) continuous (>0.5 km in length), linked faults; and (2) discontinuous, segmented faults. Continuous, fully linked normal fault segments form the main WNW and ESE dipping Gjastykki graben-bounding structures, and accommodate the greatest displacements in the rift zone. At map scale, traces are straight, with minor undulations occurring between formerly isolated segments, now hard-linked by obliquely oriented steps.

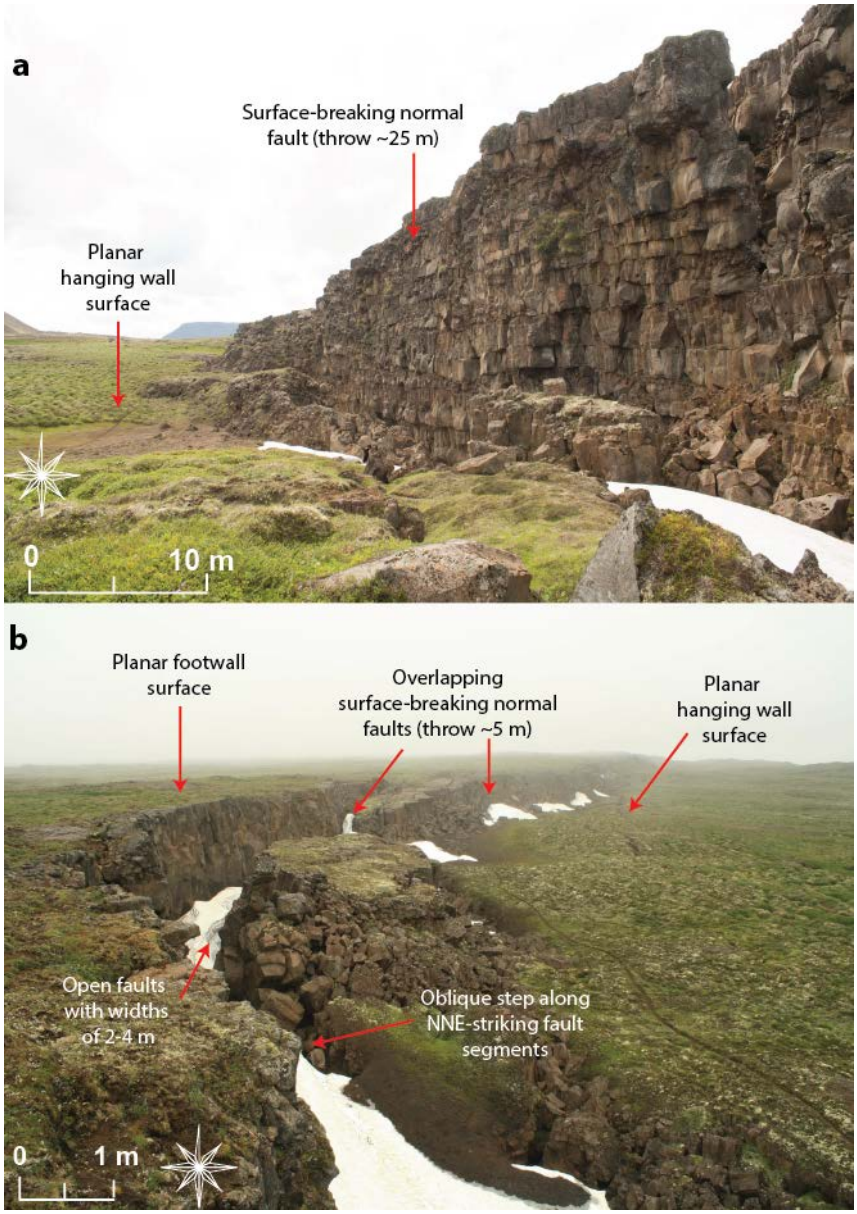

Figure 5.13. Examples of surface-breaching rift-parallel fault segments in the Gjastykki area of the Krafla fissure swarm. a) Subvertical normal faults demonstrate throws of up to 25-30 m. b) Faults are characterised by horizontal openings of 2-4 m and most commonly offset planar footwall and hanging wall surfaces.

Composite faults reach total lengths of up to 1.5 km, with centrally located throw maxima of up to 30 m and horizontal openings of up to 4 m, which are commonly filled with rubble shed from

the exposed scarp. Discontinuous faults are composed of segments with lengths <0.5 km and most commonly show orientations that are highly oblique to the main NNE-SSW trend.

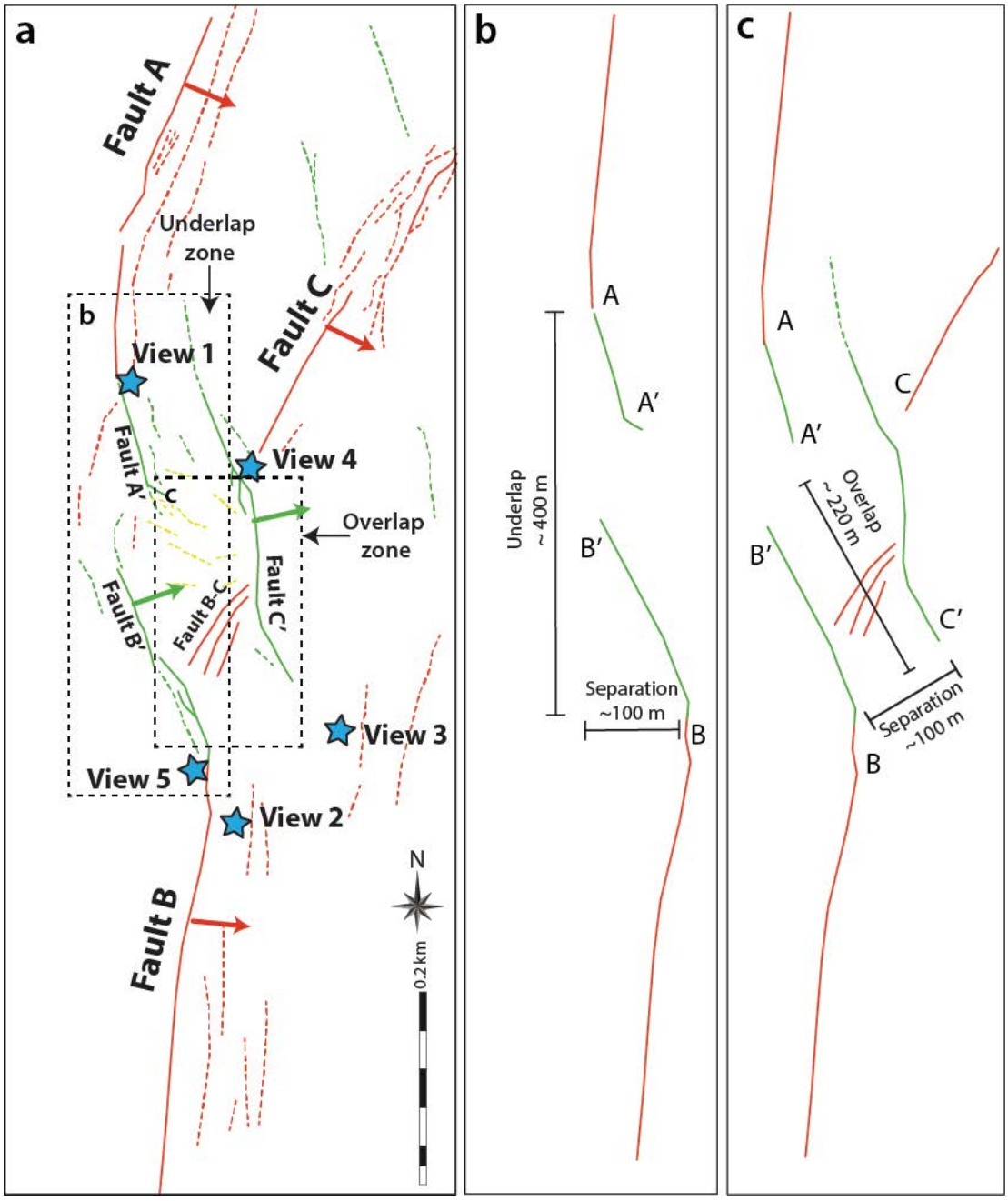

Figure 5.14. a) Obliquely oriented faults mapped in a zone ahead of NNE-SSW striking rift-fault segments: faults A, B and C. Dashed inset boxes highlight locations for (b) and (c). Coloured arrows indicate fault dip directions. b) Extent of the primary region of deformation between faults A and B. c) Extent of deforming region between faults B and C-C'. Views indicate field of view for photos that are shown in Figure 5.15.

Within the AOI (Figure 5.14a) are three continuous, rift-parallel normal faults: fault A, fault B and fault C. They do not form isolated, straight traces, but typically display curved trace pathways, away from the tips of NNE-SSW striking normal faults (Figure 5.14a). Throws are spatially variable along these faults (throws of 3-20 m: Figure 5.13a) and they commonly show strongly asymmetrical displacement gradients towards their lateral tips. Horizontal openings are 3-4 m, and are also filled with rubble as continuous examples.

Fault A: The composite trace length is ~ 1.5 km (Figure 5.5), and appears to be comprised of at least 4 linked fault segments. Maximum throws of 15 m are located towards the southern tip (Figure 5.15a).

Fault B: This fault has a composite trace length of ~1.4 km, comprising approximately 5 linked segments (Figure 5.5). Faults A and B are separated by approximately 100 m (measured parallel to dip) and underlap along strike by ~400 m. Maximum estimated throws are ~30 m for this fault (Figure 5.14b*i*). The greatest throw is located towards the northern tip of the fault where it decreases to zero over a distance of ~180 m across a NW-SE striking normal fault segment (Figure 5.15b, c).

Fault C: This fault has a total length of ~1.4 km and comprises 4-5 individual, linked fault segments. The southern 0.5 km of this fault follows a NE-SW strike towards the relay zone between faults A and B (Figure 5.5). Fault C shows vertical displacements of up to 3 m and much of this displacement is found along the NE-SW striking segment, proximally to the tips of faults A and B (Figure 5.15d, e).

The volume surrounding the terminations of faults A, B and C is a deformed zone containing WNW-ESE (rift-normal) striking extension fractures and a set of NW-SE striking extensional-shear fractures and normal faults. WNW-ESE striking extension fractures occur in the volume ahead of faults A and B. Three prominent NW-SE oriented normal faults, A', B' and C', and a series of extension fractures that also show strike-slip displacement components, show a close

spatial relationship to the tips of the bounding faults. Based on the configuration of the bounding faults, and this internal deformation, transfer of extensional strain is interpreted to be taking place and the volume is referred to as a *relay zone*.

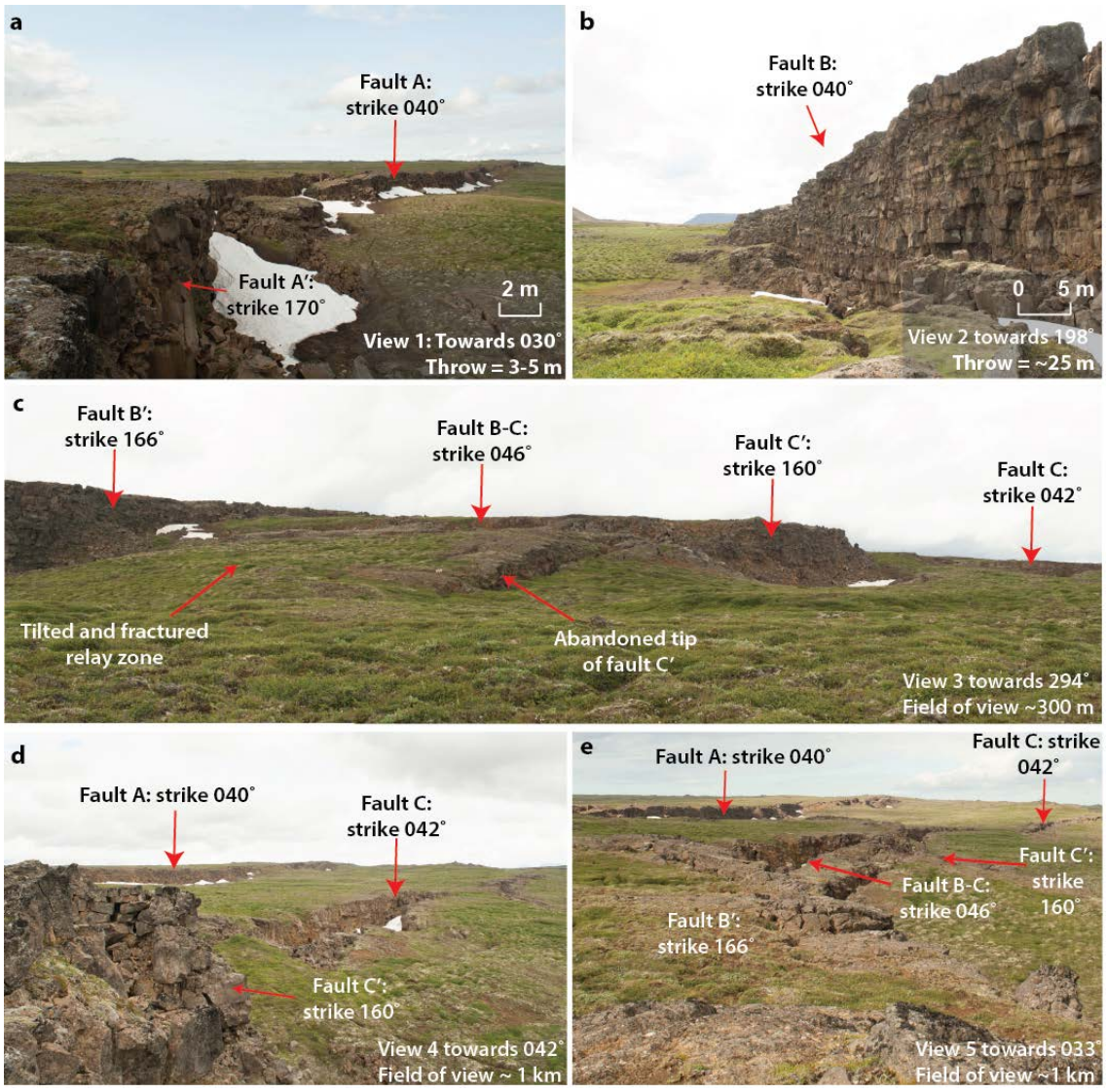

Figure 5.15. Views of faults developing in the relay zone(s) highlighted in Figure 5.14a. a) View NNE from the footwall of fault segment A' highlighting the curve of rift-parallel fault A into the relay zone. Fault A shows maximum vertical displacements of up to ~15 m. b) View south along rift-parallel fault B, showing a maximum vertical displacement of up to 30 m. c) View NNE from the footwall of fault C' overlooking the tip of fault C, which shows a maximum vertical displacement of 3-4 m that decreases oto zero over a short distance seen in the image. d) View NNE across the relay zone from the footwall (and tip) of fault B, which begins to curve towards the NW (becoming fault segment B'). To the north are rift-parallel faults A and C

and linking fault B-C. e) View WNW across the relay zone between fault B' and C' highlighting the abandoned tip of C' and rotation of the volume between B' and C'. Fault C' shows a maximum displacement of ~15 m.

Fault A': This fault segment forms the southernmost ~100 m of fault A. It has a maximum throw of ~5 m and follows a NW-SE trajectory rather than the NE-SW orientation of fault A (Figure 5.15a).

Faults B' and C': These faults are both 150-200 m long and have displacements of up to ~20-30 m. Fault B' is the northernmost segment of fault B and follows a NW-SE trajectory in the vicinity of fault A. Fault C' also follows the same NW-SE trend but appears to be a separate segment, developing ahead of the tip of fault C.

With the growth of faults B' and C', an additional zone of dense fracturing, horizontal axis rotation (to the south) and inferred displacement transfer, has developed between them (Figure 5.16c, e). This second relay zone is ~100 m wide and bound by faults B' and C', which have an overlap of ~220 m (Figure 5.14bii). Internal to this second relay zone are a set of NNE-SSW (rift-parallel) striking extension fractures and a normal fault that show apertures of 2-3 m and throw of ~2 m and (fault B-C: Figure 5.15e).

The terminations of faults A and B at the map scale appear to comprise single, broadly straight segments (Figure 5.16a). Field mapping of these faults reveals a more complex configuration, with the fault bends composed of a series of smaller co-linear, or overlapping curved segments that show a progressive rotation in their strike orientation around the bend into the relay zone (Figure 5.16, *i-iii*).

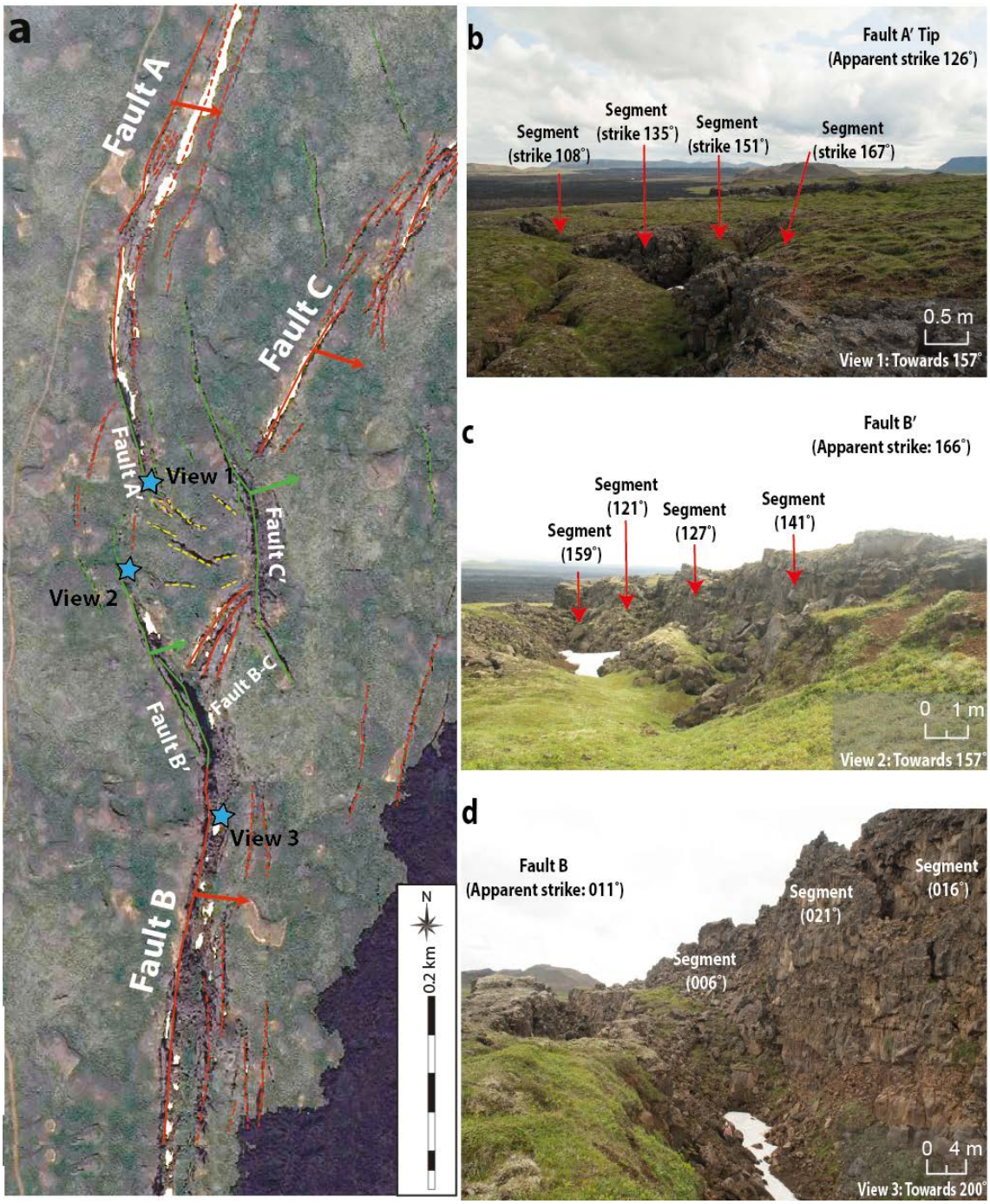

Figure 5.16. a) Mapped faults (and extension fractures) in the AOI and viewpoints of curving portions of normal fault scarps. Faults appear to comprise single segments that show gently curving geometries into the relay zone. At the tens of metre scale, the segments are composed of multiple, kinematically coherent fault segments that overlap one another and show gradual rotations in their strike dimension (b-d).

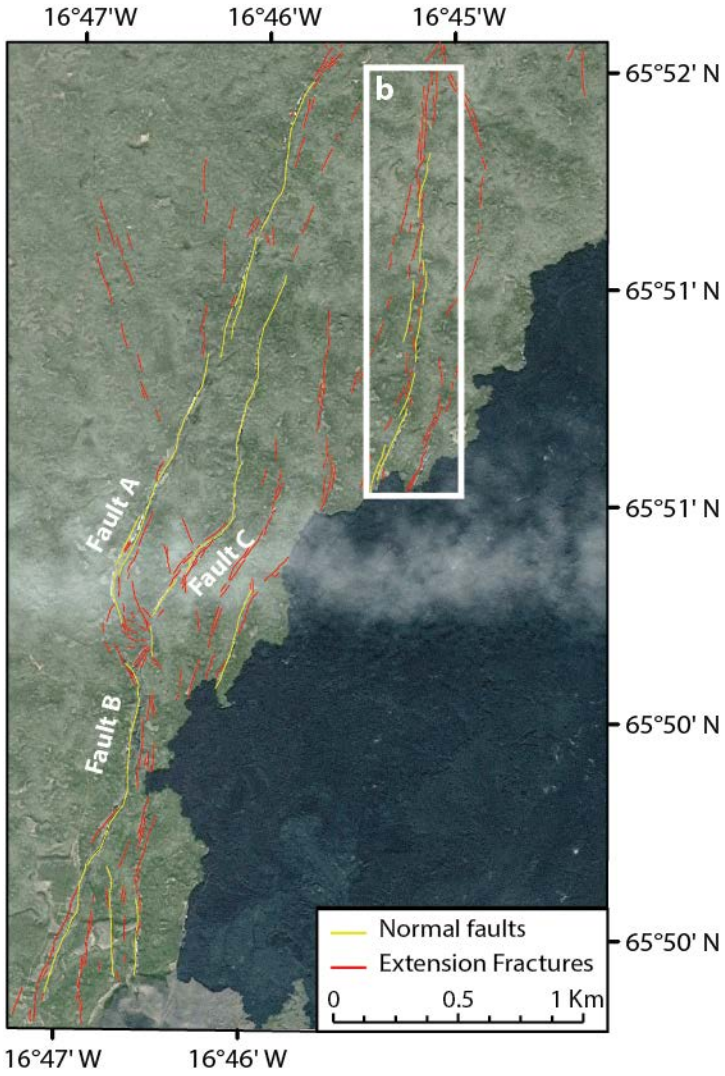

Figure 5.17. A minor graben is identified along the eastern set of normal faults that bound the Gjastykki graben. Observations that were made here are highlighted in Figure 5.19. Major faults investigated are also highlighted.

In addition to the main Gjastykki rift graben, fault mapping has also revealed a second graben along the main eastern bounding fault (Figure 5.17, inset box). The graben follows the NNE-SSW main rift-fault trend for a distance of approximately 3 km and shows a near constant width of ~50m for much of its length. Deformation within it is dominantly localised on the eastern (west dipping) bounding fault, which also bounds the main Gjastykki valley graben and comprises continuous fault segments with maximum throws of 20-30 m (Figure 5.18a and b).

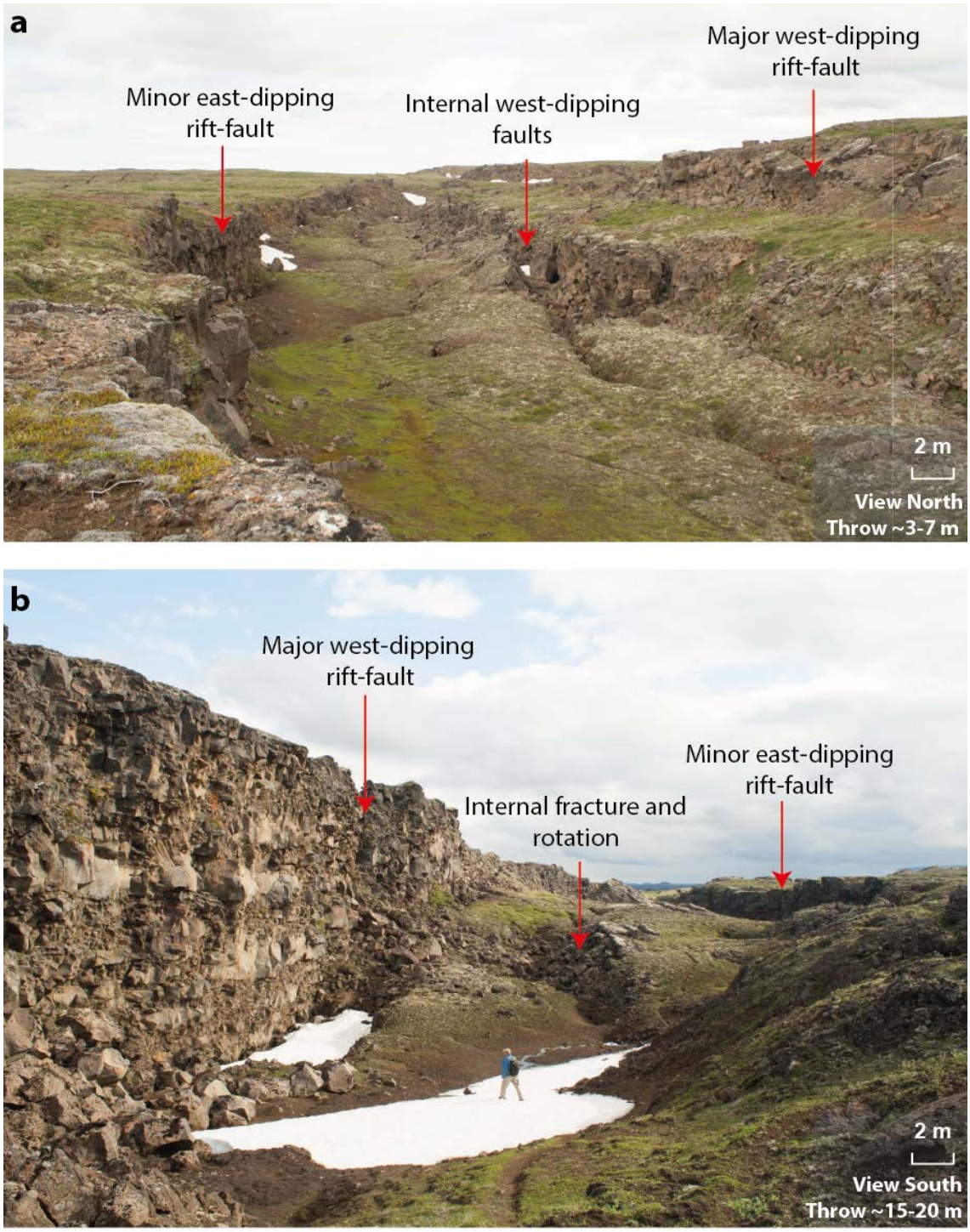

Figure 5.18. A NNE-SSW striking minor graben ~3 km long and up to 50 m wide along the eastern margin of the Gjastykki valley (see inset box in 5.17 for location and extent). East and west dipping bounding faults show throws of 5-30 m. The floor of the graben is disrupted in numerous places by internal east and west-dipping faults, extension fractures and flexure.

The eastern (west-dipping) bounding fault comprises segments between 0.2-0.5 km long with maximum throws of ~7 m (Figure 5.18a). Approximately 40% of the inferred fault trace is composed of surface-breaking fault segments; the other 60% features flexure of the ground surface where the amplitude of the flexure typically matches the amount of throw on adjacent fault segments. Internal to the graben are a series of segmented, subsurface (manifest as monoclinal surface flexures) and surface-breaking normal faults, synthetic to the eastern bounding fault (Figure 5.18a and b). These internal faults and flexures are typically <200 m longand, show maximum throws or heights of ~3 m. Such fault patterns have been recorded in Iceland in previous studies and have been attributed to dike emplacement at depth (e.g. Tentler, 2005).

5.4.2.1. Fault Kinematics and Segmentation

Continuous sub-vertical normal faults in the Gjastykki valley most commonly follow the NNE-SSW rift trend, and accommodate a rift-normal (WNW-ESE) extension (red set; Figure 5.19a, b). Discontinuous NW-SE striking faults, with orientations oblique to the main rift trend, have been mapped in a zone of complex deformation surrounding the terminations of rift-parallel normal faults and show normal-sense displacements across fault scarps that dip towards the NE (Figure 5.19b). The walls of extension fractures in the same trend show left- and right-lateral strike-slip components of displacement, in addition to horizontal opening. Orientations may imply the formation of conjugate fracture sets (Figure 5.20a). Lateral slip has not been observed across fault segments B', A', and C' due to their open nature when they reach the surface (i.e. no slickenlines) and the degree of wall collapse that has taken place. They are therefore interpreted to be normal faults but dip-oblique kinematics on these structures cannot be ruled out.

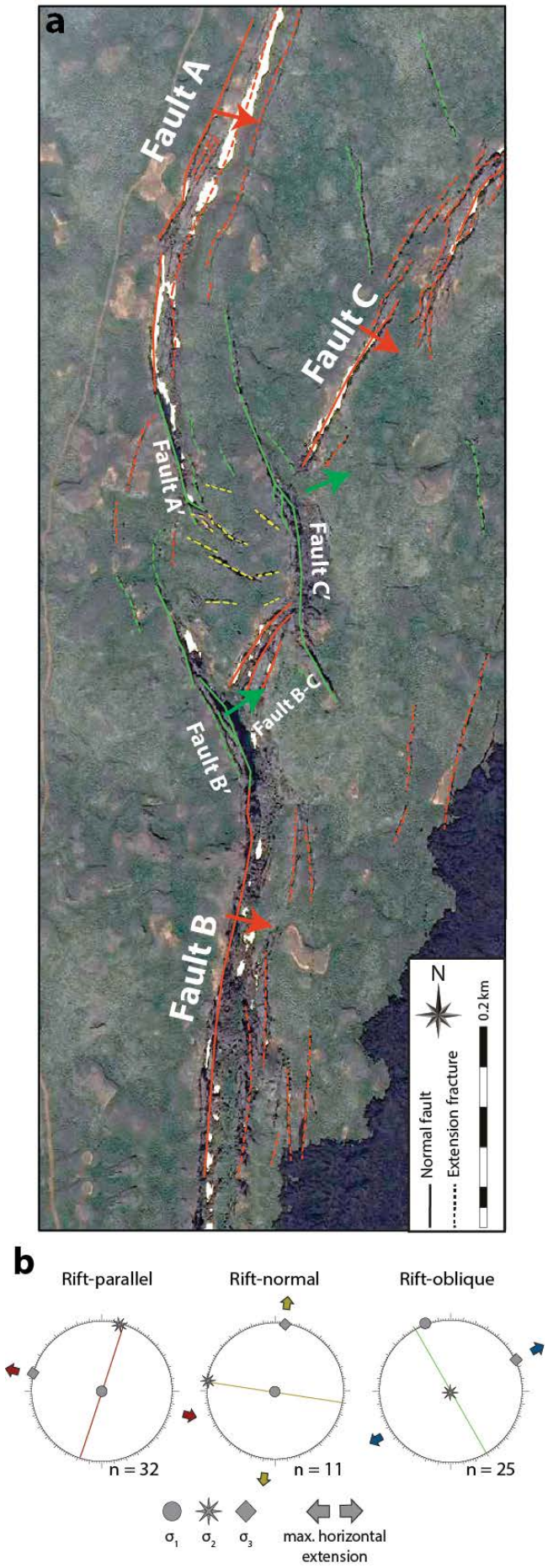

Figure 5.19. a) Mapped fractures and faults in the study area, colour-coded based on orientation and opening mode: (1) rift-parallel normal faults (solid red polylines) and mode-I fractures (dashed red polylines); (2) rift-oblique extensional-shear (mixed-mode) fractures (dashed green polylines) and normal faults (solid green polylines); and (3) rift-normal extension fractures (dashed yellow polylines). Coloured arrows indicate fault dip direction for each set. b) Lower hemisphere stereographic projections summarise fault/fracture orientations and measured extension directions for each of the three structural sets. Principal compressive stress axes (where $\sigma_1 > \sigma_2 > \sigma_3$) are calculated using Win-Tensor (see Delvaux and Sperner, 2003).

The combined result is (1) **rift-normal** (WNW-ESE) extension regionally, and external to the primary relay zone; (2) **rift-parallel** (N-S to NNE-SSW) and oblique (NE-SW) extension internal to the primary interpreted relay zone; and (3) **oblique** (NE-SW) and **rift-normal** (WNW-ESE) extension internal to the second interpreted relay zone (Figure 5.19a, b).

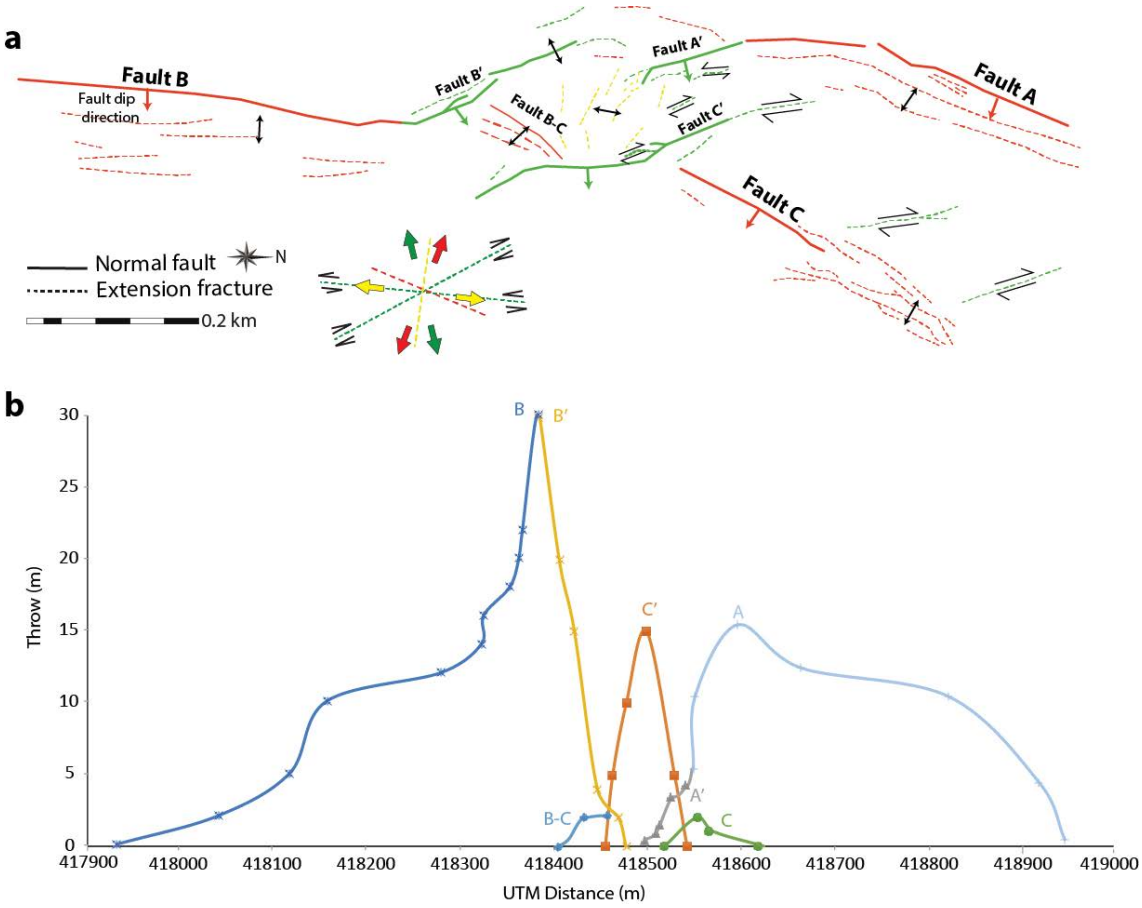

Figure 5.20. (a) Summary of mapped faults and fractures, showing estimated extension directions for each structural set. Black arrows indicate extension directions across each set, which are based on rose plots from Figure 5.8. Coloured arrows indicated fault dip directions for each set. b) Estimated throw profiles for faults in the AOI**.** Faults A', B' and C' are labelled as separate segments of primary normal faults A, B and C because their formation is associated with local stress effects, rather than regional tectonics and because extension directions are different to the primary faults.

Fault A: This normal fault trends NNE-SSW and accommodates WNW-ESE (rift-normal) extension (Figure 5.19a and b). Estimates of throw along the scarp of fault A shows an asymmetrical displacement profile, with a maximum of ~15 m located at the southern termination where the trace curves into the orientation of normal fault A' (Figure 5.20a, b) and the displacement decreases steeply where this takes place.

Fault B: This normal fault trends NNE-SSW and accommodates WNW-ESE (rift-normal) extension (Figure 5.19a, b). Estimates of scarp height along fault B also shows an asymmetrical displacement profile, with a maximum of ~25-30 m located at the northern termination where the trace curves into the orientation of fault B' (Figure 5.20a, b).

Fault C: The southernmost 0.5 km of this normal fault trends NE-SW and accommodates NW-SE extension. The remaining 1 km of the total fault trace trends NNE-SSW, accommodating WNW-ESE (rift-normal) extension (Figures 5.17 and 5.19a, b). Estimates of scarp height along fault C show an asymmetrical displacement profile, with a maximum throw of ~3 m, which is located at the southern termination where the trace abuts the NW-SE striking fault C' (Figure 5.20a, b).

Fault B': This normal fault segment has propagated from the tip of fault B, following a NW-SE trajectory and accommodating NE-SW (rift-oblique) extension (Figure 5.19 a and b). Maximum throw occurs where fault B bends into the orientation of segment B' (25-30 m) and decreases rapidly to zero at the NW-tip, over approximately 100 m (Figure 5.20a, b). The result is a high displacement gradient on fault B into the relay zone.

Fault A': This normal fault segment has propagated from the tip of fault A and follows a NW-SE trajectory, accommodating NE-SW (rift-oblique) extension (Figure 5.19a and b). Throw decreases from a maximum of ~5 m, at the tip of fault A, to zero at the SE-tip over approximately 50 m (Figure 5.20a, b). The result is a high displacement gradient on fault A into the relay zone.

Fault C': This normal fault segment follows a NW-SE trajectory, accommodating NE-SW (rift-oblique) extension (Figure 5.19a and b). Estimates of scarp height along this fault show a relatively symmetrical displacement profile, with a maximum of ~15 m that is located centrally along the fault trace and decreases to zero towards the NW and SE terminations (Figure 5.19a, b).

Fault B-C: This normal fault has developed in the overlap zone between fault B' and C' and follows a NNE-SSW trajectory, accommodating WNW-ESE (rift-normal) extension (Figure 5.19a and b). Estimates of scarp height along this fault also shows a highly asymmetrical displacement profile, with a maximum of ~2 m that is located centrally along the fault trace and decreases to zero towards the SSW terminations but remains at this value where it abuts fault C' (Figure 5.19a, b).

5.4.3. Surface Flexure

Deformation in the Krafla fissure swarm is largely characterised by surface-breaking faults, with very few examples of surface flexure observed. Where present, the crests of the flexures follow the same NNE-SSW trend of laterally continuous rift faults and extension fractures in the rift zone. The flexures are always contiguous with these structural features. Observed surface flexures are split into two types based on their morphology and spatial extent: (1) laterally continuous and (2) laterally discontinuous. Laterally continuous flexures are rarely breached by surface-breaking faults and examples of *breached* laterally discontinuous flexures have not been observed. Zones of laterally continuous flexure show low amplitudes (<10 m) and rounded morphologies with open fractures along the upper surface, which show occasional breaching by normal fault segments with typical offsets of 0.5-1.0 m across open fractures (Figure 5.21a*i*). Where flexures are breached early in their development, amplitudes are <2 m and extensional strains are localised on the breaching fault segment (Figure 5.21a*i*, *ii*).

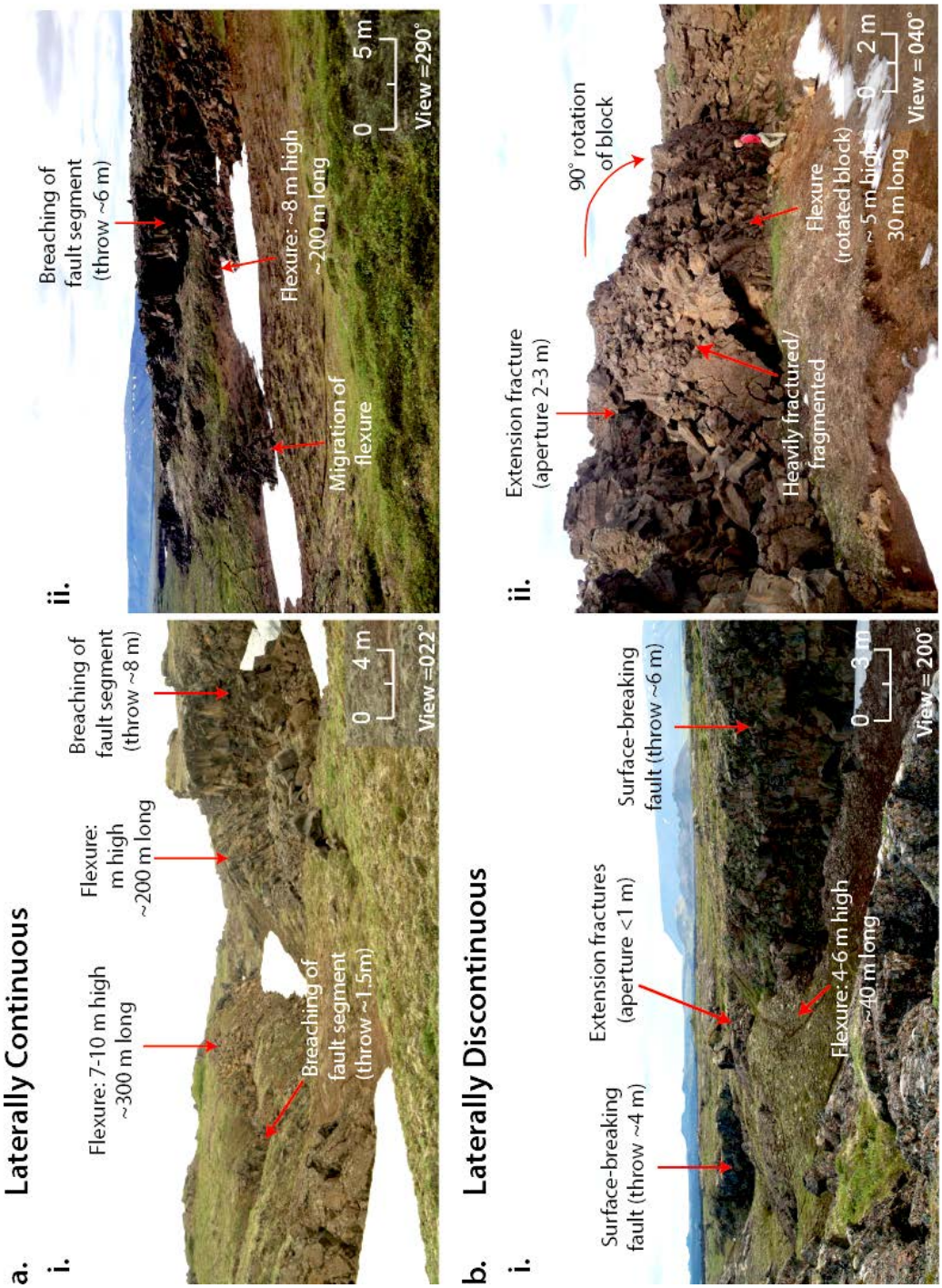

Figure 5.21. Examples of surface flexures in the Krafla fissure swarm: a) laterally continuous and b) laterally discontinuous. Continuous flexures show lengths of several hundred metres and variable amplitudes that commonly show sections that are partly breached by normal fault segments (a*i*). In some instances flexures are breached early by fault segments leaving an amplitude of ~2 m (a*ii*). Coupled with ~ 6m of throw on the breaching fault segment, the total vertical displacement in this example is comparable

to throw on purely surface-breaking segments of co-linear faults. Image also shows the initiation of new flexure in the hanging wall ahead of a previously breached zone of flexure. Discontinuous flexures are shorter in length (<50 m) with amplitudes that match the throw on adjacent fault segments (b*i*) or they are strongly fragmented and rotated; these are referred to as rotated hanging wall blocks (b*ii*).

In some instances, after breaching of a flexure has taken place and faults have accrued several metres of throw, new flexures begin to develop in the hanging wall (Figure 5.21a*ii*). Zones of laterally discontinuous flexure are less common, but where they do exist, tend to be short (<50 m long) and associated with co-linear or overlapping surface-breaking normal fault segments (Figure 5.21b*i*). These discontinuous flexures show heavily fractured or disintegrated morphologies that demonstrate rotations of up to 90° in some places (Figure 5.21b*ii*).

Surface flexures of either type are relatively rare in the Krafla fissure swarm and do not represent characteristic features of all faults, as predicted in existing models. They are most commonly identified in the narrow graben that is highlighted in Figure 5.17, where they comprise >60% of some inferred fault traces.

5.5. Discussion

Crustal extension is known to take place through the heterogeneous distribution of normal faults in a range of extensional settings (e.g., Nelson, 1992; Trudgill and Cartwright, 1994; Gawthorpe et al., 1997; Cowie, 1998; Faulds and Varga, 1998; Peacock, 2002). The preceding chapters have shown that intrinsic segmentation in basaltic sequences is influenced by different controls depending on the scale of observation. A sub-layer (mm-m scale) segmentation is controlled by: (1) the mechanical controls imposed by the variable physical (e.g. porosity) and elastic (e.g. Young's modulus) properties of the deforming sequence; and (2) the distribution, orientation, continuity and geometry of cooling joint networks. Segmentation beyond this scale

in the Koa'e fault system appears to be related to variations in locally applied stresses associated with magma emplacement within the shallow crust of the rift zone (see Chapter 4). The temporal and spatial distribution (as well as magnitude) of magma supply and emplacement defines a second, magma-driven segmentation that operates at the hundreds of metre-kilometre scale. This scale is more pronounced in the Krafla fissure swarm where there is a dominance of surface-breaking normal faults with throws >20 m.

5.5.1. Segmentation and Interaction in the Krafla Fissure Swarm

Two fracture categories are identified in the Krafla fissure swarm, based on the shape of displacement profiles and fracture propagation pathways: (1) interacting, en-echelon (apertures < 1.5 m); and (2) linked, composite fractures (commonly breached) with apertures > 1.5 m. There are relatively few examples of isolated, non-interacting fractures, implying that the population is experiencing a stage of linkage and localisation rather than formation of new structures. The greatest extension (fracture aperture, or fault throw) in the rift zone is accommodated by rift-parallel (NNE-SSW striking) extension fractures and normal faults that demonstrate a WNW-ESE extension direction. Within the relay zones described in the AOI, the greatest extension is taken up on NW-SE striking normal faults and extensional-shear fractures producing a NE-SW extension direction (Figures 5.19b and 5.20a). Evidence for extension fracture or normal fault interaction is interpreted using the geometry of observed fracture and fault traces, the asymmetrical geometry of displacement profiles and their distributions.

5.5.1.1. Evidence for Segmentation and Interaction: Path Geometry

Examination of the geometry of fracture propagation pathways at the metre- to tens of metre-scale provides a first order interpretation of the in-situ stresses responsible for fracture

development in the Krafla fissure swarm. In Chapter 4, extension fracture propagation pathways are shown to reflect the relative contributions of local (induced) vs. regional (applied) stresses during their evolution. Propagating fracture tips follow modified trajectories as controlled by the local redistribution of stress surrounding en echelon fracture tips, resulting in the characteristic hook-shaped fracture geometry (e.g., Gudmundsson et al., 1993; Acocella et al., 2000).

Mapped fractures at the m-scale and faults at the km-scale in the Krafla fissure swarm show dominantly straight or gently sinuous propagation pathways. Instances of convergent or divergent pathways and asymmetrical displacement gradients have been observed; these are associated with areas of en echelon normal faults. In the AOI, fault segments show a marked departure from the main NNE-SSW rift trend to a NW-SE orientation towards their tips with the introduction of obliquely oriented (NW-SE) normal fault and extensional-shear fracture segments and WNW-ESE oriented extension fractures (Figure 5.19, Figure 5.22).

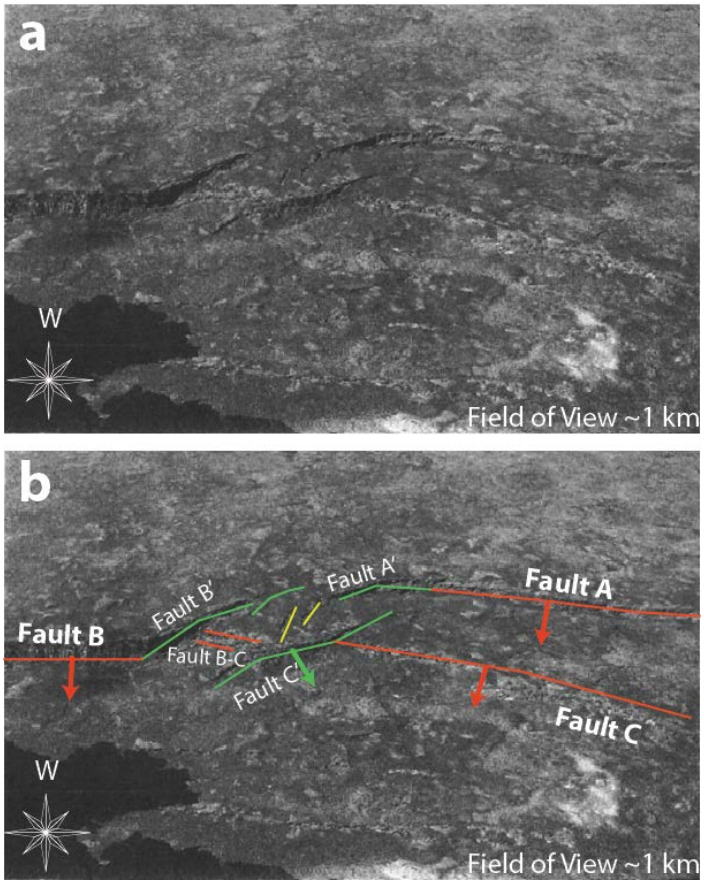

Figure 5.22. Oblique aerial view of the AOI in the Gjastykki valley (a) with fault and fracture sets highlighted (b) (aerial image taken from Opheim and Gudmundsson, 1989). Coloured arrows indicate fault dip directions.

The orientation and kinematics of the deformation in this zone is consistent with existing interpretations of the distribution of fractures, and their associated geometries and kinematics based on analytical solutions of interacting cracks. Local perturbations of the remote stress (Figure 5.23) and variations in the ratio of mode-I and mode-II stress intensity factors (K_I and K_{II} respectively) occur as a result of the mechanical interference of neighbouring crack tip stress fields (Pollard et al., 1982; Pollard and Aydin, 1984; Olson and Pollard, 1989; Engelder, 1993).

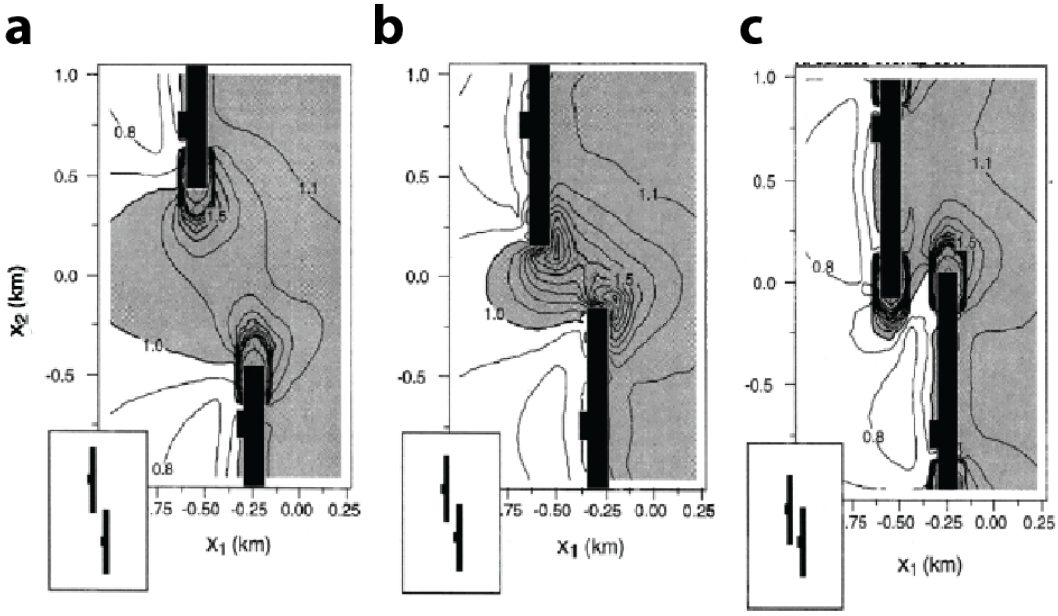

Figure 5.23. Distribution of maximum shear stresses in the relay zone between propagating en echelon normal faults. As the overlap reduces to zero, shear stress contours within the relay rotate through ~90° from the bounding fault structures (from Crider and Pollard, 1998).

For a single fracture experiencing zero shear stress, the K_{II} stress intensity factor is also zero and the fracture will follow a straight propagation pathway. As a consequence of the progressive mechanical interference of the opposing stress fields of en echelon cracks, Coulomb shear stress within the overlap zone will increase (Figure 5.23a, b and c) and fractures will develop under a combination of induced mode I/II loading. When the stress intensity factor at a fracture tip exceeds the fracture toughness of the host material, multiple sets of extensional and

extensional-shear ancillary faults and fractures develop to accommodate the locally increased strains in this region (Segall and Pollard, 1980; Renshaw and Pollard, 1994; Crider and Pollard, 1998). Predictions are consistent with the curved, "hook-shaped" propagation pathways of faults A, B and C', which are inferred to be responsible for transfer of extensional strain in the relay zone. Similar patterns of deformation have been described for fissure swarms across Iceland (e.g. Gudmundsson, 1992; Acocella et al., 2000; Grant and Kattenhorn, 2004; Hjartardöttir, 2010; Hjartardöttir and Einarsson, 2012). Two types of fracture linkage have been identified in the Vogar and Thingvellir fissure swarms in southern Iceland: (1) non-overlapping (between co-linear fractures), and (2) overlapping en echelon fractures that display curved fracture pathways (Acocella et al., 2000; Villemin and Bergerat, 2013). Remote and field mapping of fractures in these areas recognise similar strain distributions: dominant NE-SW fracture sets that are parallel to the trend of normal faults across the region, with oblique and sub-parallel fractures forming subordinate sets (Bergerat et al., 1999; Villemin and Bergerat, 2013). Where kinematic measurements of individual fractures have been collected, fractures demonstrate purely extensional openings on straight fractures that strike parallel to the main (NE-SW) seismogenic faults, and locally reoriented extension directions and strike-slip components occur on curved portions of overlapping fractures (Acocella et al., 2000).

5.5.1.2. Evidence for Segmentation and Interaction: D-L Profiles.

Profiles for many of the mapped extension fractures show centrally located displacement maxima with some undulations in their profile (i.e. they are not smooth bell-shaped curves). Total displacement profiles and extension fracture path geometries are consistent with that of a series of initially segmented fractures that have evolved into composite fractures through the process of interaction and linkage. The traces of surface-breaking normal faults show gentle sinuosity with minor deviations from the regional NNE-SSW rift trend (at the total length scale),

and maximum throws that are most typically located centrally along the fault traces. This is not the case in the AOI, where interaction of fault segments is interpreted to be taking place based on: (1) the asymmetry of throw profiles; (2) the curved trajectories that the main fault segments follow; and (3) the distribution of minor, obliquely oriented deformation at their lateral tips. Displacement profiles for the primary rift faults in the AOI show displacement maxima that are located at towards their terminations, where they curve into the relay zone. Here, throws of up to 25 m decrease to zero across a short distance. Findings are consistent with the high elastic strains and restricted propagation associated with models of displacement transfer (e.g. Childs et al., 1995; Hus et al., 2006).

5.5.2. Lateral Fault Propagation

The distributions, kinematics and geometries of fault and fracture sets in the overlap zone in the AOI are consistent with existing analogue models of en echelon fractures (e.g. Figure 5.24 a*i*, a*ii:* Tentler and Acocella, 2010); such models are used here to aid the interpretation of an incremental evolution for the relay zone in the AOI. Structural mapping of fault sets has revealed the following normal fault sets that are associated with the tip regions of NNE-SSW striking normal faults (Figure 5.24, b and c*i*): (1) ESE-WNW striking extension fractures, accommodating a rift-parallel (N-S to NNE-SSW) extension (Figure 5.24, b (yellow set) and *cii*) (2) NW-SE striking normal faults and oblique-extensional fractures, accommodating NE-SW extension (Figure 5.24, b (green set), *ciii*), and (3) NNE-SSW striking normal faults and extension fractures, accommodating the regional ESE-WNW extension. There are no examples of rift-parallel extension on rift-normal strike-slip (transfer zone) faults within the AOI; each normal fault and extension fracture set accommodates a unique extension direction, consistent with a progressive clockwise vertical axis rotation in extension direction, resulting in local and regional extension taking place simultaneously with continued extension on the bounding faults (Figure

5.24, c,*iv*). On the basis that obliquely oriented structures are spatially limited to relay zones between en echelon rift faults, it is inferred that progressive interaction is responsible for their development, and the following evolution is proposed:

Stage I: Initiation of segmented NNE-SSW striking normal faults (fault A and B), with networks of extension fractures developing in their footwalls. Normal faults and extension fractures accommodate the regional WNW-ESE extension direction (Figure 5.24b: red set; c*i,* d*i*).

Stage II: Continued lateral propagation and initial mechanical interaction of the stress fields surrounding the tips of en echelon fault segments A and B results in perturbed stresses and the development of a relay zone. Based on analogue models of en echelon extensional faults, the configuration of left-stepping en echelon faults A and B is predicted to result in minor *clockwise* vertical axis block rotation (Tentler and Acocella, 2010). Continued propagation of faults A, B and C along modified trajectories produces obliquely oriented segments A', B' and C'.

Stage III: With continued extension, oblique and rift-normal normal faults and extension fractures develop within the relay zone (Figure 5.24b: c*ii*, c*iii*, d*ii*). There is little evidence for horizontal-axis rotation in this relay zone; this may be because the volume is so deformed, or because inelastic break down took place relatively rapidly. The relative timing of these sets is unknown: development of rift-normal extension fractures followed by partial tip propagation of faults A/A' and B/B' along modified trajectories, and growth of fault C, or vice versa.

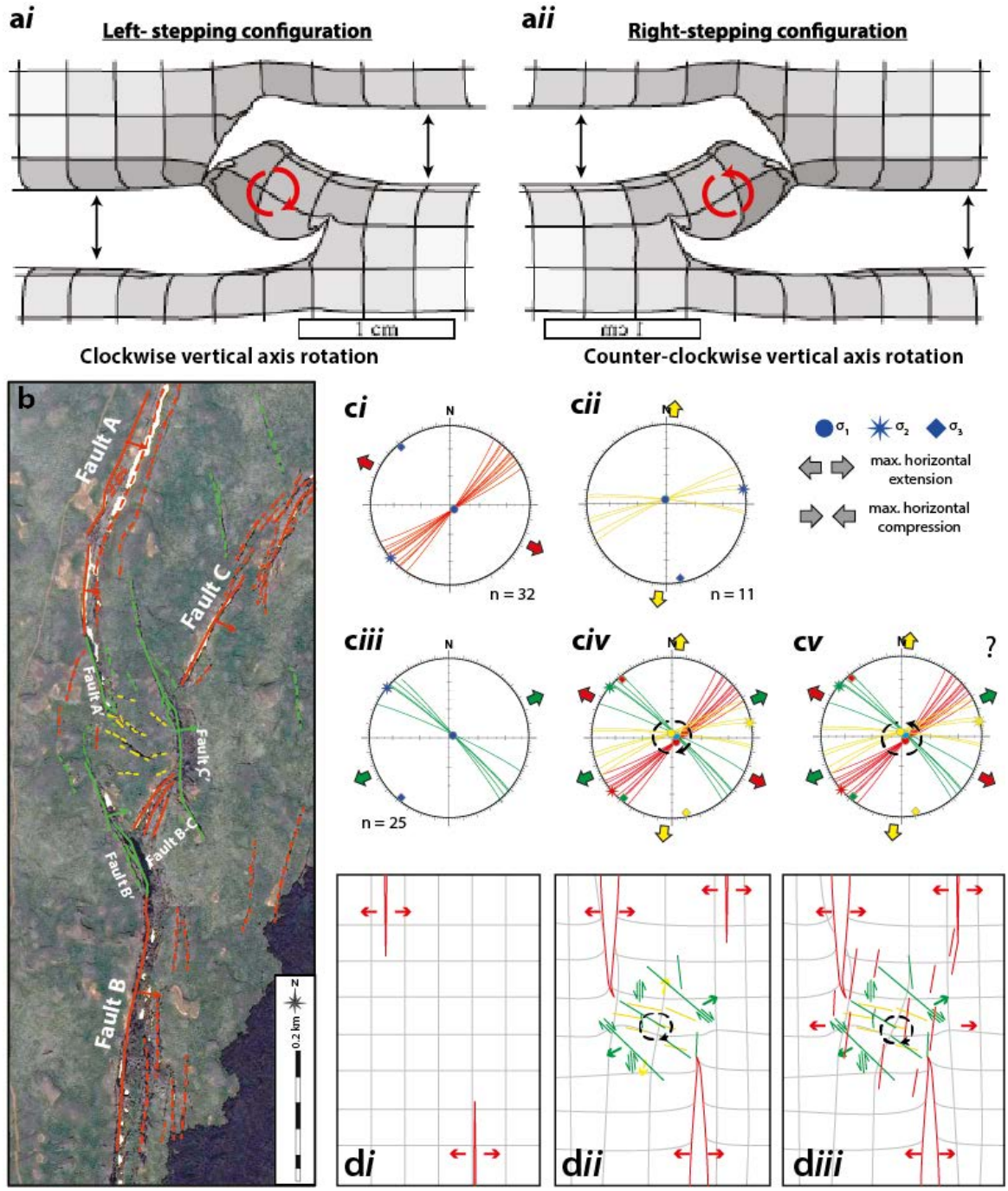

Figure 5.24. a) Modelled strain fields surround two interacting fractures (darker grey is higher strain intensity) based on the analogue models of Tentler and Acocella (2010) showing a (i) left-stepping en echelon fracture configuration, resulting in a clockwise vertical axis rotation and (ii) a right-stepping fracture configuration that produces a counter-clockwise vertical axis rotation (ii). b) Mapped faults (solid polylines) and extension fractures (dotted polylines) in the AOI in the Krafla fissure swarm. Coloured arrows indicate fault dip directions. c) Individual stereographic projections for each structural set (c*i-iii*) and a combined stereographic projection summarizes the clockwise rotation in extension direction from

the regional ESE-WNW, to NNE-SSW, to WSW-ENE before the breaching of the relay zone (c*iv*). d) Proposed evolution of fault sets: (i) Propagation of the main normal-fault set; (ii) Interaction between the main left-stepping normal faults leads to clockwise vertical axis block rotation in the relay zone, and induced local reorientation of extension direction accommodated on variably oriented ancillary faults and fractures; (iii) continued propagation of one of the bounding normal faults leads to the development of new rift-parallel structures and bypassing of the relay zone.

Stage IV: Based on studies of interacting normal faults, a hard linkage is expected to develop between faults A and B, with either (1) the continued propagation of one, or both fault tips, or (2) the formation of a separate connecting fault (e.g. Peacock and Sanderson, 1992; Childs et al., 1995; Hus et al., 2005). In the study area, there is evidence for the former with the development of fault segments A' and B'. Hard linkage on either of these NW-SE striking faults is, however, incomplete. The growth of fault C, which has a smaller vertical displacement (up to ~5 m) and appears to have followed a modified trajectory from a NNE-SSW trend to a NE-SW one in the vicinity of the relay zone, adds further complexity. The tip of fault C appears to terminate against a NW-SE striking normal fault (with a greater throw of 15 m) that is referred to as fault C'. The geometric and timing relationship between the faults C and C' is also unclear but the en echelon configuration of faults B' and C' produces an additional relay zone.

Stage V: Breaching of the relay zone might have been expected with the growth of fault B', A' or C', resulting in localisation on an obliquely oriented (NW-SE striking) fault step(s). Before a NW-SE striking hard link developed, a set of NE-SW (rift-parallel) extension fractures and a normal fault (fault B-C) developed to connect NW-SE striking fault segments B' and C' (Figure 5.24b). Extension fractures and fault comprising B-C shows relatively minor displacements compared to neighbouring sets. Fault B-C is interpreted to be a later structure that developed to accommodate the transfer of displacement in a secondary relay zone between faults B' and C'. The cumulative result of this displacement transfer is a straightening out of the entire relay

zone, and localisation on a new through-going rift-parallel normal fault (Figure 5.24, civ, v, diii). The formation of this link will ultimately lead to either: (1) the abandonment of the tip of fault A/A' with rift extension accommodated solely on this new through-going fault; or (2) continued propagation of fault A and partitioned extension. Most importantly, instead of instantaneously breaching, structures in the relay zone record a progressive kinematic evolution from rift-normal extension to rift-parallel/rift-oblique extension, and finally rift-normal extension once more. The earlier obliquely oriented structures are abandoned in favour of a new rift-parallel normal fault.

No clear cross-cutting relationship was observed between rift-normal and oblique sets. As such, it is unclear whether the sets developed as the result of (1) clockwise block rotation with early formation of rift-normal fractures (Figure 5.24c*iv*); or (2) a stage of anticlockwise block rotation with and the early formation of rift-oblique sets (Figure 5.24c*v*). Although the relative timings of the fault and fracture sets are uncertain, they provide evidence for the progressive inelastic break down of a region undergoing simultaneous rift-normal and rift-parallel/rift-oblique extension (non-plane strain), in this case as a result of the complex stress distributions surrounding the terminations of the bounding rift faults (e.g. Griffiths, 1980).

5.5.3. Implications for rift zone kinematics

Results from laboratory-derived data and field observations of faults and fractures show that segmentation is a natural result of fault development in anisotropic volumes (Chapter 3) under varying boundary conditions (Chapter 4). A product of this intrinsic segmentation is progressive strain partitioning and three-dimensional strains in relay zones at a range of scales (m- to km-scale; Chapter 4 and this chapter).

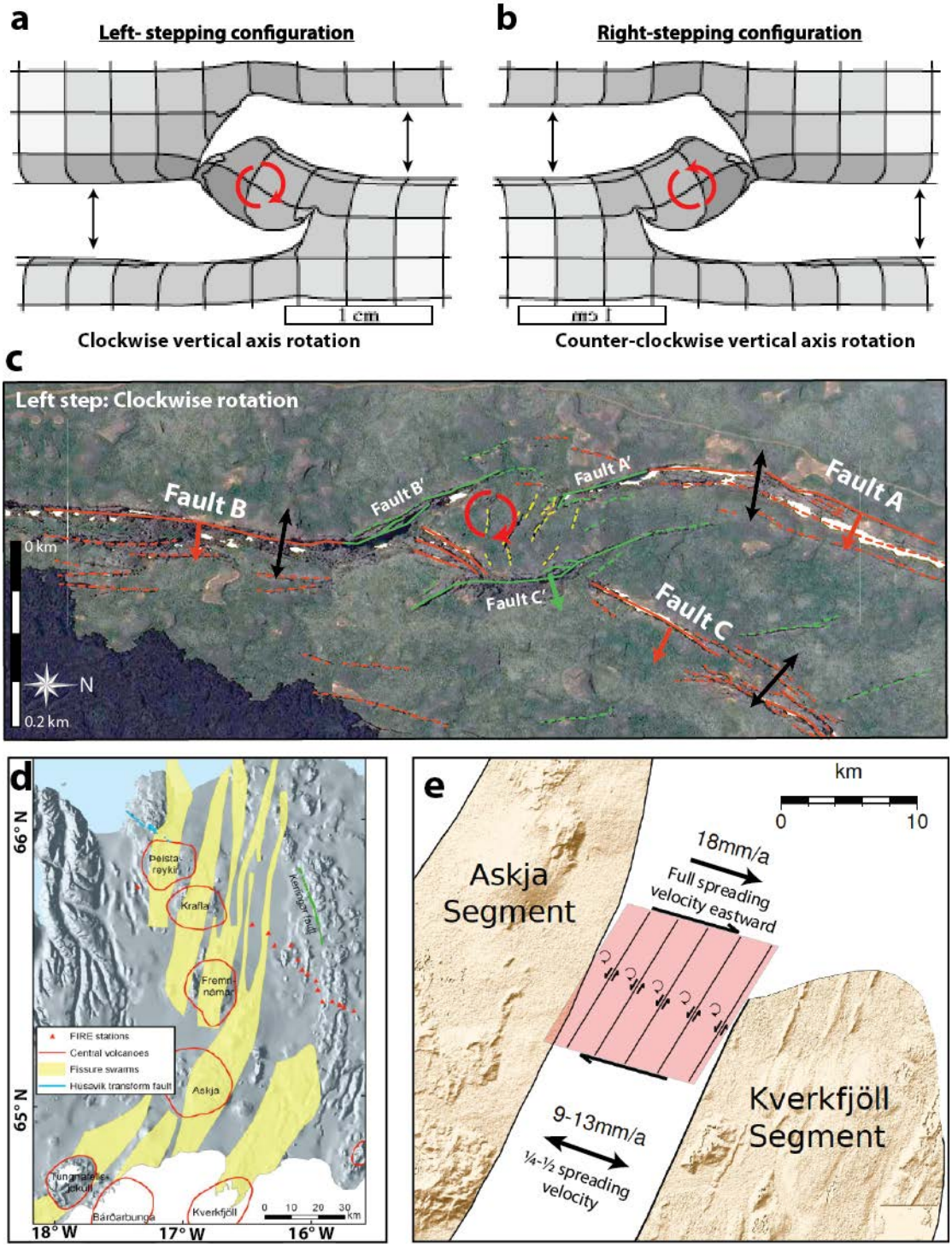

Figure 5.25. Modelled strain fields surround two interacting fractures (darker grey is higher strain intensity) based on the analogue models of Tentler and Acocella (2010) for left-stepping en echelon fractures (a) and right-stepping fractures (b). c) Mapped faults (solid polylines) and extension fractures (dotted polylines) in the AOI in the Krafla fissure swarm. Red polylines represent the dominant rift-parallel fault and fracture set that accommodate the regional ESE-WNW extension direction. Additional oblique

fracture and fault sets have developed at the tips of en echelon rift faults (faults A, B and C). The en echelon configuration of the main fault sets A and B (Gjaystykki graben-bounding faults) shows a left step over and structures developing here are consistent with a clockwise vertical axis rotation. Coloured arrows indicate fault dip directions. d) Map of en echelon rift segments in the NVZ (from Hjartardöttir, 2010). e) Interpretation of microseismicity between the Askja and Kverkfjöll rift segments suggests left-lateral strike slip faults in the overlap zone represent bookshelf faults that accommodate right-lateral shear and clockwise vertical axis rotation between the Askja and Kverkfjöll rift segments in northern Iceland (modified from Green et al., 2014). The stepping configuration and associated rotation is consistent with the models of Tentler and Acocella, 2010.

The scale invariance of the observations made suggests that a common process of segmentation, propagation and interaction may contribute to fault distribution and geometry. Findings of this study fit well with reports of complex three-dimensional strain partitioning between en echelon fractures or faults in numerical simulations (e.g. Segall and Pollard, 1980; Pollard and Aydin, 1984), analogue studies (e.g. Tentler and Acocella, 2010; Figure 5.25a, b) and field studies (e.g. Griffiths, 1980; Nelson et al., 1992; Acocella et al., 2000).

The process of fault segment propagation and linkage is not an instantaneous process (e.g. Imber et al., 2004) and deformation ahead of propagating and interacting fault segments should therefore be expected to follow a progressive deformational evolution. Here, such a progressive kinematic evolution is presented. Strains within the relay zone are inherently non-coaxial with NNE-SSW to NE-SW extension taking place contemporaneously with continued rift-normal (WNW-ESE) extension on the bounding fault structures (Figure 5.25c). Comparable clockwise rotations and oblique deformation is also identified at a larger rift-scale for left-stepping rift segments in the Afar region of the East Africa Rift (e.g. Tapponier et al., 1990) and the axial rift zone of Iceland.

Approximately 19 mm/yr-1 of plate motion across the axial rift zone in Iceland is compartmentalised onto five fissure swarms: Thiestareykir, Krafla, Fremri-Namur, Askja and

Kverkfjöll (Figure 5.25d). The characteristic deformation within these fissure swarms has been documented in detail but segmentation and strain partitioning at the scale of the individual fissure swarms is less well documented. In the Krafla fissure swarm, the largest displacements are identified along NNE-SSW striking faults; distributed, obliquely oriented fractures are present in overlap zones between normal faults but show smaller displacements. In the relay zone between the Askja- Kverkfjöll fissure systems, remote aerial mapping of surface fractures reveals the same primary (continuous) and secondary (discontinuous) orientations that have been presented in this study: (1) primary NNE-SSW to NE-SW; (2) secondary WSW-ENE to WNW-ESE; and (3) secondary NW-SE (Hjartardöttir, 2010). These fracture sets may be analogous to sets mapped in the AOI and generated by similarly perturbed stresses surrounding the en echelon fracture systems. In the absence of published kinematic data for these sets, a comparison with results from mapped sets from the study area in the Krafla fissure swarm is not possible. Currently, WNW-ESE striking fracture sets at the one to tens of kilometre-scale between the Krafla and Askja systems are interpreted to accommodate transform motion (i.e. rift-normal extension) between the en echelon rift zones, inducing a segmentation of the fissure systems (Hjartardöttir, 2010). Field measurements of WNW-ESE striking fractures in the Krafla fissure swarm contradict this model by showing purely extensional openings, accommodating a rift-parallel extension.

Beyond this scale, and at greater depths, the identification of rift-parallel and/or rift-oblique extension is less common and plane strain conditions are preferentially interpreted. Between 2009-2012, microseismicity (Mw 0.5-3) records from the relay zone between the Askja and Kverkfjöll fissure swarms, at depths of 2-6 km, highlight right-lateral transform motion (Figure 5.25e). The transform motion is thought to be accommodated on a series of left-lateral strike slip faults that trend subparallel (NE-SW) to the adjacent NNE-SSW striking fissure swarms, resulting in a vertical axis rotation, or bookshelf mechanism (Green et al., 2014). No conjugate sets are recorded and there is no expression of these deeper strike-slip faults at the surface

where NNE-SSW striking normal faults and extension fractures dominate. There is no evidence in the microseismicity catalogue for either the WNW-ESE or NW-SE striking fracture sets that have been mapped remotely by Hjartardöttir (2010) in this area. The oblique surface fractures may be the surface expression of oblique deformation at depth, implying that additional structural complexity exists in the region but remains unseen in microseismicity catalogues.

The reasons for the disparity between Green et al., (2014) and Hjartardöttir (2010) are not clear. Differences in fault orientations and kinematics may be attributed to the type of data being analysed in this study. Green et al (2014) do not recognise the same oblique structural sets; this may be because they do not exist, or that they are minor or closely spaced structures that produce focal mechanisms outside the resolution of the dataset. The Green et al. (2014) model, and others in Iceland (e.g. Bergerat et al., 1998) and the East Africa Rift (e.g. Tapponnier et al., 1990) typically filter seismicity datasets to exclude non-double couple (non-DC) focal mechanisms, limiting datasets to double couple focal mechanisms that represent shear faulting events within a magnitude range M1-5. Non-DC mechanisms are commonly interpreted as noise or artefacts and are therefore isolated and removed during processing steps if any of the following criteria are satisfied: (1) slip or opening occurs above 2 km depth; (2) faults are closely spaced between 2-6 km; (3) slip occurs on a small number of structures with short recurrence intervals (multiple subevents); (4) there is a combination of normal and strike-slip faulting, resulting in composite non-DC mechanisms; or (5) if diking and crack extension is dominant below these depths (Kawakatsu, 1991; Julian et al., 1998). Filtering of this information removes non-shear processes associated with dilatancy and tensile failure, including diking and fracture growth (Julian et al., 1998). Green et al. (2014) do not specify whether their data is filtered to only include DC earthquake mechanisms; if this is the case, it may explain inconsistencies between their findings and the relatively heterogeneous results from Krafla in this chapter and the study of Hjartardöttir (2010). The result is an inherently two-dimensional model based on a

primary dataset that may exclude smaller scale complexity (e.g. multiple, potentially synchronous extension directions).

At a larger scale still, interpretations of complex strain partitioning are also reported for the transform zones located in the south and north of Iceland: the Tjornes Fracture Zone (TFZ) and the South Iceland Seismic Zone (SISZ), which connect the axial rift zone of Iceland with the Kolbeinsey and Reykjanes spreading ridges, respectively. Extension in these zones is partitioned onto multiple sets of en echelon strike-slip faults, normal faults, extension fractures/veins and dikes (Bergerat and Angelier, 1998; Angelier et al., 2000; Gudmundsson et al., 2001; Garcia et al., 2002; Homberg et al., 2010).

Paleostress analyses (e.g. Bergerat et al., 1990; Bergerat and Angelier, 2008), and seismicity data (e.g. Dauteuil and Bergerat, 2005; Bergerat and Angelier, 2008), from onshore areas surrounding the TFZ, reveal highly heterogeneous fault patterns that are not resolved using a straightforward succession of events. Paleostress methodologies provide a common stress tensor that best fits measured and calculated slip vectors; in this region, analyses predict up to six separate brittle events, which give a primary WNW-ESE extension and a secondary ENE-WSW extension. The remaining 4 regimes comprise a smaller but equally represented component of the dataset: (1) NE-SW extension, (2) NW-SE extension, (3) NNW-SSE extension and, (4) NNE-SSW extension (Angelier et al., 2000; Garcia et al., 2002). Evidence for unambiguous timing relationships were not identified by these authors but results of Ar-Ar dating in the same area show that dikes with orthogonal orientations have similar ages (Garcia et al., 2003), implying a strong, but undocumented potential for non-plane strain.

Paleostress analyses from the SISZ also reveal a heterogeneous stress regime that cannot be defined using a single stress tensor (e.g. Bergerat et al., 1998, 1999). NW-SE extension here is primarily partitioned onto a series of conjugate normal faults and conjugate strike slip "bookshelf faults"; the overall effect of which is left-lateral transform motion, accommodating the offset between the Reykjanes ridge and the axial rift (Bergerat et al., 1998; Bergerat and

Angelier, 1999; Acocella et al., 2000; Einarsson, 2010). A second NE-SW extension is also recognised however, implying synchronous orthogonal extension or an extreme reversal in stress regime (Bergerat et al., 1998; Bergerat and Angelier, 1999). Based on mutually cross-cutting relationships, these authors propose that such heterogeneity is the result of multiple reversals of extension direction through time, most likely due to the effects of crustal heterogeneities.

Data from the study area in the Krafla fissure swarm highlights a region of non co-axial strain, characterised by complex structural sets – the product of modified elastic strain fields during interaction that accommodate the transfer of extensional strains in a relay zone between synthetic normal faults. Theoretical results from numerical-based models imply that observations scale with fault size, and as such we might expect similarly complex strains at the scale of Green et al. (2014) and Bergerat et al. (1998, 1999), associated with the mechanical interaction of the Askja-Kverkfjoll rift segments and the Reykjanes ridge and the Neo-Volcanic zone (NVZ). Beyond the scale of this study however, interpretations of en echelon rift zone segments are inherently limited by the resolution of onshore satellite data or offshore bathymetry data, as well as the resolution and processing methods of seismicity data and paleostress inversion techniques. As such, beyond the km-scale and for interpretations of faulting at depth, smaller, obliquely oriented deformation is lost, and it is therefore very difficult to characterise three-dimensional strain at these scales. To fully reconcile field observations and interpretations of non co-axial strain at the sub-km scale with results of larger scale studies requires datasets that include both DC and non-DC events at a high spatial and temporal resolution for a range of event magnitudes.

5.6. Summary

- Mapping of the distribution, geometry and kinematics of faults, and of fault-related deformation, in the Krafla fissure swarm has shown that extension is dominantly accommodated on NNE-SSW striking subvertical, surface-breaking normal faults with maximum throws of up to 30 m.
- Based on the shape of displacement profiles and the geometry of propagation pathways, two fracture and fault categories are identified: (1) interacting, en-echelon (apertures < 1.5 m); and (2) linked, composite fractures (commonly breached) with apertures > 1.5 m. There are relatively few examples of isolated, non-interacting fractures and composite fractures are most common.
- In addition to rift-parallel normal faults and extension fractures, multiple ancillary fault and fracture sets exist at the lateral terminations of rift faults and strike at high angles to them. Geometric and kinematic analysis of these structures suggests transfer of elastic strain is taking place between bounding normal faults in a relay zone on the following sets: (1) minor WNW-ESE striking extension mode fractures, accommodating a rift-parallel (NNE-SSW) extension; and (2) a more significant set of NW-SE striking normal faults and extensional-shear fractures that accommodate a NE-SW extension. An additional set of rift-parallel normal faults and extension fractures appear to cut these oblique sets, connecting bounding segments to produce a new through-going rift fault.
- There are no instances of rift-normal strike-slip (transfer) faults within the Krafla fissure swarm: each fault/fracture set accommodates a unique extension direction consistent with the progressive mechanical interaction of the bounding fault stress fields, which results in incremental inelastic deformation that follow modified stress trajectories and complex non co-axial strain.

- Current models of relay zone development do not demonstrate the progressive breakdown and complex stress rotations internal to a relay zone that are interpreted to be taking place in the study area.
- Faults in the Krafla fissure swarm show a greater proportion of linked, surface-breaking normal fault and extension fracture geometries, with greater maximum displacements than structures that were mapped in the Koa'e fault system. This also coincides with greater levels of magmatic activity within the rift zone.

Chapter 6

Discussion

6.1 Comparison of the Koa'e fault system and Krafla fissure swarm

Observations of fault distributions and geometries in the Koa'e fault system and the Krafla fissure swarm show that there are some similarities to the predicted geometries of Kaven and Martel (2007) and Martel and Langley (2006) (i.e. extension fracture formation and surface flexure development), but also many inconsistencies that suggest the two locations do not represent the same stages of fault evolution. Additionally, flexures in both the Koa'e and Krafla fault system are not present along all fault traces where they ought to be systematically breached, as existing models predict (e.g. Grant and Kattenhorn, 2004; Holland et al., 2006; Martel and Langley, 2006). There are also pronounced differences in deformation style between the two fault systems that show a correlation with variations in mechanical stratigraphy (i.e. compositional variations, fluid content) and magma emplacement in the shallow crust. Existing models dominantly involve geometric or kinematic linkage only, and do not consider the relative timing of fault nucleation and propagation; nor strain rate or distribution. A model that accounts for a heterogeneous and anisotropic sequence, under anisotropic (i.e. variable in space/time/magnitude), cyclic loading may therefore provide a better estimate of their evolution.

6.1.1 Structural Style

The Koa'e and Krafla systems share common structural features, which implies that a common process may be responsible for their development. These include: (1) linear zones

of interacting and coalescing subvertical extension fractures; (2) monoclinal surface flexures and (3) subvertical fault scarps with prominent openings of 2-4 m (Figure 6.1). Existing models (e.g. Grant and Kattenhorn, 2004; Kaven and Martel, 2007) to account for these features in the growth of normal faults in basaltic sequences are based on 2D analytical solutions.

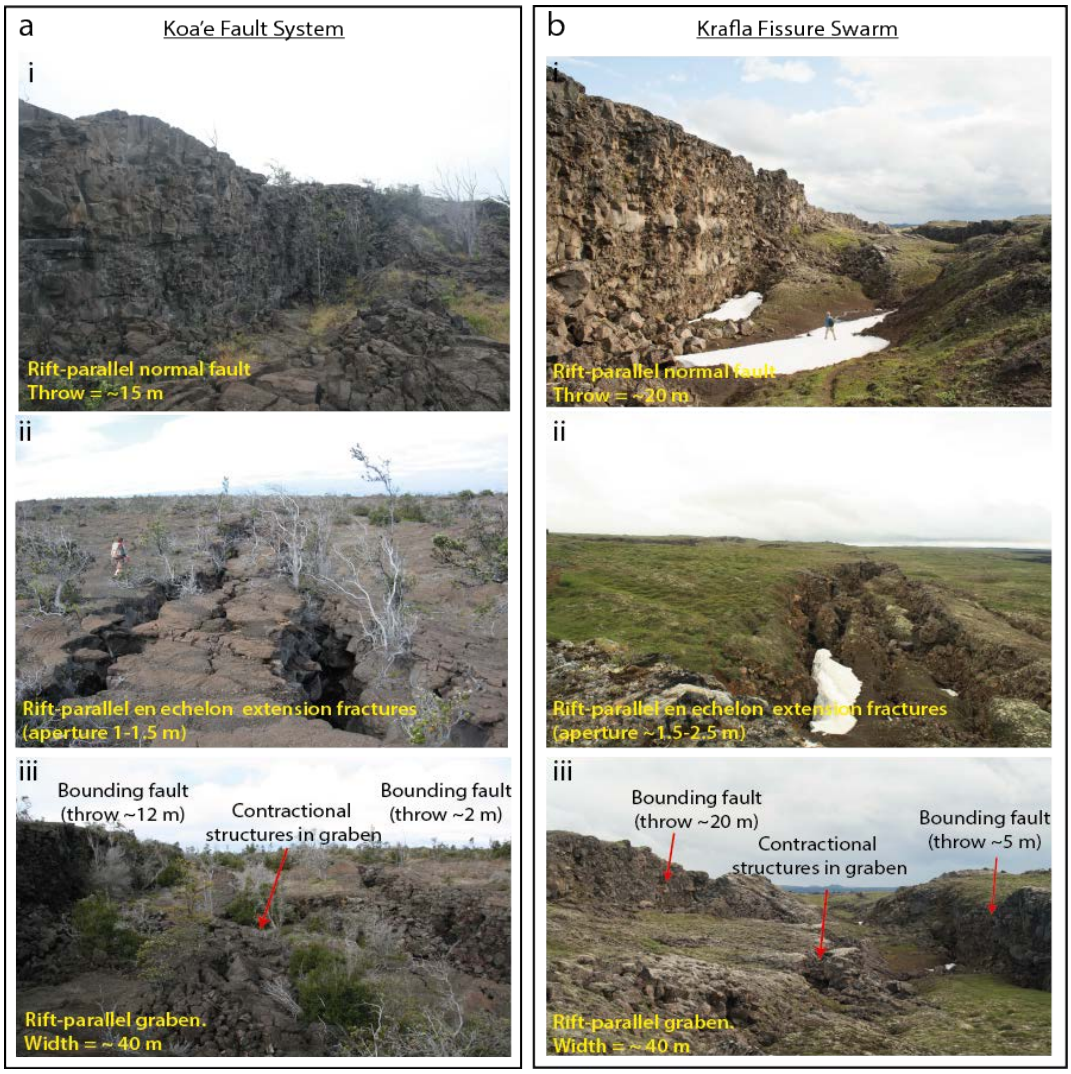

Figure 6.1. Extensional structures in the Koa'e fault system and the Krafla fissure swarm show similar characteristics: 1) surface-breaking normal faults with maximum vertical offsets >10 m, and open fractures along the hanging wall cut-off (a*i*; b*i*); (2) networks of en echelon (interacting) and coalesced extension fractures that show zig-zag openings along pre-existing cooling joints (a*ii*; b*ii*); and 3) narrow, fault-bound graben structures that feature internal deformation that includes faults

and contractional ridges (a*iii*; b*iii*) that may be related to fault slip and opening on oppositely dipping faults that bound the grabens.

Notably numerical-based models involve isotropic rocks under isotropic loading conditions, treating the host rock as a linear elastic, isotropic, isothermal, semi-infinite continuum. Faults are modelled as isolated, planar and frictionless structures that are infinite, and constant in their lateral dimensions. The faults are discrete structures that propagate upwards to the free surface in their own plane, generating compressive and tensile stresses around the tip as they grow (e.g. Martel and Langley, 2006; Kaven and Martel, 2007). These models are unable to account for the effects of a mechanically heterogeneous sequence (e.g. joint fabrics, segmentation and refracted geometries: Ferrill and Morris, 2001; Schöpfer et al., 2006; Walker et al., 2013) or local, interaction-induced stress distributions. Faults are represented by a series of discrete triangular elements and slip is induced by applying a shear stress to these elements. Analysis of the resulting stress field surrounding the isolated fault structure is then used to predict the location and kinematics of potential ancillary deformation. Based on these numerical simulations and field observations, the development of normal faults in basaltic sequences is thought to follow a systematic growth process (Grant and Kattenhorn, 2004; Martel and Langley, 2006; Kaven and Martel, 2007):

Stage I: Upward propagation of a blind normal fault, above which we observe flexure of the ground surface and the development of subvertical extension fractures parallel to the tip line at the surface.

Stage II: Continued slip and upward propagation is coupled with a steepening of the surface monocline and a widening of extension fractures.

Stage III: Eventually, normal faults link with extension fractures at depth, resulting in surface-breaching faults with an open, and vertical component of displacement. Surface monoclines are breached and transferred to the hanging wall.

Experimental analyses of the physical and mechanical properties of lavas (Chapter 3), coupled with detailed, and extensive field mapping in both the Koa'e fault system (Chapter 4) and the Krafla fissure swarm (Chapter 5), suggest that this evolution may be true only in some instances. A combination of two factors appears to exert a strong influence on fault segmentation and propagation of faults in basaltic sequences: (1) heterogeneous and anisotropic loading, as a result of variable syn-tectonic magmatism (intrusion); and (2) loading of a mechanically layered sequence.

6.1.2 Magmatic Effects

Applied stresses in the Koa'e and Krafla rift settings are neither homogenous nor isotropic. Extension in both areas is governed by cyclic inflation-deflation events, the scale and timing of which result in heterogeneous and anisotropic stresses that are relieved during rifting episodes, which vary in scale accordingly. Records of ground deformation in the Krafla fissure swarm, dating back to 1976, have highlighted pronounced and repeated episodes of steady inflation followed by rapid deflation (and subsidence), associated with rift zone extension (Bjornsson et al., 1978; Tryggvason, 1981, 1984, 1994; Rubin, 1992). Between 1974-78, up to eight separate inflation-deflation events were recorded and 80-90 km of the ~100 km long rift zone extended (Tryggvason, 1984). Recurrence intervals for volcano-tectonic activity, associated with episodic deflation of the magma reservoir, are on the order of 100-200 years (Tryggvason, 1984; Bjornsson et al., 2007). Inflation is interpreted as the gradual accumulation of magma in the reservoir ~3 km beneath the summit

(Brandsdottir and Einarsson, 1979). During each deflation event, magma is discharged from the central reservoir, where it travels through the fissure swarm as dikes, or erupted as lava on the surface (Tryggvason, 1981). Seismicity and fissure widening accompany the release of magma from the reservoir and subsidence of the caldera, implying that a genetic link exists between rifting and the lateral migration of magma within the rift zone (Brandsdottir and Einarsson, 1979). The amount of extension across the rift zone during each rifting episode is estimated at 0.3 km^2 (~1-2 m of fissure zone widening), approximately proportional to the volume of subsidence within the caldera (Tryggvason, 1984, 1994). Magma volumes, and the rate they are released, can vary significantly, however, along with the amount of dilation, during each deflation event in a single rift episode. Records from an event in 1980 estimate that during one event, a magma volume of ~6 x 10^6 m^3 was released over 4-5 days with little to no measured dilation in the fissure swarm. A second event shortly after this is estimated to have released 30-40 x 10^6 m^3 of magma over approximately 12 hours, which was associated with 1.2-1.7 m of dilation within the fissure swarm (Tryggvason, 1984). Over a period of 39 days, Krafla erupted 198 x 10^6 m^3 of magma during six separate events (Harris et al., 2000).

Similar patterns of inflation-deflation have been recorded at the summit of Kilauea volcano, where magma is repeatedly transferred from the central reservoir into the adjacent rift zones that radiate southwest and east (Duffield et al., 1982; Delaney et al., 1998; Poland et al., 2008). Records of sustained eruptions at Kilauea's summit also show variable magma volumes and event durations: In June 1952, 38 x 10^6 m^3 of magma was erupted over 136 days and in November 1967, 64 x 10^6 m^3 of magma was erupted over 251 days. Between 1983-2003, Kilauea was in a phase of continuous eruption with ~200 x 10^6 m^3 of magma released (Dvorak and Dzurisin, 1993; Poland et al., 2012). Magma supply rates for Kilauea are estimated at ~0.1 km^3 y^{-1} (Swanson et al., 1976; Dzurisin et al., 1984) whereas estimates for Krafla are up to ~1.6 km^3 y^{-1} (Tryggvason, 1986; Harris et al., 2000).

Models of magma partitioning within Kilauea suggest that during the period 1840-1989, ~57% of magma supplied to the volcano was emplaced and erupted within the East Rift Zone (ERZ) (1575 x 10^6 m^3) with ~2% (45x 10^6 m^3) erupted from the Southwest Rift Zone (SWRZ) (Dzurisin et al., 1984; Dvorak and Dzurisin, 1993). The result of this partitioning has led to more than 20 eruptions since 1950, associated with deflation of Kilauea's summit reservoir, with only two of these events taking place in the southwest rift zone. These temporal and spatial variations in magma emplacement have had a significant effect on the distribution and geometry of surface strains in the Koa'e fault system: surface-breaking faults, and much of the recorded seismicity, occur within 6 km of the ERZ (Figure 6.2a, inset box). Towards the SWRZ, faults have remained segmented at depth, and strains are characterised by surface flexures and extension fracture growth.

In contrast, seismicity records from Krafla suggest that magma is released into the rift zone during a deflation period and migrates laterally, as dikes, up to 50 km along the length of the rift zone north of Krafla (Bjornsson et al., 1978; Buck et al., 2006; Hjartardóttir et al., 2012; Figure 6.2b, inset box). During the most recent episode between 1975-1984, an early forming dike propagated to the northern end of the rift zone where it continued to dilate and drain the central reservoir for 3 months (Buck et al., 2006). Between 1975-1984, surface-breaking faults accommodated maximum vertical displacements of 35 m, up to ~20 km away from the source, suggesting dike propagation is closely related to the formation and reactivation of fault structures along the entire length of the rift zone.

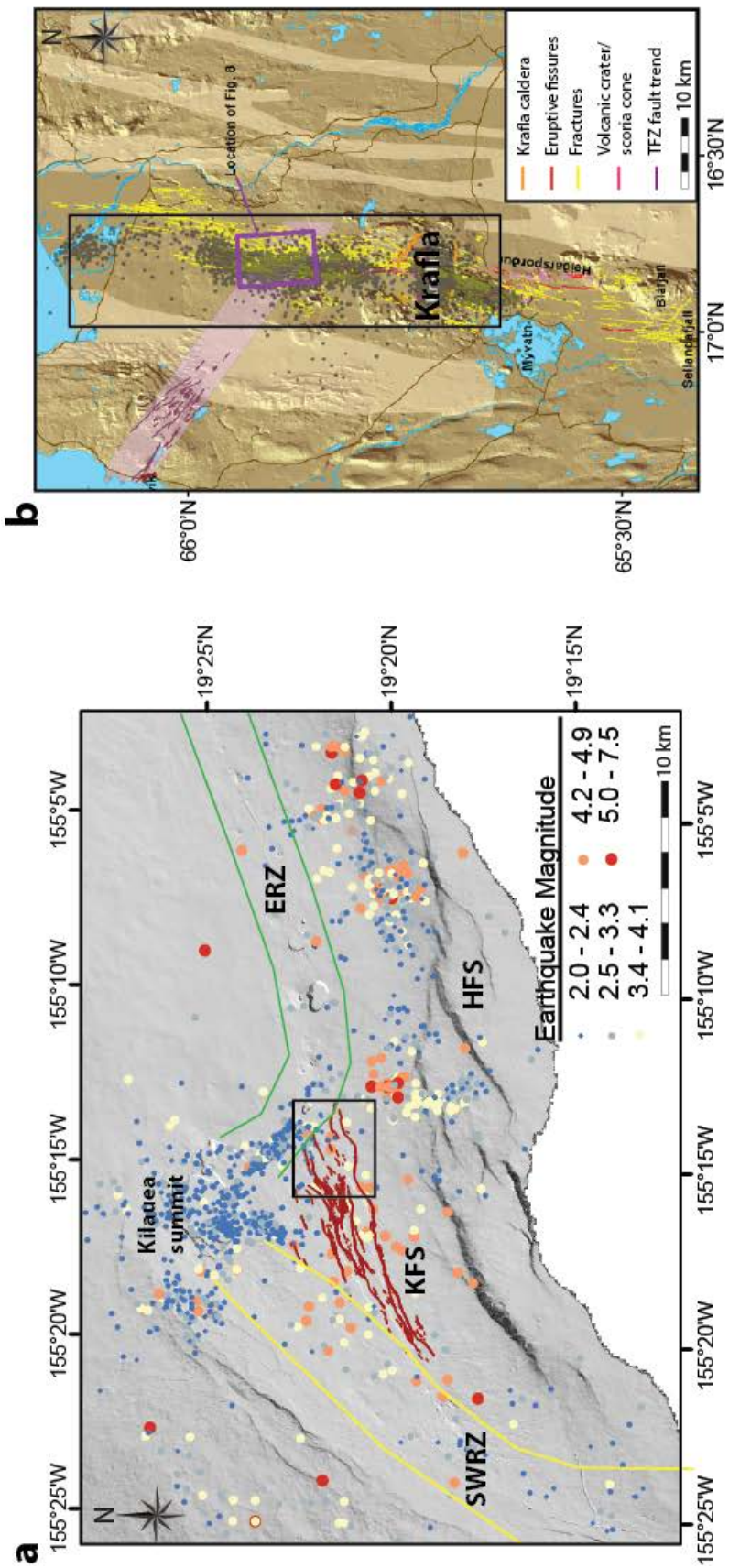
b
66°0'N
65°30'N
16°30'W
17°0'N
Krafla
Location of Fig. 8
Krafla caldera
Eruptive fissures
Fractures
Volcanic crater/ scoria cone
TFZ fault trend
10 km
a
19°25'N
19°20'N
19°15'N
155°25'W
155°20'W
155°15'W
155°10'W
155°5'W
ERZ
HFS
KFS
SWRZ
Kilauea summit
Earthquake Magnitude
2.0 - 2.4
2.5 - 3.3
3.4 - 4.1
4.2 - 4.9
5.0 - 7.5
10 km

Figure 6.2. (a) Seismicity map for the south flank of Kilauea, Hawai'i. Inset box highlights a region of large surface-breaking normal faults. The region is connected to a zone in and around the upper ERZ where seismicity levels are elevated. With progressive distance from this zone, surface-breaking faults become increasingly rare and remain segmented at depth. (b) Seismicity map for the Krafla fissure swarm. Inset box shows seismicity during a rifting episode, associated with dilation of the rift zone, and dike migration along the ~100 km length of the Krafla fissure swarm. (Krafla map from Hjartardóttir et al., 2012). SWRZ: south west rift zone; ERZ: east rift zone; KFS: Koa'e fault system; HFS: Hilina fault system.

Dike propagation is controlled by the driving pressure, which is defined as the difference between the total fluid (magma) pressure and the normal stress (equal to the least compressive stress) acting on the dike (e.g. Gudmundsson, 2003). This in turn generates a stress intensity at the tip (a function of the driving stress and the length of the dike); when this value exceeds the tensile strength, or exceeds the fracture toughness of the surrounding host rock, the propagation criterion is satisfied and the dike will dilate and lengthen (e.g. Pollard and Muller, 1976; Buck et al., 2006). Propagation will continue until either: (1) the driving pressure decreases and the stress intensity factor at the dike tip is less than the fracture toughness of the host or (2) the dike encounters a stress barrier (e.g. an area of higher compressive stress or layer with a low Young's modulus). With magma supply rates more than an order or magnitude higher in Krafla than in Kilauea, dikes are driven significantly further into the rift zone by higher driving pressures and strain rates are correspondingly higher throughout the fault system. This assumes that the hydrofracture is driven by magma pressure, which could be argued true either in the case of high magma pressures during low differential stress, or magma pressure tipping the balance in an otherwise critically stressed area. Dike emplacement may also follow episodes of faulting, which increases the accommodation space available for intrusion. Records from Kilauea highlight deflation episodes that are preceded by faulting (Owen et al., 2000; D. Swanson,

Pers coms. 2014), and others that are preceded by dike emplacement (Klein et al., 1987; Lundgren et al., 2013). For instance, between 1960 and 1983, only 17 out of 57 eruptions and intrusions were preceded by fault seismicity (Bell and Kilburn, 2011).

Regardless of specific timing and mechanisms, a genetic link exists between faulting and intrusion that should be accounted for in models of rift fault development. Existing models based on analytical solutions are good approximations for the stresses around propagating fault tips but they are unable to reproduce the mechanical anisotropy of the deforming sequence that results in a stepwise evolution of faults, or the variable, and cyclic, intrusion of magma and the subsequent variations in strain rate in each setting, which may be responsible for the distinctive geometries of faults that have been observed.

6.1.3 Mechanical Stratigraphy

In addition to magmatically induced segmentation patterns, related to temporally and spatially variable stresses (driven by variable magma supply rates) within the rift zones, mechanical anisotropies play an important role in fault growth. At the metre-scale, these anisotropies pertain to varying physical and mechanical properties within individual lavas and networks of pre-existing cooling joints, which are common to both settings. At the tens to hundreds of metre-scale, differences in compositional layering could also account for the distribution and geometry of surface strains in the two fault systems. Deep drilling of the 1700 m Scientific Observation Hole (SOH 1) into Kilauea's East Rift Zone produced a continuous drill core that sampled the entire shield stage of the volcano's development (Quane et al., 2000; Figure 6.3a). The drill core has revealed a sequence of subaerially quenched lava (36% Aa, 22% pahoehoe, 4 % massive basalt), with only minor amounts of tephra, to a depth of approximately 1 km, below which intrusions (dikes) dominate (Figure 6.3b). Of the 1700 m deep borehole, lavas comprise 60%, dikes 26%, and hyaloclastite 7%.

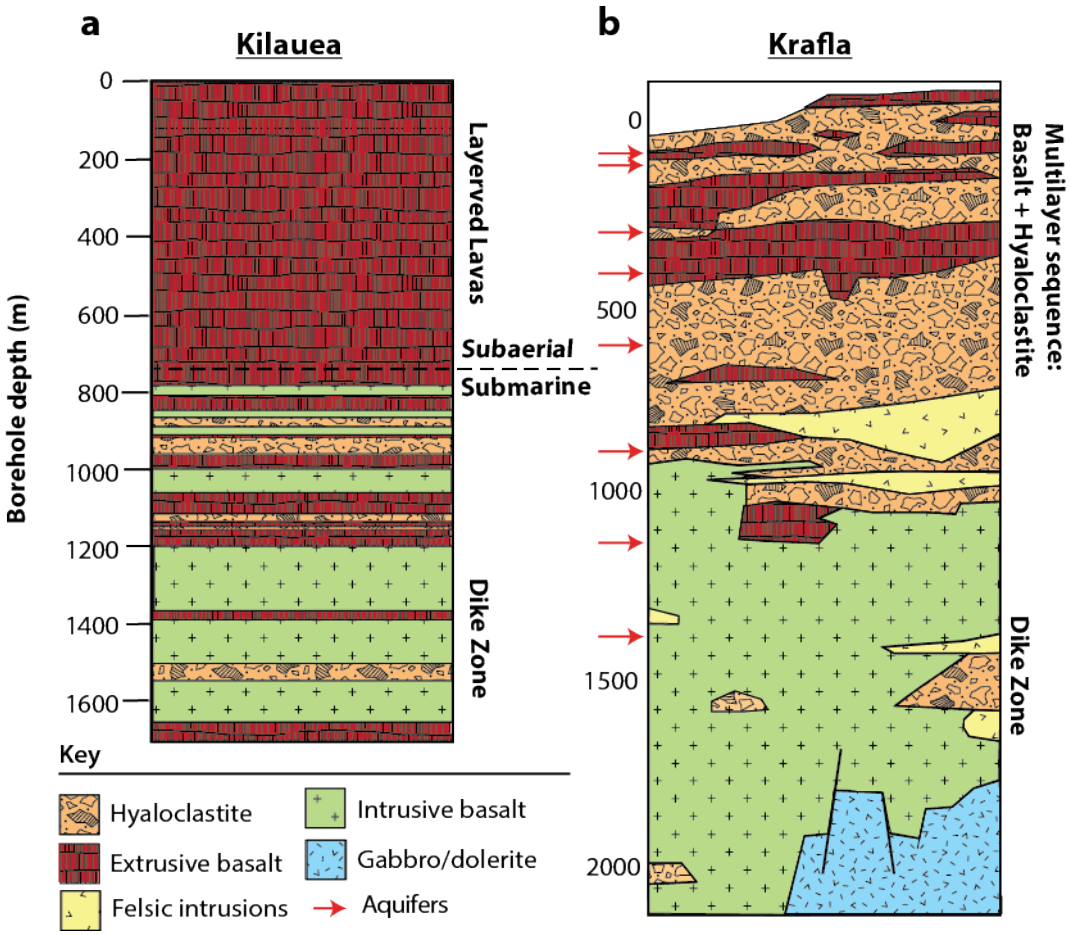

Figure 6.3. (a) Borehole data from the ERZ on Kilauea's south flank. Results from the Kilauea borehole show a relatively homogenous sequence of layered lavas above 1 km, with a zone of intrusive basalt (interpreted to be dikes) below this (data from Quane et al., 2000). (b) Borehole data from Krafla. Data from Krafla shows a more heterogeneous sequence of lavas, hyaloclastite and dike intrusions. Subsurface aquifers are also common in the Krafla rift (borehole data from Fridleifsson et al., 2006; aquifer data from Gudmundsson et al., 2010).

In contrast, core that was recovered from a ~2200 m drillhole at Krafla, drilled by the Iceland Deep Drilling Project (IDDP), highlights a more heterogeneous sequence (Figure 6.3b), comprising: (1) layered lavas and hyaloclastite in the upper 1 km; (2) dikes between 1-2 km; and (3) intrusive gabbro/dolerite below 1600 m. In addition to a compositionally multi-layered sequence, the upper 1.5 km is further influenced by geothermal activity. Many of these geothermal fields are located dominantly within the lava-hyaloclastite

sequence in the upper 700 m. It is thought that rifting activity during the last episode in 1974-1984 contributed to additional fracturing that facilitated the development of new geothermal fields, as well as the reactivation of older ones (Bjornsson et al., 1978). A contrasting physical stratigraphy, as well as the differences in the amount of hydrous fluid available in each study area, yields mechanically variable stratigraphies that are reflected in the surface strains in both locations (i.e dominantly segmented, blind faults in the Koa's fault system and dominantly localised, surface-breaking faults in the Krafla fissure swarm).

Unconfined compressive strength testing of core samples recovered during the Hawaiian Scientific Drilling Project (HSDP) drilling project of the submarine flank of Mauna Kea measured a strong mechanical contrast between lavas and hyaloclastites (Schiffman et al., 2006). Subaerial basalts showed a range of strength measurements from 53-150 MPa, comparable to the results for lava components presented in Chapter 3. In contrast, testing of hyaloclastites from the same drillhole revealed UC strengths of 2-28 MPa (depending on the degree of alteration); the weakest lavas in these drill holes still have a UC strength that is twice that of the strongest hyaloclastites (Schiffman et al., 2006; Thompson et al., 2008). Results from Chapter 3 show that base components of a lava have comparable compressive strengths to the hyaloclastites in this drill hole and similar values of elastic modulus: 5 GPa for the lava and ~1 GPa for hyaloclastites (Gudmundsson, 2004). Depending on their composition (i.e. clay content and composition), the hyaloclastites may deform in a ductile manner (cf. volcaniclastic horizons of Walker et al., 2013) at relatively low effective stresses. The lavas, in contrast, will localise deformation more rapidly. Thick accumulations of hyaloclastite in the Krafla fissure swarm will also have a significant effect on the displacement scaling of faults in both settings. Fault displacement is inversely proportional to the Young's modulus of the deforming host rock; where a fault propagates into a stiffer host, from a softer one, the displacement will decrease (Gudmundsson, 2004). Studies of exposed faults in Holocene lavas in Iceland have shown that their displacement rarely

exceeds 40 m, and is commonly several metres; it was found that the same faults could accumulate 100-200 m of throw when they propagated into hyaloclastite layers (Gudmundsson, 2004).

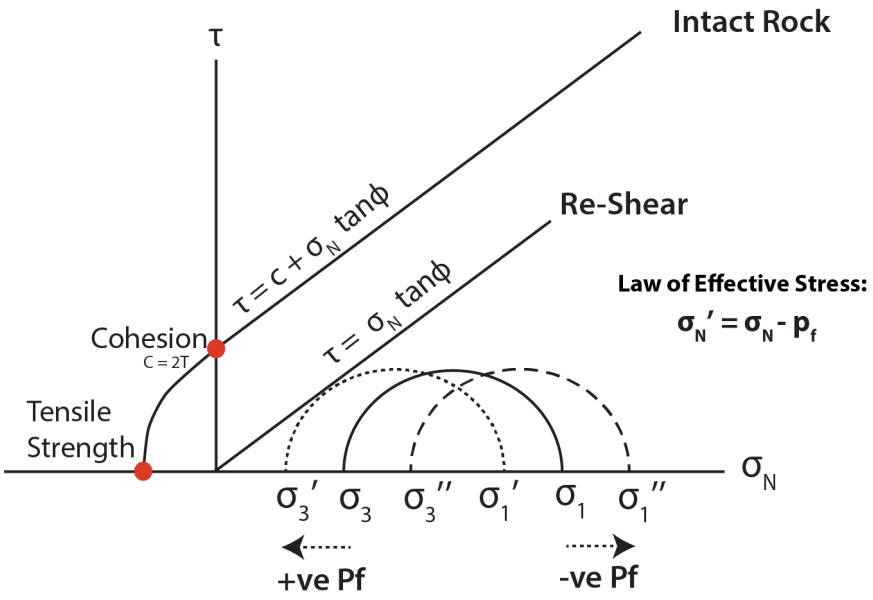

Figure 6.4. The effect of pore fluid pressure on rock failure. An increase in pore fluid pressure (or magma pressure) reduces the effective mean stress, shifting the stress state towards frictional sliding or fracture formation. Depending on mechanical properties of the intact rock (internal friction) or the orientation of a pre-existing structure relative to the principal stresses, a tensile fracture can form (σ3' < 0) or a shear fracture (σ3' > 0). After Hubbert and Rubey (1959).

The mechanical stratigraphy in the Gjastykki valley is also affected by large volumes of geothermal fluids that have been identified within both the hyaloclastite and basalt sequences (Gudmundsson et al., 2010). These fluids, if pressurized, could drive critically stressed materials to failure, facilitating either the formation of new faults or the reactivation of joints, fractures and existing faults, even in the absence of dike emplacement (see Figure 6.4). This fits well with field observations of surface deformation in both fault systems. In the Koa'e fault system there is a defined pattern of

segmentation; faults are able to propagate the whole way through the sequence where magmatic driving pressures and resulting strain rates are high, and elsewhere, strain rates are lower and faults remain segmented at depth where they slip more slowly and flex the surface ahead of the fault tip line. In contrast, a combination of greater magma supply rates, a hyaloclastite-rich sequence and large pore fluid pressures in the Gjastykki area of the Krafla fissure swarm may facilitate fault propagation and leads to widespread through-going faults (with minor, or no flexure prior to breaching the surface) with substantial displacements (>10 m).

6.2 Rift Fault Development in Layered Basaltic Sequences

Much of our understanding of the development of faults in basaltic sequences comes from existing numerical and analogue modelling coupled with field observations. A single propagation model, however, does not predict the system-wide distribution of extensional strains in either the Koa'e or Krafla fault systems. The process of fault evolution appears to be made significantly more complicated by: (1) local inelastic deformation and interaction during propagation and segmentation at a variety of scales; (2) magmatic input variations, which result in heterogeneous and anisotropic extension (spatially and temporally variable, as well as in magnitude); and (3) a heterogeneous and anisotropic mechanical stratigraphy (at the scale of individual lavas and the deforming volume as a whole). These factors have significant influence on fault evolution, distribution and geometry, as well as the distribution of fracture damage throughout the deforming volume. The following stages of fault growth attempt to account for all of these factors and explain the patterns of deformation observed in both the Koa'e fault system and the Krafla fissure swarm.

Stage I: Initial increments of extension may result from magma release during deflation of the central reservoir where high magma pressure will drive dikes into existing adjacent joints or discontinuities. In this scenario, while driving pressures are high enough to exceed the fracture toughness of the surrounding rock, dikes will propagate vertically and horizontally according to the hydrofracture criterion (after Jaeger et al., 2007):

$$P_e = \sigma_3 + T_o$$

The criterion states that dike emplacement will be facilitated by either: (1) an increase in magma pressure (P_e), (2) a reduction in the minimum compressive stress (σ3) or, (3) a reduction in the tensile strength (T_o) of the host rock (Bell and Kilburn, 2011; Gudmundsson, 2011). Although the cause of dike tip propagation cessation is unclear, a drop in magma pressure, below the minimum compressive strength, would prevent a dike tip from exceeding the tensile strength of the host material; this may occur during periods of low magma supply or contact with a layer with a higher resistance to tensile fracture (where stress is relieved in ductile flow). According to borehole data, intrusive basalt is emplaced at 1000-2000 m depth below the surface of Krafla (Fridleifsson et al., 2006) and 1200-1600 m below the summit of Kilauea (Quane et al., 2000; Figure 6.3). In the Krafla rift, dikes at this depth reach a sequence of hyaloclastite and lavas. The presence of the dike tip will perturb the local stress field around it and stresses will be relieved in precursory fracturing within the low fracture resistance lavas, and ductile flow in the higher resistance hyaloclastites (Figure 6.5a), similar to volcaniclastic sandstones (Walker et al., 2013) or "weak", low competence layers (Ferrill and Morris, 2003; Schöpfer et al., 2006). The high fracture resistance of the hyaloclastites will inhibit further fracturing and propagation until magma pressures are high enough to overcome this resistance and promote failure (Figure 6.5).

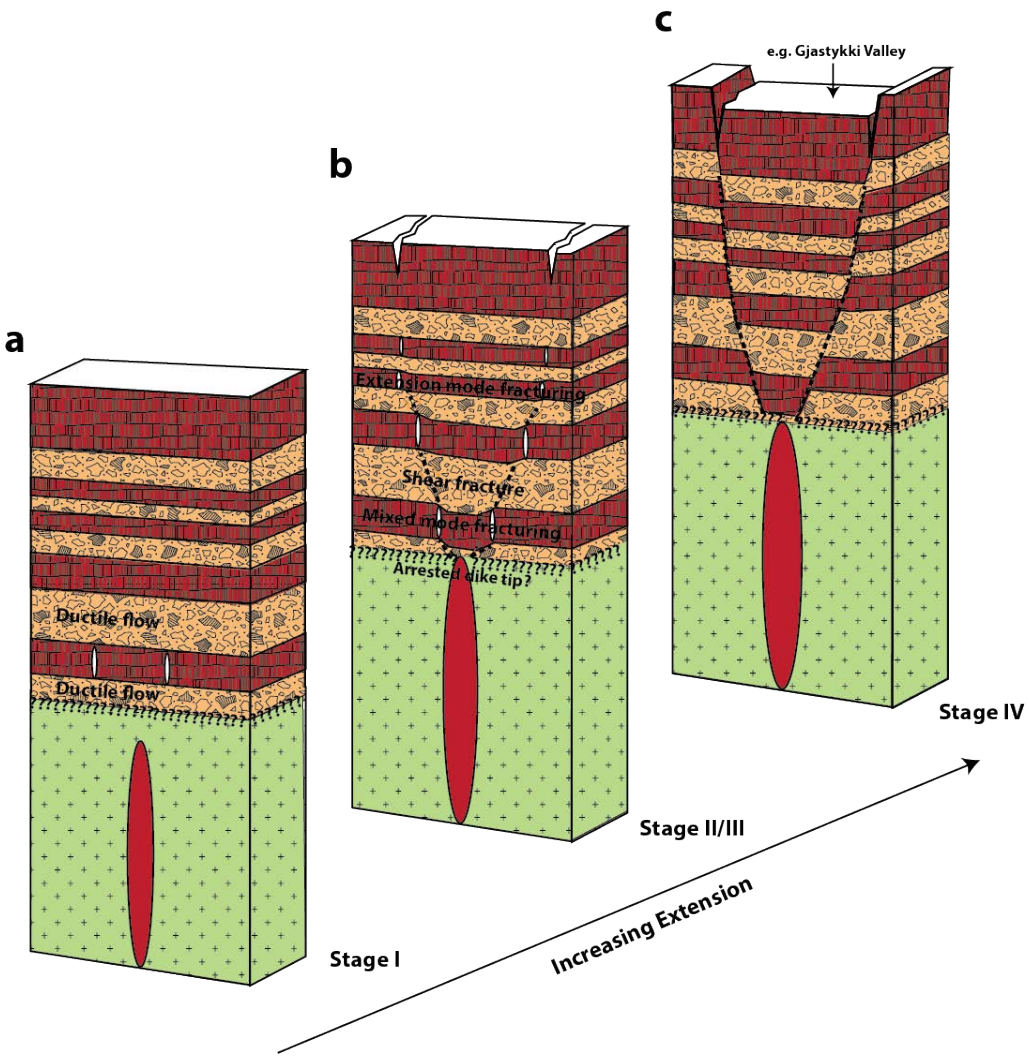

Figure 6.5. Model for dike propagation and fault initiation in the Krafla fissure swarm. (a) During stage I, a dike tip (or series of dike tips) propagates laterally and vertically. Stresses ahead of the dike tip (the magnitude of which are controlled by the stress intensity at the dike tip) are initially accommodated by flow within the high fracture resistance units and extension mode fracturing in the low fracture resistance units. (b) During stage II and III, the dike tip(s) terminate and shear fractures develop in high resistance layers, connecting with extension fracture segments in the adjacent lavas. Ahead of these blind normal faults, extension fractures develop at the free surface in linear zones. (c) During stage IV, fault and fracture segments connect to form through-going, surface-breaking normal faults. If magma supply rates are low, strain rates are correspondingly lower, and surface flexure develops to accommodate slip at depth on segmented faults. When supply rates are high, strain rates are high and faults propagate without flexing the surface. (Graben formation model after Tentler, 2005; Rowland et al., 2007)

An absence of high resistance layers (e.g. hyaloclastite) in Kilauea's flank implies that dike propagation may be dominantly controlled by driving pressure at the 100 m-1 km scale; below this, variations in the shear strength and orientation of joints and the mechanical properties of the intact lava sequence will be important.

Stage II: In the following strain increment, higher fracture resistance hyaloclastite layers will develop shear fractures (normal faults), possibly facilitated by high pore fluid pressures within these mechanically resistant but porous layers (Figure 6.5b). During the same increment, earlier formed fractures in the lower resistance lavas will continue to grow and large fracture volumes will develop in these layers.

Stage III: In the zone ahead of upward propagating fractures and/or dikes, at a critical distance (controlled by the magnitude of the stress intensity at the tip) from the free surface (where shear stresses are zero), extension fractures begin to localise in linear zones along pre-existing cooling joints that are optimally oriented. These zones parallel the structures at depth, accommodating the same extension and gradually propagate vertically and horizontally (Figure 6.5b).

Stage IV: Continued upward propagation of faults and downward growth of extension fractures is possible through the interaction and eventual linkage and coalescence of a descending scale of precursory structures that have developed. The result is composite extension fractures that are continuous in length for several 10s of m to 200 m, with apertures up to ~4 m. At a critical depth, they will interact and coalesce with fault segments to form through-going faults (Figure 6.5c) and a smaller number of large structures will accommodate regional extension. At this stage, strain localisation dominates over new fracture growth and an exponential scaling is predicted (e.g. Ackerman et al., 1997, 2001).

The process of fault evolution in shallow basaltic sequences may take place relatively quickly in some places, as evidenced by a lack of surface flexure of the surface. This implies that faults were able to propagate straight to the surface without flexing it first, which requires a combination of large driving stresses, a low σ_3', and/or sequences with a low fracture resistance. Where driving stresses are too low to overcome the intact rock strength, or the effective shear strength of irregular pre-existing joints, faults will remain segmented and strain is accommodated in surface fracturing and flexure. Here, breached flexures could be evidence of a temporary hiatus in dike emplacement (locally) but continued strain at a lesser rate. With renewed magmatic activity in the area, faults may propagate again and these surface flexures may be breached along newly linked fault-fracture networks, or new faults may develop in the hanging wall, having nucleated from a point of stress concentration (e.g. a restricted tip, fault bend or overlap zone). Some flexures observed in the Krafla fissure swarm show small (1-2 m) amplitudes with larger (4-6 m) fault scarps breaching them, and others amplitudes of ~6 m with small scarps (0.5-1.0 m) breaching them. This implies that in some locations, faults are restricted at depth before breaking upwards through the sequence. Elsewhere they have been held at depth for longer periods during which they accrue several metres of vertical uplift across the flexure before strains are high enough to breach the surface.

The evolution of normal faults in volcanic rift zones from nucleation to the formation of through-going rift-faults is not a linear process. Any change in boundary stress conditions and/or fluid pressures, as well as the existence of any mechanical anisotropy, will have a pronounced effect on the distribution and geometry of extensional strains through time. According to existing numerical and scaled analogue simulations, faults are expected to follow a step-wise evolution, with earlier features evident in advanced stages; e.g. surface flexure is expected during upward propagation and they are later transferred and preserved on the hanging wall side when the fault breaches the surface. In both of the

study areas, however, there are few instances of preserved, breached monoclines, implying that the development of normal faults in volcanic rift zones is not a systematic process. Extensional strains that have been mapped in the Koa'e fault system will not necessarily represent an earlier stage that faults in Krafla have evolved through. A single model, which does not account for the differences in mechanical stratigraphy and applied stresses, will not predict the natural spatial and temporal distribution and geometry of fault populations in developing rift systems.

6.3 Implications for Porosity Maintenance

Variations in the distribution and degree of primary and secondary porosity in flood basaltic sequences has been studied previously (e.g. Wilkens et al., 1991; Planke, 1994; Planke et al., 2000). Primary porosities and permeability within lavas are most commonly associated with joint sets and vesicles, features ubiquitous to the lavas that develop during their emplacement (Petford, 2003). This intrinsic porosity and permeability governs transport and diffusion processes (e.g. Saar and Manga, 1999; Petford, 2003). The long-term maintenance of porosity in basaltic sequences is becoming increasingly important for the storage of economically important fluid-related resources and CO_2 sequestration reservoirs, which rely on basaltic stratigraphy (Anderson and Bowers, 1995b; Schutter, 2003; Oelkers and Cole, 2008; Rezvani Khalilabad et al., 2008; Gislason et al., 2010). Layered compound basaltic sequences exhibit a distinctive physical stratigraphy that, in turn, dictates the mechanical behaviour of the material (see Chapter 3). Primary and secondary porosities in these sequences represent two classes: (1) class D: diffusion porosity and (2) class F: flow porosity (Petford, 2003; Figure 6.6). Secondary flow porosity (tortuosity) in basaltic sequences may be more significant to fluid flow where interconnected networks of subvertical joints provide a high tortuosity. As such, primary (class D) porosity, associated

with vesicle distributions, is less important to the overall permeability structure of a lava, particularly at depths where these open voids may close. Effective permeability, however, will be promoted by failure of the intact lava and the development of new through-going fracture pathways.

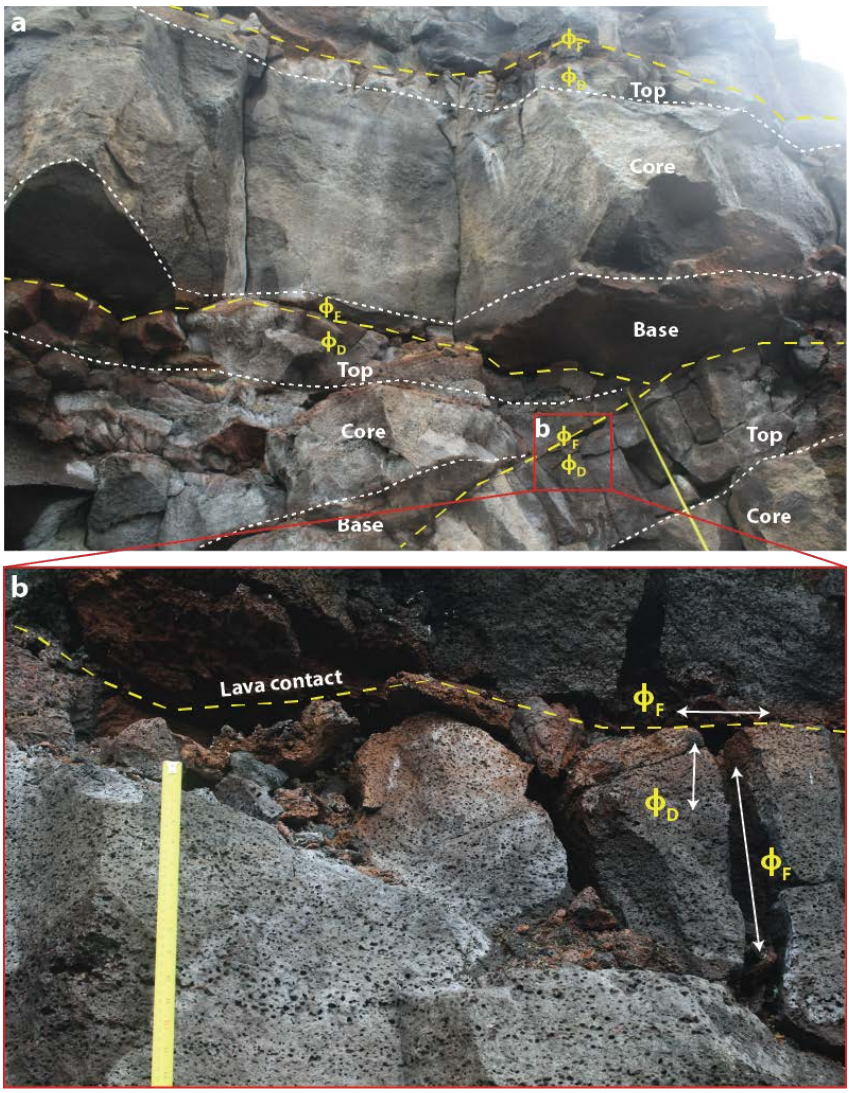

Figure 6.6. Example of primary and secondary porosity in Hawaiian lavas sampled in this study. Tape measure in bottom right of figure (a) is 1 m in length. Inset (b) indicates diffusion-dominant porosity (ϕ_D) in the highly vesicular flow top of the lower unit and bedding- and joint-parallel porosity (ϕ_F) at the contact between flow units and within joints of the lower unit (after Petford, 2003).

It is well known that burial-related mechanical compaction of sedimentary sequences results in loss of their primary porosities (e.g. Terzaghi, 1925; Rieke and Chilingarian, 1974; Wong, 1990; Allen and Allen, 2013). For sandstones, porosity is intergranular, and a product of the solid framework of the rock, i.e. grain size, sphericity, and sorting (e.g. Allen and Allen, 2013). When these rocks are buried and compacted, some of the space around grains is closed, severely restricting their porosity and permeability. The change in effective volume when the rock is buried, referred to as mechanical compaction, is controlled by the elastic response of the material under an increasing load. Loss of volume is related to an applied load using the compressibility modulus (bulk modulus, K); a volume reduction is accompanied by an increase in K. For homogenous and isotropic linear elastic materials, the bulk modulus can be calculated using Young's modulus and the Poisson's ratio for the deforming material:

Equation 6.1:

$$K = \frac{E}{3(1-2v)}$$

Where

E is Young's Modulus

v is Poisson's ratio

While this is not ideally applied to basalts, which are neither isotropic nor linear elastic, it still provides a useful comparison with other rock types and a first estimate of what could be expected for relatively porous basalt (>4%). Based on this calculation, the core of the lava is characterised by the highest bulk modulus (13 GPa); the top of the lava has an intermediate bulk modulus of ~9 GPa, and the base of the lava has the lowest value (3.33 GPa). These results suggest that under an increasing lithostatic load, the core of the lava will compress very little relative to the rest of the unit. These values of bulk moduli are broadly comparable to drained tests of the Berea Sandstone (17% porosity), which give

values of 5-8 GPa of similar porosities (Hart and Wang, 1995; Liu et al., 2009; Kolditz et al., 2012). For comparison the drained tests of the Westerly Granite (<2% porosity) give values of ~25 GPa (Kolditz et al., 2012). Basalts may therefore follow a similar compaction trend that is predicted for sandstones (Figure 6.8). Primary porosity in basalt, however, is a product of volatile degassing during emplacement and results in a vuggy rather than intergranular porosity.

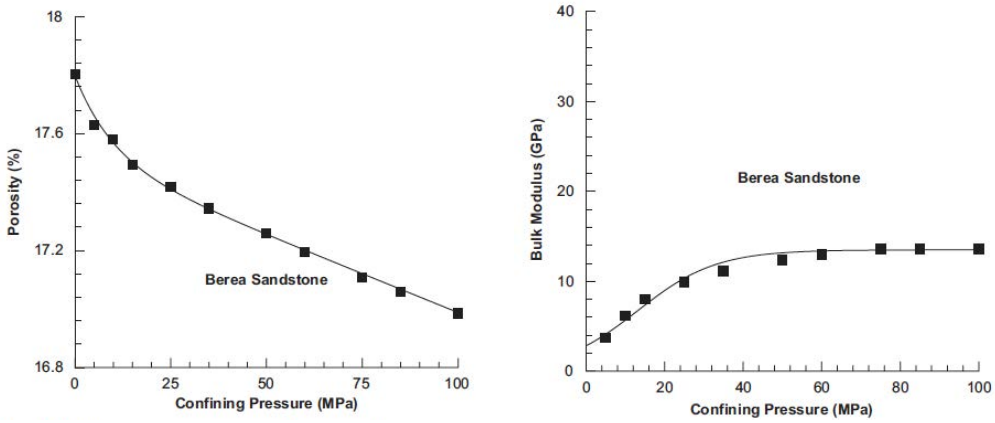

Figure 6.7. A comparison of porosity and bulk modulus for the Berea Sandstone under increasing confining pressure (from Liu et al., 2009).

Consequently, the porosity of basalt may reach values of 50% (Anderson and Bowers, 1995) but being generally unconnected, except for minor microcracks that formed during cooling, their effective permeabilities are low. Permeability is dominantly increased in basalts when it is fractured, which occurs at shallow depths under modest differential stresses (~16 MPa for the lava base). Initial burial and compaction of basalt may result in similar porosity loss as we predict for sandstone, but the effect on effective permeability at this stage will be negligible due to increasing fracture volume. Pore geometry may also influence loss of porosity; pore compressibility has been shown to vary with aspect ratio: spherical holes are the stiffest geometry and their compressibility increases with decreasing aspect ratio (e.g. Jaeger et al., 2007). Interpretations of burial and porosity pathways based on compaction models for sandstones may only be appropriate during the early stages of burial. With

increasing, or cyclic compaction, secondary class F porosity and tortuosity will become more important; brittle fracturing of the lavas will not only introduce additional fracture volume into the rock, but linkage of vesicles will access the void fraction volume also, resulting in even higher permeabilities. This fracture volume will be generated initially in the base of the lava, followed by the lava top.

Connected porosity in basaltic sequences provides enormous storage potential for fluid-related resources and waste. This is especially relevant in areas such as the Pacific NW of America, Iceland and Hawaii where basaltic aquifers are important water sources (Anderson and Bowers, 1995; Saar and Manga, 1999; Khodayar and Bjornsson, 2013) and regions such as the NE Atlantic where vast accumulations of Paleocene-Eocene basalts form important components of prospective petroleum basin fill along the margin (Planke et al., 1999; Schutter, 2003). The long-term potential of fluid flow through these materials is therefore critically important.

6.4 Evolution of Inter-Rift Zones: the NE Atlantic

The NE-SW trend of Cretaceous-Cenozoic rift basins along the NE Atlantic margin is widely inferred to be segmented by a series of NW-SE lineaments (Figure 6.8) that have been proposed based on gravity, magnetic, and seismic reflection datasets (Rumph et al., 1993; Doré et al., 1997; Kimbell et al., 2005). Some of these lineaments are projected from steps in the continent-ocean boundary, and a genetic link has previously been hypothesized. Early interpretations of these structures describe them to basin-wide ‘transfer zone faults’, or major strike-slip structures that accommodate major strike-slip offsets between basins and represent reactivated Pre-Cambrian shear zones or inherited Caledonian structures (Rumph et al., 1993; Doré et al., 1997; Doré et al., 1999; Kimbell et al., 2005; Ellis et al., 2009a).

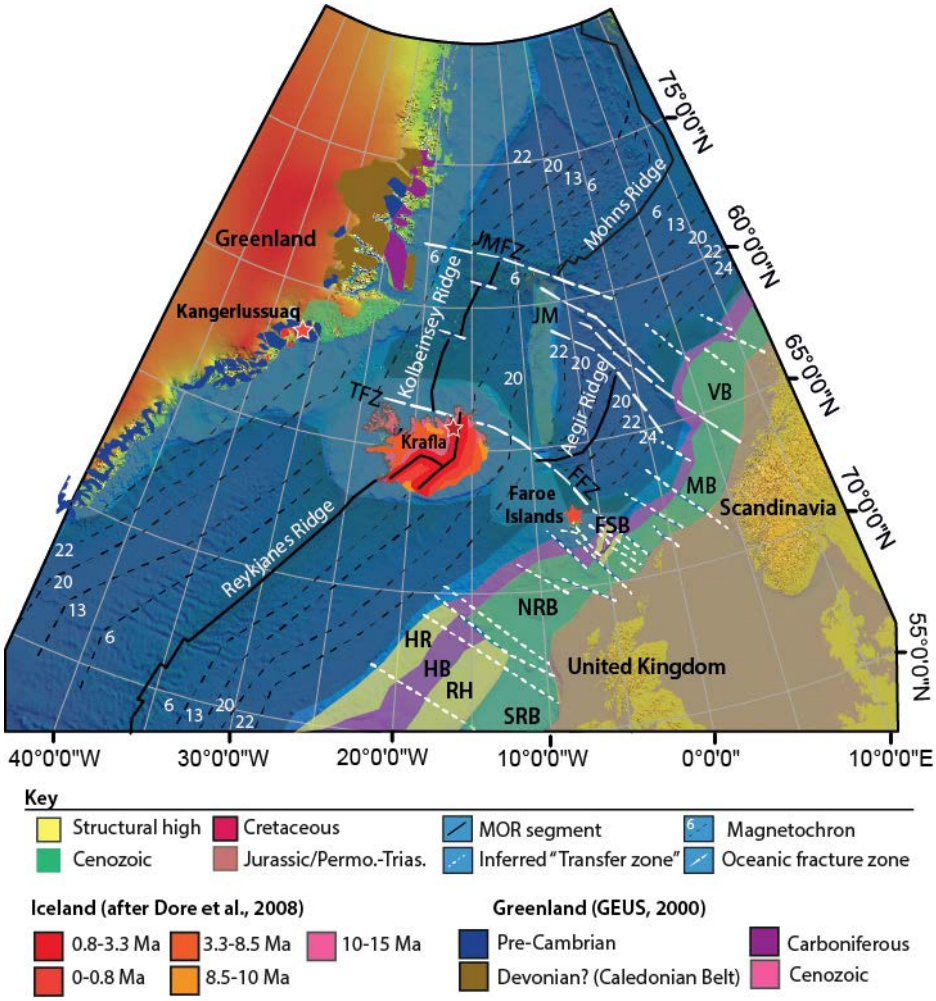

Figure 6.8. Map of the NE Atlantic margins highlighting major tectonic elements and basins: Hatton Rise (HR), Hatton Basin (HB), Rockall High (RH), South Rockall Basin (SRB), North Rockall Basin (NRB), Møre Basin (MB), Vøring Basin (VB), Jan Mayan (JM), Jan Mayan Fracture Zone (JMFZ), Tjornes Fracture Zone (TFZ), Faroes Fracture Zone (FFZ); and study locations: the Krafla Fissure Swarm, the Faroe-Shetland Basin (FSB), and the Skaergaard Intrusive Suite in Kangerlussuaq, SE Greenland. Basin ages after Doré and Lundin, 1997. Oceanic magnetic anomalies after Gaina et al., 2009.

The scale of the resulting segmentation is highly variable and would have had a significant influence on sediment distribution along the margin during the Cretaceous and Early Paleogene (e.g. Sorensen, 2003; Ellis et al., 2009a; Moy and Imber, 2009). The Faroe-Shetland rift basin comprises a series of NE-SW oriented depocentres, segmented by these NW-SE trending "transfer zone" faults; several of these features are projected onshore,

across the Faroe Islands (Ellis et al., 2009b; Figure 6.8 and Figure 6.9a). However, the origins, continuity and kinematics as well as the tectono-stratigraphic significance of transfer zones remain unclear, despite their obvious implications for sediment transport, hydrocarbon prospectivity and plate boundary reconstructions.

Recent and relatively high-resolution seismic surveys and potential field datasets have shown no evidence for basin-wide transfer-zone fault structures (e.g., Moy and Imber, 2009; Rippington et al., 2015). Instead, the term "transfer zone" has been replaced by "rift-oblique lineament", referring to second-order structures related to rift zone architecture and the transfer of strain between adjacent NE-SW trending fault systems, rather than regional scale strike-slip faulting (Moy and Imber, 2009; Ellis and Stoker, 2014).

To further constrain the spatial extent and kinematic evolution of these structures, high-resolution field data and paleostress analysis from the Faroe Islands (published) and Kangerlussuaq, East Greenland (unpublished), is compared to studies of segmented rift-faults and non-coaxial strains in Krafla Fissure Swarm, NE Iceland.

6.4.1 European Margin (Faroe Islands)

The Faroe Islands and Faroe-Shetland Basin are located on the European side of the NE Atlantic margin, at the southern termination of the Aegir spreading ridge segment, which initiated oceanic spreading in the Early Ypresian (~55-53 Ma: Gernigon et al., 2012; magnetochron C24: Figure 6.8). Onshore deformation in the Faroe Islands is characterized by spatially and temporally-related sets of crosscutting faults and intrusive igneous sheets (dikes and sills) that reflect a progressive reorientation of the local extension vector over a period of approximately 10 My during the Paleogene (Walker et al., 2011, 2012. See Figure 6.9).

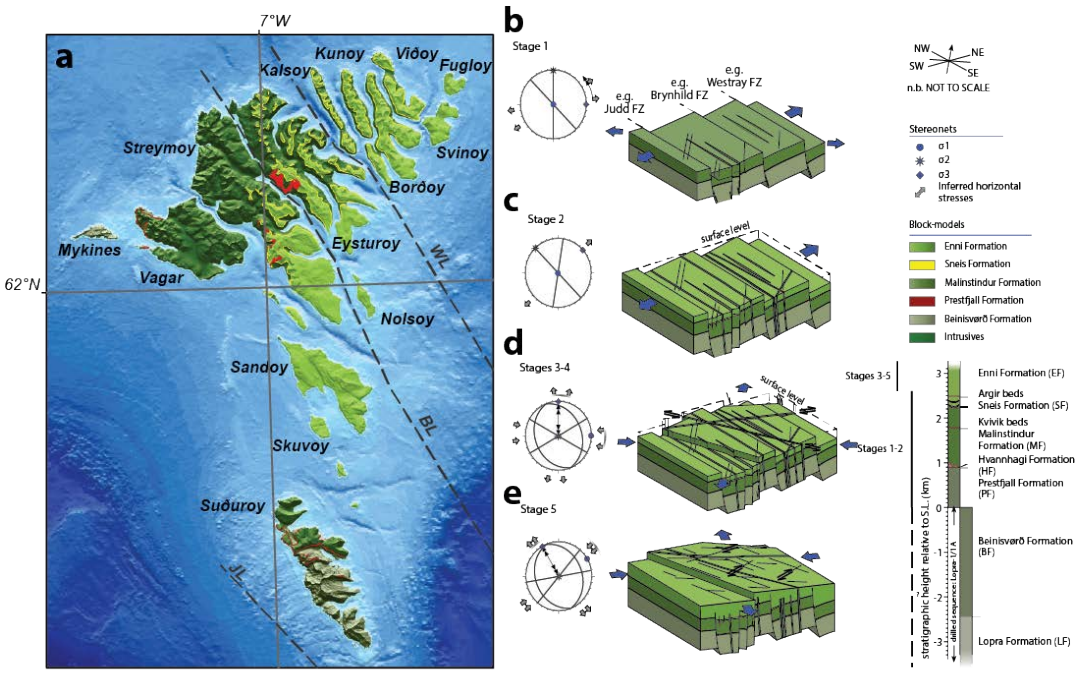

Figure 6.9. (a) Map of the Faroe Islands and inferred NW-SE striking lineaments. (b) Simplified summary block models for structural trends observed on the Faroe Islands, and their timings relative to the FIBG (after Walker et al., 2011). Fault structures in the Faroe Islands record a progressive anticlockwise rotation in extension direction during rift phases associated with the opening of the NE Atlantic.

High-resolution kinematic mapping and paleostress analysis conducted by Walker et al. (2011) of onshore structures in the Faroes recognizes the following phases: 1) Paleocene E-W to NE-SW extension on N-S and NW-SE trending normal faults and dikes (Figure 6.9b and c), followed by 2) Late Paleocene (possibly Early Eocene) N-S extension on ENE-WSW to ESE-WNW conjugate dike sets and strike-slip faults (Figure 6.9d), which are cut by; 3) NW-SE extension on NE-SW and NNE-SSW-striking oblique-slip faults (Figure 6.9e). Rift margin-oblique features in the Faroes accommodate only minor amounts of margin-normal extension and, crucially, NW-SE trending features (parallel to the transfer zone trend) accommodate a margin-parallel extension rather than margin-normal extension, as predicted in the transfer zone model.

6.4.2 North American Margin (Kangerlussuaq, E Greenland)

The Kangerlussuaq region of SE Greenland is on the North American side of the NE Atlantic margin and represents the most northerly penetration of the Reykjanes ridge segment, which also initiated oceanic spreading in the Early Ypresian (~55-53 Ma: Gernigon et al., 2012; magnetochron C24: Figure 6.8). Prior to NE Atlantic spreading, the Faroe Islands and Kangerlussuaq are thought to have been 60-100 km apart (Ellis et al., 2002). This is based on (1) the extent of Cenozoic North Atlantic Igneous Province lavas and intrusions, which dominate both areas and (2) the lack of evidence for feeder systems capable of sourcing the eruptions in Faroes (Ellis et al., 2002). Igneous activity in Kangerlussuaq, associated with continental break-up, is thought to have occurred in three phases: 62-59 Ma, 57-54 Ma and 50-47 Ma (Tegner et al., 1998), with emplacement of the Skaergaard intrusion at ~56 Ma (Wotzlaw et al., 2012). As with the Faroe Islands, deformation is characterized by geometrically- and temporally-linked suites of cross-cutting faults and dikes, hosted within the Archaen basement and Cenozoic stratigraphy (unpublished field data).

Faults and dikes cut the Skaergaard intrusion, and compositionally similar macrodikes (e.g., the Mikifjord macrodike: Figure 6.10a) thought to have been intruded contemporaneously with the Skaergaard intrusion (Holwell et al., 2012), giving a well-constrained maximum age. For example, the 500 m thick Mikifjord macrodike, which is parallel to the margin and Reykjanes ridge segment (i.e., NE-SW; Figure 6.10a) and accommodates margin-normal (NW-SE) extension. The dike is cut and offset by ESE-WNW oblique-extensional faults, which show displacements of at least ~100 m (e.g. Figure 6.10a), and form a conjugate set with ENE-WSW-striking faults that accommodate margin-oblique (N-S) extension (Figure 6.10b). These faults are parallel to conjugate dikes, which show a mutual cross-cutting relationship and also cut the Skaergaard intrusion (Figure 6.10c).

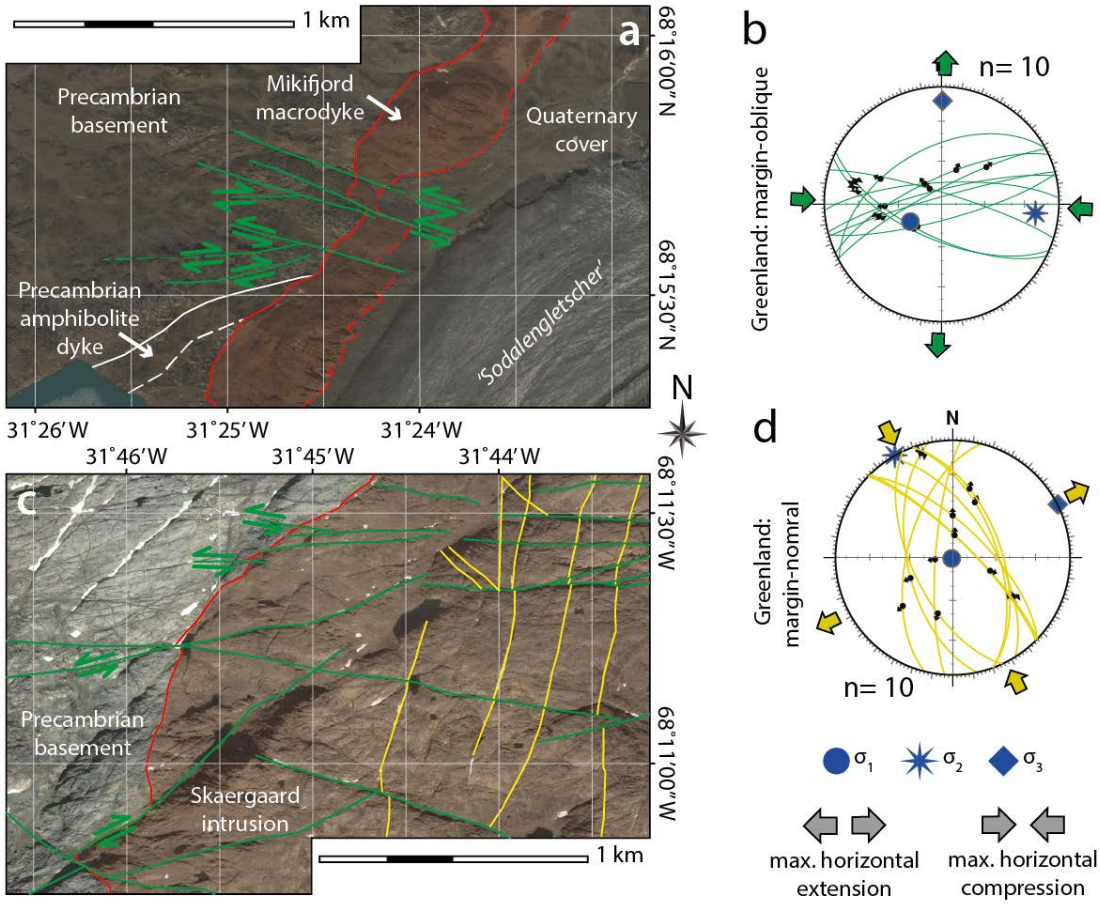

Figure 6.10. Structural sets in Kangerlussuaq region of E Greenland from unpublished field data collected by Richard Walker. (a) rift-oblique faults cut the rift-parallel Mikifjord macrodike; (b) rift-normal faults and dikes cut the Skaergaard intrusion, which are in turn cut by rift-oblique faults and dikes.; (c) Lower hemisphere stereographic projection for rift-oblique faults; and (d) Lower hemisphere stereographic projection for rift-normal faults.

The Skaergaard intrusion additionally hosts margin-normal (N-S to NW-SE) faults and dikes, accommodating margin-parallel (NE-SW) extension (Figure 6.10d), which are cut by the margin-oblique structures (Figure 6.10c). Locally, margin-parallel dikes are observed in the Skaergaard intrusion, which cut the ESE-WNW faults and dikes and the N-S to NW-SE fault sets. These structures are directly comparable to fault and dike sets in the Faroe Islands, implying that they share a common geometric, kinematic, and temporal evolution. The geometry and kinematics of these structures are compared with mapped structures in the

Krafla fissure swarm to test where deformation along the E Greenland and European margins are comparable to the rotational strains described and interpreted in Chapter 5.

6.4.3 Comparison with the Krafla Analogue

Faults and fractures in the Krafla system can be separated into three structural sets based on kinematics and orientation (Figure 6.11): (1) rift-parallel (NE-SW striking) sets of extension fractures and normal faults, that accommodate NW-SE extension; (2) rift-oblique NW-SE striking normal faults and mixed-mode fractures that accommodate ENE-WSW extension; and (3) rift-normal WNW-ESE striking extension fractures, accommodating NNE-SSW extension. Rift-oblique faults (set 2) are well-developed (throws >2 m) and form segments of rift-parallel faults that have followed locally modified trajectories. Rift-normal (set 3) fractures represent the smallest strains in the relay zone, with maximum apertures of 0.8 m and no vertical displacement (throw). Rift-normal and rift-oblique sets are cut by rift-parallel normal faults and extension fractures, which accommodate rift-normal extension, with faults demonstrating throws of ~ 3m and maximum apertures of ~5 m on fractures. Structural mapping of the Krafla system has not revealed evidence for rift-normal strike-slip faults: each fault/fracture set accommodates a unique extension direction, consistent with the accommodation of a progressive clockwise vertical axis block rotation (Chapter 5). Rift-parallel fractures form the bounding structures of the relay zone, which appears to be cut by an additional rift-parallel fault, indicating that NE-SW striking faults represent the first and final stage of deformation in the rift. No consistent cross-cutting relationships are observed between rift-oblique and rift-normal structures within the relay zone, suggesting that they formed contemporaneously as a result of non-coaxial deformation during vertical axis rotation and continued rift-normal extension on the bounding rift faults.

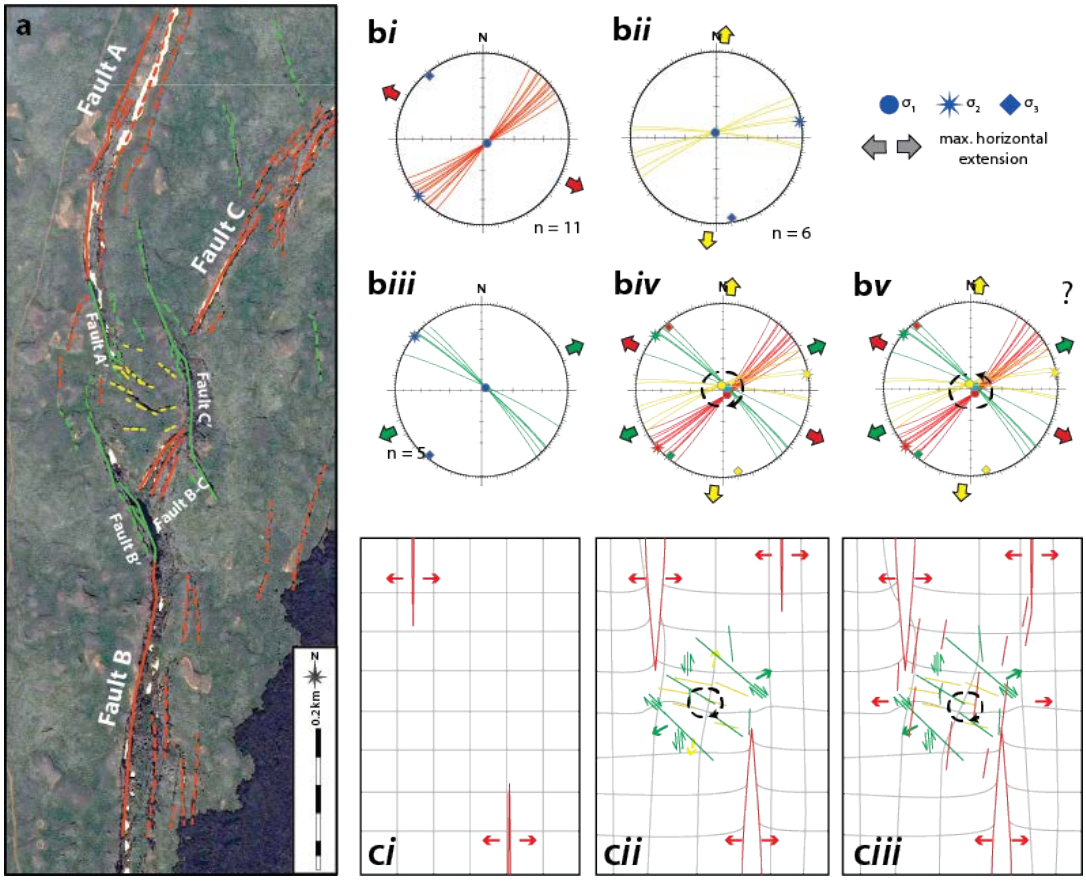

Figure 6.11. (a) Mapped faults and extension/extensional-shear fractures in the study area, color-coded based on orientation and kinematics. (b) Stereographic projections showing measured fault/fractures as planes and measured extension directions for each of the three structural sets: (1) rift-parallel faults and fractures (red; b*i*); (2) rift-normal fractures (yellow; b*ii*); and (3) rift-oblique faults and fractures (green; b*iii*). The left-stepping configuration of faults A and B are consistent with clockwise rotations in extension direction (b*iv*), whereas the right-stepping configuration of fault B and C is consistent with a counter-clockwise rotation (b*v*). (c) Proposed evolution of fault sets: (c*i*) Propagation of the main rift-fault set; (c*ii*) Interaction between the main rift faults leads to vertical axis rotation in the relay zone, and induced local reorientation of extension direction accommodated on variably oriented ancillary faults and fractures; (c*iii*) continued propagation of the main rift faults and clockwise rotation, or counter-clockwise rotation associated with a new right-stepping configuration leads to the development of new rift-parallel structures.

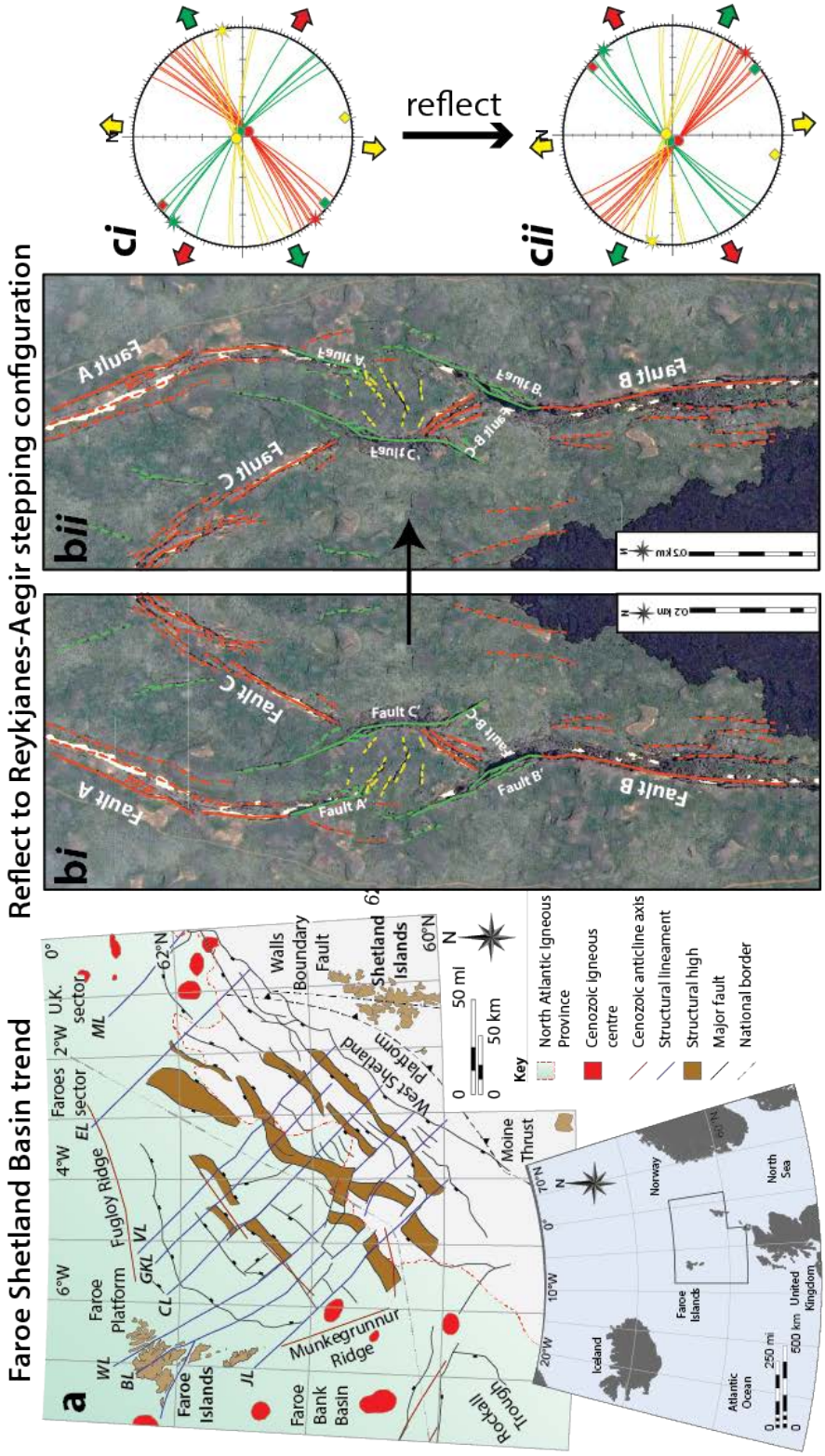

Figure 6.12. (a) Map of the tectonic elements of the Faroe Shetland basin (FSB). (b) Krafla fault data is reflected from a left-stepping configuration (b*i*) to a right-stepping one (b*ii*) to match the configuration of the Reykjanes-Aegir ridge segment offset. (c) Stereographic projections show the original trace orientation (*ci*) and the rotated trace orientations and extension directions (c*ii*).

To compare relative orientations and kinematics, the Krafla rift datasets have been reflected and rotated into the orientation and overlap configuration of the Atlantic European margin basin systems: i.e. a NE-SW trending, right-stepping rift (Figure 6.12). To achieve this, a right-stepping mirror image of the Krafla data is used (Figure 6.12b*ii*, c*ii*) and compared with the Reykjanes-Aegir system, with the rift-parallel faults rotated into parallelism with those of the NE Atlantic margin (Figure 6.13a, b and c). Data manipulation is undertaken in two ways for comparison: (1) by rotating the mapped fault traces in Krafla (Figure 6.13b), which represent an irregular topographic intersection of planar faults, into an orientation that matches the mapped traces of European margin rift faults; and (2) by rotating the Krafla data (Figure 6.13c) so that the average strike of the rift-parallel structures match the measured strike of rift-parallel structures in the Faroes and east Greenland. Both types of rotation lead to the ancillary data becoming parallel with structural sets mapped in the Faroe Islands and Kangerlussuaq (Figure 6.14).

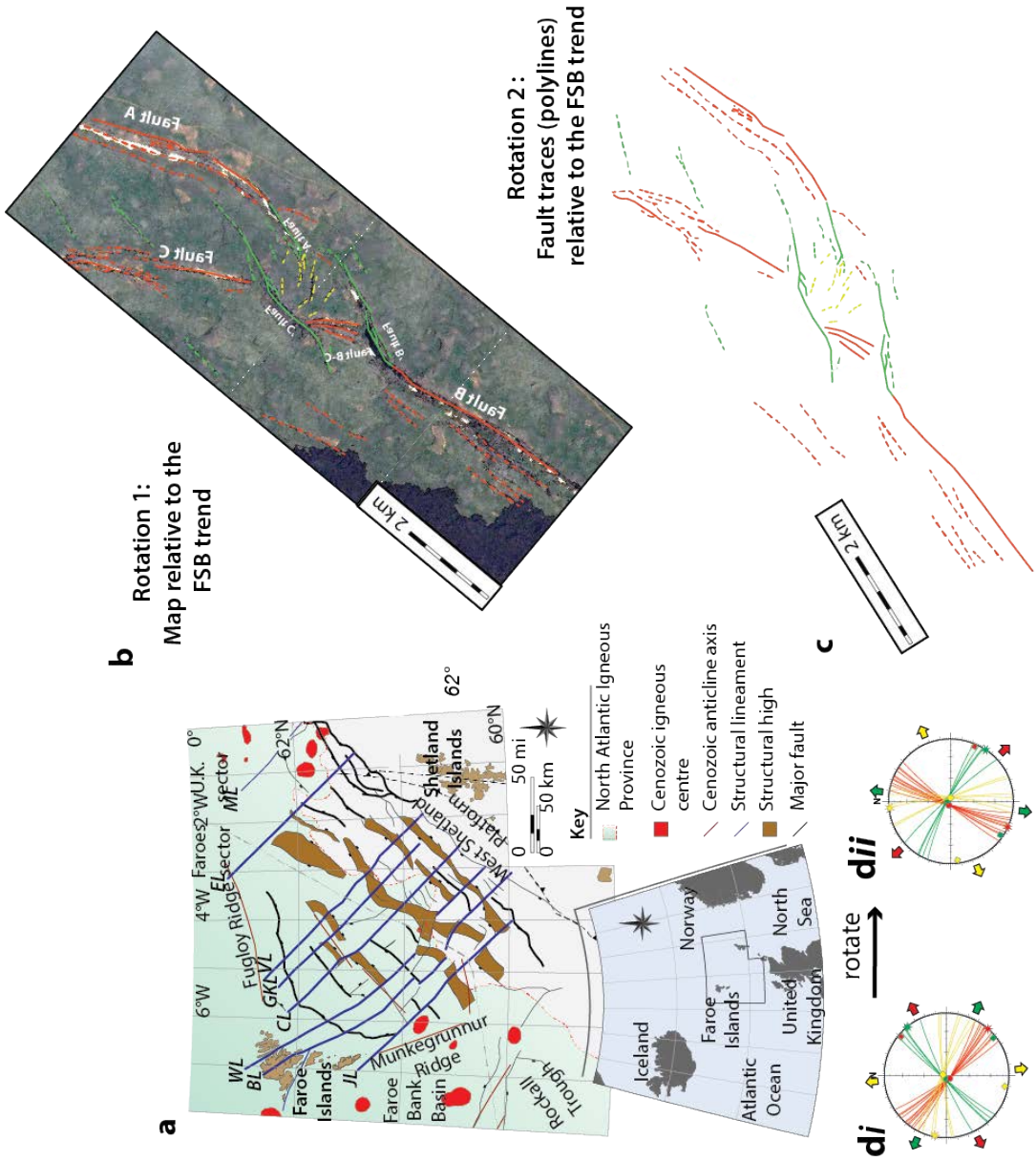

Figure 6.13. Rotation of Krafla fault data is undertaken in two ways here for comparison: (1) a map rotation, where the edges of the map parallel the trend of the FSB; and (2) a data rotation, where fault traces (polylines) are rotated until rift-parallel faults follow the trend of the FSB. Each rotation produces similar results.

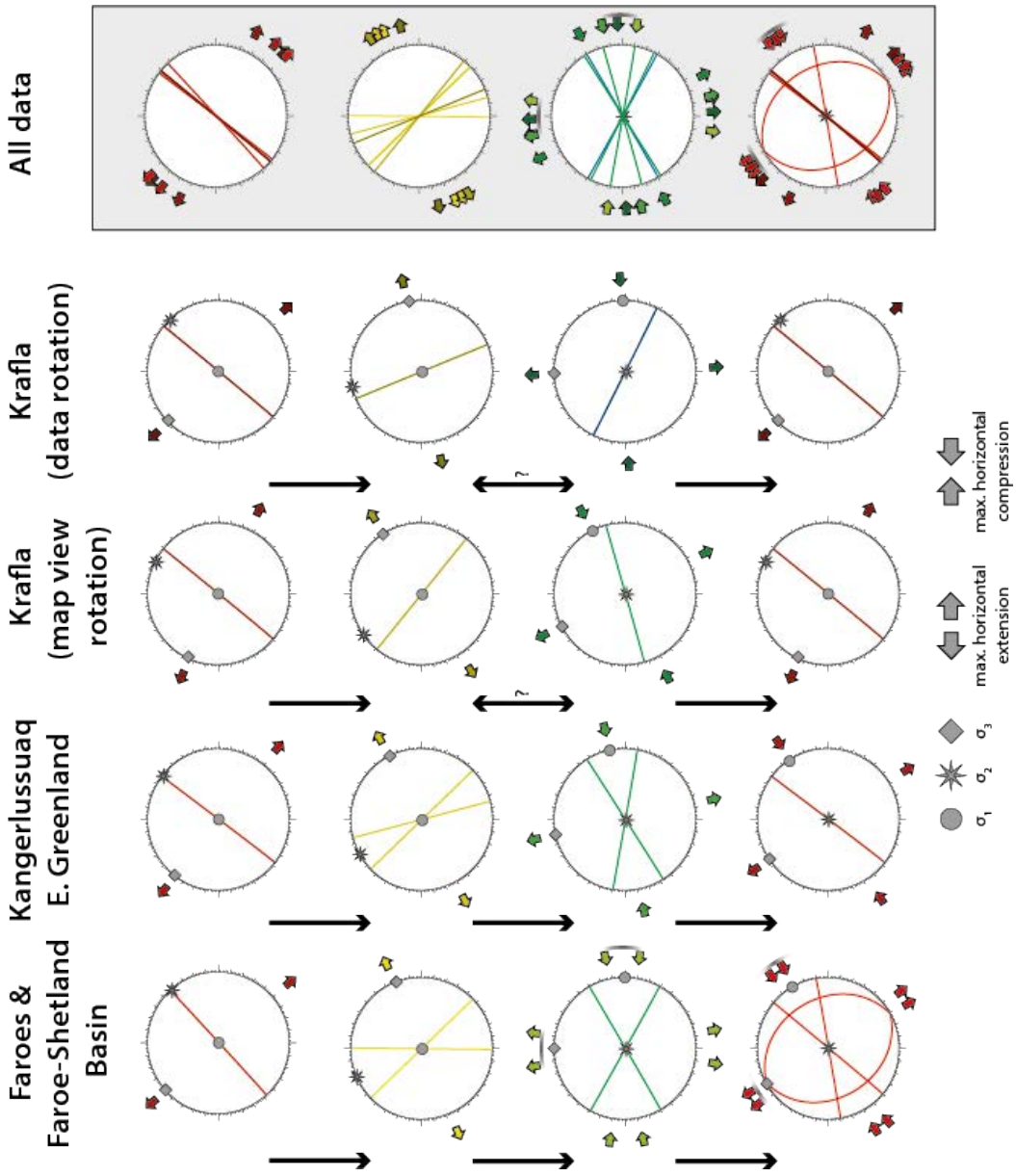

Figure 6.14. Combined summary of orientations and kinematics from each study locality that shows a counter-clockwise rotation in extension vector: (a) structural data from the Faroe Islands; (b) structural data from Kangerlussuaq, SE Greendland; (c) reflected and rotated map data from the Krafla fissure swarm; (d) reflected and rotated fault traces from the Krafla fissure swarm; and (e) comparison of NE Atlantic data with rotated and reflected datasets from Krafla.

Comparison of all normalized datasets shows kinematically near-identical fault sets. Importantly, each dataset comprises: (1) rift-parallel faults that represent the first and final structural set, opening normal to the rift axis; (2) a set of rift-normal structures that accommodate rift-parallel extension; and (3) rift-oblique structures that accommodate extension oblique to the rift (Figure 6.14). Although the relative timings of the latter two sets in Krafla cannot be confidently determined, their orientations and kinematics fit with those observed in the Faroe Islands and Kangerlussuaq.

6.4.4 Scaling of Interpretations

Analytical solutions for isolated cracks under a uniform applied stress produce resolvable sets of internal stresses, but the addition of neighboring cracks results in the superposition and modification of their opposing three-dimensional elastic fields (e.g. Pollard and Aydin, 1984; Crider and Pollard, 1998; Maerten et al., 2002). The magnitude of the resulting stress field is approximated by the stress intensity factor (K), a function of the applied stress, geometry (length, depth) and position of a crack (Sih, 1976; Segall and Pollard, 1980; Engelder et al., 1993; Crider and Pollard, 1998). With the magnitude of K scaling linearly with crack length, the effect is expected to scale with fault size (Pollard and Aydin, 1984). This is supported by worldwide catalogues of relay zone geometry that demonstrate a power-law scaling relationship over approximately 8 orders of magnitude (Peacock, 2003; Long and Imber, 2011). For example, the Baikal rift zone, where faults bound a 400 km^2 relay zone (Hus et al., 2006). The relay zone in the Baikal rift that is referred to in the study of Hus et al. (2006) shows many characteristics that have been observed at smaller scales in the Koa'e and Krafla, including: (1) overlapping rift faults; (2) progressive development of obliquely oriented ancillary fault structures internal to the relay; and (3) formation of connecting faults.

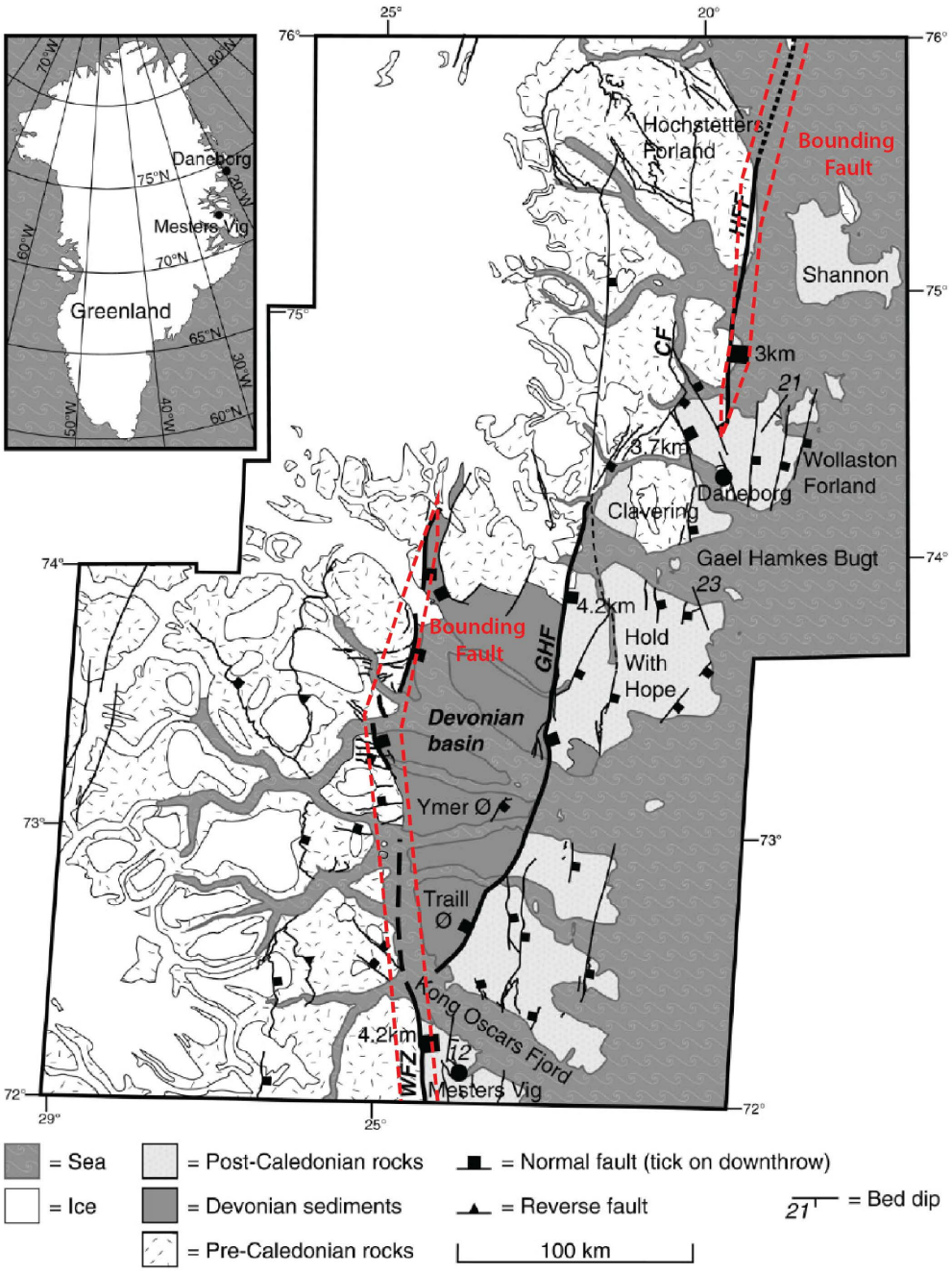

Figure 6.15. Map of the Hold With Hope relay zone in NE Greenland. The zone highlighted by the red box is bound by large km-scale displacement normal faults (from Peacock et al., 2000).

The Hold With Hope relay zone in NE Greenland is larger still, and bound by two basin-margin normal faults that are separated by approximately 100 km (Figure 6.16, inset box). It is considered to be the world's largest zone of interaction, covering an area of 25,000 km^2 (Peacock et al., 2000). A descending scale of ancillary normal faults and ancillary relay

zones, internal to the primary relay zone, accommodates transfer of displacement between these two large normal faults. In these examples, hard linkages are not discrete, well-expressed structures that develop instantaneously, but a zone of non-coaxial strain that evolves with the progressive displacement and/or propagation of the bounding fault structures.

Recent Geomechanical elastic modeling of en echelon faults in the northern Viking Graben in the North Atlantic has reconstructed the stress field associated with complex distributions of major N-S to NW-SE trending normal faults and smaller scale oblique ancillary faulting (Maerten et al., 2002). The resulting elastic deformation field produce stress perturbations consistent with the distribution and orientation of ancillary faults in the seismic dataset presented in the same study. Alternatively, they propose that subordinate fault sets in the seismic dataset have developed as a result of local stress distributions surrounding the larger faults, and importantly, that this is a process that may be common across a range of scales. The results of Maerten et al. (2002) remove the need for multiple tectonic episodes or reactivation of basement lineaments that may otherwise be used to account for the obliquely oriented ancillary fault sets surrounding en echelon bounding faults. This raises an important question, based on the scale invariance of interaction-related stresses and expected inelastic processes: why are large-scale transfer zone faults invoked to account for NE Atlantic margin-oblique lineaments?

6.4.5 A Dual-Rift Model

Findings from the Faroe Islands and Kangerlussuaq suggest that rift-oblique structures along the NE Atlantic margins are sub-basin-scale dikes and normal faults, rather than basin-scale strike-slip systems, recording a distinct phase of margin-parallel extension (Walker et al., 2011). These patterns are difficult to explain using the transfer zone models

(e.g. Ellis et al., 2009; Guarnieri, 2015). Structural sets in both of these study sites exhibit distinct extension directions relative to the main rift trend, with structural geometry and measured extension vectors sharing near-identical orientations with analogous structures in the Krafla fissure swarm relay zone. Assuming stress field interaction is responsible for the development of these fault sets, at both scales, the following evolution is proposed: 1) Initially segmented rift faults and networks of mode-I fractures accommodate the regional NW-SE extension direction (Figure 6.16a); 2) propagation of fractures and initial interaction of stress fields surrounding the tips of en echelon fault segments results in the development of a relay zone, characterized by vertical axis rotation and the formation of highly oblique extension fractures accommodating NE-SW extension (Figure 6.16b); 3) continued displacement on the rift-fault set results in further anticlockwise rotation towards a N-S extension and the abandonment of the highly oblique fault sets in favour of the development of a hard linkage that is comprised of less oblique extensional shear sets and normal faults (Figure 6.16c); 4) Further anticlockwise rotation shuts off the oblique fault sets and results in new margin-parallel faults and extension fractures that begin to cut the relay zone (Figure 6.16d); 5) later rift-parallel fault structures link together to produce a new through going rift fault (system), accommodating the regional NW-SE extension direction. In the Faroe Islands this may have taken place when spreading in the Reykjanes and Aegir ridges was great enough to create a through-going sea floor.

With evidence suggesting that initial break-up in the NE Atlantic was strongly segmented (Gaina et al., 2009; Gernigon et al., 2012; Ellis and Stoker, 2014), it is proposed that margin-oblique and margin-normal structures in the Faroes and Kangerlussuaq reflect locally heterogeneous stress distributions associated with the progressive propagation of two active rift systems during the Paleogene: a SW to NE propagating Reykjanes rift segment and a NE to SW propagating Aegir rift segment.

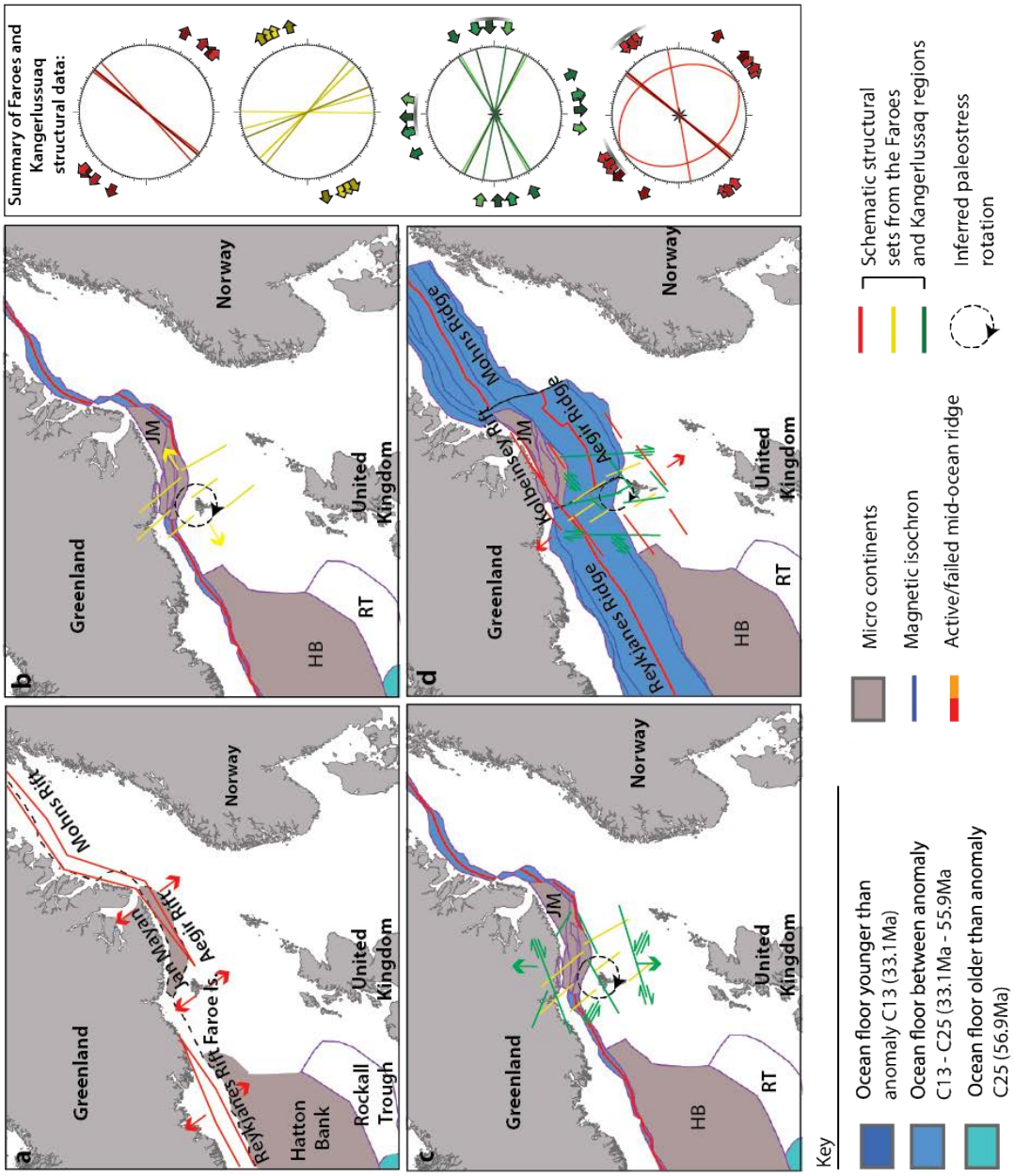

Figure 6.16. A dual rift model for the opening of the NE Atlantic. A regional clockwise rotation in extension direction is replaced locally by an anticlockwise rotation in the relay zone that separated SE Greenland and the Faroe-Shetland region: 1) NE-SW extension; 2) N-S extension; and 3) NW-SE extension. The development of this zone and associated deformation is related to the propagation of two active rift systems during the Paleogene: the Reykjanes and Aegir ridge systems.

The Faroe Islands sit ahead of the tip of the Aegir spreading ridge and represent the eastern extremity of this proposed, relay zone. Kangerlussuaq lies at the western margin of this zone and represents the most northerly penetration of the Reykjanes ridge segment. Progressive propagation of these two active rift segments, the Reykjanes ridge from the SW towards the NE and the Mohns-Aegir ridges from the NE towards the SW, would induce stress perturbations through time in response to progressive mechanical interactions of the two opposing stress fields and result in non-coaxial strains. The model thus removes the need for transfer zones due to basement reactivation, or some other as yet unidentified process.

A progressive rotation and deformation in a relay zone is concordant with sediment source datasets, borehole analysis, and volcanic-stratigraphic mapping on the European and Greenland Atlantic margins, which suggest that a topographic high separated the Faroe-Shetland Basin from Kangerlussuaq during the Paleocene-Eocene (Ellis and Stoker 2014). In the Ellis and Stoker (2014) model, the topographic high forms an inter-rift high (relay zone) as a result of a dual-rift configuration where a NE-propagating Reykjanes ridge did not meet the SW-propagating Mohns and Aegir ridges in the Cenozoic, leading to a high centred on the Jan Mayen-proto Iceland region. This (continental) high divided Kangerlussuaq from the Faroe-Shetland Basin (FSB) until the eventual abandonment of the Aegir Ridge in favour of a through-going link between the Reykjanes and Kolbeinsey Ridge segments during the Eocene and into the Miocene. Structural findings here support this model.

Early-forming and pre-existing damage surrounding evolving rift systems is traditionally thought to control the distribution of new faults, and therefore the segmentation of previously continuous rift basins along the NE Atlantic margins (e.g. Doré et al., 1999). In the model proposed here, basin segmentation occurs as a result of obliquely oriented structures that represent ancillary normal and oblique-slip faults and

dikes rather than large-scale strike-slip systems that developed ahead of two propagating rift systems. The scale of this segmentation is controlled by the initial segmentation of the developing rift system, which is in turn influenced by the emplacement of magma during it's formation and at a smaller scale still, the mechanical stratigraphy imposed by the physical properties of the deforming host volume.

With well-known seismic imaging issues within basaltic sequences (Doré et al., 1997; Planke et al., 1999; Schutter, 2003; Kimbell et al., 2005; Moy and Imber, 2009) and problems regarding core recovery and the resolution of flow-scale interpretations based on petrophysical measurements (Planke, 1994; Yale and Nieto, 1995), fieldwork and detailed analysis of exhumed fault zones in basaltic sequences remains the best way to investigate the segmentation of faults and their potential impact on fluid resource-related exploration and exploitation along volcanic passive margins.

Chapter 7

Conclusions and Further Research

7.1 Conclusions

1) Basaltic lava units show three components defined by the relative distribution and geometry of vesicles, which control their mechanical response to uniaxial compression. While porosity, as a scalar quantity, exerts a strong influence on the strength of intact basalt, the primary control on intact rock strength is the geometric anisotropy associated with the shape of pores and their orientation with respect to an applied stress. This intact lava mechanical stratigraphy imposes a sub-unit scale control on the segmentation and growth of fractures: initial failure of the weak base component (16 MPa), followed by the top (60-80 MPa) before eventually linkage through the core (110 MPa).

2) Analysis of the geometry and displacement characteristics of extension fractures at the cm- to 10s-of-metre-scale in the Koa'e fault system show path geometries and displacement-length profiles consistent with progressive stages of interaction and linkage of segmented fractures. Straight, convergent, divergent and abutting path geometries show consistent extension-mode opening, indicating two simultaneous components of strain: a regional extension and a local extension associated with the process of fracture growth and linkage.

3) At the individual fracture scale, the geometry of fractures is controlled by the anisotropy of the deforming lava, the pre-existing joint network, and the varying intact strength properties of the lava. The distribution of surface fractures is driven by stresses associated with fault growth at depth.

4) Analysis of the geometry and displacement characteristics of normal faults at the 100s-of-metre to 1 km-scale in the Koa'e fault system and Krafla fissure swarm also show path geometries and displacement-length profiles consistent with progressive stages of interaction and linkage of segmented faults.

5) Extensional strains in the Koa'e fault system are characterised by a combination of surface-breaking normal faults (displacement <15 m) and blind normal faults associated with flexure of the ground surface. In the Krafla fissure swarm, extensional strains are dominated by surface-breaking normal faults with displacements > 15m, implying faults are in a more advanced stage of development.

6) The initial distribution of rift faults in both fault systems is likely to be determined by dike tip-related stresses at depth. Their subsequent propagation is strongly influenced by the strain rate within each system, and facilitated by a mechanically layered and anisotropic volume. The fault population in Iceland coincides with a plate boundary setting where magma supply rates (and corresponding strain rates) are higher and the deforming sequence contains significant quantities of weak hyaloclastite and large fluid volumes that help lower the required driving stresses to cause failure, and repeated fault slip. Fault slip throughout the Koa'e system is more difficult to drive with lower magma supply rates, spatially limited dike emplacement and a sequence of dominantly dry lavas.

7) The formation and propagation of faults in basaltic sequences, and resulting geometries and kinematics, cannot be predicted by models that assume in-plane propagation of a structure through a linear elastic, isotropic, isothermal volume that undergoes constant and uniform boundary stress conditions.

8) At all scales, there are no instances of rift-normal strike-slip (transfer) faults within the Koa'e fault system, or the Krafla fissure swarm: each fault/fracture set in these rift zones accommodate a unique extension direction. Oblique extension is only observed on discontinuous faults located at the lateral terminations of rift faults. Their orientations and kinematics are consistent with the progressive mechanical interaction of the bounding fault stress fields, which has resulted in incremental inelastic deformation that follow modified stress trajectories and accommodate non co-axial strain.

9) Interpretations of local mechanical interaction-induced stresses and resultant 3D strains have implications for larger scale investigations of en echelon rift systems. Break-up related extension in the NE Atlantic, which is traditionally thought to be accommodated by margin-parallel (NE-SW) normal faults and margin-normal (NW-SE) strike-slip "*transfer zone faults*", instead records progressive *counter-clockwise* rotation of extension direction during the Cenozoic, prior to and during break up.

10) Structural sets along the European and North American margins (Faroe Islands and Kangerlussuaq, E Greenland) are consistent with ancillary fault and fracture sets and inferred progressive stress rotations that were mapped in the relay zone of en echelon rift faults in Krafla.

11) It is proposed that NW-SE trending transfer zone fault lineaments along the NE Atlantic margin structures represent sub-basin scale normal and oblique-slip faults and dikes rather than large-scale strike-slip systems. These structural sets are attributed to an evolving stress field ahead of two active rift systems: a NE-propagating Reykjanes ridge, and a SW-propagating Aegir ridge from the NE.

7.2 Further Research

7.2.1 Rock Strength Anisotropy

Experimental data gathered in Chapter 3 has shown a significant variation in the strength profile, indicating that studies using very low porosity lava components will not be representative of the whole lava unit. Additionally, results identify pore shape as a primary control on rock strength; potentially more important than porosity as a scalar. This is important for models of volcanic flank stability, where parameters are typically derived from tests on isotropic, low porosity basalts (porosities of 1-4%). The amount of open pore space in the rock has been shown to control elastic properties, and the ultimate strength of the material; pore shape has a similar control on elastic properties, and it is therefore important to consider these effects when "upscaling" to consider the volcanic edifice as a whole. Further possible work in this area can be split into the following questions:

1) **What is the role of pore volume in controlling rock strength?** Testing of synthetic samples with a known (isotropic and homogenous) porosity and additional lava unit samples will allow systematic and quantitative characterisation of the role of void volume on the mechanical response of porous solids under an applied compression. Characterising 3D porosity of natural samples should be addressed using high-resolution X-ray Computed

Tomography (CT) scanning to determine the distribution and size population of voids. For synthetic samples, the pore size and distribution can be controlled during the manufacturing process. Results would provide a well-constrained range of elastic and mechanical properties for a range of void volumes to compare with natural samples. Additional testing of lava unit top and core components using a greater number of larger (100 mm diameter) samples would minimise any potential size effects from large vesicles. Tests should be conducted using the 4.6 kN MTS® triaxial rock deformation apparatus at the Rock Deformation Lab at the British Geological Survey, currently the only unit in the UK capable of testing the 100 mm diameter samples. Tests could be conducted at a range of confining pressures, and low temperatures, to simulate the role of pressure and temperature in the upper crust (0-5 km).

2) **What is the role of pore shape in controlling rock strength?** Systematic testing of synthetic samples with a known, anisotropic, porosity will isolate the role of void geometry as a control on the brittle strength of porous materials. The same test conditions could be applied to manufactured samples with varying aspect ratio voids and additional samples from the anisotropic base component of lavas. Characterising the 3D geometries of voids in natural samples can also be addressed using high-resolution X-ray Computed Tomography (CT) scanning. For synthetic samples, the void geometries will be controlled during the manufacturing process. Conducting tests (on both natural and synthetic samples) at a range of inclination angles between the applied σ1 direction and the long axis of ellipsoidal voids will show how the strength of a curved surface under compression varies. We might expect the rock strength to progressively decrease from a maximum value when σ_1 is parallel to the void long-axis (i.e. the maximum curvature), to a minimum strength when σ_1 is oriented perpendicular to the void long-axis (i.e. the minimum curvature). Numerical modelling of irregular void shapes to produce the 3D stress distributions associated with

different void volumes could be conducted to model geometries that are a closer representation of the often irregular and amalgamated vesicles in natural lava samples.

3) **What is the effect of stress cycling on anisotropic rocks?** Volcanic flanks and rift systems are known to undergo cyclic stressing, related to repeated magma intrusion and rifting episodes. Such stress conditions are typically represented in numerical models as being isotropic and homogenous (i.e. uniformly applied and constant in time and magnitude). Rock deformation experiments investigate time-dependent brittle behaviour using increasing-amplitude cyclic stress testing (uniaxial and triaxial) to measure the evolution in elastic moduli of low porosity (<4%) samples (e.g. Heap et al., 2010, 2011). Initial testing could recreate existing test conditions, but applied first to higher porosity lava and synthetic samples (isotropic porosity) to compare with those results. Further testing would also use anisotropic samples and data could be plot with isotropic results, and published data to establish the effect of (isotropic) stress cycling on samples that are more representative of a flank or rift sequence. Current predictions expect a reduction in Young's modulus from about 30 GPa to 22 GPa, following tens of cycles (Heap et al., 2010). These values are significantly less diverse than the starting properties of basalts presented in Chapter 3 (i.e. about 26 GPa to 5 GPa). The effect of increasing crack damage is likely to be underestimated for these samples, compared with the naturally variable lava components. New tests could also attempt to replicate the naturally anisotropic and heterogeneous stress conditions affecting volcanic flanks and rift systems, resulting from varying magnitude, timing and distribution of magma intrusions. Conducting tests under a varying load and changing the amplitude and length of cycles would produce results that closer represent a natural system and provide values that could not only inform models of fault growth in basaltic sequences but also be used in volcano-tectonic models of flank

stability and seismicity. Results are likely to show that current predictions vastly overestimate the strength of lavas.

Addressing these questions would have broad ranging implications, not only for volcano-tectonic modelling and hazard prediction but also our understanding of lava-hosted fault growth. Experimental results, coupled with further field studies (and possibly analogue modelling, see section 7.2.3) in Hawai'i, Iceland and the Faroe Islands to characterize fault zone architecture as a function of displacement and lithological components will constrain the effects of mechanical stratigraphy within basalt lava piles, on fault nucleation and propagation.

7.2.2 Crack Propagation in Porous Solids

Current models of brittle failure in porous solids under compression show concentrations of tensile stresses at the north and south poles of pores or voids, which induces microcracking and redistributes stress into the surrounding intact rock (Sammis and Ashby, 1986; Ingraffea, 1989). Cracks are predicted to grow in a direction parallel to the applied maximum compression, with an increasing load, until cracks reach a critical length where their stress fields begin to interact. At this stage, coalescence of individual pore-crack arrays lead to the formation of through-going fractures and brittle failure. Vesicles in basalts are predicted to behave in the same manner by concentrating tensile stresses at the north and south poles and lowering the differential stress required to cause catastrophic failure (Heap et al., 2014). Macrofractures are predicted to propagate out from and link individual vesicles, parallel to the applied compressive stress direction.

Analysis of X-ray CT scans of lava samples that were tested in Chapter 3 has not revealed instances of cracks propagating from the north and south poles of vesicles. Instead

fractures occur at the side edges of vesicles, usually converging towards a neighbouring vesicle. This inconsistency in propagation pathway implies that the process is more complicated than existing models predict, and that the distribution of mechanical inclusions (vesicles in this instance) and locally amplified stresses may be important influences on rock failure. Further analysis of the 3D distributions and geometries of cracks and vesicles is required to understand their potential interaction and, ultimately, brittle failure of porous materials.

The pore-emanating crack model may be valid for dilute porosities (<5-10% according to Rice, 1997), where void spacing is great relative to their size. For higher porosities (and small pore-pore distances), the stress concentrations associated with vesicles are less critical in the nucleation of microcracks than the stress field interaction and resulting stress amplification in the neck regions between neighbouring vesicles. This fits well with observations of pore-stress concentrations in porous ceramic materials (under tensile loading) In this model, void stress concentrations have a limited effect on the mechanical behaviour of the material and it is local stress perturbations, coupled with the failure of fewer elements that promotes failure in the absence of increasing load.

CT scanning of samples (natural and manufactured), and comparison of scan data before and after uniaxial and triaxial strength tests could be used to constrain the role of porosity and shape on the distribution of stress within porous materials and their strength. Numerical-based modelling of vesicle geometry and distribution may provide useful predictions and comparisons of the magnitude and configuration of stresses surrounding closely spaced vesicles versus the stresses generated by isolated vesicles.

7.2.3 Numerical and Scaled Analogue Modelling

Current interpretations of normal fault growth in basaltic sequences are based on 2D analytical solutions and scaled analogue models. Numerical-based simulations involve deformation of a linear elastic, isotropic, isothermal, semi-infinite continuum volume under isotropic and homogenous loading conditions. Faults are treated as fixed, planar, frictionless structures that are infinite in their lateral dimension. Models provide first order estimates of the stress distribution surrounding two en echelon faults (or extension mode fractures) with varying overlap separations. However, they cannot predict the effects of: (1) spatially and temporally variable syn-tectonic magmatism; (2) a mechanically anisotropic sequence; or (3) local, interaction-induced stress distributions. Each of these has been shown to be influential in the Koa'e and Krafla fault systems.

Recent scaled analogue modelling have provided a good estimation of upward propagating faults in both a homogenous sequence using hemihydrate powder with a measured cohesion and tensile strength (e.g. Holland et al., 2006) and multilayer sequence using hemihydrate powder interlayered with cohesionless sand (Van Gent et al., 2010). While this is a closer step to understanding fault growth in basaltic sequences, fault geometries and extent are fixed and controlled by the configuration of the experimental set up. They do not reproduce overlapping fault geometries and therefore do not provide any insight into the evolution or distribution of 3-D strains surrounding fault tips. Subsequently, they predict some, but not all, of the surface deformation that has been observed in the Koa'e and Krafla fault systems.

Designing an analogue experimental procedure that is capable of modelling the progressive growth of segmented faults with boundary conditions that replicate the syn-tectonic volume change that occurs during episodic rifting events could produce closer

approximations extensional strains and further improve our understanding of fault growth. This could be achieved by testing a combination of the following:

1) ***Deformable boundaries:*** This would produce a controlled but heterogeneous stress that could additionally be applied at a constant or non-constant rate, to consider the effect of lateral and temporal strain rate on fault geometry.
2) ***Mechanical layering:*** A deforming sequence of mechanically variable layers, where layers would also be laterally and vertically variable in thickness to replicate the variable architecture of lavas.
3) ***En echelon faults:*** Faults that are arranged en echelon, rather than fixed across the length of the box, could also be designed to propagate towards each other through the anisotropic sequence, under heterogeneous and anisotropic boundary conditions. Testing different separation distances could also be used to study the effects on the orientations of the incremental inelastic strains that develop ahead of their lateral tips.

Numerical modelling could also be used to investigate whether oblique slip on a fault at depth will induce fractures with extensional-shear openings ahead of the tip. In southern Iceland, for example, arrays of left- and right-stepping en echelon extension mode fractures are interpreted to be related to right- and left-lateral components of slip on normal faults at depth, respectively (Grant and Kattenhorn, 2004). Kinematic data, however, are not presented for these structures, and they are simply referred to as *fractures.* It is unclear therefore, whether oblique slip at depth also takes place at the surface, or whether fractures demonstrate extensional-openings. It is an assumption to assume they have extensional-shear kinematics.

Similar issues are also apparent in the work of Hjartardöttir (2010) where rift-normal (WNW-ESE) trending fracture lineaments that are observed in satellite data are assumed to accommodate a strike-slip offset between en echelon volcanic systems. Fractures in the same

orientation in the study area in Chapter 6 show purely extensional opening, highlighting the importance of field data. Studies that involve remote sensing-based mapping of fracture networks are unable to resolve kinematic information and are only able to provide orientation and geometric information. Without careful, and high-resolution field data collection data pertaining to the minor, sub-image-resolution, structures, their possible timings and kinematic nature will be missed and a kinematic and geometric evolution cannot be established. A combination of analogue and numerical modelling, coupled with further field observations, will greatly expand our understanding of the kinematic evolution of segmented faults and their role in rift development and fluid flow.

7.2.4 The Role of Cooling Joints in Normal Fault Growth

Existing observations of normal faults in basaltic sequences have led to the assumption that faults will initiate from pre-existing cooling joints internal to the lava units (e.g. Gudmundsson and Backstrom, 1991; Gudmundsson, 2011). The architecture of basalt-hosted faults is thought to be controlled by the distribution and geometry of these pre-existing cooling joints, which in turn control the surface expression of faults and faciliates folding and fault zone asymmetry (Crider, 2015). The scale and distribution of joints are controlled by the cooling rate of the lava; joints are shorter and more closely spaced in the top and base of a lava where cooling is rapid, and larger and more widely-spaced in the core where cooling is slower (DeGraff and Aydin, 1987; Crider, 2015). Thus, the distribution and continuity of joints varies significantly both within, and between lavas. Evaluation of the rock mass properties of basalt has highlighted the significant weakening effects caused by the presence of these joints (Schultz, 1993, 1995). Theoretical studies of fault growth in a lava pile suggest that faults will develop when a set of cooling joints become inclined with respect to the principal stress planes during burial (due to lava flow accumulation and/or rotation with fault slip) and are thus subject to shear stresses.

Alternatively, faults may develop when an extension fracture (which also initiates from joints at the free surface) reaches a critical depth that is determined by:

$$Z_{max} = \frac{3T_0}{\rho g}$$

Where:

T_0 is the tensile strength, ρ is the density of the lava pile and g is the acceleration of gravity (Gudmundsson and Backstrom, 1991; Gudmundsson, 1992, 2011). Zmax is thought to lie in the range 133-799 m for a density of 2300 kg (Gudmundsson and Backstrom, 1991). Joints in lavas are comparable to en echelon extension fractures; a normal fault developing from a joint does not propagate in it's own plane through the sequence, but through the development and linkage of extension fractures around the joint tips (Gudmundsson and Backstrom, 1991). The formation of a through-going normal fault is therefore governed by the intact strength of the lava surrounding the joint tips and the shear strength of the asperities of contact on joint surfaces for repeated slip.

It is, however, important to recognize that these models are not well-evidenced in field characterisation. Walker et al. (2011; 2013) show that fault zones representative of 1-3 km depth, provide evidence that although joints are reactivated, faults cut through intact portions of the volcanic pile. This empirical observation should be accounted for. It is possible that the idealised flat joint surface used in models is an oversimplification: natural joint surfaces are highly irregular, discontinuous, weathered, and sometimes mineralised. The models assume cohesionless structures, but this may not be true in the subsurface, making joint strength an important material parameter when considering fault development. Further work on this subject would benefit from additional field study of the relationships between cooling joints and faults that developed in lavas at depths >1 km (e.g. the Faroe Islands). This would be complimented by experimental characterisation of healing and sealing times for natural or artificial joints surfaces, and the frictional strength of naturally-formed, irregular joints.

Appendix I

1.1. Methodology and Full Results: Porosity and Density.

Once cored and surface-ground, samples were placed in an oven for approximately 24 hours at 105^{o}C to dry off any moisture gathered during the preparation process. Using a set of precision scales, the **grain mass** (M_s) was measured for each sample, taken as the equilibrium mass after oven drying. Samples were measured and stored in a desiccator with an airtight lid during cooling. Following this, **bulk volume** (V) was obtained using a set of micrometre callipers, accurate to 0.01 mm. For each sample five measurements of length and diameter were recorded and averaged to obtain a single reading with high accuracy. Alternatively, bulk volume may be determined using the buoyancy method, based on Archimedes Principle.

Equation 1.

$$\boldsymbol{V = \frac{(M_{sat} - M_{sub})}{\rho_{water}}}$$

Where

$\boldsymbol{M_{sat}}$ = Saturated, surface dry grain mass

$\boldsymbol{M_{sub}}$ = Saturated, submerged grain mass

$\boldsymbol{\rho_{water}}$ = Density of water

With bulk volume and grain mass for each sample, we were able to calculate the **Dry density** (ρd):

Equation 2.

$$\boldsymbol{\rho_d = \frac{(M_s)}{V}}$$

Where

$\boldsymbol{M_s}$ = Grain mass

$\boldsymbol{V}$ = Bulk volume

The **pore volume** (V_v), requires the grain mass (M_s) of each sample to be subtracted from a **saturated, surface-dry** grain mass parameter (M_{sat}); this is typically measured along with a **saturated, submerged** grain mass (M_{sub}) parameter. M_{sub} represents the saturated and submerged mass after a period of immersion in de-aired, distilled water under vacuum of 8 mbar for 2 hours with periodic agitation to remove any trapped air in the vesicles. Saturated samples were transferred to a water bath containing a wire basket, attached to a set of scales and their submerged mass recorded, within an accuracy of 0.001 g. After M_{sub} has been recorded, samples are dried with a cloth to remove surface water. M_{sat} may then be measured using a set of scales to within an accuracy of 0.001 g. However, due to the high number of large, open pore spaces in our samples, it is possible that the water would drain out rapidly, rendering this method unsuitable. Instead, bulk volume was calculated using a calliper method and rearranged Equation 1 to obtain M_{sat}.

Equation 3:

$$\boldsymbol{M_{sat} = (V \times \rho_{water}) + M_{sub}}$$

Where

$\boldsymbol{V}$ = Bulk volume
$\boldsymbol{\rho_{water}}$ = Density of water
$\boldsymbol{M_{sub}}$ = Saturated, submerged grain mass

The equation for volume of pore space in the rock sample then becomes:

Equation 4:

$$\boldsymbol{V_v = \frac{(M_{sat} - M_s)}{\rho_{water}}}$$

Where

$\boldsymbol{M_{sat}}$ = Saturated, surface dry grain mass

$\boldsymbol{M_s}$ = Grain mass
$\boldsymbol{\rho_{water}}$ = Density of water

Effective porosity (P), or the proportion of voids per unit of total volume becomes:

Equation 5:

$$\boldsymbol{P = \frac{V_v}{V} \times 100}$$

Where

$\boldsymbol{V_v}$ = Pore volume
$\boldsymbol{V}$ = Bulk volume

Table 1. Tested sample dimensions and physical properties (mass, density and effective porosity). N.B Only samples with directionality (H/V: horizontal/vertical) were tested for UCS, Young's modulus and Poisson's ratio, other samples were offcut pieces unsuitable for testing.

Flow Location		**Dimension**			**Mass (g)**			Density, Mg/m3		Porosity
	Sample	Volume (m^3) Total	Volume (m^3) Solids	Volume (m^3) Voids	Oven Dry	Saturated under water	Saturated surface-dry	Dry	Particle	Effective porosity %
Upper unit top	KUA3B/H	0.00009369	0.00006871	0.00002498	202.10	133.39	227.08	2.16	2.94	26.66
	KUA3B/V1	0.00007609	0.00005904	0.00001705	166.58	107.54	183.63	2.19	2.82	22.41
	KUA3B/V2	0.00007380	0.00005653	0.00001727	161.26	104.73	178.53	2.19	2.85	23.40
	KUA3A/H1	0.00007504	0.00005388	0.00002116	159.84	105.96	181.00	2.13	2.97	28.20
	KUA3A/H2	0.00007491	0.0000521	0.00002281	157.68	105.58	180.49	2.10	3.03	30.45
	KUA3A/V2	0.00007354	0.00005195	0.00002159	153.83	101.88	175.42	2.09	2.96	29.36
	KUA3A	0.00001341	0.00001047	0.00000294	28.17	17.70	31.11	2.10	2.69	21.94
	KUA3A	0.00002245	0.00001669	0.00000576	48.73	32.04	54.49	2.17	2.92	25.66
	KUA3A	0.00003394	0.00002548	0.00000846	72.59	47.11	81.05	2.14	2.85	24.93
	KUA3A	0.00003961	0.00002794	0.00001167	79.78	51.84	91.45	2.01	2.86	29.47
	KUA3C/H1	0.00007839	0.0000548	0.00002359	163.45	108.65	187.04	2.09	2.98	30.09
	KUA3C/V1	0.00008058	0.00005575	0.00002483	167.35	111.60	192.18	2.08	3.00	30.81
	KUA3C	0.00003064	0.0000217	0.00000894	62.68	40.98	71.62	2.05	2.89	29.19
	KUA3C	0.00003569	0.00002566	0.00001003	72.31	46.65	82.34	2.03	2.82	28.11
	KUA3C	0.00002767	0.00001997	0.00000770	56.67	36.70	64.37	2.05	2.84	27.83
	KUA3C	0.00002584	0.00001926	0.00000658	55.12	35.86	61.70	2.13	2.86	25.47
Lower unit top	KUA02/H1	0.00008023	0.00006596	0.00001427	196.59	130.63	210.86	2.45	2.98	17.79
	KUA02/H2	0.00007916	0.00006493	0.00001423	191.51	126.58	205.74	2.42	2.95	17.97
	KUA02/V1	0.00007779	0.00005762	0.00002017	171.81	114.19	191.98	2.21	2.98	25.93
	KUA02/V3	0.00008190	0.00006427	0.00001763	192.23	127.96	209.86	2.35	2.99	21.52
	KUA02	0.00001892	0.0000153	0.00000362	44.60	29.30	48.22	2.36	2.92	19.13
	KUA02	0.00002061	0.00001704	0.00000357	47.62	30.58	51.19	2.31	2.79	17.31
	KUA02	0.00001835	0.00001496	0.00000339	41.45	26.49	44.84	2.26	2.77	18.46

	Sample	Volume (m^3) Total	Volume (m^3) Solids	Volume (m^3) Voids	Oven Dry	Saturated under water	Saturated surface-dry	Dry	Particle	Effective porosity %
Lower unit top	KUA02	0.00001985	0.00001627	0.00000358	47.47	31.20	51.05	2.39	2.92	18.02
	KUA02	0.00001844	0.00001525	0.00000319	44.76	29.51	47.95	2.43	2.94	17.32
	KUA02	0.00001742	0.00001405	0.00000337	40.81	26.76	44.18	2.34	2.90	19.32
	KUA02	0.00004978	0.00004182	0.00000796	118.63	76.81	126.59	2.38	2.84	15.99
	KUA02	0.00003517	0.00002494	0.00001023	73.06	48.12	83.29	2.08	2.93	29.09
	KUA02	0.00001839	0.0000144	0.00000399	42.47	28.07	46.46	2.31	2.95	21.68
	KUA02	0.00006118	0.00005126	0.00000992	146.56	95.30	156.48	2.40	2.86	16.21
	KUA02	0.00005279	0.00004394	0.00000885	128.26	84.32	137.11	2.43	2.92	16.76
	KUA02	0.00002216	0.00001906	0.00000310	53.72	34.66	56.82	2.42	2.82	14.00
	KUA02	0.00005558	0.00004365	0.00001193	125.28	81.63	137.21	2.25	2.87	21.47
	KUA02	0.00000725	0.0000055	0.00000175	16.85	11.35	18.60	2.32	3.06	24.12
Unit Core	KUA01/H1	0.00007805	0.00006828	0.00000977	206.06	137.78	215.83	2.64	3.02	12.52
	KUA01/V1	0.00007890	0.00006849	0.00001041	207.21	138.72	217.62	2.63	3.03	13.19
	KUA01/V2	0.00007829	0.00006791	0.00001038	205.68	137.77	216.06	2.63	3.03	13.26
	KUA01/V3	0.00007471	0.00006561	0.00000910	196.55	130.94	205.65	2.63	3.00	12.18
	KUA01	0.00004653	0.00004227	0.00000426	128.38	86.11	132.64	2.76	3.04	9.16
	KUA01	0.00004114	0.00003544	0.00000570	108.12	72.68	113.82	2.63	3.05	13.86
	KUA01	0.00002156	0.00001733	0.00000423	52.93	35.60	57.16	2.45	3.05	19.63
	KUA01	0.00001867	0.00001648	0.00000219	48.70	32.22	50.89	2.61	2.96	11.71
	KUA01	0.00002623	0.00002308	0.00000315	68.63	45.55	71.78	2.62	2.97	12.02
	KUA01	0.00002005	0.00001774	0.00000231	53.59	35.85	55.90	2.67	3.02	11.54
Unit base	KUA04/H1	0.00007510	0.00006239	0.00001271	188.83	126.44	201.54	2.51	3.03	16.92
	KUA04/V2	0.00008037	0.00006752	0.00001285	203.67	136.15	216.52	2.53	3.02	15.99
	KUA04	0.00003550	0.00002981	0.00000569	90.80	60.99	96.49	2.56	3.05	16.02

Full results from UCS testing:

Upper Unit Top:

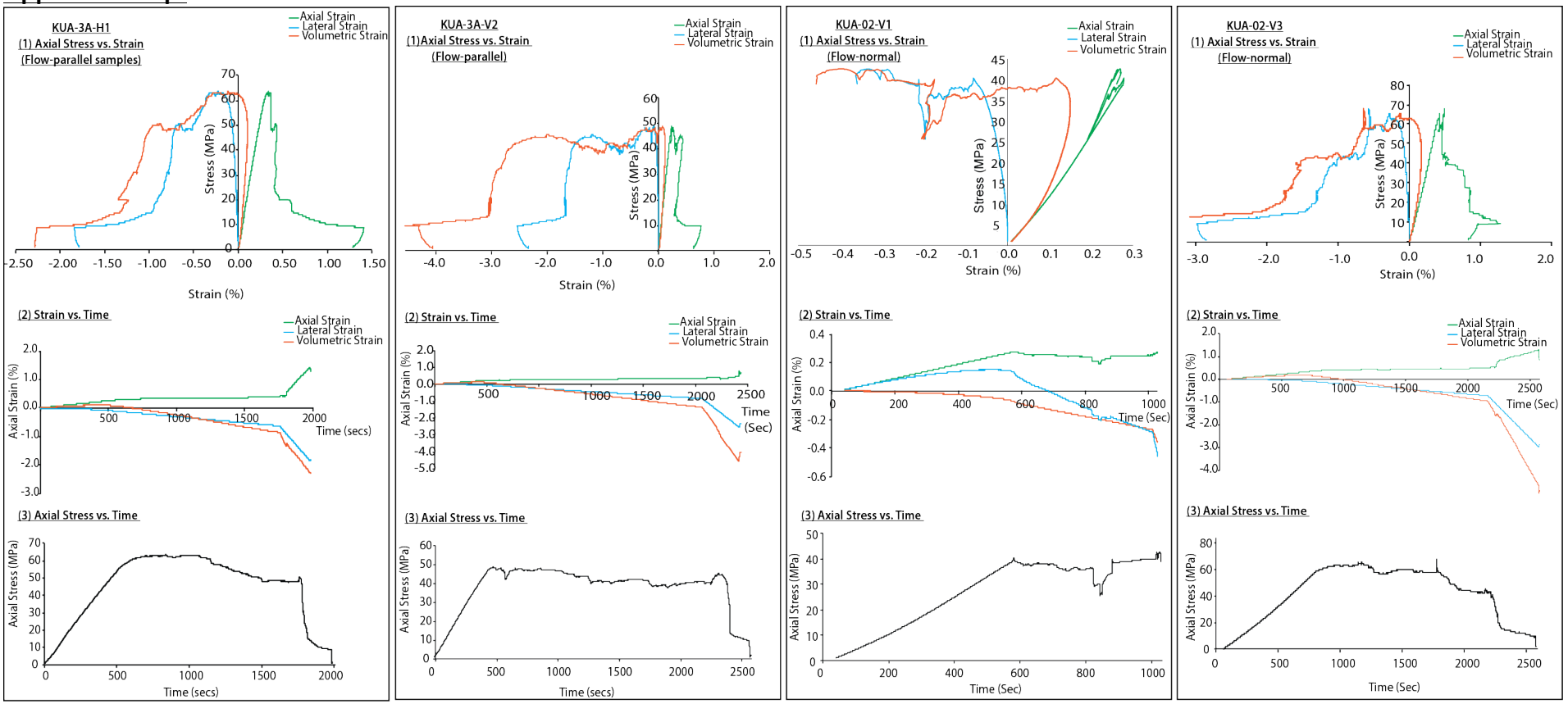

Figure 1. Compete stress-strain, strain-time and stress-time plots for bedding-perpendicular samples from the upper lava top component.

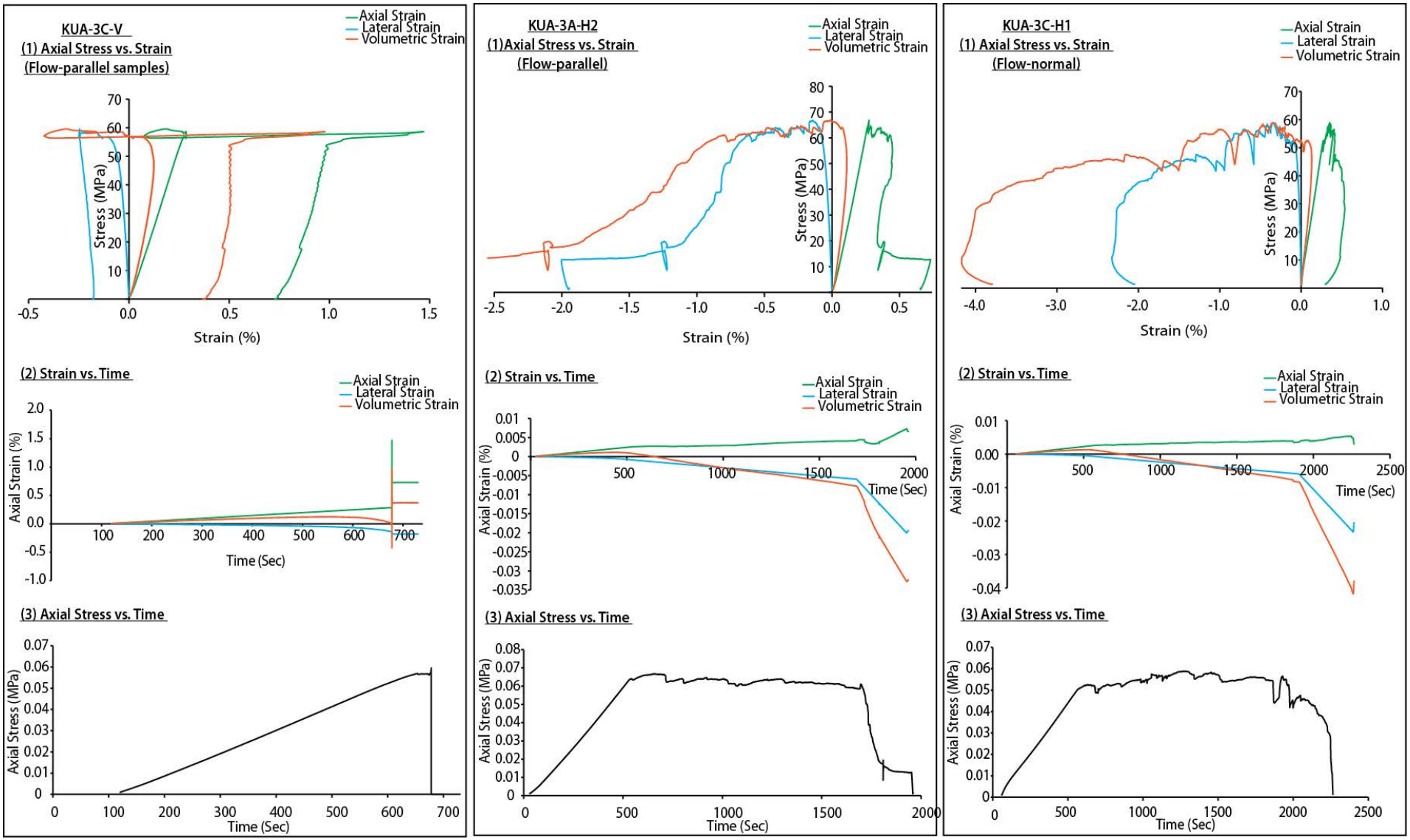

Figure 2. Compete stress-strain, strain-time and stress-time plots for bedding-perpendicular and -parallel samples from the upper lava top component.

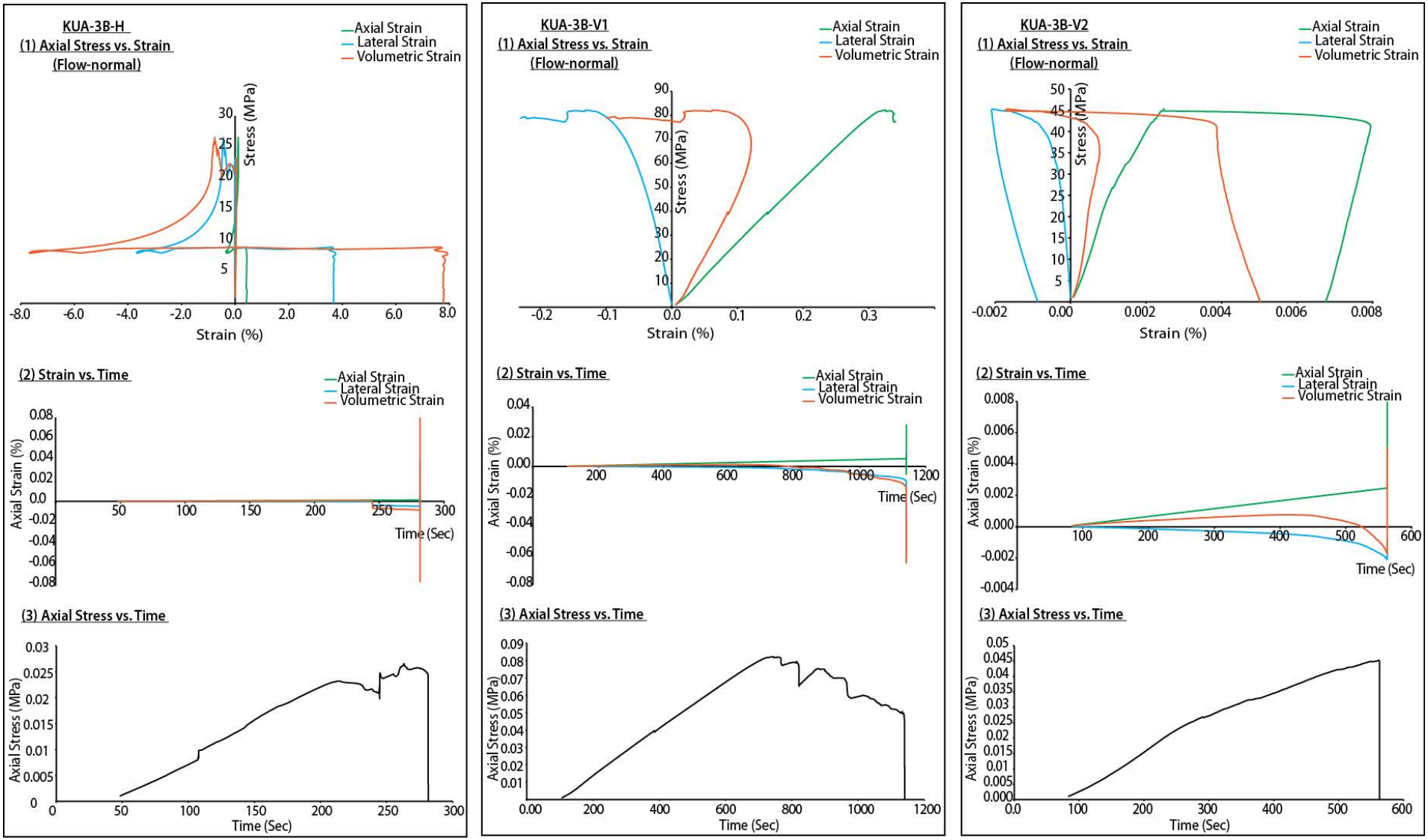

Figure 3. Compete stress-strain, strain-time and stress-time plots for bedding-perpendicular and -parallel samples from the upper lava top component.

Lower Unit Top:

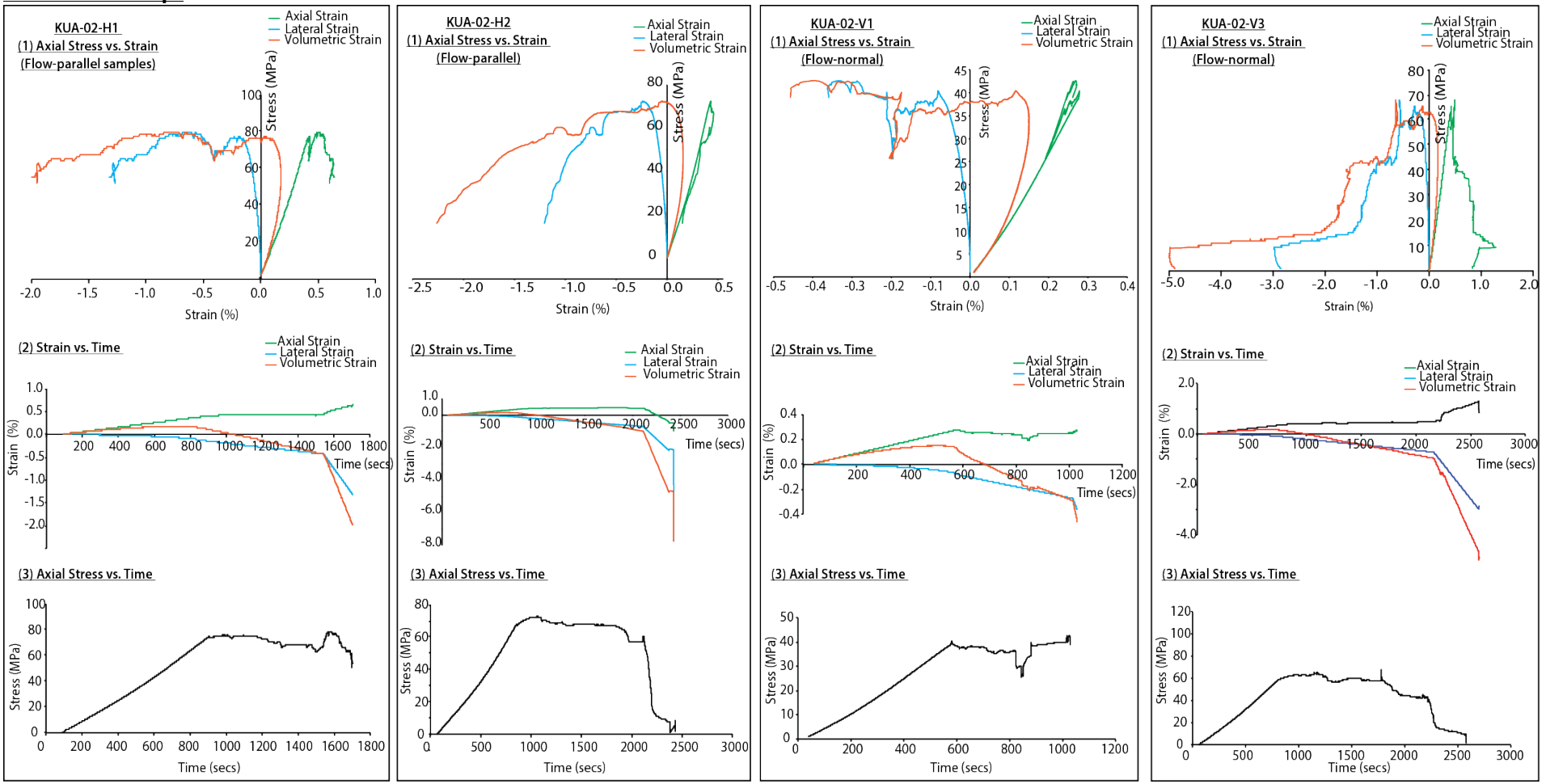

Figure 4. Compete stress-strain, strain-time and stress-time plots for bedding-perpendicular and -parallel samples from the lower lava top component.

Unit Core

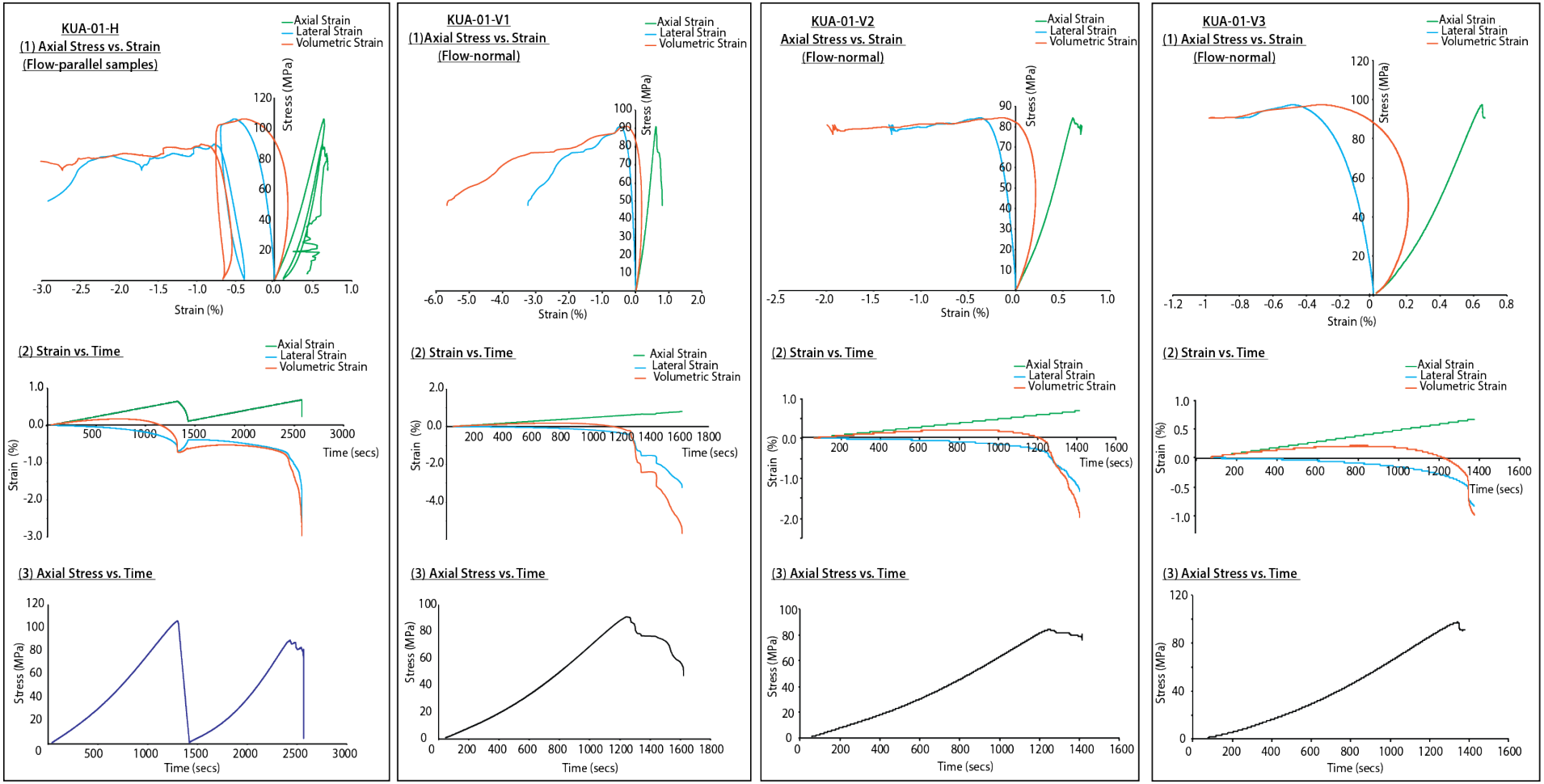

Figure 5. Compete stress-strain, strain-time and stress-time plots for bedding-perpendicular and -parallel samples from the lava core component.

Unit Base

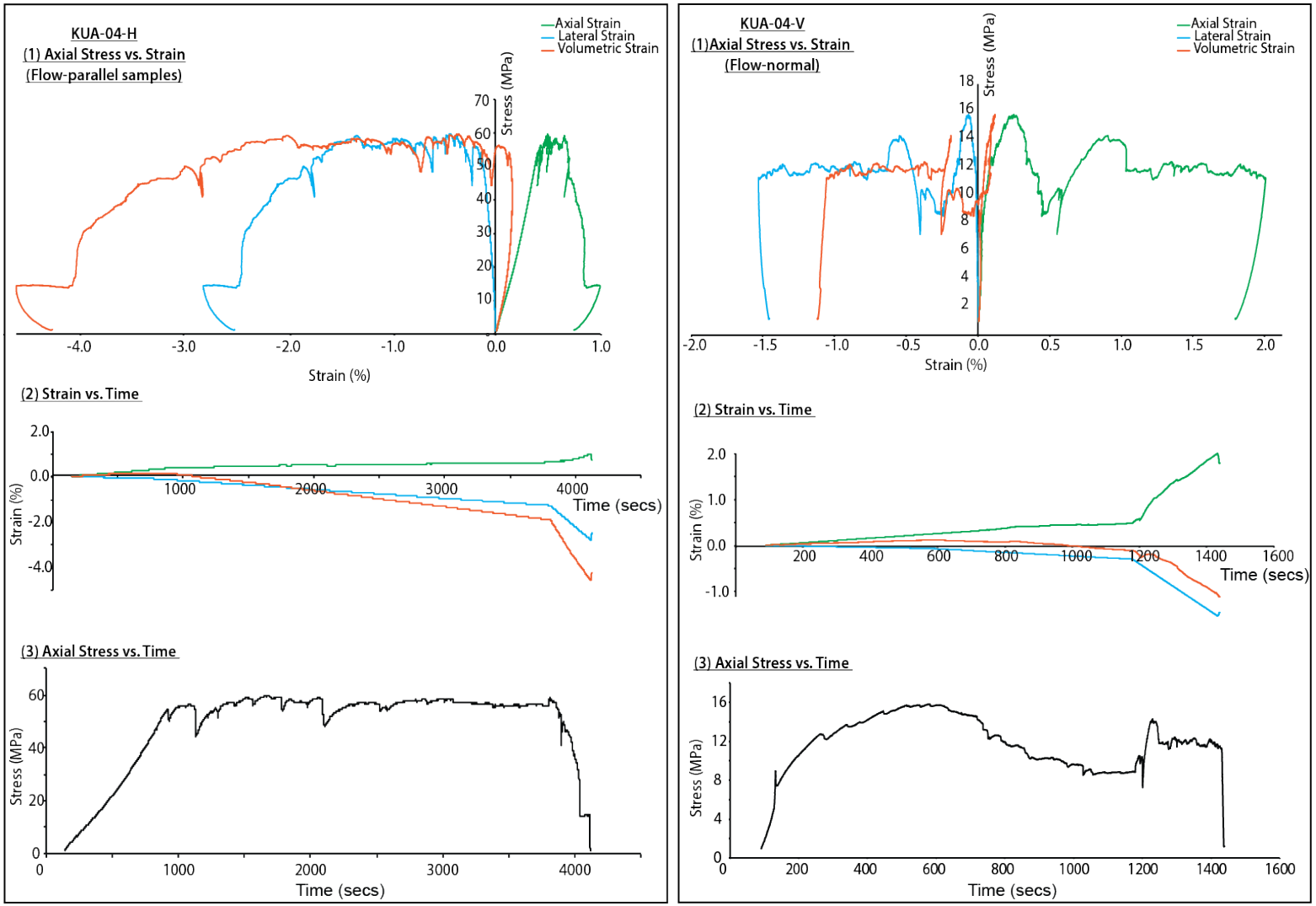

Figure 6. Compete stress-strain, strain-time and stress-time plots for bedding-perpendicular and -parallel samples from the lava base component.

References

1. Abe, S., Van Gent, H. & Urai, J. L. 2011. DEM simulation of normal faults in cohesive materials. *Tectonophysics,* 512**,** 12-21.
2. Ackermann, R. V. & Schlische, R. W. 1997. Anticlustering of small normal faults around larger faults. *Geology,* 25, p. 1127-1130.
3. Ackermann, R. V., Schlische, R. W. & Withjack, M. O. 2001. The geometric and statistical evolution of normal fault systems: an experimental study of the effects of mechanical layer thickness on scaling laws. *Journal of Structural Geology*, 23, 1803-1819.
4. Acocella, V., Faccenna, C., Funicello, R. & Rossetti, F. 1999. Sand-box modelling of basement-controlled transfer zones in extensional domains. *Terra Nova*, 11, 149-156.
5. Acocella, V., Gudmundsson, A. & Funicello, R. 2000. Interaction and linkage of extension fractures and normal faults: examples from the rift zone of Iceland. *Journal of Structural Geology*, 22, 1233-1246.
6. Acocella, V., Korme, T. & Salvini, F. 2003. Formation of normal faults along the axial rift zone of the Ethiopian Rift. *Journal of Structural Geology,* 25**,** 503-513.
7. Acocella, V., Morvillo, P. & Funiciello, R. 2005. What controls relay ramps and transfer faults within rift zones? Insights from analogue models. *Journal of Structural Geology*, 27, 397-408.
8. Al-Harthi, A. A., Al-Amri, R. M. & Shehata, W. M. 1999. The porosity and engineering properties of vesicular basalt in Saudi Arabia. *Engineering Geology*, 54, 313-320.
9. Allen, P. A. & Allen, J. R. 2013. Basin Analysis: Principles and Application to Petroleum Play Assessment, Chichester, UK, John Wiley & Sons, Ltd.
10. Allken, V., Huismans, R. S. & Thieulot, C. 2012. Factors controlling the mode of rift interaction in brittle-ductile coupled systems: A 3D numerical study. *Geochemistry Geophysics Geosystems*, 13, p. 1-18.
11. Anderson, S. R. & Bowers, B. 1995. Stratigraphy of the unsaturated zone and uppermost part of the Snake River Plain aquifer at Test Area North, Idaho National Engineering Laboratory, Idaho. *Water Resources Investigations Report 95-4130. US Geological Survey*.

12. Angelier, J. & Bergerat, F. 1997. Effective tension-shear relationships in extensional fissure swarms, axial rift zone of northeastern Iceland. *Journal of Structural Geology*, 19, 673-685.
13. Angelier, J., Bergerat, F. & Homberg, C. 2000. Variable coupling across weak oceanic transform fault: Flateyjarskagi, Iceland. *Terra Nova,* 12, 97-101.
14. ASTM International, 2008. ASTM D4543 - 85. Standard Practices for Preparing Rock Core as Cylindrical Test Specimens and Verifying Conformance to Dimensional and Shape Tolerances. ASTM International: West Conshohocken, PA, 690-693.
15. Atkinson, B. K. 1987. Introduction to fracture mechanics. In: ATKINSON, B. K. (ed.) Fracture Mechanics of Rock, p. 1-23. London: Academic Press Ltd.
16. Aydin, A. & Schultz, R. A. 1990. Effect of mechanical interaction on the development of strike-slip faults with echelon patterns. *Journal of Structural Geology*, 12, 123-129.
17. Bagdahn, J., Sharpe Jr, W. N. & Jadaan, O. 2003. Fracture strength of polysilicon at stress concentrations. *Journal of Microelectromechanical Systems*, 12, 302-312.
18. Barton, N. 2013. Shear strength criteria for rock, rock joints, rockfill and rock masses: Problems and some solutions. *Journal of Rock Mechanics and Geotechnical Engineering,* 5**,** 249-261.
19. Barton, N. 2014. Most rock masses are likely to be anisotropic. *SBMR 2014-ISRM Specialized Conference.* Goiania, Brazil: Rock Mechanics for Natural Resources and Infrastructure.
20. Becker, K., Shapiro, S. A., Stanchits, S., Dresen, G. & Vinciguerra, S. 2007. Stress induced elastic anisotropy of the Etnean basalt: Theoretical and laboratory examination. *Geophysical Research Letters*, 34, 1-5.
21. Bell, A. F. & Kilburn, C. R. J. 2011. Precursors to dyke-fed eruptions at basaltic volcanoes: insights from patterns of volcano-tectonic seismicity at Kilauea volcano, Hawaii. *Bulletin of Volcanology*, 74, 325-339.
22. Bergerat, F. & Angelier, J. 1999. Fault and stress patterns at different stags of development of oceanic transform zones: the South Iceland seismic zone and the Tjörnes frcature zone (Iceland) as case examples. *Earth and Planetary Sciences*, 329, 653-659.
23. Bergerat, F. & Angelier, J. 2008. Immature and mature transform zones near a hot spot: The South Iceland Seismic Zone and the Tjörnes Fracture Zone (Iceland). *Tectonophysics*, 447, 142-154.

24. Bergerat, F., Gudmundsson, A., Angelier, J. & Rögnvaldsson, S. T. 1998. Seismotectonics of the central part of the South Iceland Seismic Zone. *Tectonophysics*, 298, 319-335.
25. Bieniawski, Z. T. & Bernede, M. J. 1979a. Suggested methods for determining the uniaxial compressive strength and deformability of rock materials: Part 1. Suggested method for determining deformability of rock materials in uniaxial compression, Pergamon.
26. Bieniawski, Z. T. & Bernede, M. J. 1979b. Suggested methods for determining water content, porosity, density, absorption and related properties and wwelling and slake-durability index properties. Pergamon.
27. Bjornsson, A., Johnsen, G., Sigurdsson, S., Thorbergsson, G. & Tryggvason, E. 1978. Rifting of the plate boundary in North Iceland 1975-1978. National Energy Authority Report 0S-JHD-78-21. Nordic Volcanological Institute: University of Iceland.
28. Bjornsson, A., Saemundsson, K., Sigmundsson, F., Halldorsson, P., Sigbjornsson, R. & Snaebjornsson, J. T. 2007. Geothermal projects in NE Iceland at Krafla, Bjarnarflag, Gjastykki and Theistareykir: assessment of geo-hazards affecting energy production and transmission systems emphasizing structural design criteria and mitigation of risk. Landsvirkjun report LV-2007/075.
29. Blenkinsop, T. G. 2000. Recognition of Deformation, Microstructures and Mechanisms in Rocks, London, Chapman and Hall Press.
30. Blenkinsop, T. G. 2008. Relationships between faults, extension fractures and veins, and stress. *Journal of Structural Geology*, 30, 622-632.
31. Boccaccini, A. R. 1999. Fabrication, microstructural characterisation and mechanical properties of glass compacts containing porosity of spheroidal shape. *Journal of Porous Materials*, 6, 369-379.
32. Boccaccini, A. R. & Fan, Z. 1997. A new approach for the Young's Modulus-porosity correlation of ceramic materials. *Ceramics International*, 23, 239-245.
33. Bosworth, W. 1985. Geometry of propagating continental rifts. *Nature*, 316, 625-627.
34. Brady, B. H. G. & Brown, E. T. 2004. Rock Mechanics for Underground Mining, London, Kluwer Academic Publishers.
35. Brandsdottir, B. & Einarsson, P. 1979. Seismic activity associated with the September 1977 deflation of the Krafla central volcano in north-eastern Iceland. *Journal of Volcanology and Geothermal Research*, 6, 197-212.

36. Buck, W. R., Einarsson, P. & Brandsdóttir, B. 2006. Tectonic stress and magma chamber size as controls on dike propagation: Constraints from the 1975–1984 Krafla rifting episode. *Journal of Geophysical Research*, 111, 1-15.

37. Bürgmann, R. & Pollard, D. 1994. Slip distributions on faults: effects of stress gradients, inelastic deformation, hetergeneous host-rock stiffness, and fault interaction. *Journal of Structural Geology*, 16, 1675-1690.

38. Byerlee, J., 1978. Friction of rocks. *Pure and Applied Aeophysics*, *116* (4-5), 615-626.

39. Caine, J. S., Evans, J. P. & Forster, C. B. 1996. Fault zone architecture and permeability structure. *Geology*, 24, 1025-1028.

40. Cartwright, J., Mansfield, C. S. & Trudgill, B. 1996. The growth of normal faults by segment linkage. In: BUCHANAN, P. G. & NIEULAND, D. A. (eds.) Modern Developments in Structural Interpretation, Validation and Modelling. London, UK: The Geological Society. No. 99, 163-177.

41. Cashman, K. V. & Kauahikaua, J. P. 1997. Reevaluation of vesicle distributions in basaltic lava flows. *Geology*, 25, 419-422.

42. Chang, C., Zoback, M. D. & Khaksar, A. 2006. Empirical relations between rock strength and physical properties in sedimentary rocks. *Journal of Petroleum Science and Engineering*, 51, 223-237.

43. Childs, C., Watterson, J. & Walsh, J. J. 1995. Fault overlap within developing normal fault systems. *Journal of the Geological Society*, *London*, 152, 535-549.

44. Clague, D. A. & Denlinger, R. P. 1994. Role of olivine cumulates in destabilizing the flanks of Hawaiian volcanoes. *Bulletin of Volcanology,* 56**,** 425-434.

45. Clifton, A. E., Schlische, R. W., Withjack, M. O. & Ackermann, R. V. 2000. Influence of rift obliquity on fault-population systematics: results of experimenal clay models. *Journal of Structural Geology*, 22, 1491-1509.

46. Costin, L. S. 1987. Time-dependent deformation and failure. *In:* ATKINSON, B. K. (ed.) *Fracture Mechanics of Rock.* P. 167-211. London: Academic Press.

47. Cowie, P. 1998. Normal fault growth in three-dimensions in continental and oceanic crust. In: BUCK, W. R., DELANEY, P. T., KARSON, J. A. & LAGABRIELLE, Y (eds.) Faulting and magmatism at mid-ocean ridges. P. 325-348. Washington, D.C.: American Geophysical Union.

48. Cowie, P. A. & Scholz, C. H. 1992. Physical explanation for the displacement-length relationship of faults using a post-yield fracture mechanics model. *Journal of Structural Geology*, 14, 1133-1148.

49. Cowie, P. A. & Shipton, Z. K. 1998. Fault tip displacement gradients and process zone dimensions. *Journal of Structural Geology*, 20, 983-997.

50. Crider, J. G. 2015. The initiation of brittle faults in crystalline rock. *Journal of Structural Geology*, 77, 159-174.

51. Crider, J. G. & Peacock, D. C. P. 2004. Initiation of brittle faults in the upper crust: a review of field observations. *Journal of Structural Geology*, 26, 691-707.

52. Crider, J. G. & Pollard, D. D. 1998. Fault linkage: Three-dimensional mechanical interaction between echelon normal faults. *Journal of Geophysical Research*, 103, 24,373-24,391.

53. Dauteuil, O., Angelier, J., Bergerat, F., Verrier, S. & Villemin, T. 2001. Deformation partitioning inside a fissure swarm of the northern icelandic rift. *Journal of Structural Geology*, 23, 1359-1372.

54. Davis, P. A. 2006. Calibrated Landsat ETM+ nonthermal-band image mosaics of Afghanistan. *Geological Survey Open-File Report 2006-1345. U.S. Geological Survey.*

55. Davison, I., Stasiuk, S., Nuttall, P. & Keane, P. 2004. Sub-basalt hydrocarbon prospectivity in the Rockall, Faroe-Shetland an Møre Basins, NE Atlantic. Geological Society London. In: VINING, B.A. & PICKERING, S.C. (eds.) Petroleum Geology: from mature basins to new frontiers. *Proceedings of the 7th Petroleum Geology Conference,* 1025-1032. Petroleum Geology Conferences Ltd, published by the Geological Society, London.

56. Dawers, N. H. & Anders, M. H. 1995. Displacement-length scaling and fault linkage. *Journal of Structural Geology*, 17, 607-614.

57. Degraff, J. M. & Aydin, A. 1987. Surface morphology of columnar joints and its significance to mechanics and direction of joint growth. *Geological Society of America,* 99**,** 605-617.

58. Delaney, P. T. & Pollard, D. 1981. Deformation of host rocks and flow of magma during the growth of Minette Dikes and breccia-bearing intrusions near Ship Rock, New Mexico. *Geological Survey Professional Paper*, 1202.

59. Delaney, P. T., Denlinger, R. P., Lisowski, M., Miklius, A., Okubo, P. G., Okamura, A. T. & Sako, M. K. 1998. Volcanic Spreading at Kilauea, 1976–1996. *Journal of Geophysical Research*, 103, 18,003-18,023.

60. Delvaux, D. & Sperner, B. 2003. Stress tensor inversion from fault kinematic indicators and focal mechanism data: the TENSOR program. In: New Insights into Structural Interpretation and Modelling, *Geological Society London.*

61. Deng, Z. Y., She, J., Inagaki, Y., Yang, J. F., Ohji, T. & Tanaka, Y. 2004. Reinforcement by crack-tip blunting in porous ceramics. *Journal of the European Ceramic Society*, 24, 2055-2059.

62. Denlinger, R. P. & Okubo, P. G. 1995. Structure of the mobile south flank of Kilauea Volcano, Hawaii. *Journal of Geophysical Research,* 100**,** 24499.

63. Dieterich, J. H. 1988. Growth and persistence of Hawaiian volcanic rift zones. *Journal of Geophysical Research* 93(B5), 4258-4270.

64. Doré, A. G., Lundin, E. R., Birkeland, O., Eliassen, P. E. & Jensen, L. N. 1997. The NE Atlantic margin; implications of late Mesozoic and Cenozoic events for hydrocarbon prospectivity. Petroleum Geoscience, 3, 117-131.

65. Doré, A. G., Lundin, E. R., Jensen, L. N., Birkeland, Ø., Eliassen, P. E. & Fichler, C. 1999. Principal tectonic events in the evolution of the northwest European Atlantic margin. In: FLEET, A.J and BOLDY, S.A.R. Petroleum geology of Northwest Europe: Proceedings of the 5th Conference. 41-61.

66. Dresen, G. & Gueguen, Y. 2004. Damage and Rock Physical Properties. In: GUEGUEN, Y. & BOUTECA, M. (eds.) Mechanics of Fluid Saturated Rocks. London: Elsevier Academic Press.

67. Duffield, W. A. 1975. Structure and Origin of the Koae Fault System, Kilauea Volcano, Hawaii. *Geological Survey Professional Paper 856.*

68. Duffield, W. A., Christiansen, R. L., Koyanagi, R. Y. & Peterson, D. W. 1982a. Storage, migration and eruption of magma at Kilauea Volcano, Hawaii, 1971-1972. *Journal of Volcanology and Geothermal Research*, 13, 273-307.

69. Duffield, W. A., Stieltjes, L. & Varet, J. 1982b. Huge landslide blocks in the growth of Piton de la Fournaise, La Reunion, and Kilauea Volcano, Hawaii. *Journal of Volcanology and Geothermal Research,* 12**,** 147-160.

70. Dunn, D. E., Lafountain, L. J. & Jackson, R. E. 1973. Porosity dependence and mechanism of brittle fracture in sandstones. *Journal of Geophysical Research*, 78, 2403-2417.

71. Dvorak, J. J. & Dzurisin, D. 1993. Variations in Magma Supply Rate at Kilauea Volcano, Hawaii. *Journal of Geophysical Research-Solid Earth*, 98, 22255-22268.

72. Dzurisin, D., Koyanagi, R. Y. & English, T. T. 1984. Magma supply and storage at Kiluea Volcano, Hawaii, 1956-1983. *Journal of Volcanology and Geothermal Research*, 21, 177-206.

73. Ebinger, C. J. 1989. Geometric and kinematic development of border faults and accommodation zones, Kivu-Rusizi rift, Africa. *Tectonics*, 8, 117-133.

74. Ebinger, C. J., Deino, A. L., Drake, R. E. & Tesha, A. L. 1989. Chronology of volcanism and rift basin propagation: Rungwe Volcanic Province, East Africa. *Journal of Geophysical Research*, 94, 885-903.

75. Einarsson, P. 1991. Earthquakes and present-day tectonism in Iceland. *Tectonophysics*, 189, 261-279.

76. Einarsson, P. 2010. Mapping of Holocene surface ruptures in the South Iceland Seismic Zone. *Jökull***,** No. 60, 117-131.

77. Eldholm, O. & Grue, K. 1994. North Atlantic volcanic margins: Dimensions and production rates. Journal of Geophysical Research, 99, 2955-2968.

78. Ellis, D., Bell, B. R., Jolley, D. W. & O'Callaghan, M. 2002. The stratigraphy, environment of eruption and age of the Faroes Lava Group, NE Atlantic Ocean. In: JOLLEY, D. W. & BELL, B. R. (eds.) The North Atlantic Igneous Province: Stratigraphy, Tectonic, Volcanic and Magmatic Processes. Geological Society, London. Special Publication 197, 253-269.

79. Ellis, D., Passey, S. R., Jolley, D. W. & Bell, B. R. 2009. Transfer zones: the application of new geological information from the Faroe Islands applied to the offshore exploration of intra and sub-basalt strata. In: VARMING, T. & ZISKA, H. (eds.) Faroe Islands Exploration Conference: Proceedings of the 2nd Conference. Torshavn, Faroe Islands: Faroese Academy of Sciences.

80. Ellis, D. & Stoker, M. S. (eds.) 2014. The Faroe-Shetland Basin: a regional perspective from the Paleocene to the present day and its relationship to the opening of the North Atlantic Ocean, London, UK: *Geological Society, London, Special Publications*.

81. Engelder, T. 1993. Stress regimes in the Lithosphere. Chichester, West Sussex, Princeton University Press.

82. Fairhurst, C. E. & Hudson, J. A. 1999. Draft ISRM suggested method for the complete stress-strain curve for intact rock in uniaxial compression. *International Journal of Rock Mechanics and Mining Sciences*, 36, 279-289.

83. Fakhimi, A. & Gharahbagh, E. A. 2011. Discrete element analysis of the effect of pore size and pore distribution on the mechanical behavior of rock. *International Journal of Rock Mechanics and Mining Sciences*, 48, 77-85.

84. Faulds, J. E. & Varga, R. J. 1998. The role of accommodation zones and transfer zones in the regional segmentation of extended terranes. In: FAULDS, J. E. & STEWART, J. H. (eds.) Accommodation Zones and Transfer Zones: the Regional Segmentation of the Basin and Range Province: Boulder, Colorado. *Geological Society of America Special Paper* 323, 1-45.

85. Faulkner, D. R., Jackson, C. A. L., Lunn, R. J., Schlische, R. W., Shipton, Z. K., Wibberley, C. A. J. & Withjack, M. O. 2010. A review of recent developments concerning the structure, mechanics and fluid flow properties of fault zones. *Journal of Structural Geology*, 32, 1557-1575.
86. Ferrill, D. A. & Morris, A. P. 2001. Displacement gradient and deformation in normal fault systems. *Journal of Structural Geology*, 23, 619-638.
87. Ferrill, D. A. & Morris, A. P. 2003. Dilational normal faults. *Journal of Structural Geology*, 25, 183-196.
88. Ferrill, D. A. & Morris, A. P. 2008. Fault zone deformation controlled by carbonate mechanical stratigraphy, Balcones fault system, Texas. *AAPG Bulletin*, 92, 359-380.
89. Ferrill, D. A., Morris, A. P. & McGinnis, R. N. 2012. Extensional fault-propagation folding in mechanically layered rocks: The case against the frictional drag mechanism. *Tectonophysics*, 576-577, 78-85.
90. Ferrill, D. A., Stamatakos, J. A. & Sims, D. 1999. Normal fault corrugation: implications for growth and seismictiy of active normal faults. *Journal of Structural Geology*, 21, 1027-1038.
91. Fischer-Cripps, A. C. 2007. Introduction to Contact Mechanics, New York, Springer-Verlag.
92. Fiske, R. S. & Koyanagi, R. Y. 1968. The December 1965 Eruption of Kilauea Volcano, Hawaii. *Geological Survey Professional Paper*, 607, 1-21.
93. Fleck, N. A. & Smith, R. A. 1981. Effect of density on tensile strength, fracture toughness, and fatigue crack propagation behaviour of sintered steel. *Powder Metallurgy*, Vol. 3, 121-125.
94. Forslund, T. & Gudmundsson, A. 1991. Crustal spreading due to dikes and faults in southwest Iceland. *Journal of Structural Geology*, 13, 443-457.
95. Fossen, H. 2010. Structural Geology, Cambridge University Press. Cambridge, UK.
96. Fowler, A. C., Rust, A. C. & Vynnycky, M. 2015. The formation of vesicular cylinders in pahoehoe lava flows. *Geophysical & Astrophysical Fluid Dynamics*, Vol. 109, No.1, 39-61..
97. Fridleifsson, G. O., Armannsson, H. & Mortensen, A. K. 2006. Geothermal conditions in the Krafla caldera with focus on well KG-25: a review in relation to the Iceland Deep Drilling Project. Reykjavik, Iceland: Iceland Geosurvey report 2006-030.
98. Gaina, C., Gernigon, L. & Ball, P. 2009. Palaeocene-Recent plate boundaries in the NE Atlantic and the formation of the Jan Mayen microcontinent. *Journal of the Geological Society*, 166, 601-616.

99. Garcia, S., Angelier, J., Bergerat, F. & Homberg, C. 2002. Tectonic analysis of an oceanic transform fault zone based on fault-slip data and earthquake focal mechanisms: the Husavık–Flatey Fault zone, Iceland. *Tectonophysics,* 344**,** 157-174.

100. Garcia, S., Arnaud, N. O., Angelier, J., Bergerat, F. & Homberg, C. 2003. Rift jump process in Northern Iceland since 10 Ma from 40Ar/39Ar geochronology. *Earth and Planetary Science Letters*, 214, 529-544.

101. Gates, W. 2008. Estimating the unconfined compressive strength of vesicular basalts via bulk specific gravity of the rock sample. *42nd US Rock Mechanics Symposium. San Francisco: American Rock Mechanics Association.*

102. Gawthorpe, R. L. & Hurst, J. M. 1993. Transfer zones in extensional basins: their structural style and influence on drainage development and stratigraphy. *Journal of the Geological Society*, 150, 1137-1152.

103. Gawthorpe, R. L., Sharp, I., Underhill, J. R. & Gupta, S. 1997. Linked sequence stratigraphic and structural evolution of propagating normal faults. *Geology,* 25**,** 795-798.

104. Geoffroy, L. 2005. Volcanic passive margins. *Comptes Rendus Geoscience*, 337, 1395-1408.

105. Gernigon, L., Gaina, C., Olesen, O., Ball, P. J., Péron-Pinvidic, G. & Yamasaki, T. 2012. The Norway Basin revisited: From continental breakup to spreading ridge extinction. *Marine and Petroleum Geology,* 35, 1-19.

106. Gerya, T. 2012. Origin and models of oceanic transform faults. *Tectonophysics,* 522-523**,** 34-54.

107. Gibbs, A. D. 1984. Structural evolution of extensional basin margins. *Journal of the Geological Society*, 141, 609-620.

108. Gillespie, P., Walsh, J. J., Watterson, J., Bonson, C. G. & Manzocchi, T. 2001. Scaling relationships of joint and vein arrays from The Burren, Co. Clare, Ireland. *Journal of Structural Geology*, 23, 183-201.

109. Gislason, S. R., Wolff-Boenisch, D., Stefansson, A., Oelkers, E. H., Gunnlaugsson, E., Sigurdardottir, H., Sigfusson, B., Broecker, W. S., Matter, J. M. & Stute, M. 2010. Mineral sequestration of carbon dioxide in basalt: A pre-injection overview of the CarbFix project. *International Journal of Greenhouse Gas Contro*l, 4, 537-545.

110. Grant, J. V. & Kattenhorn, S. A. 2004. Evolution of vertical faults at an extensional plate boundary, southwest Iceland. *Journal of Structural Geology*, 26, 537-557.

111. Green, R. G., White, R. S. & Greenfield, T. 2014. Motion in the north Iceland volcanic rift zone accommodated by bookshelf faulting. *Nature Geoscience*, 7, 29-33.

112. Griffiths, P. S. 1980. Box-fault systems and ramps: atypical associations of structures from the eastern shoulder of the Kenya Rift. *Geological Magazine*, 117, 579-586.

113. Guarnieri, P. 2015. Pre-break-up palaeostress state along the East Greenland margin. *Journal of the Geological Society*, 172, 727-739.

114. Gudmundsson, A. 1986. Formation of crustal magma chambers in Iceland. *Geology*, 14, 164-166.

115. Gudmundsson, A. 1992. Formation and growth of normal faults at the divergent plate boundary in Iceland. *Terra Nova*, 4, 464-471

116. Gudmundsson, A. 2003. Surface stresses associated with arrested dykes in rift zones. *Bulletin of Volcanology*, 65, 606-619.

117. Gudmundsson, A. 2004. Effects of Young's modulus on fault displacement. *Comptes Rendus Geoscience*, 336, 85-92.

118. Gudmundsson, A. 2007. Infrastructure and evolution of ocean-ridge discontinuities in Iceland. *Journal of Geodynamics*, 43, 6-29.

119. Gudmundsson, A. 2011. Rock Fractures in Geological Processes, Cambridge, UK, Cambridge University Press.

120. Gudmundsson, A., 2006. How local stresses control magma-chamber ruptures, dyke injections, and eruptions in composite volcanoes. *Earth-Science Reviews*, *79* (1), 1-31.9

121. Gudmundsson, A. & Backstrom, K. 1991. Structure and development of the Sveinagja graben, Northeast Iceland. *Tectonophysics*, 200, 111-125.

122. Gudmundsson, A., Bergerat, F. J. & Angelier, J. 1996. Off-rift and rift-zone palaeostresses in Northwest Iceland. *Tectonophysics*, 255, 211-228.

123. Gudmundsson, A., Brynjolfsson, S. & Jonsson, M. T. 1993. Structural analysis of a transform fault-rift zone junction in North Iceland. *Tectonophysics*, 220, 205-221.

124. Gudmundsson, A., Mortensen, A. K., Hjartarson, A., Karlsdottir, R. & Armannsson, H. 2010. Exploration and utilisation of the Namafjall high temperature area in N Iceland. *Proceedings World Geothermal Congress*. Bali, Indonesia.

125. Gueguen, Y., Dormieux, L. & Bouteca, M. 2004. Fundamentals of Poromechanics. In: GUEGUEN, Y. & BOUTECA, M. (eds.) Mechanics of Fluid Saturated Rocks. London: Elsevier Academic Press.

126. Gupta, A. & Scholz, C. H. 2000. A model of normal fault interaction based on observations and theory. *Journal of Structural Geology*, 22, 865-879.
127. Harris, A. J. L., Murray, J. B., Aries, S. E., Davies, M. A., Flynn, L. P., Wooster, M. J., Wright, R. & Rothery, D. A. 2000. Effusion rate trends at Etna and Krafla and their implications for eruptive mechanisms. *Journal of Volcanology and Geothermal Research*, 102, 237-270.
128. Hart, D. J. & Wang, H. F. 1995. Laboratory measurements of a complete set of poroelastic moduli for Berea sandstone and Indiana limestone. *Journal of Geophysical Research*, 100, 17,741-17,751.
129. Hatzor, Y. H. & Palchik, V. 1998. Technical note: A microstructural-based failure criterion for Aminadav Dolomites. *International Journal of Rock Mechanics and Mining Sciences*, 35, 797-805.
130. Hayward, N. J. & Ebinger, C. J. 1996. Variations in the along-axis segmentation of the Afar Rift system. *Tectonics*, 15, No. 2, 244-257.
131. Healy, D. 2009. Anisotropy, pore fluid pressure and low angle normal faults. *Journal of Structural Geology*, 31, 561-574.
132. Healy, D., Jones, R. & Holdsworth, R. 2006. New insights into the development of brittle shear fractures from a 3-D numerical model of microcrack interaction. *Earth and Planetary Science Letters*, 249, 14-28.
133. Heap, M. J., Faulkner, D. R., Meredith, P. G. & Vinciguerra, S. 2010. Elastic moduli evolution and accompanying stress changes with increasing crack damage: implications for stress changes around fault zones and volcanoes during deformation. *Geophysical Journal International*, 183, 225-236.
134. Heap, M. J., Xu, T. & Chen, C.F. 2014. The influence of porosity and vesicle size on the brittle strength of volcanic rocks and magma. *Bulletin of Volcanology*, 76, 1-15.
135. Heidari, M., Khanlari, G. R., Torabi-Kaveh, M., Kargarian, S. & Saneie, S. 2013. Effect of Porosity on Rock Brittleness. *Rock Mechanics and Rock Engineering*, 47, 785-790.
136. Helm-Clark, C. M., Rodgers, D. W. & Smith, R. P. 2004. Borehole geophysical techniques to define stratigraphy, alteration and aquifers in basalt. *Journal of Applied Geophysics*, 55, 3-38.
137. Hencher, S.R. 1995. Interpretation of direct shear tests on rock joints. In *Proceedings 35th US symposium on rock mechanics. Lake Tahoe* (pp. 99-106).
138. Hjartardóttir, Á. R. 2010. *Fissure swarms of the Northern Volcanic Rift Zone, Iceland.* Doctor of Philosophy, University of Iceland

139. Hjartardóttir, Á. R., Einarsson, P., Bramham, E. & Wright, T. J. 2012. The Krafla fissure swarm, Iceland, and its formation by rifting events. *Bulletin of Volcanology*, 74, 2139-2153.

140. Holcombe, R. T. 1987. Eruptive history and long-term behaviour of Kilauea Volcano. *In:* DECKER, R. W., WRIGHT, T. L. & STAUFFER, P. H. (eds.) Volcanism in Hawaii*. US Geological Survey Professional Paper* 1350.

141. Holland, M., Urai, J. L. & Martel, S. J. 2006. The internal structure of fault zones in basaltic sequences. *Earth and Planetary Science Letters*, 248, 301-315.

142. Holland, M., Van Gent, H., Bazalgette, L., Yassir, N., Hoogerduijn Strating, E. H. & Urai, J. L. 2011. Evolution of dilatant fracture networks in a normal fault — Evidence from 4D model experiments. *Earth and Planetary Science Letters,* 304**,** 399-406.

143. Hollingsworth, J., Leprince, S., Ayoub, F. & Avouac, J. P. 2013. New constraints on dike injection and fault slip during the 1975-1984 Krafla rift crisis, NE Iceland. *Journal of Geophysical Research: Solid Earth*, 118, 3707-3727.

144. Holwell, D. A., Selby, D., Boyce, A. J., Gilbertson, J. A. & Abraham-James, T. 2012. An Re-Os date for molybdenite-bearing quartz vein mineralisation within the Kangerlussuaq Alkaline Complex, East Greenland: implications for the timing of regional metallogenesis. *Society of Economic Geology*, 107, 713-722.

145. Homberg, C., Bergerat, F., Angelier, J. & Garcia, S. 2010. Fault interaction and stresses along broad oceanic transform zone: Tjörnes Fracture Zone, north Iceland. *Tectonics*, 29, 1-12.

146. Hon, K., Kauahikaua, J. P., Denlinger, R. P. & Mackay, K. 1994. Emplacement and inflation of pahoehoe sheet flows: observations and measurements of active lava flows in Kilauea Volcano, Hawaii. *Geological Society of America Bulletin*, 106, 353-370.

147. Hubbert, M. K. & Rubey, W. W. 1959. Role of fluid pressure in mechanics of overthrust faulting. *Bulletin of the Geological Society of America*, 70, 115-166.

148. Huggins, P., Watterson, J., Walsh, J. J. & Childs, C. 1995. Relay zone geometry and displacement transfer between normal faults recorded in coal-mine plans. *Journal of Structural Geology*, 17, 1741-1755.

149. Hus, R., Acocella, V., Funiciello, R. & De Batist, M. 2005. Sandbox models of relay ramp structure and evolution. *Journal of Structural Geology*, 27, 459-473.

150. Hus, R., De Batist, M., Klerkx, J. & Matton, C. 2006. Fault linkage in continental rifts: structure and evolution of a large relay ramp in Zavarotny; Lake Baikal (Russia). *Journal of Structural Geology*, 28, 1338-1351.

151. Imber, J., Tuckwell, G. W., Childs, C., Walsh, J. J., Manzocchi, T., Heath, A. E., Bonson, C. G. & Strand, J. 2004. Three-dimensional distinct element modelling of relay growth and breaching along normal faults. *Journal of Structural Geology*, 26, 1897-1911.

152. Inglis, C. E. 1913. Stresses in a plate due to the presence of cracks and sharp corners. *Spring Meetings of the 54th Session of the Institution of Naval Architects.* P. 219-241.

153. Ingraffea, A. R. (ed.) 1989. Theory of Crack Initiation and Propagation in Rock, London: Academic Press.

154. Jaeger, J. C. & Cook, N. G. W. 1979. Fundamentals of Rock Mechanics, London, Chapman and Hall.

155. Jaeger, J. C., Cook, N. G. W. & Zimmerman, R. W. 2007. Fundamentals of Rock Mechanics, Oxford, UK, Blackwell Publishing Ltd.

156. Jerram, D. A. 2002. Volcanology and facies architecture of flood basalts. In M. A. Menzies, Klemperer, S.L., Ebinger, C.J. and Baker, J., (Ed.), Volcanic Rifted Margins. *Geological Society of America Special Paper 362.*

157. Jerram, D. A., Single, R. T., Hobbs, R. W. & Nelson, C. E. 2009. Understanding the offshore flood basalt sequence using onshore volcanic facies analogues: an example from the Faroe–Shetland basin. *Geological Magazine*, 146, 353-367.

158. Julian, B. R., Angus, D. M. & Foulger, G. R. 1998. Non-double couple earthquakes: theory. *Reviews of Geophysics*, 36, 525-549.

159. Jung, H. S., Lu, Z., Won, J. S., Poland, M. P. & Miklius, A. 2010. Mapping three-dimensional surface deformation by combining multiple-aperture interferometry and conventional interferometry: application to the June 2007 eruption of Kilauea Volcano, Hawaii. *IEEE Geoscience and Remote Sensing Letters,* 8, 34-38.

160. Kahraman, S., Gunaydin, O. & Fener, M. 2005. The effect of porosity on the relation between uniaxial compressive strength and point load index. *International Journal of Rock Mechanics and Mining Sciences*, 42, 584-589.

Karson, J. A. & Brooks, C. K. 1999. Structural and magmatic segmentation of the Tertiary East Greenland Volcanic Rifted Margin*. In:* MAC NIOCAIL, C. & RYAN, P.D. (eds.) Continental Tectonics. *Geological Society London, Special Publication* 164, 313-338.

161. Kaven, J. O. & Martel, S. J. 2007. Growth of surface-breaching normal faults as a three-dimensional fracturing process. *Journal of Structural Geology*, 29, 1463-1476.

162. Kawakatsu, H. 1991. Enigma of earthquakes at ridge-transform plate boundaries - distribution of non-double couple parameter of Harvard CMT solutions. *Geophysical Research Letters*, 18, 1103-1106.

163. Khodayar, M. & Bjornsson, S. 2013. Preliminary fracture analysis of Theistareykir geothermal field and surroundings, northern rift zone and Tjornes fracture zone. *Landsvirkjun* report LV-2013/136.

164. Kim, Y. S., Peacock, D. C. P. & Sanderson, D. J. 2004. Fault damage zones. *Journal of Structural Geology,* 26**,** 503-517.

165. Kim, Y. S. and D. J. Sanderson (2005). "The relationship between displacement and length of faults: a review." *Earth-Science Reviews* 68(3-4), 317-334.

166. Kimbell, G. S., Ritchie, J. D., Johnson, H. & Gatliff, R. W. 2005. Controls on the structure and evolution of the NE Atlantic margin revealed by regional potential field imaging and 3D modelling. In: Doré and Vining (eds.) Petroleum Geology: Northwest Europe and Global Perspectives. *Proceedings of the 6th Petroleum Geology Conference.* P. 933-945 Geological Society, London.

167. Klein, F. W., Koyanagi, R. Y., Nakata, J. S. & Tanigawa, W. R. 1987. Volcanism in Hawaii. In: DECKER, R. W., WRIGHT, T. L. & STAUFFER, P. H. (eds.) US Geological Survey Professional Paper 1350.

168. Kolditz, O., Gorke, U. J., Shao, H. & Wenqing, W. (eds.) 2012. Thermo-Hydro-Mechanical-Chemical Processes in Fractured Porous Media, London: Springer.

169. Krantz, R. L. 1979. Crack-crack and crack-pore interactions in stressed granite. *International Journal of Rock Mechanics and Mining Sciences*, 16, 37-47.

170. Kranz, R. L. 1980. The effects of confining pressure and stress difference on static fatigue of granite. *Journal of Geophysical Research*, 85, 1854-1866.

171. Kuster, G. T. & Toksoz, M. 1974. Velocity and attenuation of seismic waves in two-phase media: Part 1. Theoretical formulations. *Geophysics*, 39, 587-606.

172. Lajtai, E. Z. 1974. Brittle fracture in compression. *International Journal of Fracture*, 10, 525-536.

173. Lambiase, J. J. & Bosworth, W. 1995. Structural controls on sedimentation in continental rifts. In: LAMBIASE, J. J. (ed.) Hydrocarbon habitat in rift basins. Geological Society Special Publication no. 80. The Geological Society, London.

174. Langbacka, B. O. & Gudmundsson, A. 1995. Extensional tectonics in the vicinity of a transform fault in north Iceland. *Tectonics*, 14, 294-306.

175. Lawn, B. 1993. Continuum aspects of crack propagation I: linear elastic crack-tip field. In: LAWN, B. (ed.) Fracture of Brittle Solids. P. 16-50. Cambridge, UK: Cambridge University Press.

176. Lazarus, A., Florijn, H. C. B. & Reis, P. M. 2012. Geometry-induced rigidity in non-spherical pressurized elastic shells. *Physical Review Letters*, 109, 1-5.

177. Le Corvec, N. & Walter, T. R. 2009. Volcano spreading and fault interaction influenced by rift zone intrusions: Insights from analogue experiments analyzed with digital image correlation technique. *Journal of Volcanology and Geothermal Research,* 183**,** 170-182.

178. Leguillon, D. & Piat, R. 2008. Fracture of porous materials – Influence of the pore size. *Engineering Fracture Mechanics*, 75, 1840-1853.

179. Li, H., Oppenheimer, S. M., Stupp, S. I., Dunand, D. C. & Brinson, L. C. 2004. Effects of pore morphology and bone ingrowth on mechanical properties of microporous titanium as an orthopaedic implant material. *Materials Transactions*, 45, 1124-1131.

180. Lin, G., and Paul G. Okubo, P.G. 2016. A large refined catalog of earthquake relocations and focal mechanisms for the Island of Hawai'i and its seismotectonic implications. *Journal of Geophysical Research: Solid Earth,* 121.7, 5031-5048.

181. Liu, H. H., Rutqvist, J. & Berryman, J. G. 2009. On the relationship between stress and elastic strain for porous and fractured rock. *International Journal of Rock Mechanics and Mining Sciences*, 46, 289-296.

182. Long, J. J. 2011. Geometry, evolution and scaling of fault relay zones in 3D using detailed observations from outcrops and 3D seismic data. Doctor of Philosophy, Durham University.

183. Long, J. J. & Imber, J. 2010. Geometrically coherent continuous deformation in the volume surrounding a seismically imaged normal fault-array. *Journal of Structural Geology*, 32, 222-234.

184. Long, J. J. & Imber, J. 2011. Geological controls on fault relay zone scaling. *Journal of Structural Geology*, 33, 1790-1800.

185. Lundgren, P., Poland, M., Miklius, A., Orr, T., Yun, S. H., Fielding, E., Liu, Z., Tanaka, A., Szeliga, W., Hensley, S. & Owen, S. 2013. Evolution of dike opening during the March 2011 Kamoamoa fissure eruption, Kīlauea Volcano, Hawai`i. *Journal of Geophysical Research: Solid Earth*, 118, 897-914.

186. Lyle, P. 2000. The eruption environment of multi-tiered columnar basalt lava flows. *Journal of the Geological Society,* 157**,** 715-722.

187. Macdonald, K. C., Sempere, J. C., Fox, P. J. & Tyce, R. 1987. Tectonic evolution of ridge-axis discontinuities by the meeting, linking, or self-decapitation of neighbouring ridge segments. *Geology*, 15, 993-997.

188. Maerten, L., Gillespie, P. & Pollard, D. D. 2002. Effects of local stress perturbation on secondary fault development. *Journal of Structural Geology*, 24, 145-153.

189. Manighetti, I., King, G. & Sammis, C. G. 2004. The role of off-fault damage in the evolution of normal faults. *Earth and Planetary Science Letters*, 217, 399-408.

190. Manzocchi, T., Childs, C. & Walsh, J. J. 2010. Faults and fault properties in hydrocarbon flow models. *Geofluids*, No. 10, 94-113.

191. Marchisio, G., Pacifici, F. & Padwick, C. 2010. On the relative predicative value of the new spectral bands in the WorldView-2 sensor. P. 2723-2726. *International Geoscience and Remote Sensing Symposium.*

192. Martel, S. J. & Langley, J. S. 2006. Propagation of normal faults to the surface in basalt, Koa'e fault system, Hawaii. *Journal of Structural Geology*, 28, 2123-2143.

193. McCaffrey, K.J.W. 2003. Fracture formation and evolution in crystalline rocks: Insights from attribute analysis. *In:* PETFORD, N. & MCCAFFREY, K. J. W. (eds.) Hydrocarbons in Crystalline Rocks. Geological Society London Special Publication 214, 109-124. The Geological Society, London.

194. McClay, K. R. & White, M. J. 1995. Analogue modelling of orthogonal and oblique rifting. *Marine and Petroleum Geology*, 12, 137-151.

195. Meyer, V., Nicol, A., Childs, C., Walsh, J. J. & Watterson, J. 2002. Progressive localisation of strain during the evolution of a normal fault population. *Journal of Structural Geology*, 24, 1215-1231.

196. Michie, E. a. H., Haines, T. J., Healy, D., Neilson, J. E., Timms, N. E. & Wibberley, C. a. J. 2014. Influence of carbonate facies on fault zone architecture. *Journal of Structural Geology,* 65**,** 82-99.

197. Moore, R. B. & Trusdell, F. A. 1993. Geology of Kilauea Volcano. *Geothermics,* 22**,** 243-254.

198. Morewood, N. C. & Roberts, G. P. 2000. The geometry, kinematics and rates of deformation within an en echelon normal fault segment boundary, central Italy. *Journal of Structural Geology*, 22, 1027-1047.

199. Morgan, J. K., Moore, G. F., Hills, D. J. & Leslie, S. 2000. Overthrusting and sediments accretion along Kilauea's mobile south flank, Hawaii: Evidence for volcanic spreading from marine seismic reflection data. *Geology,* 28**,** 667-670.

200. Morley, C. K., Nelson, R. A., Patton, T. I. & Munn, S. G. 1990. Transfer zones in the East Africa Rift System and their relevance to hydrocarbon exploration in rifts. *The American Association of Petroleum Geologists Bulletin*, 74, 1234-1253.

201. Moy, D. J. & Imber, J. 2009. A critical analysis of the structure and tectonic significance of rift-oblique lineaments ('transfer zones') in the Mesozoic-Cenozoic

succession of the Faroe-Shetland Basin, NE Atlantic margin. *Journal of the Geological Society*, 166, 831-844.

202. Nakajima, H. 2007. Fabrication, properties and application of porous metals with directional pores. *Progress in Materials Science*, 52, 1091-1173.
203. Nakamura, T., Qian, G. & Berndt, C. C. 2000. Effects of pores on the mechanical properties of plasma-sprayed ceramic coatings. *Journal of American Ceramics Society*, 83, 578-584.
204. Nasto, A. M. 2011. Localisation of Deformation in Thin Shells Under Indentation. Master of Science, Massachusetts Institute of Technology.
205. Neal, C. A. & Lockwood, J. P. 2003. Geologic map of the summit region of Kilauea volcano, Hawaii. *USGS Geologic Investigation Series,* I-2759.
206. Nelson, R. A., Patton, T. L. & Morley, C. K. 1992. Rift-segment interaction and its relation to hydrocarbon explortion in continental rift systems. *The American Association of Petroleum Geologists Bulletin*, 76, 1153-1169.
207. Nicol, A., Walsh, J., Berryman, K. & Villamor, P. 2006. Interdependence of fault displacement rates and paleoearthquakes in an active rift. *Geology*, 34, 865-868.
208. Nicol, A., Watterson, J., Walsh, J.J and Childs, C. 1996. The shapes, major axis orientations and displacement patterns of fault surfaces. *Journal of Structural Geology*, 18, 235-248.
209. Nicol, A., Walsh, J. J., Villamor, P., Seebeck, H. & Berryman, K. R. 2010. Normal fault interactions, paleoearthquakes and growth in an active rift. Journal of Structural *Geology*, 32, 1101-1113
210. Nixon, C. W., Sanderson, D. J., Dee, S. J., Bull, J. M., Humphreys, R. J. & Swanson, M. H. 2014. Fault interactions and reactivation within a normal-fault network at Milne Point, Alaska. *The American Association of Petroleum Geologists Bulletin*, 98, 2081-2107.
211. Oelkers, E. H. & Cole, D. R. 2008. Carbon dioxide sequestration a solution to a global problem. *Elements*, 4, 305-310.
212. Okubo, P. G., Benz, H. M. & Chouet, B. A. 1997. Imaging the crustal magma sources beneath Mauna Loa and Kilauea volcanoes, Hawaii. *Geology,* 25**,** 867-870.
213. Olson, J. & Pollard, D. D. 1989. Inferring paleostresses from natural fracture patterns: A new method. *Geology,* 17**,** 345-348.
214. Opheim, J. A. & Gudmundsson, A. 1989. Formation and geometry of fractures, and related volcanism, of the Krafla fissure swarm, northeast Iceland. *Geological Society of America Bulletin,* 101**,** 1608-1622.

215. Owen, S., Segall, P., Lisowski, M., Miklius, A., Denlinger, R. P. & Sako, M. 2000. Rapid deformation of Kilauea Volcano: Global Positioning System measurements between 1990 and 1996. *Journal of Geophysical Research*, 105, 18,983-18,998.

216. Palchik, V. 1999. Technical note: Influence of porosity and elastic modulus on uniaxial compressive strength in soft brittle porous sandstones. *Rock Mechanics and Rock Engineering*, 32, 303-309.

217. Palchik, V. & Hatzor, Y. H. 2002. Crack damage stress as a composite function of porosity and elastic matrix stiffness in dolomites and limestones. *Engineering Geology*, 63, 233-245.

218. Palchik, V. & Hatzor, Y. H. 2004. The Influence of Porosity on Tensile and Compressive Strength of Porous Chalks. *Rock Mechanics and Rock Engineering*, 37, 331-341.

219. Parfitt, E. A. & Peacock, D. C. P. 2001. Faulting in the south flank of Kilauea volcano, Hawai'i. *Journal of Volcanology and Geothermal Research,* 106**,** 265-284.

220. Peacock, D. C. P. 2002. Propagation, interaction and linkage in normal fault systems. *Earth Science Reviews*, 58, 121-142.

221. Peacock, D. C. P. 2003. Scaling of transfer zones in the British Isles. *Journal of Structural Geology*, 25, 1561-1567.

222. Peacock, D. C. P. & Parfitt, E. A. 2002. Active relay ramps and normal fault propagation on Kilauea Volcano, Hawaii. *Journal of Structural Geology*, 24, 729-742.

223. Peacock, D. C. P. & Sanderson, D. J. 1991. Displacements, segment linkage and relay ramps in normal fault zones. *Journal of Structural Geology*, 13, 721-733.

224. Peacock, D. C. P. & Sanderson, D. J. 1992. Effects of layering and anisotropy on fault geometry. *Journal of the Geological Society*, 149, 793-802.

225. Peacock, D. C. P. & Sanderson, D. J. 1994. Geometry and Development of Relay Ramps in Normal Fault Systems. *The American Association of Petroleum Geologists Bulletin,* 78, 147-165.

226. Peacock, D. C. P., Price, S. P., Whitham, A. G. & Pickles, C. S. 2000a. The World's biggest relay ramp: Hold With Hope, NE Greenland. *Journal of Structural Geology*, 22, 843-850.

227. Peacock, D. C. P., Knipe, R. J. & Sanderson, D. J. 2000b. Glossary of normal faults. *Journal of Structural Geology*, 22, 291-305.

228. Pedersen, R., Sigmundsson, F. & Masterlark, T. 2009. Rheologic controls on inter-rifting deformation of the Northern Volcanic Zone, Iceland. *Earth and Planetary Science Letters*, 281, 14-26.

229. Perdigou, C. 2010. Geometrically Induced Rigidity of Thin Shells and Negative Poisson's Ratio Structures. Masters Thesis, Massachusetts Institute of Technology.
230. Petford, N. 2003. Controls on primary porosity and permeability development in igneous rocks. *In:* PETFORD, N. & MCCAFFREY, K. J. W. (eds.) *Hydrocarbons in Crystalline Rocks.* Geological Society London Special Publication 214, 1-5. The Geological Society, London.
231. Phillips, J. C., Humphreys, M. C. S., Daniels, K. A., Brown, R. J. & Witham, F. 2013. The formation of columnar joints produced by cooling in basalt at Staffa, Scotland. *Bulletin of Volcanology*, 75.
232. Planke, S. 1994. Geophysical response of flood basalts from analysis of wire line logs: Ocean Drilling Program Site 642, Vöring volcanic margin. *Journal of Geophysical Research*, 99, 9279-9296.
233. Planke, S. & Eldholm, O. 1994. Seismic response and construction of seaward dipping wedges of flood basalts: Vøring volcanic margin. *Journal of Geophysical Research*, 99, 9263-9278.
234. Planke, S., Alvestad, E. & Eldhom, O. 1999. Seismic characteristics of basaltic extrusive and intrusive rocks. *The Leading Edge*, March 1998, 342-348.
235. Planke, S., Symonds, P. A., Alvestad, E. & Skogseid, J. 2000. Seismic volcanostratigraphy of large-volume basaltic extrusive complexes on rifted margins. *Journal of Geophysical Research*, 105, 19335.
236. Plattner, C., Amelung, F., Baker, S., Govers, R. & Poland, M. 2013. The role of viscous magma mush spreading in volcanic flank motion at Kīlauea Volcano, Hawai'i. *Journal of Geophysical Research: Solid Earth,* 118**,** 2474-2487.
237. Podolsky, D. M. W. & Roberts, G. P. 2008. Growth of the volcano-flank Koa'e fault system, Hawaii. *Journal of Structural Geology,* 30**,** 1254-1263.
238. Poland, M., Miklius, A., Orr, T., Sutton, J., Thornber, C. & Wilson, D. 2008. New episodes of volcanism at Kilauea Volcano, Hawaii. *Eos Transactions, American Geophysical Union*, 89, 37-48.
239. Poland, M. P., Miklius, A., Sutton, A. J. & Thornber, C. R. 2012. A mantle-driven surge in magma supply to Kilauea Volcano during 2003-2007. *Nature Geoscience*, 5, 295-300.
240. Pollard, D. D. & Aydin, A. 1984. Propagation and linkage of oceanic ridge segments. *Journal of Geophysical Research*, 89, 10,017-10,028.
241. Pollard, D. D. & Fletcher, R. C. 2005. Fundamentals of Structural Geology, Cambridge, UK, Cambridge University Press.

242. Pollard, D. D. & Muller, O. H. 1976. The effect of gradients in regional stress and magma pressure on the form of sheet intrusions in cross section. *Journal of Geophysical Research*, 81, 975-984.

243. Pollard, D. D. & Segall, P. 1987. Theoretical displacements and stresses near fractures in rock: with applications to faults, joints, veins, dikes and solution surfaces. *In:* ATKINSON, B. K. (ed.) *Fracture mechanics of rock.* San Diego, USA: Academic Press Inc.

244. Pollard, D. D., Segall, P. & Delaney, P. T. 1982. Formation and interpretation of dilatant echelon cracks. *Geological Society of America Bulletin*, 93, 1291.

245. Quane, S. L., Garcia, M. O., Guillou, H. & Hulsebosch, T. P. 2000. Magmatic history of the east rift zone of Kilauea volcano, Hawaii, based on drill core from SOH 1. *Journal of Volcanology and Geothermal Research*, 102, 319-338.

246. Reches, Z. & Lockner, D. A. 1994. Nucleation and growth of faults in brittle rocks. *Journal of Geophysical Research*, 99, 18,159-18,173.

247. Renshaw, C. E. & Pollard, D. D. 1994. Are large differential stresses required for straight fracture propagation paths? *Journal of Structural Geology*, 16, 817-822.

248. Rezvani Khalilabad, M., Axelsson, G. & Gislason, S. R. 2008. Aquifer characterization with tracer test technique; permanent CO2 sequestration into basalt, SW Iceland. *Mineralogical Magazine*, 72, 121-125.

249. Rhodes, J. M. & Vollinger, M. J. 2005. Ferric/ferrous ratios in 1984 Mauna Loa lavas: a contribution to understanding the oxidation state of Hawaiian magmas. *Contributions to Mineralogy and Petrology*, 149, 666-674.

250. Rice, R. W. 1997. Limitations of pore-stress concentrations on the mechanical properties of porous materials. *Journal of Materials Science*, 32, 4731-4736.

251. Rice, R. W. 1998. Porosity of Ceramics: Properties and Applications, New York, Marcel Dekker, Inc.

252. Rieke III, H.H. & Chilingarian, G.V. 1974. Compaction of Argillaceous Sediments. Developments in Sedimentology, Vol. 16. Elsevier Scientific Publishing, London.

253. Rippington, S. J., Mazur, S. & Warner, J. 2015. The crustal architecture of the Faroe-Shetland Basin: insights from a newly merged gravity and magnetic dataset. *In:* RICHARDS, F.L., RICHARDSON, N.J. RIPPINGTON, S.J., WILSON, R.W. & BOND, C.E. (eds.) *Industrial Structural Geology: Principles, Techniques and Integration.* Geological Society London Special Publication 421. The Geological Society, London.

254. Ritchie, J. D., Johnson, H. & Kimbell, G. S. 2003. The nature and age of Cenozoic contractional deformation within the NE Faroe–Shetland Basin. *Marine and Petroleum Geology*, 20, 399-409.

255. Rognvaldsson, S. T., Gudmundsson, A. & Slunga, R. 1998. Seismotectonic analysis of the Tjornes Fracture Zone, an active transform fault in north Iceland. *Journal of Geophysical Research*, 103, 30,117-30,129.

256. Rosendahl, B. R. 1987. Architecture of continental rifts with special reference to East Africa. *Ann. Rev. Earth Planet. Sci*., 15, 445-503.

257. Rosendahl, B. R., Reynolds, D. J., Lorber, P. M., Burgess, C. F., Mcgill, J., Scott, D., Lambiase, J. J. & Derksen, S. J. 1986. Structural Expressions of Rifting: Lessons from Lake Tanganyika, Africa. *In:* FROSTICK, L.E. (eds.) *Sedimentation in the African Rifts.* Geological Society London Special Publication 25, 29-43. The Geological Society, London.

258. Rotevatn, A., Fossen, H., Hesthammer, J., Aas, T. E. & Howell, J. A. 2007. Are relay ramps conduits for fluid flow? Structural analysis of a relay ramp in Arches National Park, Utah. *In:* LONERGAN, L., JOLLEY, R.J.H., RAWNSLEY, K. & SANDERSON, D.J. (eds.) *Fractured Reservoirs.* Geological Society London Special Publication 270, 55-71. The Geological Society, London.

259. Rowland, J. V., Baker, E., Ebinger, C. J., Keir, D., Kidane, T., Biggs, J., Hayward, N. & Wright, T. J. 2007. Fault growth at a nascent slow-spreading ridge: 2005 Dabbahu rifting episode, Afar. *Geophysical Journal International, 171*(3), 1226-1246.

260. Rubin, A. M. 1990. A comparison of rift-zone tectonics in Iceland and Hawaii. *Bulletin of Volcanology,* 52**,** 302-319.

261. Rubin, A. M. 1992. Dike-induced faulting and graben subsidence in volcanic rift zones. *Journal of Geophysical Research: Solid Earth*, 97, 1839-1858.

262. Rubin, A. M. 1993. Tensile fracture of rock at high confining pressure: implications for dike propagation. *Journal of Geophysical Research*, 98, 15,919-15,935.

263. Rubin, A. M. 1995. Propagation of magma-filled cracks. *Ann. Rev. Earth Planet. Sci*., 23, 287-336.

264. Rumph, B., Reaves, C. M., Orange, V. G. & Robinson, D. L. 1993. Structuring and transfer zones in the Faeroe Basin in a regional tectonic context. *Petroleum Geology Conference Series*, 4, 999-1009.

265. Saar, M. O. & Manga, M. 1999. Permeability-porosity relationship in vesicular basalts. *Geophysical Research Letters*, 26, 111-114.

266. Sabatakakis, N., Koukis, G., Tsiambaos, G. & Papanakli, S. 2008. Index properties and strength variation controlled by microstructure for sedimentary rocks. *Engineering Geology*, 97, 80-90.

267. Sæmundsson, K. 1974. Evolution of the axial rifting zone in northern Iceland and the Tjörnes Fracture Zone. *Geological Society of America Bulletin*, 85, 495-504.

268. Sammis, C. G. & Ashby, M. F. 1986. The failure of brittle porous solids under compressive stress. *Acta Metallurgica*, 34, 511-526.

269. Savage, J.C., Byerlee, J.D. and Lockner, D.A., 1996. Is internal friction friction?. *Geophysical research letters*, 23 (5), pp.487-490.

270. Schaefer, L. N., Kendrick, J. E., Oommen, T., Lavallee, Y. & Chigna, G. 2015. Geomechanical rock properties of a basaltic volcano. *Frontiers in Earth Science*, 3.

271. Schiffman, P., Watters, R. J., Thompson, N. & Walton, A. W. 2006. Hyaloclastites and the slope stability of Hawaiian volcanoes: Insights from the Hawaiian Scientific Drilling Project's 3-km drill core. *Journal of Volcanology and Geothermal Research*, 151, 217-228.

272. Schöpfer, M. P. J., Childs, C. & Walsh, J. J. 2006. Localisation of normal faults in multilayer sequences. *Journal of Structural Geology*, 28, 816-833.

273. Schöpfer, M. P. J., Childs, C., Walsh, J. J., Manzocchi, T. & Koyi, H. A. 2007. Geometrical analysis of the refraction and segmentation of normal faults in periodically layered sequences. *Journal of Structural Geology*, 29, 318-335.

274. Schöpfer, M. P. J., Abe, S., Childs, C. & Walsh, J. J. 2009. The impact of porosity and crack density on the elasticity, strength and friction of cohesive granular materials: Insights from DEM modelling. *International Journal of Rock Mechanics and Mining Sciences*, 46, 250-261.

275. Schutter, S. R. 2003. Hydrocarbon occurrence and exploration in and around igneous rocks. *In:* PETFORD, N. & MCCAFFREY, K. J. W. (eds.) *Hydrocarbons in Crystalline Rocks.* Geological Society London Special Publication 214, 7-33. The Geological Society, London.

276. Seebeck, H., Nicol, A., Walsh, J. J., Childs, C., Beetham, R. D. & Pettinga, J. 2014. Fluid flow in fault zones from an active rift. *Journal of Structural Geology*, 62, 52-64.

277. Segall, P. & Pollard, D. D. 1980. Mechanics of discontinuous faults. *Journal of Geophysical Research*, 85, 4337-4350.

278. Self, S., Thordarson, T., Keszthelyi, L., Walker, G. P. L., Hon, K., Murphy, M. T., Long, P. & Finnemore, S. 1996. A new model for the emplacement of Columbia

River basalts as large, inflated Pahoehoe Lava Flow Fields. *Geophysical Research Letters*, 23, 2689-2692.

279. Self, S., Coffin, M. F., Rampino, M. R. & Wolff, J. A. 2015. Large igneous provinces and flood basalt volcanism. In: SIGURDSSON, H., HOUGHTON, B., MCNUTT, S., RYMER, H. & STIX, J. (eds.) The Encyclopedia of Volcanoes (Second Edition), 441-455. London, UK: Academic Press.
280. Sevostianov, I. & Kushch, V. 2009. Effect of pore distribution on the statistics of peak stress and overall properties of porous material. *International Journal of Solids and Structures*, 46, 4419-4429.
281. Sharp, I., Gawthorpe, R. L., Armstrong, B. & Underhill, J. R. 2000. Propagation history and passive rotation of mesoscale normal faults: implications for syn-rift stratigraphic development. *Basin Research*, 12, 285-305.
282. Shen, S. S., Puetz, A. M., Lee, K., Olsen, C. R. & Lewis, P. E. 2009. WorldView-2 data simulation and analysis results. *In:* SHEN, S.S. & LEWIS, P.E. Algorithms and Technologies for Multispectral, Hyperspectral, and Ultraspectral Imagery XV. *Proceedings of SPIE*, vol. 7334, 1-10.
283. Sibson, R. H. 1977. Fault rocks and fault mechanisms. *Journal of the Geological Society London*, 133, 191-213.
284. Sibson, R. H. 1985. Short notes: a note on fault reactivation. *Journal of Structural Geology*, 7, 751-754.
285. Sibson, R. H. 1990. Conditions for fault-valve behaviour. *In:* KNIPE, R.J. & RUTTER, E.H. (eds.) Deformation Mechanisms, Rheology and Tectonics. Geological Society London Special Publication 54, 15-28. The Geological Society, London.
286. Sibson, R. H. 1994. Crustal stress, faulting and fluid flow. *In:* PARNELL, J. (eds.) Geofluids: Origin, Migration and Evolution of Fluids in Sedimentary Basins. Geological Society London Special Publication 78, 69-84.
287. Sibson, R. H. 2004. Controls on maximum fluid overpressure defining conditions for mesozonal mineralisation. *Journal of Structural Geology*, 26, 1127-1136.
288. Sih, G. C. 1976. Fracture toughness concept. *In:* Properties Related to Fracture Toughness. American Society for Testing and Materials, Vol.605.
289. Smallwood, J. R. & White, R. S. 2002. Ridge-plume interaction in the North Atlantic and its influence on continental breakup and seafloor spreading. In: JOLLEY, D. W. & BELL, B. R. (eds.) The North Atlantic Igneous Province: Stratigraphy, Tectonic, Volcanic and Magmatic Processes. Geological Society London Special Publication 197, 15-37. The Geological Society, London.

290. Soliva, R. & Benedicto, A. 2004. A linkage criterion for segmented normal faults. *Journal of Structural Geology*, 26, 2251-2267.

291. Sorensen, A. B. 2003. Cenozoic basin development and stratigraphy of the Faroes area. *Petroleum Geoscience*, 9, 189-207.

292. Stewart, I. S. & Hancock, P. L. 1991. Scales of structural heterogeneity within neotectonic normal fault zones in the Aegean region. *Journal of Structural Geology*, 13, 191-204.

293. Sveinbjornsdottir, A., Armannsson, H., Oskarsson, F., Olafsson, M. & Sigurdardottir, A. K. 2015. A conceptual hydrological model of the thermal areas within the Northern Neovolcanic Zone, Iceland using stable water isotopes. *Proceedings World Geothermal Congress*. Melbourne, Australia, 19th-25th April, 2015, 1-7.

294. Swanson, D. A., Duffield, W. A. & Fiske, R. S. 1976. Displacement of the south flank of Kilauea Volcano: the result of forceful intrusion of magma into the rift zones. *US Geological Survey Professional Paper*, 963.

295. Swanson, D. A., Fiske, R. S. & Thornber, C. 2012. Vents and dikes in the heart of the Koa'e Fault System at Kilauea. *American Geophysical Union Fall Meeting.* San Francisco.

296. Tapponier, P., Armijo, R., Manighetti, I. & Courtillot, V. 1990. Bookshelf faulting and horizontal block rotations between overlapping rifts in Southern Afar. *Geophysical Research Letters*, 17, 1-4.

297. Tegner, C., Duncan, R. A., Bernstein, S., Brooks, C. K., Bird, D. K. & Storey, M. 1998. 40Ar-39Ar geochronology of Tertiary mafic intrusions along the East Greenland rifted margin: Relation to flood basalts and the Iceland hotspot track. *Earth and Planetary Science Letters*, 156, 75-88.

298. Tentler, T. 2003. Analogue modeling of overlapping spreading centers: insights into their propagation and coalescence. *Tectonophysics*, 376, 99-115.

299. Tentler, T. 2005. Propagation of brittle failure triggered by magma in Iceland. *Tectonophysics*, 406, 17-38.

300. Tentler, T. & Acocella, V. 2010. How does the initial configuration of oceanic ridge segments affect their interaction? Insights from analogue models. *Journal of Geophysical Research*, 115, 1-16.

301. Terzaghi, K. V. 1925. Principles of soil mechanics II. Compressive strength of clays. *Eng. News. Rec.,* 95, 796-800.

302. Terzaghi, K. V. 1943. Theoretical Soil Mechanics, New York, Wiley.

303. Thomas, A. L. & Pollard, D. D. 1993. The geometry of en echelon fractures in rock: implications from laboratory and numerical experiments. *Journal of Structural Geology*, 15, 323-334.

304. Thompson, N., Watters, R. J. & Schiffman, P. 2008. Stability analysis of Hawaiian Island flanks using insight gained from strength testing of the HSDP core. *Journal of Volcanology and Geothermal Research*, 171, 163-177.

305. Trudgill, B. & Cartwright, J. 1994. Relay-ramp forms and normal fault linkages. Canyonlands National Park, Utah. *Geological Society of America Bulletin,* 106**,** 1143-1157.

306. Tryggvason, E. 1981. Pressure variations and volume of the Krafla magma reservoir. University of Iceland: Nordic Volcanological Institute 8105, 1-19.

307. Tryggvason, E. 1984. Widening of the Krafla fissure swarm during the 1975-1981 volcano-tectonic episode. *Bulletin of Volcanology*, 47-1, 47-69.

308. Tryggvason, E. 1986. Multiple magma reservoirs in a rift-zone volcano - ground deformation and magma transport during the September 1984 eruption of Krafla, Iceland. *Journal of Volcanology and Geothermal Research*, 28, 1-44.

309. Tryggvason, E. 1994. Surface deformation at the Krafla volcano, North Iceland. *Bulletin of Volcanology*, 56, 98-107.

310. Tuğrul, A. 2004. The effect of weathering on pore geometry and compressive strength of selected rock types from Turkey. *Engineering Geology*, 75, 215-227.

311. Tuğrul, A. & Gurpinar, O. 1997. A proposed weathering classification for basalts and their engineering properties (Turkey). *Bulletin of the International Association of Engineering Geology*, 55, 139-149.

312. Turk, N. & Dearman, W. R. 1983. A practical classification of rocks for engineering purposes. *Bulletin of the International Association of Engineering Geology*, No. 28, 161-167.

313. Van Gent, H. W., Holland, M., Urai, J. L. & Loosveld, R. 2010. Evolution of fault zones in carbonates with mechanical stratigraphy – Insights from scale models using layered cohesive powder. *Journal of Structural Geology*, 32, 1375-1391.

314. Vanorio, T., Prasad, M. & Nur, A. 2003. Elastic properties of dry clay mineral aggregates, suspensions and sandstones. *Geophysical Journal International*, 155, 319-326.

315. Vasseur, J., Wadsworth, F. B., Lavallee, Y., Bell, A. F., Main, I. G. & Dingwell, D. B. 2015. Heterogeneity: The key to failure forecasting. *Nature Scientific Reports*, 5, 1-7.

316. Vaziri, A. 2009. Mechanics of highly deformed elastic shells. *Thin-Walled Structures*, 47, 692-700.

317. Vella, D., Ajdari, A., Vaziri, A. & Boudaoud, A. 2012. Indentation of Ellipsoidal and Cylindrical Elastic Shells. *Physical Review Letters*, 109, 1-5.

318. Vermilye, J. M. & Scholz, C. H. 1995. Relation between vein length and aperture. *Journal of Structural Geology,* 17**,** 423-434.

319. Vermilye, J. M. & Scholz, C. H. 1998. The process zone: A microstructural view of fault growth. *Journal of Geophysical Research*, 103, 12223.

320. Villemin, T. & Bergerat, F. 2013. From surface fault traces to a fault growth model: The Vogar Fissure Swarm of the Reykjanes Peninsula, Southwest Iceland. *Journal of Structural Geology,* 51**,** 38-51.

321. Vinciguerra, S., Trovato, C., Meredith, P. G. & Benson, P. M. 2005. Relating seismic velocities, thermal cracking and permeability in Mt. Etna and Iceland basalts. *International Journal of Rock Mechanics and Mining Sciences*, 42, 900-910.

322. Walker, R. J. 2010. The Structural Evolution of the Faroe Islands, NE Atlantic Margin. Doctor of Philosophy, Durham Univerisity.

323. Walker, R. J., Holdsworth, R. E., Imber, J. & Ellis, D. 2011. Onshore evidence for progressive changes in rifting directions during continental break-up in the NE Atlantic. *Journal of the Geological Society*, 168, 27-48.

324. Walker, R. J., Holdsworth, R. E., Imber, J. & Ellis, D. 2012. Fault-zone evolution in layered basalt sequences: A case study from the Faroe Islands, NE Atlantic margin. *Geological Society of America Bulletin*, 124, 1382-1393.

325. Walker, R. J., Holdsworth, R. E., Imber, J., Faulkner, D. R. & Armitage, P. J. 2013. Fault zone architecture and fluid flow in interlayered basaltic volcaniclastic-crystalline sequences. *Journal of Structural Geology*, 51, 92-104.

326. Walsh, J. J. & Watterson, J. 1987. Distributions of cumulative displacement and seismic slip on a single normal fault surface. *Journal of Structural Geology*, 9, 1039-1046.

327. Walsh, J. J. & Watterson, J. 1991. Geometric and kinematic coherence and scale effects in normal fault systems. *In:* ROBERTS, A. M., YIELDING, G. & FREEMAN, B. (eds.) *The Geometry of Normal Faults.* Geological Society London Special Publication 56, 193-203. The Geological Society, London.

328. Walsh, J. J., Nicol, A. & Childs, C. 2002. An alternative model for the growth of faults. *Journal of Structural Geology*, 24, 1669-1675.

329. Walsh, J. J., Bailey, W. R., Childs, C., Nicol, A. & Bonson, C. G. 2003. Formation of segmented normal faults: a 3D perspective. *Journal of Structural Geology*, 25, 1251-1262.

330. Wang, E. Z. & Shrive, N. G. 1999. A 3-D ellipsoidal flaw model for brittle fracture in compression. *International Journal of Solids and Structures*, 36, 4089-4109.

331. White, I. R. & Crider, J. G. 2006. Extensional fault-propagation folds: mechanical models and observations from the Modoc Plateau, northeastern California. *Journal of Structural Geology*, 28, 1352-1370.

332. Wilkens, R. H., Fryer, G. J. & Karsten, J. 1991. Evolution of porosity and seismic structure of upper oceanic crust: Importance of aspect ratios. *Journal of Geophysical Research*, 96, 17,981-17,995.

333. Willemse, E. J. M., Pollard, D. D. & Aydin, A. 1996. Three-dimensional analyses of slip distributions on normal fault arrays with consequences for fault scaling. *Journal of Structural Geology*, 18, 295-309.

334. Withjack, M. O., Olsen, J. & Peterson, E. 1990. Experimental models of extensional forced folds. *The American Association of Petroleum Geologists Bulletin,* 74**,** 1038-1054.

335. Wolfe, E. W. & Morris, J. 1996. Geologic map of the island of Hawaii. USGS Numbered Series 2524.

336. Wotzlaw, J. F., Bindeman, I. N., Schaltegger, U., Brooks, C. K. & Naslund, R. H. 2012. High-resolution insights into episodes of crystallization, hydrothermal alteration and remelting in the Skaergaard intrusive complex. *Earth and Planetary Science Letters*, 355-356, 199-212.

337. Wong, T.F. 1990. Mechanical compaction and the brittle-ductile transition in porous sandstones. *In:* KNIPE, R.J. & RUTTER, E.H. (eds.) Deformation Mechanisms, Rheology and Tectonics. Geological Society London Special Publication 54, 15-28. The Geological Society, London.

338. Wright, T. L. & Klein, F. W. 2006. Deep magma transport at Kilauea volcano, Hawaii. *Lithos,* 87**,** 50-79.

339. Wright, T. J., Sigmundsson, F., Pagli, C., Belachew, M., Hamling, I. J., Brandsdottir, B., Keir, A., Pedersen, R., Ayele, A., Ebinger, C., Einarsson, P., Lewi, E. & Calais, E. 2012. Geophysical constraints on the dynamics of spreading centres from rifting episodes on lands. *Nature Geoscience*, 5, 242-250.

340. Yale, D. P. & Nieto, J. A. 1995. The effect of cementation on the static and dynamic mechanical properties of the Rotliegendes sandstone. *In:* DAEMEN, J.J.K. &

SCHULTZ, A.A. (eds.) Proceedings of the 35th US Syposium on Rock Mechanics. A.A Balkema, Rotterdam, Netherlands.

341. Yesou, H., Besnus, Y. & Rolet, J. 1993. Extraction of spectral information from LandsatTM data and merger with SPOT panchromatic imagery - a contribution to the study of geological structures. *Journal of Photogrammetry and Remote Sensing,* 48, 23-36.

342. Zugic, R., Szpunar, B., Krstic, V. D. & Erb, U. 2006. Effect of porosity on the elastic response of brittle materials: an embedded-atom method approach. *Philosophical Magazine A*, 75, 1041-1055.